ABSTRACT

Title of dissertation:	ELECTRONIC TRANSPORT MEASUREMENTS IN THE ELECTRON-DOPED HIGH-TEMPERATURE SUPERCONDUCTOR Pr$_{2-x}$Ce$_x$CuO$_{4\pm\delta}$
	Paul Leonard Bach, Doctor of Philosophy, 2011
Dissertation directed by:	Professor Richard L. Greene Department of Physics

This thesis is composed of four major parts centered around the electron-doped superconductor Pr$_{2-x}$Ce$_x$CuO$_{4\pm\delta}$: angular magnetoresistance studies of antiferromagnetism, doping effects of oxygenation, T_c enhancement by the creation of superlattices, and comparison of high-temperature resistivity with the pnictides.

The first part focuses on transport measurements of the magnetism in Pr$_{2-x}$Ce$_x$CuO$_{4\pm\delta}$ and La$_{2-x}$Ce$_x$CuO$_{4\pm\delta}$. It was found that the thermal evolution of the angular dependence of magnetoresistance in Pr$_{2-x}$Ce$_x$CuO$_{4\pm\delta}$ can be used to determine the Néel temperature in that material. This angular magnetoresistance technique was also applied to La$_{2-x}$Ce$_x$CuO$_{4\pm\delta}$; evidence for antiferromagnetism in this system was observed as well. This section additionally develops angular magnetoresistance as a useful probe in other cuprate projects here described.

The second part investigates over-oxygenated and irradiated Pr$_{2-x}$Ce$_x$CuO$_{4\pm\delta}$, in under- and optimal dopings. Resistivity, Hall effect, and angular magnetoresistance measurements show oxygen both doping and disordering the system, in agreement with over-

doped films. The evolution of both the Hall effect and angular magnetoresistance shows that over-oxygenation results in significant changes in the number of charge carriers, regardless of the increase in scattering incurred. Additionally, this study indicates that annealing primarily removes apical oxygen, rather than other proposed behaviors.

The third part studies multi-layer films of $Pr_{2-x}Ce_xCuO_{4\pm\delta}$ and $La_{2-x}Ce_xCuO_{4\pm\delta}$. These superlattices exhibit a significant T_c enhancement over component layers' T_cs. Interface effects are excluded as a source of this T_c increase based upon critical current measurments. The T_c enhancement is found to be due to charge redistribution. Based on Hall and angular magnetoresistance measurements, the result of this redistribution is slightly net-under-doped films.

The fourth part uses $Pr_{2-x}Ce_xCuO_{4\pm\delta}$ and $Nd_{2-x}Ce_xCuO_{4\pm\delta}$ as comparisons to investigate the high-temperature resistivity behavior in the $SrFe_2As_2$ system. $Pr_{2-x}Ce_xCuO_{4\pm\delta}$ and $Nd_{2-x}Ce_xCuO_{4\pm\delta}$ are shown to be similar to other cuprate systems in that they strongly violate the Mott-Ioffe-Regel limit, an indication of strong correlations. The $SrFe_2As_2$ system was found to saturate near the Mott-Ioffe-Regel resistivity, ruling out strong, cuprate-like correlations in the pnictide superconductors.

Finally, some aborted attempts at synthesis of thin films of superconducting Pr_2CuO_4 and iron-based superconductors are discussed. Pr_2CuO_4 is suggested to be an important system for understanding oxygenation in $Pr_{2-x}Ce_xCuO_{4\pm\delta}$.

ELECTRONIC TRANSPORT MEASUREMENTS IN THE
ELECTRON-DOPED HIGH-TEMPERATURE SUPERCONDUCTOR
$Pr_{2-x}Ce_xCuO_{4\pm\delta}$

by

Paul Leonard Bach

Dissertation submitted to the Faculty of the Graduate School of the
University of Maryland, College Park in partial fulfillment
of the requirements for the degree of
Doctor of Philosophy
2011

Advisory Committee:
Professor Richard L. Greene, Chair/Advisor
Professor Ichiro Takeuchi
Professor Johnpierre Paglione
Professor J. Robert Anderson
Professor H. Dennis Drew

Table of Contents

List of Tables

List of Figures

List of Abbreviations

11	compounds related to FeSe
1111	compounds related to LaOFeAs
122	compounds related to $SrFe_2As_2$
214	compounds related to RE_2CuO_4
AC	alternating current
$AC\chi$	AC susceptibility
AFM	antiferromagnetism
AMR	angular magnetoresistance
ARPES	angle-resolved photoemission spectroscopy
BCS	Bardeen, Cooper, Schrieffer theory
BZ	Brillouin zone
DC	direct current
ECCO	$Eu_{2-x}Ce_xCuO_{4\pm\delta}$
EELS	electron energy-loss spectroscopy
FS	Fermi surface
INS	inelastic neutron scattering
LCCO	$La_{2-x}Ce_xCuO_{4\pm\delta}$
LSCO	$La_{2-x}Sr_xCuO_{4\pm\delta}$
LSGO	$LaSrGaO_4$
LYCO	$La_{2-x}Y_xCuO_{4\pm\delta}$
MIR	Mott-Ioffe-Regel
MOD	metal organic deposition
MR	magnetoresistance
μSR	muon spin resonance
NCCO	$Nd_{2-x}Ce_xCuO_{4\pm\delta}$
NCO	Nd_2CuO_4
NS	neutron scattering
O(1)	oxygen in in-plane lattice sites
O(2)	oxygen in out-of-plane lattice sites
O(3)	oxygen at apical sites
OD	over-doped
PCCO	$Pr_{2-x}Ce_xCuO_{4\pm\delta}$
PCO	Pr_2CuO_4
PLCCO	$Pr_{2-z-x}La_zCe_xCuO_4$
PLD	pulsed laser deposition
PPMS	Quantum Design Physical Properties Measurement System
QCP	Quantum Critical Point
QPT	quantum phase transition
RE	a rare-earth element
SC	superconductivity
SCCO	$Sm_{2-x}Ce_xCuO_{4\pm\delta}$
SCO	Sm_2CuO_4

SDW	spin density wave
SL	superlattice
Sr-122	$SrFe_2As_2$
STO	$SrTiO_3$
T' and T	214 crystal structures (Figure 2.1)
T_c	superconductivity transition temperature
T_N	Néel temperature
UD	under-doped
UHB and LHB	upper and lower Hubbard bands
VDP	van der Pauw
XRD	X-ray diffraction
YBCO	$YBa_2Cu_3O_7$

Chapter 1

Introduction

1.1 Introduction to Superconductivity

A superconductor conducts electricity without resistance. This phenomenon was first discovered in mercury in 1911 by Heike Kamerlingh Onnes [1]. The DC resistance of that material was observed to rapidly transition to zero at 4.2 K. A wide range of materials were subsequently shown to superconduct: chemical elements like lead ($T_c = 7.2$ K), alloys like $Nb_3Al_{0.75}Ge_{0.25}$ ($T_c \approx 20$ K), and many compounds [2]. The transition temperature, T_c, slowly increased over the years, but remained at low temperatures, 25 K or less, for decades [3]. Niobium, with $T_c = 9.2$ K, is the highest T_c elemental superconductor at ambient pressure; from 1972, Nb_3Ge with a T_c of 23.3 K was the highest T_c recorded until 1986 [4]. This dramatically changed in 1986 when Bednorz and Müller reported the discovery of superconductivity at 35 K, the first high-temperature copper-oxide (cuprate) superconductor [5]. The maximum cuprate T_c obtainable was rapidly advanced to 90 K in $YBa_2Cu_3O_7$ and up to 135 K in related cuprates. More recently, in 2008, a second class of high-temperature superconductors was discovered with iron arsenide (FeAs) layers [6, 7] following the discovery of superconductivity in LaFePO [8]. The iron-pnictides now have T_cs up to 55 K [9]. Although both the cuprates and the iron-pnictides will be discussed in this thesis, most of the focus is on the cuprates.

Superconductors also expel magnetic fields. This property was discovered in 1933

by Walther Meissner and Robert Ochsenfeld [10]. This perfect diamagnetism, the Meissner effect, makes superconductors different from an idealized perfect conductor with zero resistance. Superconductors will always expel magnetic flux, even if cooled through T_c in a magnetic field. Therefore, the Meissner effect demonstrates that the superconducting state is not an ideal conductor but is rather the result of the material undergoing a thermodynamic phase transition [3]. If the magnetic field grows too large, however, it will kill superconductivity. Quenching superconductivity by magnetic field also implies that there is a maximum current that the superconductor can carry due to $\nabla \times \vec{B} = \mu_0 \vec{J}$ [11]. Type I superconductors have a single critical field, H_c, that suppresses superconductivity. Type II superconductors have two critical fields, H_{c2} above which superconductivity is completely killed, and H_{c1} below which no magnetic flux penetrates. Between H_{c1} and H_{c2} magnetic flux can pass through the superconductor in normal state vortices surrounded by superconductor [12]. In this mixed state, magnetic flux lines pass through the center of individual vortex cores; a superconducting screening current circulates around each core [11]. All high temperature superconductors are Type II.

Superconductors are understood theoretically through the London equations, the Ginzburg-Landau theory, and BCS theory (and other more complicated models). The London equations are phenomenological equations that describe the current density in superconductors in electric and magnetic fields [12]. H. London and F. London developed this theory in 1935 [13, 14]. The theory takes the form of a two-fluid model with some fraction of the conduction electrons taking part in the superfluid while the remaining electrons form a normal fluid [11]. The London equations roughly capture much of the basic superconductor phenomenology.

The Ginzburg-Landau theory [15] was developed as a phenomeological theory to describe superconductivity. In this theory, there is an order parameter based on the local concentration of conducting electrons that characterizes the superconducting state [3]. Applying the variational method to this pseudo-wavefunction provides a powerful generalization to the London equations [12]. This theory was able to go beyond the London theory and was eventually shown to be a limiting form of subsequent BCS theory [12].

BCS theory, developed by Bardeen, Cooper, and Schrieffer [16, 17], is the modern picture of superconductors. In this model, the atoms on lattice sites are allowed some motion in response to the charged electrons. If this ionic motion "over-screens" the Coulomb repulsion, the net result is attractive interaction between electrons [11]. This attractive interaction between electrons is facilitated by large numbers of additional electrons acting through the Pauli exclusion principle [11].

Roughly, an electron traveling with a momentum $\vec{k}$ drives a lattice vibration which synchronizes a second electron traveling with momentum $-\vec{k}$ with the first [18]. This lattice motion, phonons, causes pairs of quasiparticles (electrons or holes) with opposite spin to interact and become attracted to each other. These pairs together have slightly lower energies as a pair than as separate electrons and, therefore, they form a lower energy state of Cooper pairs. As the pairing is in momentum space, generally there are many Cooper pairs in the same spatial range [19]. The Cooper pair, then, is in a coherent ground state below the Fermi energy; there is an energy gap that is the difference between the Fermi energy and the ground state of the Cooper pairs that is responsible for many of the superconductor's properties [3]. While the high temperature superconductors are probably non-BCS superconductors, the BCS theory still provides a useful framework

for thinking about superconductivity. Probably non-BCS in this context is a statement that the Cooper pairs in the high-temperature cuprate superconductors are unlikely to be mediated by phonon interactions.

Superconductivity was believed to have been well understood in the 1980s, prior to the discovery of the cuprates. Since that discovery, the cuprates have been extensively studied; however, unlike the conventional, low-temperature superconductors the high-temperature superconductors are not well understood, even after 25 years. It is hoped that by studying current superconductors a deeper understanding will eventually be developed that will allow superconductors to be designed with useful properties, like room temperature T_cs. This thesis is an attempt to expand our understanding of superconductivity.

1.2 Introduction to this Thesis

The electron-doped cuprate superconductor $Pr_{2-x}Ce_xCuO_{4\pm\delta}$ is the central focus of this thesis. This system has a maximum T_c of just over 20 K and can be prepared in thin film form. $Pr_{2-x}Ce_xCuO_{4\pm\delta}$ also forms a basis for comparison of related materials studied: $La_{2-x}Ce_xCuO_{4\pm\delta}$, $SrFe_2As_2$, and Pr_2CuO_4.

The basic $Pr_{2-x}Ce_xCuO_{4\pm\delta}$ material properties are discussed in Chapter 2. Crystal structure, magnetic ordering, and electronic configuration are described. The focus of this thesis is on properties that can be investigated with transport measurements.

Basic thin film growth, preparation, and measurement of $Pr_{2-x}Ce_xCuO_{4\pm\delta}$ is covered in Chapter 3. The films are grown by pulsed laser deposition (PLD), patterned, and contacted for electronic transport measurements. Much of the experimental data

discussed was acquired in a Quantum Design Physical Properties Measurement System (PPMS).

The investigations contained herein all involve $Pr_{2-x}Ce_xCuO_{4\pm\delta}$. Firstly, a measurement technique, in-plane angular magnetoresistance, that investigates magnetoresistance as a function of applied magnetic field angle, was used to investigate the antiferromagnetism in $Pr_{2-x}Ce_xCuO_{4\pm\delta}$ and $La_{2-x}Ce_xCuO_{4\pm\delta}$. The Néel temperature as a function of doping was mapped. Secondly, the oxygen content of $Pr_{2-x}Ce_xCuO_{4\pm\delta}$ was studied. A comparison between oxygenated and irradiated films was made and oxygen doping was investigated. The role of annealing was also addressed. Thirdly, layered structures of alternating dopings were investigated in the $Pr_{2-x}Ce_xCuO_{4\pm\delta}$ and $La_{2-x}Ce_xCuO_{4\pm\delta}$ systems. A T_c enhancement due to charge redistribution was found. Fourthly, $Pr_{2-x}Ce_xCuO_{4\pm\delta}$ and $Nd_{2-x}Ce_xCuO_{4\pm\delta}$ were used as a comparison in the investigation of the high-temperature resistive behavior of the $SrFe_2As_2$ system. Pnictide resistivity was found to saturate around the Mott-Ioffe-Regel limit. Finally, other related systems, like Pr_2CuO_4, were investigated. These projects are still works-in-progress.

In the first investigation discussed, transport measurements were used to investigate the antiferromagnetism in $Pr_{2-x}Ce_xCuO_{4\pm\delta}$ and $La_{2-x}Ce_xCuO_{4\pm\delta}$. The first half of Chapter 4 discusses the $Pr_{2-x}Ce_xCuO_{4\pm\delta}$ results and the second half focuses on the $La_{2-x}Ce_xCuO_{4\pm\delta}$ results. In $Pr_{2-x}Ce_xCuO_{4\pm\delta}$, four-fold in-plane angular magnetoresistance oscillations were observed; their disappearance coincided with the Néel temperature and suggested that antiferromagnetism persists in that system up to optimal doping. This is suggestive of a quantum phase transition behind the superconductivity dome. In $La_{2-x}Ce_xCuO_{4\pm\delta}$, two-fold oscillations were observed. With the exception of reduced

symmetry, these oscillations were seen to behave similarly to the angular magnetoresistance in $Pr_{2-x}Ce_xCuO_{4\pm\delta}$. Magnetic data in $La_{2-x}Ce_xCuO_{4\pm\delta}$ has been difficult to obtain and these measurements provide evidence for antiferromagnetism in this system.

Next, $Pr_{2-x}Ce_xCuO_{4\pm\delta}$ investigations of the role of oxygenation are discussed in Chapter 5. A series of over-oxygenated under- and optimally-doped films were prepared. An under-doped irradiated $Pr_{2-x}Ce_xCuO_{4\pm\delta}$ film was used as a comparison by providing a template for disorder effects. It was observed that while resistivity data show significant disorder in oxygenated films, Hall effect data show that oxygen has a significant doping effect. Additionally, angular magnetoresistance data support the doping dependence seen in the Hall effect by examination of the Néel temperature evolution with oxygen doping. Also, this study advances the discussion of the role of annealing in the electron-doped cuprates by favoring removal of apical oxygens over other competing models.

Superlattices formed by layering under-doped and over-doped layers were studied in Chapter 6. In both the $Pr_{2-x}Ce_xCuO_{4\pm\delta}$ and $La_{2-x}Ce_xCuO_{4\pm\delta}$ systems, significant T_c enhancement was found. Critical current measurements were performed to demonstrate that the superconductivity enhancement was not due to an interface effect, but, rather, was due to charge redistribution. Investigation of these superlattices by Hall effect and angular magnetoresistance support charge redistribution. Hall effect and angular magnetoresistance measurements further suggest that charge redistributes to form superlattice thin films that are slightly net-under-doped films.

Penultimately, the high temperature resistivity behavior of the $SrFe_2As_2$ system was investigated in Chapter 7 by comparison to $Pr_{2-x}Ce_xCuO_{4\pm\delta}$ and $Nd_{2-x}Ce_xCuO_{4\pm\delta}$. $Pr_{2-x}Ce_xCuO_{4\pm\delta}$ and $Nd_{2-x}Ce_xCuO_{4\pm\delta}$ are shown to strongly violate the Mott-Ioffe-

Regel limit. This is consistent with other high-temperature superconducting cuprates and is evidence for strong correlations in the $Pr_{2-x}Ce_xCuO_{4\pm\delta}$ and $Nd_{2-x}Ce_xCuO_{4\pm\delta}$ systems. The strength of correlations in the pnictide high-temperature superconductors is still an open question. The high-temperature resistivity of the $SrFe_{2-x}(Co,Ni)_xAs_2$ system was measured and observed to saturate at around the expected Mott-Ioffe-Regel limit in these materials. Although spin-fluctuations prevent certain identification of the resistivity saturation as being a Mott-Ioffe-Regel limit, this rules out strong, cuprate-like correlations.

The final experimental chapter, Chapter 8, addresses some additional projects that have, as-yet, been less fruitful. An attempt was made to synthesize superconducting Pr_2CuO_4, the parent compound of $Pr_{2-x}Ce_xCuO_{4\pm\delta}$. The new experimental techniques used and the status of the project are discussed. Similar attempts to grow thin films of the iron-based superconductors $SrFe_{2-x}Co_xAs_2$ and $FeSe_{1-x}Te_x$ are also discussed. The pulsed laser deposition techniques necessary for pnictide and chalcogenide thin films differ somewhat from growing oxide films like the cuprates.

Together, these chapters form an investigation into the workings of high-temperature superconductivity. Studying $Pr_{2-x}Ce_xCuO_{4\pm\delta}$ and related compounds has advanced the state of knowledge with respect to high temperature superconductivity. It is hoped that this knowledge continues to advance.

Chapter 2

Cuprate Background

2.1 Introduction

The experimental works covered in this thesis focus on transport measurements in $Pr_{2-x}Ce_xCuO_{4\pm\delta}$ and related compounds. For example, the electrical resistance measurements, discussed in all experimental chapters (Chapters 4, 5, 6, 7, and 8), and the Hall effect measurements, discussed in Chapters 5 and 6, depend upon the band structure near the Fermi energy. The angular magnetoresistance measurements, discussed in Chapters 4, 5, and 6, depend upon the system's magnetic structure. The formation of superlattices (Chapter 6) and, more generally, the growth of high-quality thin films of $Pr_{2-x}Ce_xCuO_{4\pm\delta}$ (Chapter 3) used throughout this thesis depend upon knowledge of the RE_2CuO_4 crystal structure. In order to understand $Pr_{2-x}Ce_xCuO_{4\pm\delta}$ transport, some basic properties of the system must first be made familiar to the reader.

The crystal structure of $Pr_{2-x}Ce_xCuO_{4\pm\delta}$ consists of layers of CuO_2 planes; these planes are necessary for superconductivity. Magnetic moments on the copper atoms in these planes introduce a spin structure in the compound and strong Coulomb interactions cause the band structure to be gapped at the Fermi energy. While $Pr_{2-x}Ce_xCuO_{4\pm\delta}$ is a superconductor for some dopings, Pr_2CuO_4 is not. The parent compound is generally believed to be an antiferromagnetically ordered Mott insulator, although recent proposals have questioned this picture [20] (Chapter 8). Doping suppresses the antiferromagnetism

in the system and introduces charge carriers. Superconductivity in this system arises between $x = .12$ and $x = .19$ doping levels.

Related systems discussed in this thesis are discussed in their individual chapters and as necessary. Notably $La_{2-x}Ce_xCuO_{4\pm\delta}$ has many similar properties to $Pr_{2-x}Ce_xCuO_{4\pm\delta}$ and can, in many cases, be treated as a similar material save for a slightly higher T_c and a slightly lower optimal doping. The $La_{2-x}Ce_xCuO_{4\pm\delta}$ system is less explored than the $Pr_{2-x}Ce_xCuO_{4\pm\delta}$ system. Also of note is the $SrFe_{2-x}M_xAs_2$ system, with M either Co or Ni. This system deserves mention in its own right and is discussed in the $SrFe_2As_2$ section of Chapter 7.

2.2   Crystal Structure

The properties of materials ultimately depend upon their crystal structure. Crystal structure, for example, determines the spectrum of the phonons that mediate Cooper pairing in BCS superconductors. While the high-temperature cuprate superconductors are almost certainly non-BCS, superconductivity is quite sensitive to the details of the crystal structure. Both the cuprate family of high-temperature superconductors and the newer ferropnictide family have planes of atoms that are critical to superconductivity. In each case, superconductivity appears after doping an antiferromagnetically ordered parent compound.

All of the cuprate high temperature superconductors have similar crystal structures; they contain layers of copper oxide planes. Many also have tetragonal unit cells, or are at least orthorhobic. Some of the simpler cuprate crystal structures are found in the 214

family of cuprate superconductors. This family, whose members have RE_2CuO_4 formula units, contains the electron-doped cuprates, $Pr_{2-x}Ce_xCuO_{4\pm\delta}$ and $La_{2-x}Ce_xCuO_{4\pm\delta}$, discussed in this thesis. The crystal structure varies slightly depending on the choice of rare earth element, RE. For example, a hole-doped 214, LSCO ($La_{2-x}Sr_xCuO_{4\pm\delta}$), crystalizes in the T phase (Figure 2.1) whereas an electron-doped 214, NCCO ($Nd_{2-x}Ce_xCuO_{4\pm\delta}$), crystalizes in the T' phase [21]. Thin films of both PCCO ($Pr_{2-x}Ce_xCuO_{4\pm\delta}$) and LCCO ($La_{2-x}Ce_xCuO_{4\pm\delta}$) are formed in the T' phase; due to the larger size of the La^{3+} ion, LCCO will only crystalize in the T' phase in thin film preparations where the crystal lattice of the substrate stabilizes the film's crystal structure [22].

In each phase, the copper oxide layers form planer square lattices separated by charge reservoirs of the remaining elements. Oxygen is in both planer and reservoir lattice sites. The former are labeled O(1) and the latter O(2). In addition to these regular lattice sites, the T' phase also often incorporates additional oxygen in interstices directly above and below the copper atoms. These particular interstitial sites are called apical sites and frequently do contain oxygen atoms. This site corresponds, in the T phases, to the apex of the octahedral arrangement of oxygen sites that places atoms above and below the copper sites. These apical sites are O(2) sites in the T phase and are not filled in the T' phase. This is for an ideal crystal. In real materials there is some amount of impurity oxygen at the apical sites in the T' phase. These oxygens are labeled O(3). The apical sites in the T' crystal structure are convenient locations for interstitial defects to occur in the crystal lattice; it is relatively easy for O(3) oxygens to be present. Oxygen incorporated at O(3) disorders the crystal structure and alters the electronic properties.

For high quality samples, these apical oxygens are a common issue. Oxygen re-
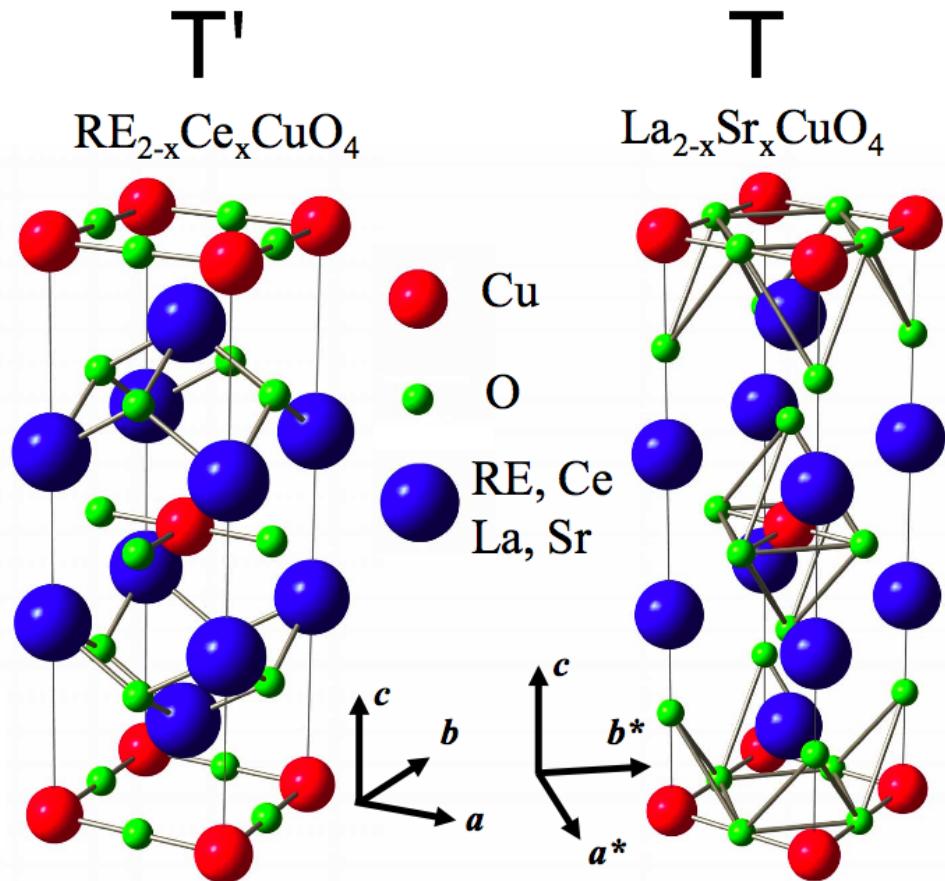
Figure 2.1: The T' (left) and T (right) crystal structures [21]. The major difference between the two structures is the placement of the oxygen atoms. The T structure surrounds the copper atoms with oxygens, forming CuO_6 octahedra, while the T' structure forms CuO_2 planes.

duction (or addition) by high temperature annealing provides some experimental control over the oxygen concentration. Excess oxygen will tend to fill apical sites as O(1) and O(2) will be fully populated; oxygen deficiencies can come from O(1), O(2), or O(3) sites. Electron-doped films and crystals need to be reduced in order to exhibit superconductivity and are, therefore, annealed in a low partial pressure of oxygen. This annealing removes oxygen; however, it is a long-standing question in the electron-doped cuprates as to from where exactly oxygen is being removed during annealing. It has been suggested that oxygen reduction effects the number of charge carriers, i.e., acting as a dopant [23], that it decreases disorder and impurity scattering [24, 25, 26, 27], that it suppresses long-range ordered antiferromagnetism [28, 29, 30], or that it repairs copper vacancies in the CuO_2 planes [31]. This issue has not been resolved in thin films or crystals due to the difficulty in determining the oxygen content. The presence of apical O(3) oxygens disorders the films. Likewise, removing oxygen from O(1) would tend to disorder the CuO_2 planes. Either case should harm superconductivity. The bond between the O(2) oxygens and the rare earth elements is stronger than the bonds between the O(1) oxygens and the copper atoms and should be affected by annealing less than O(1) or O(3) oxygens [32]. Further discussion of the role of oxygenation in PCCO can be found in Chapter 5.

In addition to oxygen, the Pr_2CuO_4 crystal structure also responds to the substitution of cerium for praseodymium. The T' crystal structure is tetragonal with lattice parameters of $a = b \approx 3.96$ Å and $c \approx 12.15$ Å in optimally doped $Pr_{2-x}Ce_xCuO_{4\pm\delta}$ [21]. Doping from $x = .00$ to $x = .19$ shrinks the c-axis by ~ 0.15 Å (Figure 2.2). This change in lattice spacing is easily measurable by X-ray diffraction and offers a useful check of the doping level. Above $x = .19$, PCCO thin films do not grow reliably as a

single phase.
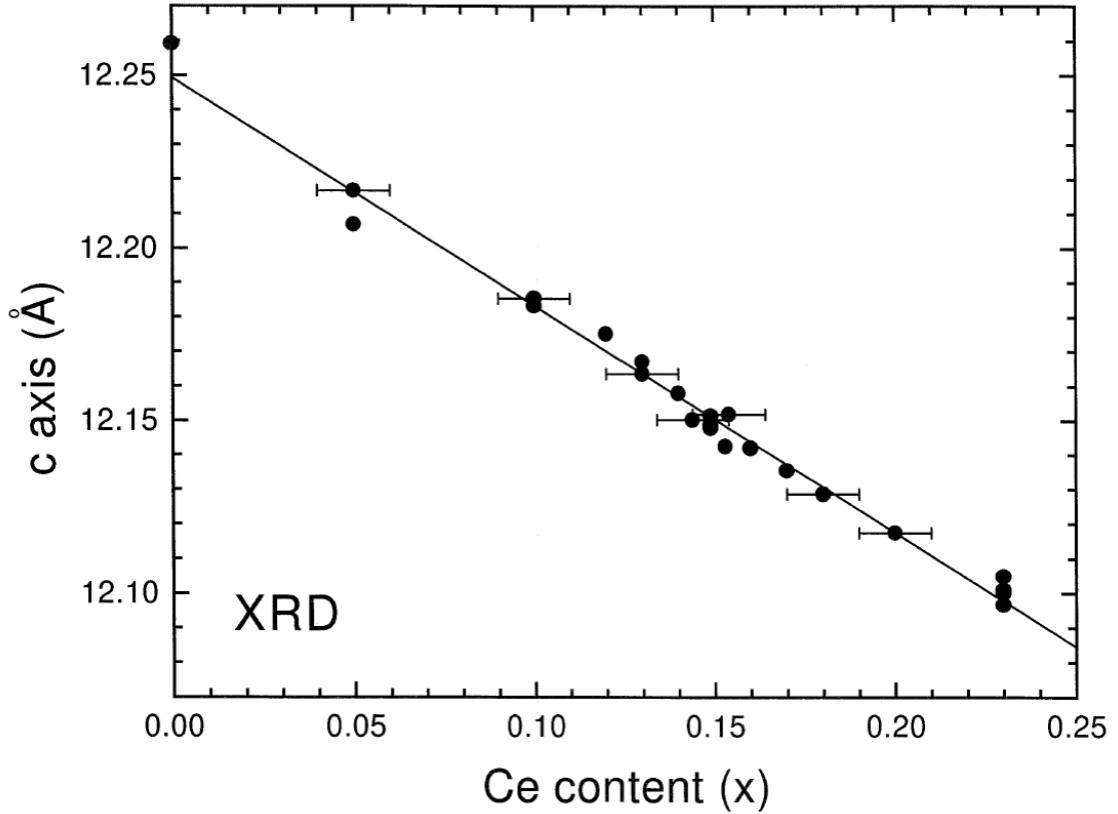
Figure 2.2: Increased cerium doping decreases the c-axis lattice parameter significantly in $Pr_{2-x}Ce_xCuO_{4\pm\delta}$ as seen by X-ray diffraction [33].

The $La_{2-x}Ce_xCuO_{4\pm\delta}$ system is quite similar to $Pr_{2-x}Ce_xCuO_{4\pm\delta}$ in these respects, although with the caveat that LCCO prefers the T structure to the T' structure. The growth of T'-LCCO is stabilized in thin films through the lattice strain induced by the substrate. Even with this strain stabilization, only doped LCCO preparations are stable; the film will not form for $x < .06$ in the T' phase. Below this doping the T-phase of LCCO has been synthesized with low concentrations of cerium [34]; however, these films are quite resistive and are contaminated with T' phase over $x \approx .05$. The T'-phase of LCCO is necessary in order to exhibit superconductivity when doped with cerium.

2.3   Spin Structure

Pr$_2$CuO$_4$ has an antiferromagnetic ground state that is slowly suppressed with doping. In this system, the largest magnetic moments lie on the copper atoms and have a non-collinear spin structure (Figure 2.3). In zero magnetic field the spins align along the [100] and [010] directions. These directions are along the copper-oxygen-copper bonds in the CuO$_2$ planes. At higher fields the spins align collinearly [35]. In the collinear structure, the spins are all aligned along the same axes, the direction determined largely by the magnetic field (Figure 2.4). The [110] directions are the easy axes for the collinear structure; these are along the copper-copper directions. High field behavior is discussed in Chapter 4.

This spin structure is slowly suppressed in the electron-doped cuprates by spin-dilution. Doping an antiferromagnet can suppress magnetic structure by replacing magnetic elements with non-magnetic ones [37]. With fewer lattice sites participating in the spin structure, the strength of the antiferromagnetic interactions is weakened. Dopants, therefore, suppress the Néel temperature and eventually destroy the spin ordering. The Néel temperature is the temperature where the antiferromagnetic (AFM) order is suppressed; it is like the Curie temperature, but for antiferromagnetism rather than for ferromagnetism. This happens in Pr$_{2-x}$Ce$_x$CuO$_{4\pm\delta}$, where doping cerium onto praseodymium lattice sites suppresses antiferromagnetism. Although in PCCO the copper lattice sites are the source of the antiferromagnetic structure, it turns out that electrons doped into the system go on the copper sites, where they dilute the spin structure [38].
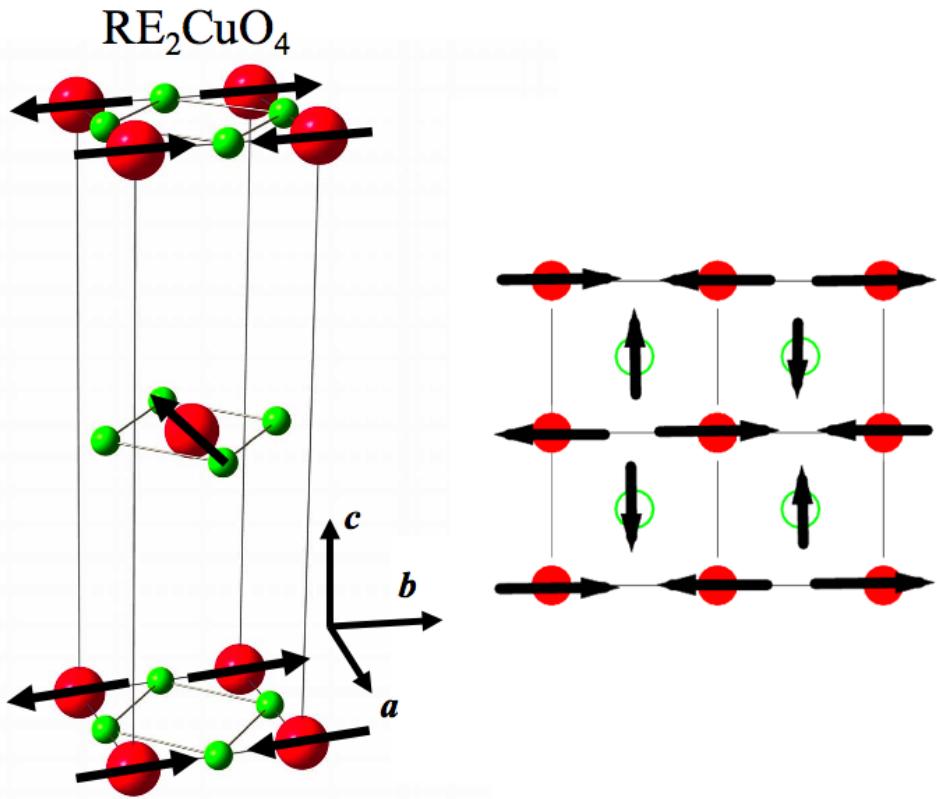
Figure 2.3: The copper magnetic moments in the PCCO crystal structure with the out-of-plane elements suppressed [21] (left) and along the c-axis [36] (right). The spins align antiferromagnetically along the Cu-O-Cu directions. Adjacent CuO_2 planes are rotated 90°.
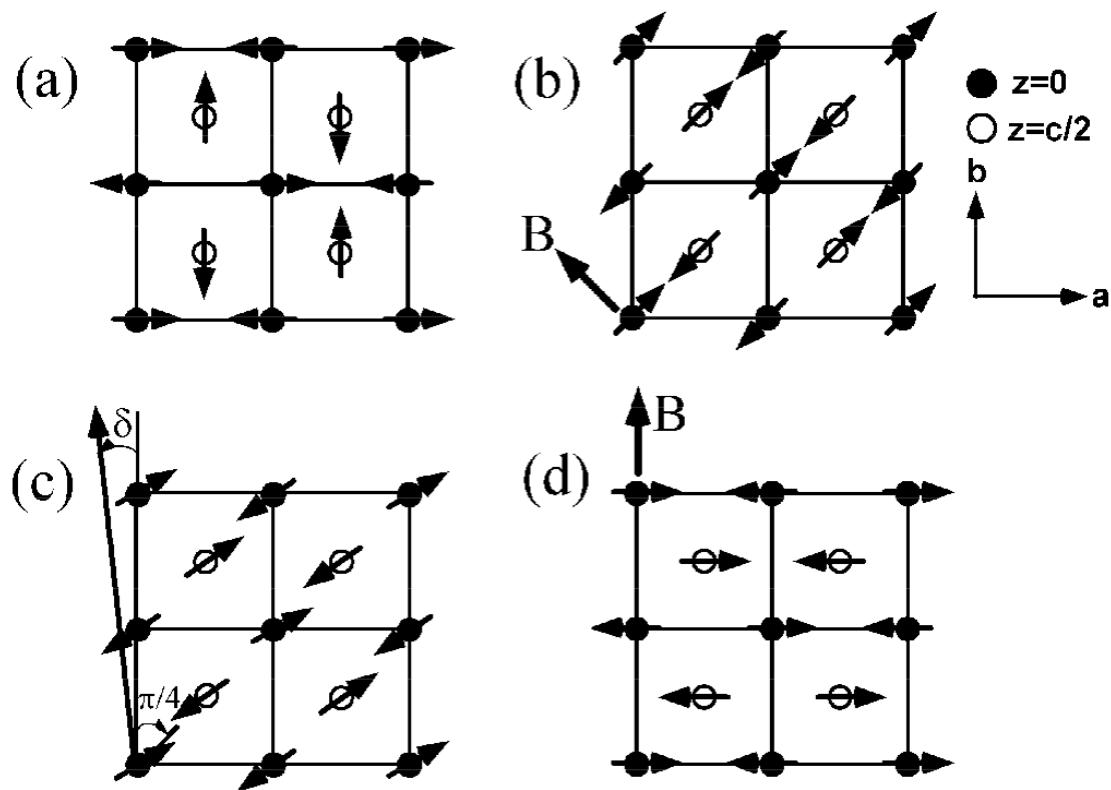
Figure 2.4: The ab-plane spin structure of $Pr_{2-x}Ce_xCuO_{4\pm\delta}$ in (a) zero magnetic field and (b), (c), (d) applied magnetic fields [35]. In field, the [110] directions are the easy axes for the collinear spin structure (b) whereas [100] and [010] are preferred for the non-collinear zero-field spin structure (a).

2.4 Band Structure

In the cuprate system, the spin structure is on the copper atoms, despite copper normally being non-magnetic; this is due to the electronic structure of the compounds [21]. If Pr_2CuO_4 were considered ionically, neglecting covalency, the praseodymium atoms form Pr^{3+} ions and the oxygens are O^{2-}. This requires, then, that copper is in the compound as Cu^{2+} [38]. When $Pr_{2-x}Ce_xCuO_{4\pm\delta}$ is doped, cerium substitution, as Ce^{4+}, adds extra electrons converting Cu^{2+} ions to Cu^+ ions. The ions are, however, embedded in a crystal structure that modifies their electronic properties (Figure 2.5). The Cu^{2+} $3d^9$ and O^{2-} $2p^6$ orbitals are modified due to crystal field effects and hybridize [39]. The result of this process is that Pr_2CuO_4 ought to be metallic due to having a half-filled band populated with one electron per copper atom.

Although the band structure in Figure 2.5 predicts metallic behavior, Pr_2CuO_4 is, instead, a Mott insulator (Figure 2.6). This type of insulator "should" be a metal, but is an insulator due to strong Coulomb interactions that dominate the transport properties [40, 41]. These interactions split the Cu $d_{x^2-y^2}$ band into an upper and lower Hubbard band, neither of which crosses the Fermi energy. This band splitting creates a Mott-Hubbard insulator.

While Coulomb interactions do, in fact, do this in Pr_2CuO_4, there are additional bands between the upper Hubbard band (UHB) and lower Hubbard band (LHB). Therefore, the gap in the band structure that causes PCO to be an insulator is due to the charge-transfer gap, Δ (Figure 2.6). The charge-transfer energy, Δ, is the energy required to move a charge between copper and oxygen sites. Because of this PCCO is more correctly
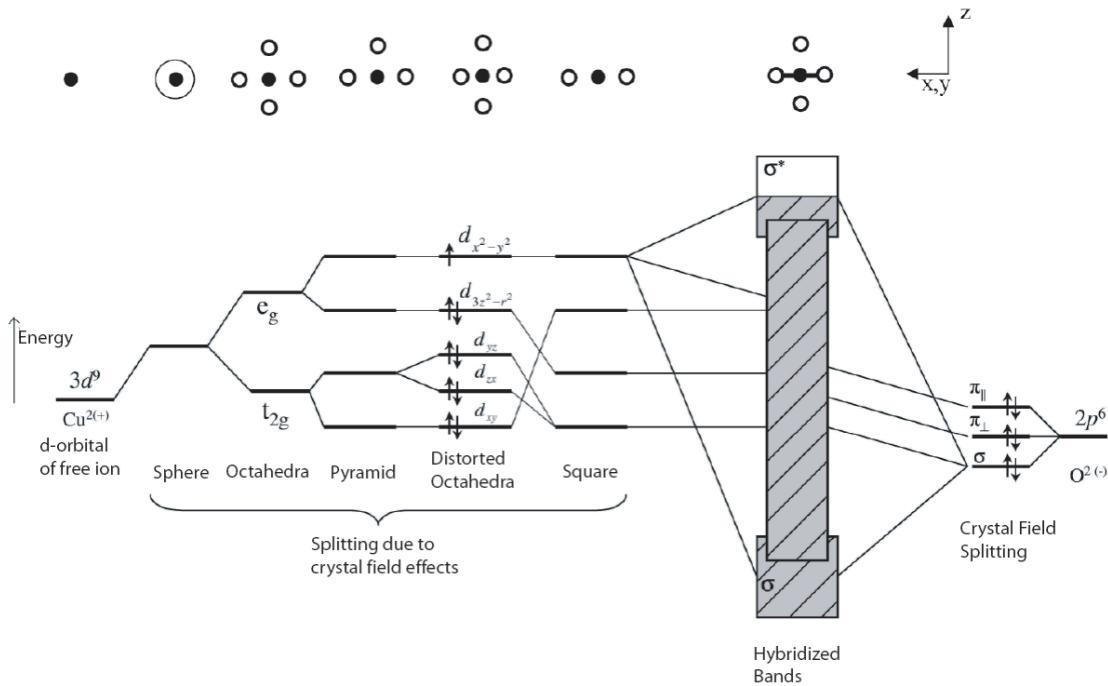
Figure 2.5: The hybridization of the copper and oxygen orbitals in the CuO_2 planes [38]. At the edges are the free ion Cu^{2+} $3d^9$ (left) and O^{2-} $2p^6$ (right) shells. The copper $3d^9$ orbital is then modified by crystal field effects due to being embedded in a crystal lattice surrounded by oxygen atoms. Spherical, octahedral coordination, pyramidal coordination, distorted octahedral coordination and a planer coordination modify the bare copper orbital as well as splitting the oxygen orbital. The mixing between the half-filled copper $d_{x^2-y^2}$ band and the oxygen σ bands that result from the crystal field splitting produces a hybridized half-filled band with a single free electron on each copper site.

called a charge-transfer (or Mott-like) insulator rather than a Mott-insulator [38].

This has implications for the magnetic properties as well as the electrical properties. The Coulomb repulsion that splits the copper $d_{x^2-y^2}$ band into an upper and lower Hubbard band results in localizing an electron on the copper site. The result is a magnetic moment on the copper atoms in addition to insulating behavior.
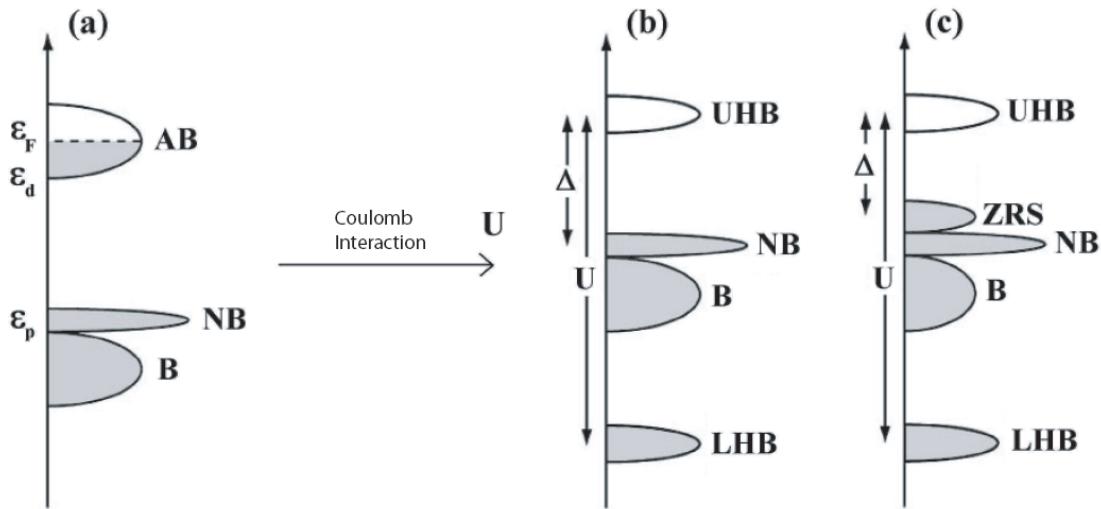
Figure 2.6: The density of states near the Fermi energy for a naïve cuprate band structure and one modified by Coulomb interactions, a Mott-Hubbard insulator [38]. (a) Without Coulomb interactions, there is a half-filled antibonding band (AB) at the Fermi energy that comes from the Cu^{2+} $3d^9$ and O^{2-} $2p^6$ orbitals hybridizing. (b) When Coulomb interactions with an energy scale U are included, the antibonding band is split into two bands, an upper Hubbard band (UHB) and a lower Hubbard band (LHB) with the Fermi energy now lying in a gap between bands. A material with no band crossing the Fermi energy will be an insulator. (c) In the cuprates additional bands lie between the UHB and LHB: a bonding (B), non-bonding (NB), and a Zhang-Rice singlet (ZRS) band. Therefore, the cuprates are insulators not due to U, but due to the charge-transfer gap, Δ.

This charge-transfer insulator description of the cuprates describes the parent compounds; however, the superconducting cuprates are doped systems. At light dopings the

charge-transfer band structure is only slightly modified to begin to have a partially filled

band at the Fermi energy (Figure 2.7). With some non-zero density of states at the Fermi

energy, the doped electron-doped cuprates have a Fermi surface (FS) (Figure 2.8).
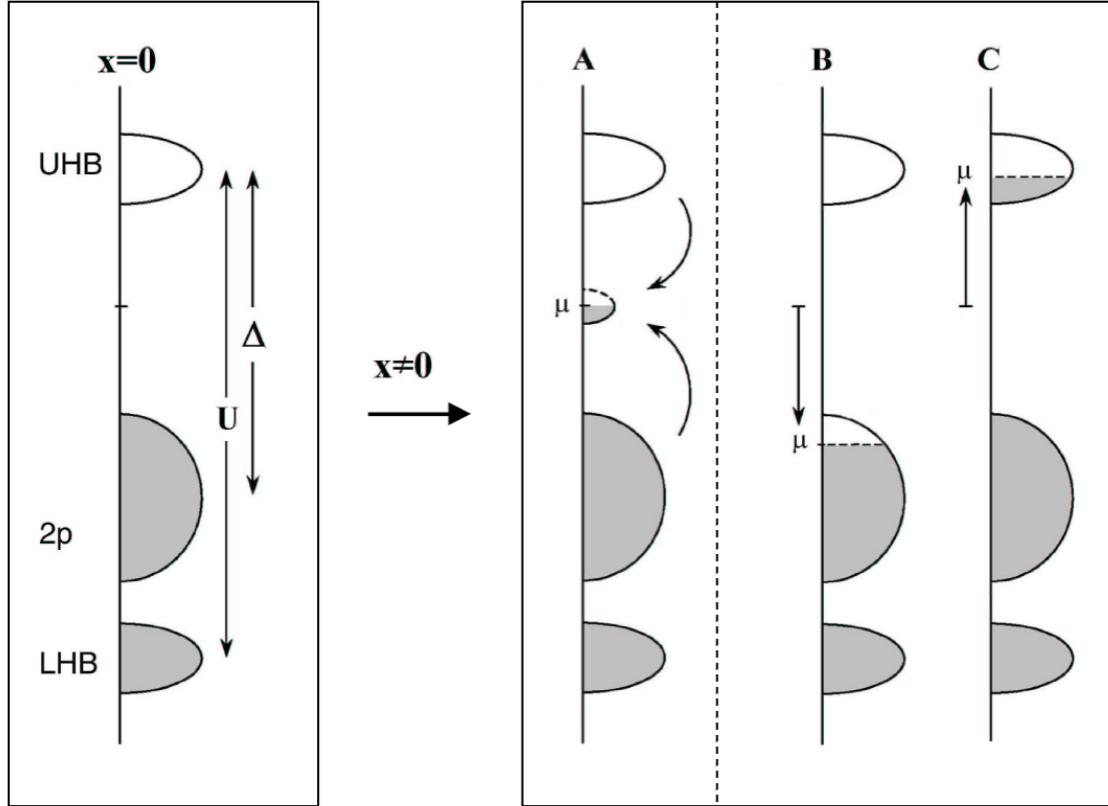
Figure 2.7: The density of states of a charge transfer insulator with doping [39]. (left) The undoped charge-transfer insulator with an energy gap Δ between filled and empty states. When electrons or holes are doped into the system, they may either create a new band in the charge transfer gap (A), or move the chemical potential into either the valance or conduction bands (B) or (C).

The magnetic Brillouin zone (BZ) indicated by dashed lines in Figure 2.8 is due to

antiferromagnetic ordering. Because the spins on the copper atoms alternate directions,

the real space lattice vectors' lengths should double to account for the periodicity of the

magnetic lattice. This halves the reciprocal space lattice vectors, resulting in a smaller

antiferromagnetic Brillouin zone. Therefore the Fermi surface should be folded along the dashed lines in Figure 2.8; X and Γ are the same point. This creates electron pockets around the M points and hole pockets around the center of the edges of the magnetic Brillouin zone.
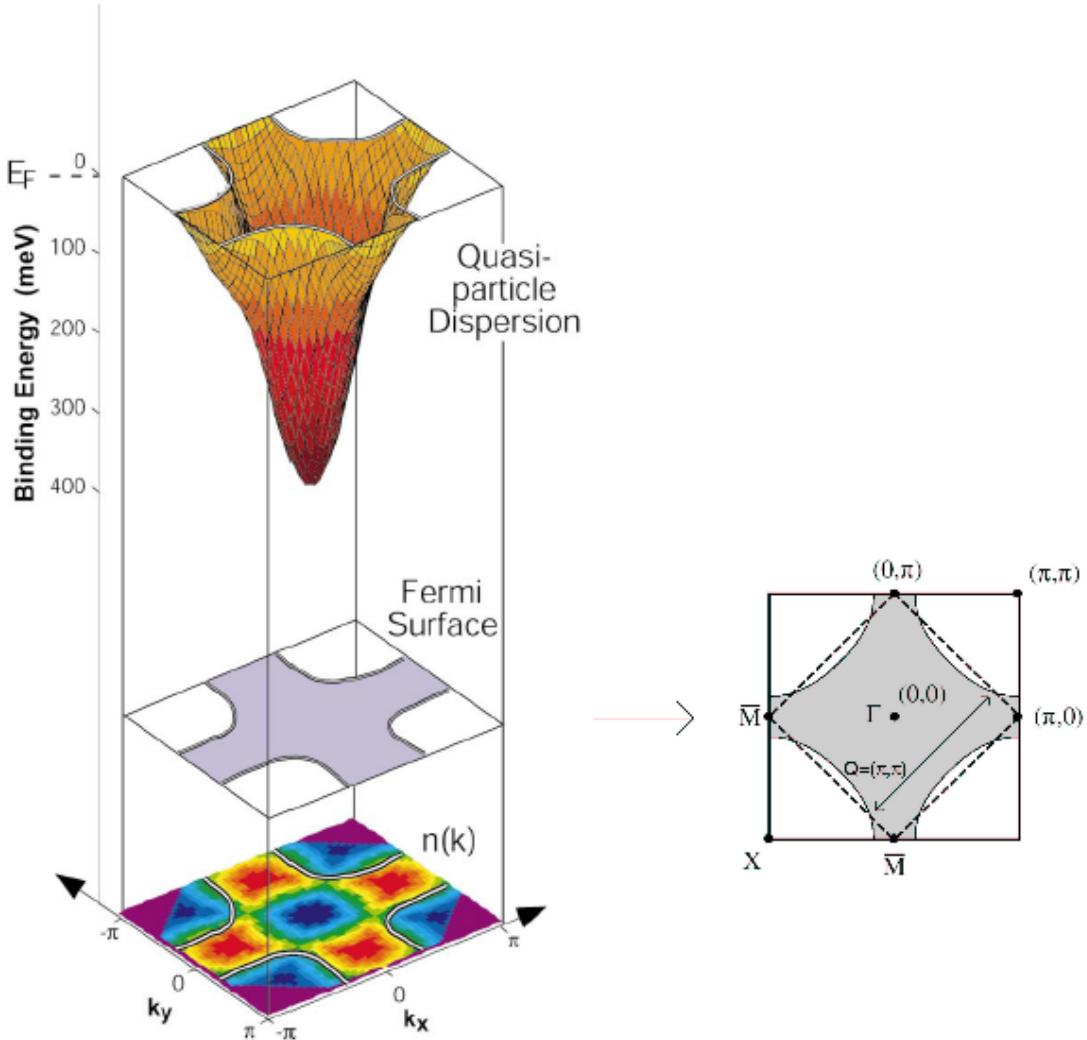
Figure 2.8: Typical Fermi surface for the electron-doped cuprates [39]. A two-dimesional cut of the quasiparticle dispersion relation $(E(k_x, k_y))$ at the Fermi energy produces the Fermi surface [42] (right). The magnetic Brillouin zone is indicated with dashed lines.

The Fermi surface retains these basic features as it evolves with doping, as shown by Angle-Resolved Photoemission Spectroscopy (ARPES) measurements on $Nd_{2-x}Ce_xCuO_{4\pm\delta}$ (Figure 2.9). ARPES is a probe of the Fermi surface that takes advantage of the photoelectric effect to map the momentum states near the Fermi energy where quasiparticles are found. Electron doping first causes electron pockets to form at the M points, $(\pi, 0)$ and $(0, \pi)$. This is the Fermi surface for the under-doped side of the electron-doped cuprate phase diagram. Near optimal doping, hole pockets appear near $(\pi/2, \pi/2)$. On the over-doped side, antiferromagnetism has been suppressed; there is no longer a magnetic Brillouin zone and the Fermi surface closes to one hole-like orbit around the X point, (π, π).
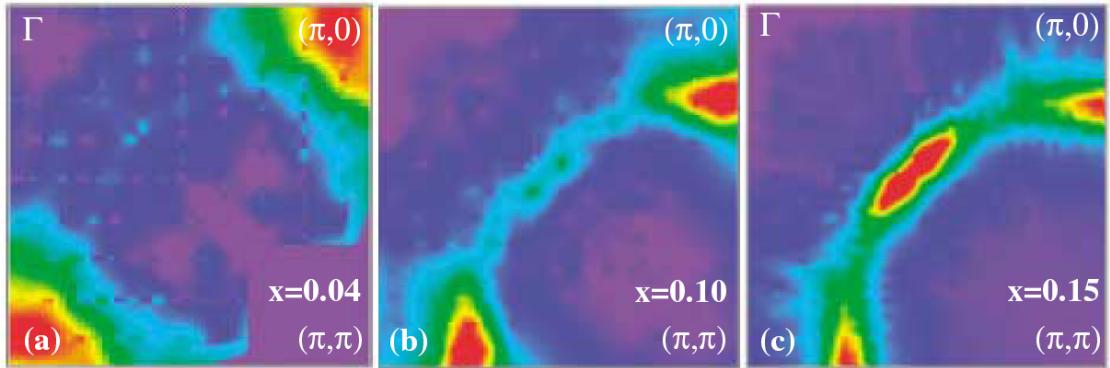
Figure 2.9: Evolution of the $Nd_{2-x}Ce_xCuO_{4\pm\delta}$ Fermi surface with doping as seen by ARPES [43]. The Γ point is in the top-left corner of each frame. (Each frame is only the lower-right quadrant of the Fermi Surface drawn in Figure 2.8.) Initially electron pockets form at $(\pi, 0)$ and $(0, \pi)$ and as doping increases hole pockets appear around $(\pi/2, \pi/2)$. At higher dopings (not shown) the hole-like Fermi surface closes and appears much as the schematic in Figure 2.8.

2.5 Phase Diagram

The magnetic moments on the copper atoms exhibit non-collinear antiferromagnetic ordering. In the electron doped cuprates, the parent compound Néel temperature is between 200 K and 400 K ($\sim$ 250 K in NCCO) [44]. The antiferromagnetism (AFM) in Pr_2CuO_4 (PCO) is commensurate and persists to similar temperatures as in NCCO, $\sim$ 250 K [21]. Commensurate antiferromagnetic ordering is periodic with rational multiples of lattice parameters. Doping electrons into PCO has the effect of suppressing this AFM state via spin dilution. In this process, replacing some fraction of Pr^{3+} with Ce^{4+}, the electrons added to the system primarily reside on the copper sites, transforming some $3d^9$ coppers into spin-less $3d^{10}$ coppers. With fewer atomic sites available to support antiferromagnetism, the long-range antiferromagnetic ordering weakens with electron doping. This is observed as a decrease in the Néel temperature with increased cerium content (Figure 2.10).

In Figure 2.10, the AFM order is clearly not suppressed symmetrically on the hole- and electron-doped sides of the cuprate phase diagram. This is due to spin dilution being the mechanism for spin suppression only in the electron doped system. Hole doping in the cuprates effectively introduces a competing ferromagnetic interaction between copper sites, suppressing antiferromagnetism due to spin frustration. This process is more rapidly destructive to the AFM state than spin dilution is on the electron-doped side of the phase diagram [21].

In addition to suppressing the Néel temperature, T_N, substituting cerium atoms for praseodymium atoms also induces superconductivity over a range of dopings. In
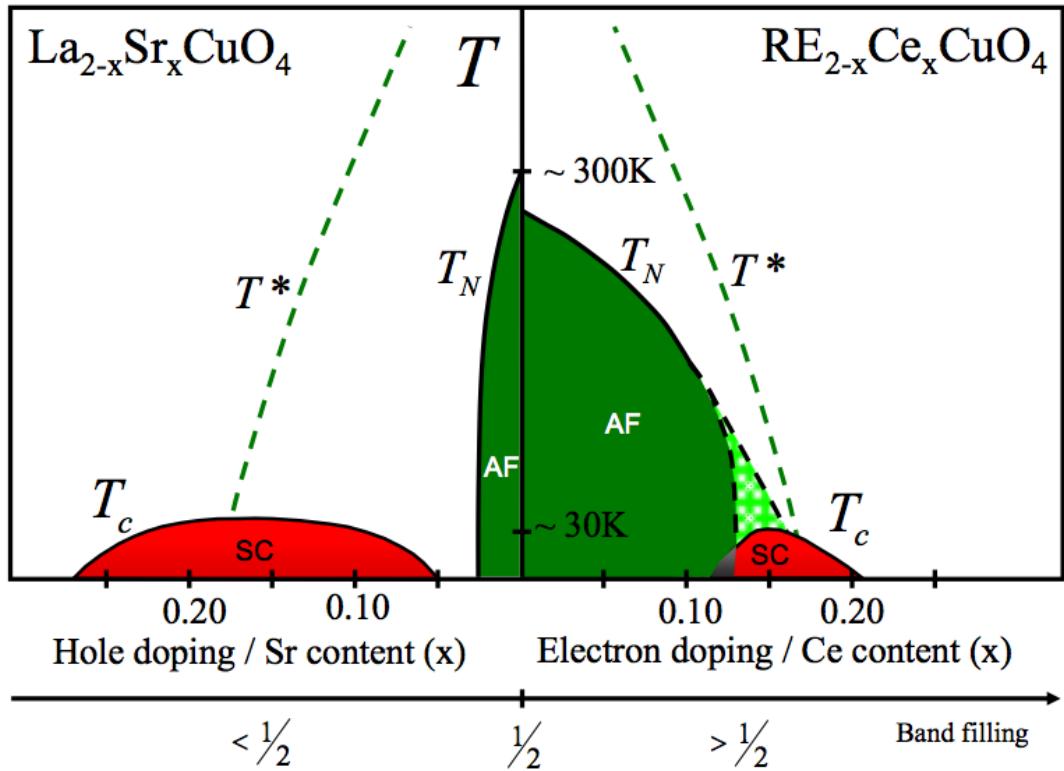
Figure 2.10: Generic doping phase diagram for the cuprates [21]. Either hole doping (left) or electron doping (right) suppresses AFM order and allows a superconducting dome to appear. On the electron-doped side there is some disagreement as to the terminus of the AF ordered region. This point is discussed in Chapter 4. The line labeled T* represents a pseudo-gap crossover (not discussed here).

$Pr_{2-x}Ce_xCuO_{4\pm\delta}$, superconductivity is observed from $x = .12$ up to $x = .19$. The maximum T_c of around 22 K is obtained for $x = .15$. Above $x = .19$, cerium cannot be reliably incorporated into the crystal lattice. Angular magnetoresistance measurements (see Chapter 4) suggest that the AFM phase persists up to $x = .16$; however, AFM disappearance at lower dopings has been reported by other techniques [45, 46]. There is some disagreement, however, among various groups [44, 45, 47, 48, 49, 50]. The optimal T_c depends upon proper annealing procedures at each cerium doping. This is due to oxygen excesses or deficiencies respectively hole- or electron-doping the material. Oxygen content can also affect the Néel temperature. Oxygen's role in PCCO is discussed in detail in Chapter 5.

Superconductivity in related T' cuprates follows similar trends. Several of the rare earth elements with $3+$ valences can form 214 cuprates that can be electron-doped to induce superconductivity. For example, $Pr_{2-x}Ce_xCuO_{4\pm\delta}$ and $Nd_{2-x}Ce_xCuO_{4\pm\delta}$ both behave quite similarly, while the phase diagram for $La_{2-x}Ce_xCuO_{4\pm\delta}$ is shifted toward lower dopings and presents a somewhat higher optimal T_c (Figure 2.11). The shift in optimal doping between LCCO and PCCO or NCCO is not well understood. Both Pr^{3+} and Nd^{3+} have similar ionic radii while La^{3+} is larger. It is possible that the different lattice spacing slightly adjusts the band structure so that doping causes a hole pocket to appear in LCCO before PCCO or NCCO. The decrease in optimal T_c with decreasing rare earth radius continues for $Sm_{2-x}Ce_xCuO_{4\pm\delta}$ and $Eu_{2-x}Ce_xCuO_{4\pm\delta}$ [51]. Similar behavior between LCCO and PCCO is also seen in antiferromagnetism; however, LCCO, unlike PCCO and NCCO, can only be prepared as a thin film in the T' phase, making magnetic measurements more difficult. The Néel temperature in PCCO and LCCO is

further discussed in Chapter 4.
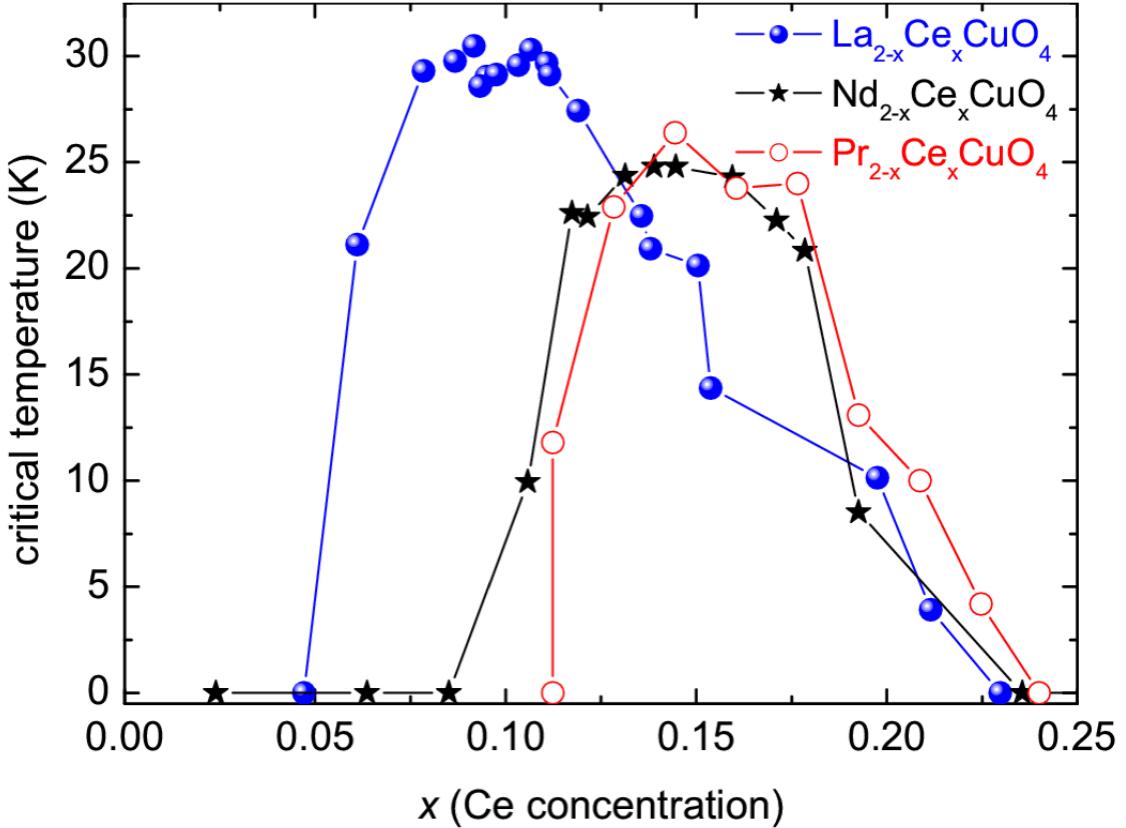
Figure 2.11: Superconducting dome for PCCO, NCCO, and LCCO [51]. Optimally grown LCCO has a higher T_c and is shifted to lower cerium dopings compared to PCCO and NCCO.

It has been reported [32, 52, 53, 54] that the electron-doped cuprates can be made superconducting solely with the careful control of oxygen in the crystal structure and without cerium doping. Our efforts along these lines are discussed in Chapter 8, but it should be noted here that this method of inducing supercondutivity in the RE_2CuO_4 family may imply that future revisions of the phase diagram are necessary. This result, however, would suggest that the parent compounds, RE_2CuO_4, are not Mott insulators, but rather (very) poorly optimized band metals. However, this picture is disputed. Nominally

undoped T' cuprates can also be synthesized through iso-valent doping by substitution of Y^{3+} for La^{3+}. $La_{2-x}Y_xCuO_{4\pm\delta}$ (LYCO) is found to superconduct over a range of yittrium dopings; transport data indicate that it is a Mott-like insulator that is electron-doped by oxygen reduction [55]. It is possible, therefore, that superconducting Pr_2CuO_4 is, in fact, doped by O_2 like LYCO. This issue requires further investigation (see Chapter 8).

Chapter 3

Preparation of $Pr_{2-x}Ce_xCuO_{4\pm\delta}$ Thin Films and Electronic Transport
Measurements

3.1 Introduction

All measurements depend upon the preparation of quality samples. In the case of
the electron-doped cuprates, good samples can be prepared as either single crystals or thin
films. Thin films of materials often are a convenient form to study transport properties.
$Pr_{2-x}Ce_xCuO_{4\pm\delta}$ is no exception. Careful control of growth parameters allows for high
quality uniform epitaxial films. Here, PCCO is prepared by pulsed laser deposition (PLD).
This technique allows for rapid and flexible sample preparation and has had good results
in the growth of the cuprate superconductors.

3.2 Pulsed Laser Deposition

The pulsed laser deposition technique ablates a stoichiometric target with a focused
high-energy laser. This ejects a plasma of the target material that deposits onto a substrate.
Typically this procedure must be performed inside of a vacuum chamber with the substrate
mounted on a heater in order to control the deposition atmosphere and temperature. The
substrate choice, deposition temperature, and chamber atmosphere determine the ability
of the deposited material to form into a thin film of the correct phase and can affect

the final properties of the film quite dramatically. In the case of oxides, the chamber atmosphere is particularly important as the low vapor pressure of oxygen relative to the other elements in the material requires that the chamber atmosphere be responsible for the film's oxygen content. This frequently necessitates a post-deposition annealing procedure to optimize film properties.

3.2.1 Target Making

In order to grow PCCO thin films by PLD, the target consists of polycrystaline PCCO synthesized by solid state chemical reactions. The process starts with commercial oxide powders of praseodymium, cerium, and copper between 4 and 5.5 9's pure. These oxides, Pr_6O_{11}, CeO_2, and CuO, are mixed to form the proper ratio of Pr:Ce:Cu, as determined by weight. For example, a 15 gram target of optimally doped $Pr_{2-x}Ce_xCuO_{4\pm\delta}$ ($x = .15$) requires just over 11 grams of Pr_6O_{11}, just under 1 gram of CeO_2, and just under 3 grams of CuO (Figure 3.1).

These numbers can be obtained from the desired doping, desired mass, and the atomic and molecular weights of the constituent atoms and oxides, summarized in Figure 3.1. The atomic masses in grams per mol are $Pr = 140.9077$, $Ce = 140.12$, $Cu = 63.546$, and $O = 15.9994$, giving molecular masses of $Pr_6O_{11} = 1021.4396$, $CeO_2 = 172.1188$, and $CuO = 79.5454$ for the starting oxides. An optimally doped $Pr_{2-x}Ce_xCuO_{4\pm\delta}$ target ($x = .15$) needs praseodymium, cerium, copper, and oxygen to be in a ideal ratio of $Pr : Ce : Cu : O = 1.85 : 0.15 : 1.00 : 4.00$. In order to synthesize $Pr_{2-x}Ce_xCuO_{4\pm\delta}$, however, the ratio $Pr : Ce : Cu : O = 1.85 : 0.15 : 1.03 : N/A$ is used

	Formula	g/m	Chemical I Mass Ratios		Masses
Formula	$Pr_{2-x}Ce_xCuO_4$		Ignore Oxygen in formula		
Doping	0.15				
Mass	15				
Elements	Pr	140.9077	1.85		
	Ce	140.12	0.15		
	Cu	63.546	1.03		
	O	15.9994	N/A		
Compounds	Pr6O11	1021.4396	0.308333	314.9438767	11.1763219
	CeO2	172.1188	0.15	25.81782	0.91618948
	CuO	79.5454	1.03	81.931762	2.90748864
		Multiplier	0.035487 *Sum*		15

Figure 3.1: Recipe for producing a 15 g, $x = .15$ $Pr_{2-x}Ce_xCuO_{4\pm\delta}$ target from constituent oxides. The atomic weights of Pr, Ce, Cu, and O give the number of grams per mol (column **g/m**) of Pr, Ce, Cu, Pr_6O_{11}, CeO_2, and CuO. The desired ratio of each element, determined from the desired doping, translates into a desired ratio for each oxide (column **Chemical Ratio**). From this ratio and the oxides' molecular weight, the ratio in units of mass is determined (column **Mass Ratio**) and normalized (by *multiplier*) for a total mass in grams of the desired amount. The masses (column **Masses**) of each starting oxide is thus determined.

as copper has a tendency to be slightly deficient in the finished target and oxygen concentration is controlled by the synthesis atmosphere as oxygen in the target is able to freely exchange with the O_2 in air. This desired ratio of elements requires that the oxides be mixed in a ratio of $Pr_6O_{11} : CeO_2 : CuO = 0.308\bar{3} : 0.15 : 1.03$, based upon the number of non-oxygen elements per formula unit. This ratio is then converted into units of mass that can be measured on a laboratory scale. With the molecular masses, the ratio becomes $Pr_6O_{11} : CeO_2 : CuO = 314.9439 : 25.8179 : 81.9318$ (grams), which can be then scaled with a multiplier to $Pr_6O_{11} : CeO_2 : CuO = 11.1763 : 0.9162 : 2.9075$ (grams), for a total weight of 15 g, which is a useful amount of material for creating 1 inch diameter targets of approximately half a centimeter thickness.

Both Pr_6O_{11} and CeO_2 will absorb moisture from the air. Therefore, the constituent oxides are first separately heated to 800 C for 12 hours in order to dry them before weighing. In all bakings, the ramp rate is between 250 and 300 C/hour. Powders are weighed to within 500 μg of the target weight; the target weights both maintain the proper $Pr : Ce : Cu$ ratio and produce a total weight of the finished target of $\sim$ 15 g. The mix is intentionally slightly copper rich (3 %) due to copper having a slight tendency to leach out of the target during baking. There is also some evidence that copper rich targets produce higher quality films [56]. Oxygen stoichiometry is not controlled and will automatically adjust itself as the PCCO forming reaction is carried out in ambient atmosphere. Unlike the other elements present, oxygen concentration in films grown is not determined by target stoichiometry, but rather by the partial pressure of oxygen during pulsed laser deposition.

Combining the weighed powders, the mixture is finely ground first by manual grind-

ing with mortar and pestle followed by an hour of ball milling. Manual grinding is effective for breaking up large chunks of material and the ball milling step produces a fine powder that maximizes surface contact for the subsequent chemical reaction. The mixed powder is then fired twice in a furnace, once at 950 C for 12 hours, and then at 1050 C for 12 hours. Manual grinding and ball milling steps are performed after each bake. This baking procedure fully reacts Pr_6O_{11}, CeO_2, and CuO to $Pr_{2-x}Ce_xCuO_{4\pm\delta}$. The reacted powder is then transferred into a 1-inch inner-diameter pellet press and subjected to a pressure of 25 k lbs. This pellet is then sintered at 1080 C for 12 hours and finally mounted with silver paint on a metal stand designed for target mounting in the PLD chamber. The final target is a non-superconducting polycrystaline PCCO puck of the desired cerium concentration. Targets are stable for (at least) several years and can be used repeatedly for film depositions, with minimal sanding to maintain a uniform surface. Cerium can be reliably incorporated into $Pr_{2-x}Ce_xCuO_{4\pm\delta}$ from $x = .00$ up to $x = .19$. Targets are generally synthesized at each .01 of cerium doping over the superconducting dome (roughly $x = .12$ to $x = .19$) and at larger intervals at lower dopings.

3.2.2 Film Growth

Pulsed laser deposition of thin films is a quite versatile technique for producing thin films. Any description of the process, therefore, will be general in nature, with specific films possibly deviating from this process described here in significant ways. Nevertheless, the procedure for growing a typical PCCO film provides a good scaffolding onto which modifications can be applied.

The most important part of the pulsed laser deposition process is cleaning and preparing the chamber, target, and substrates. The chamber is responsible for maintaining the atmosphere necessary for PLD growth, which typically ranges from a few hundred mTorr of N_2O or O_2 to vacuum depending upon details of growth. In this discussion, vacuum typically implies $P < 3 \times 10^{-5}$ Torr for good PCCO growth, although pressures of 10^{-7} Torr are preferred.

The target provides the source material for films produced by the PLD process. Synthesized prior to pulsed laser deposition, the target should be sanded prior to deposition with a fine grit sand paper, usually 600 grit, to present a uniform surface for laser ablation. Non-uniformities in the target surface have the effect of reducing the quality of the plume of material ejected with each laser pulse. Plume quality primarily determines the rate of film growth, with higher energy densities per pulse ejecting more material. Typical growth rates for high quality thin films are around 0.3 Å per pulse and 10 pulses per second.

The substrate is what ultimately determines the quality of the film's epitaxy by seeding the growth of the film's crystal lattice. Therefore, substrate surface preparation has a large effect on the ability of the PLD process to grow quality thin films. Substrates are cleaned three times, first with acetone, then with methanol, and finally with ethanol. In each case, a small glass beaker is rinsed and then partially filled with the solvent. The substrate is submerged and ultrasonicated for 5 to 7 minutes, then rinsed and blown dry with a nitrogen gun. The ultrasonication serves to rinse the substrates well and ensure that dirt on the film will be removed by the solvent. The substrates are then blown dry in order to minimize residue remaining on the film due to the evaporation of solvent. This

also accounts for the three washes; the acetone cleaning most strongly removes dirt and the subsequent rinses remove remaining residues.

Substrates are then affixed with silver paint to the chamber's heater, previously sanded clean. To attach the backs of the substrates to the PLD chamber's heater, silver paint is used due to its good thermal conductivity. Silver paint is applied generously to the heater and the substrate is then pressed into the liquid. Pressing the substrate insures uniform thermal contact (and therefore uniform substrate temperature during deposition). It also has the effect of driving out any tiny air bubbles in the silver paint from behind the substrate. If air bubbles are allowed to remain, the trapped gas inside the bubbles will expand during heating, due to the ideal gas law, and will pop the substrate off of the heater. Prior to insertion into the chamber, the heater is set to 100 C to dry the silver paint.

The choice of substrate, substrate temperature, and chamber atmosphere are the most important variables in determining whether or not a film composition, established by a target, will form. The substrate acts to "seed" the growth of the film's crystal structure; therefore, it is necessary for the substrate to have lattice parameters that are well matched to the film's. For PCCO the in-plane lattice constants are $a = b \approx 3.953$ Å. Typically, PCCO is grown on (100) oriented single crystal $SrTiO_3$ (STO), which is a cubic perovskite with a lattice constant of $a = 3.905$ Å [57] purchased from CrysTec GmbH. This is a lattice mismatch of only $\sim 1.2\%$ and seeds c-axis oriented epitaxial PCCO growth. As PLD growth increases the film thickness, this orientation ultimately produces films with the c-axis normal to the film surface and the ab-planes stacked parallel to the surface. STO also has the advantage of being quite resistive; this allows transport measurements to not be contaminated by parallel current paths through the substrate. PCCO

will tolerate use of other substrates with larger lattice mismatches. For example, tetragonal LaSrGaO$_4$ (LSGO) with $a = 0.384$ nm [57] is preferred for far-infrared optical transmission experiments where the frequency dependence of the substrate phonon modes is a concern [58, 59]. However, if the lattice mismatch is too great, the resulting film will not be epitaxial and single-phase. For example, attempting to grow Pr$_{2-x}$Ce$_x$CuO$_{4\pm\delta}$ on silicon, with a lattice constant of 0.543 nm [57], produces a film where the PCCO 00ℓ X-ray diffraction peaks are not seen.

Provided that the substrate seeds the correct lattice orientation, the temperature is primarily responsible for the Pr, Ce, and Cu atoms forming in the correct crystalographic phase. The atmosphere provides the correct oxygen concentration. Deposited at 800 C, PCCO prefers to form in the T' phase. This is the phase in which electron-doped superconductivity is found. Substrate temperature is measured by a thermocouple cemented to the back of the heater and is also monitored separately by an infrared thermometer. Temperature stability is not of great concern for PCCO as the T' crystal structure will form at a range of temperatures around 800 C.

The chamber's atmosphere is necessarily maintained at a fixed partial pressure of oxygen in order to grow PCCO. It is a general problem of laser deposition techniques that the plume of ablated material from the target does not handle well the elements with low vapor pressures. For example, in the growth of SrFe$_{2-x}$Co$_x$As$_2$ and FeSe thin films, arsenic and selenium deficiencies in the final films are a concern (Chapter 8). In the case of oxides, oxygen must be bled as a gas into the vacuum chamber in concentrations sufficient to allow its incorporation into the crystal lattice. For PCCO, oxygen is introduced either as elemental oxygen (O$_2$) or as nitrous oxide (N$_2$O) at a few hundred mTorr of pressure.

For optimally grown films, 230 mTorr of N_2O is used; however, optimally grown films can also be prepared in an O_2 atmosphere. Oxygen is ultimately, however, adjusted after growth in an in situ post-deposition annealing step described below.

After fixing temperature, pressure, atmosphere, and substrate choice, the length of deposition determines the thickness of the film. The laser is pulsed at 10 Hz at an energy density that produces a growth rate of around 0.3 Å per pulse. This is typically achieved by optimally focusing the laser on the target and operating the laser at 700 mJ/pulse although these laser parameters can be varied significantly to obtain similar energy densities on the target. In order to maintain the target under this level of ablation, the target is rotated such that laser pulses trace out a circular annulus rather than ablate the same location. This prevents local over-heating of the target. Deposition time is set such that films are typically grown to between 1000 and 3000 Å. Thicker films tend to be less uniform at the surface and thinner films have degraded transport properties.

After the film is deposited, PCCO must be annealed in order to achieve maximal T_c. This annealing process is designed to reduce the films' oxygen content and is therefore carried out in vacuum. For annealing, the temperature is reduced to 720 C and the pressure is held between $10^{-4} < P < 3 \times 10^{-5}$ Torr, with the lower pressures preferred. Annealing time varies slightly depending upon cerium concentration, reflecting the fact that more highly cerium-doped films are harder to reduce. Typically, optimal films (maximal T_c) are obtained by annealing at these conditions for one minute per .01 of cerium concentration. For example, an under-doped $x = .12$ film is annealed for 12 minutes and an over-doped $x = .19$ film is annealed for 19 minutes. It is not clear if this rule-of-thumb holds for more under-doped films as there is no T_c to optimize. However, recent work on PCO suggests

36

that it does not hold [32, 52, 53, 54].

It is advised that the annealing temperature and pressure be reached as quickly as possible as the transition period will somewhat anneal the film. This accounts for the pressure range ($10^{-4} < P < 3 \times 10^{-5}$ Torr) used in annealing; the time that the vacuum pump takes to reach the bottom of that range cannot be ignored. Annealing time is counted from when 720 C and 10^{-4} Torr are first attained. Following annealing, heater power is cut and the films are cooled at a constant atmosphere until below 420 C at which point little further annealing occurs. Films are only removed from the PLD chamber once they have cooled to room temperature. A razor blade is used to break the silver paint gluing the substrate to the heater.

3.2.3   Characterization

Prior to measurements, film quality is assessed by X-ray diffraction, AC susceptibility, and two-probe room-temperature resistance. Thickness and surface roughness are measured by a Dectak profiler. If future measurements permit contacts to be attached, resistivity from room temperature down is also measured to characterize the film.

For characterization purposes the films are typically checked using the van der Pauw method [60, 61] in either a Quantum Design Physical Properties Measurement System (PPMS) or a dip-probe setup in a storage dewar. Resistance is measured from 300 K to 2 K in the former or room temperature to ~ 4 K in the latter. Resistance is then converted into resistivity using the film thickness obtained by profilometry. Film quality is assessed by the superconducting transition temperature and transition width, the magnitude of the

normal-state resistivity, the presence and strength of a low temperature resistivity up-turn, and any non-standard transport properties that may be present.

Crystal structure in grown films is checked by X-ray diffraction. Here at Maryland, X-ray diffraction (XRD) measurements are performed in either a Bruker D8 or a Siemens D5000 X-ray diffractometer. The technique in each machine is similar. X-rays are generated at a fixed energy (Cu Kα, $\lambda = 1.5406$ Å) and are focused on the thin film. The X-rays diffract off of the crystal lattice planes at specific angles that satisfy the Bragg condition, $n\lambda = 2d\sin\theta$ (Figure 3.2). The film and detector can be rotated in θ and peaks are observed where constructive interference happens.
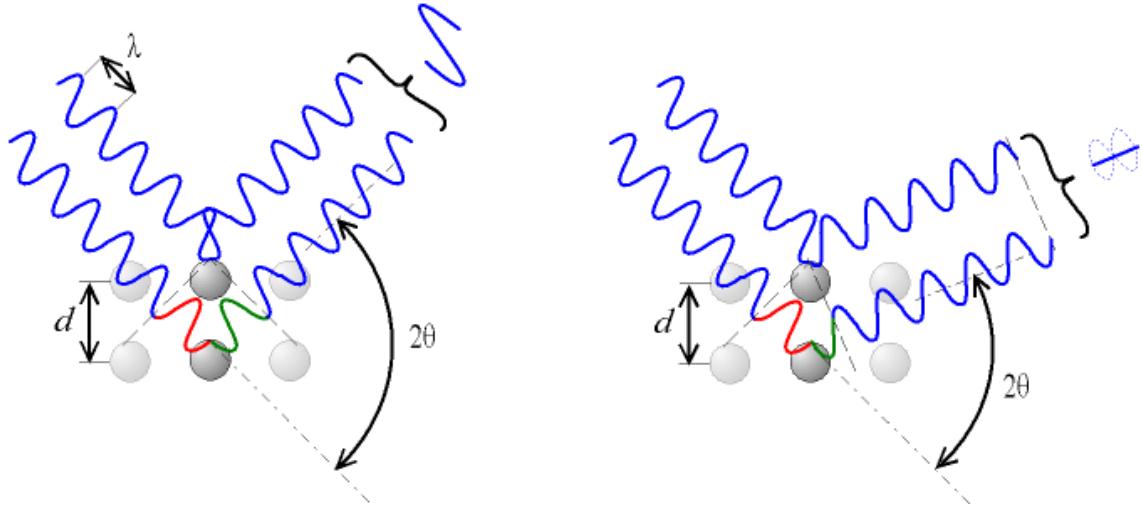
Figure 3.2: The Bragg condition for x-ray diffraction [62]. Only diffraction angles that produce constructive interference (left) will produce a diffraction peak. Angles that produce destructive interference (right) will not show peaks.

In order to characterize thin films, X-ray diffraction measurements are typically performed as $\theta - 2\theta$ scans. In this mode the sample is rotated to sweep through a range of incident angles, θ, between the sample and the x-ray beam. The detector is co-rotated at an angle of 2θ so that it will only detect x-rays that scatter off of crystallographic planes

parallel to the film surface, the CuO_2 planes in PCCO. Bragg diffraction then gives the spacing between unit cells along the c-axis, the c-axis lattice parameter.

Thus, the inter-plane spacing, d, can be extracted from the position of the Bragg peaks. This provides a useful characterization of the thin film because the film should grow epitaxially, therefore, the only planes participating in the Bragg diffraction are the ab-planes. Consequently, only the [001] peaks should be seen (Figure 3.3). Weak [001] peaks, or additional peaks indicate defects in the crystal lattice. In PLD grown PCCO, there is always a spurious peak at around $2\theta = 32°$ that is believed to be caused by an impurity cerium oxide phase. It is reported that residual resistivity is lower in films without this peak [56]. Looking at the [001] film peaks, d is a measure of the c-axis lattice constant. By this, the cerium concentration in the PCCO thin films can be verified [33].

The film's T_c and ΔT_c, the superconducting transition temperature and transition width thereof, are measured by AC susceptibility (ACχ) [38]. This dip-probe fits in a liquid helium storage dewar and thus can measure from room temperature to ~ 4 K. AC susceptibility works by driving a small current through a coil to produce a small magnetic field that then induces a small current in a second coil. The production of the drive coil signal and the detection of the pick-up coil signal are both handled by a Princeton Applied Research 5210 lock-in. When a thin film is placed between the drive and pick-up coils, the magnetic field must pass through the sample. Upon cooling the setup, the temperature will eventually fall below T_c and the thin film will enter the Meissner state. Superconductors expel all magnetic fields so the onset of superconductivity will screen the drive coil from the pick-up coil. Where a resistive transition only requires a single current path to be superconducting, good magnetic screening requires a large volume
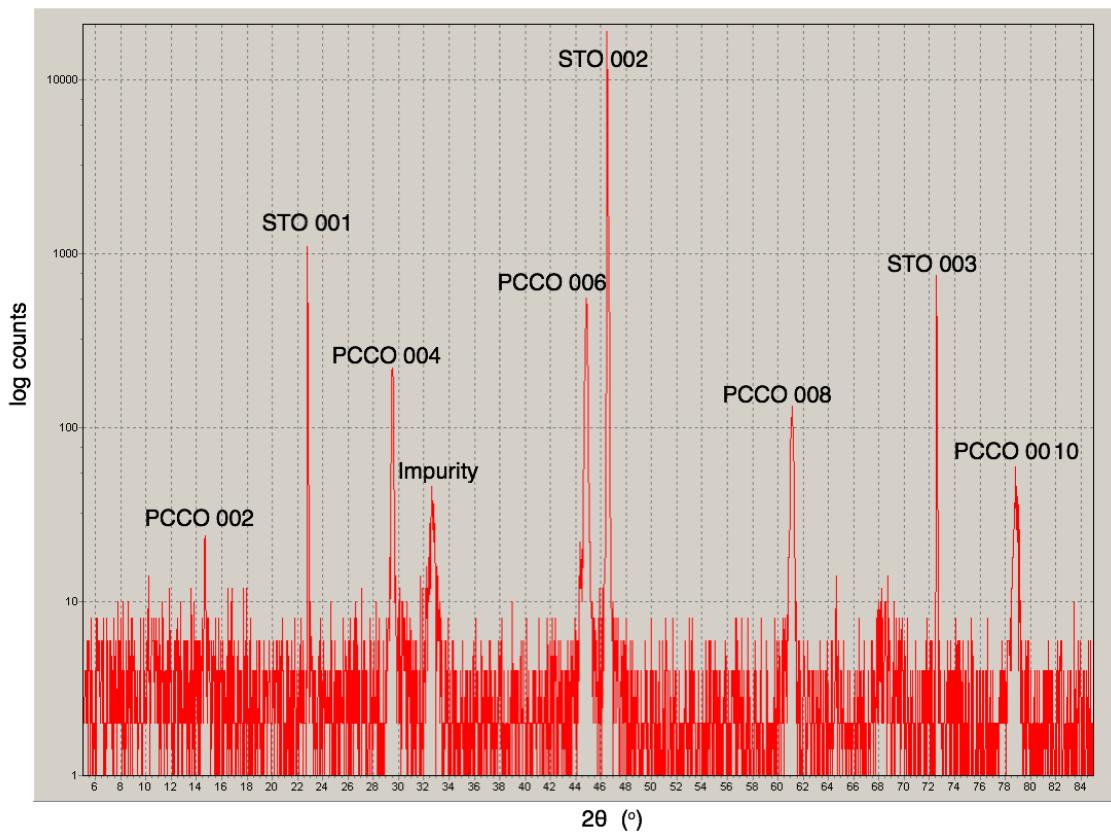
Figure 3.3: Typical X-ray diffraction data taken on a $x = .17$ $\mathrm{Pr}_{2-x}\mathrm{Ce}_x\mathrm{CuO}_{4\pm\delta}$ thin film grown on a SrTiO_3 substrate.

fraction of superconductivity.

3.3   Film Patterning

In order to extract useful parameters from electronic transport measurements, it is important to understand the path through which the current flows. This is typically achieved by patterning the thin films into convenient shapes. Films are typically patterned into an Hall bar geometry that allows for both resistivity and Hall effect measurements (Figure 3.6). This patterning forces the current to flow down the central bridge of constant width with the voltage being sampled at fixed locations. Depending upon the positioning of the voltage leads either the Hall effect or (magneto)resistance is measured.

Films can most quickly be patterned into this shape with a diamond tipped scribe, although other techniques are more precise. Scribing the film in this manner digs into the substrate and removes film material in the process, creating a barrier to current. As the film is only a few thousand ångströms thick, very little material must be removed; the scribe typically penetrates well into the substrate. Because of this, the success of this technique depends more upon the substrate being sufficiently soft to easily scratch without the application of enough force to break the substrate.

In order to pattern films more precisely, shadow masks are manufactured out of metal in the desired geometry for patterning. These masks are designed to cover the parts of the film intended to remain after patterning and allow exposure of the remaining film to some processing. This processing can be either chemical or mechanical in nature. PCCO films are patterned with both acid etches or ion milling.

A more careful technique than scribing, yet still relatively quick technique is to use acid to etch the film. Hydrochloric acid (HCl) will etch PCCO at a rate that is on the order of a kiloångström per minute for a ~ 15 % acid solution. This same technique is also appropriate for LCCO; however, in that system the etch rate is significantly faster. This difference is probably due to LCCO films being less stable; the T' phase cannot be synthesized in bulk crystals. In order to prepare the film for acid etching, the film is first spin-coated in a Headway Research PWM32 photoresist spinner with positive photoresist. For positive photoresist, the part exposed to ultraviolet light is etched; for negative photoresist, the unexposed part is etched. Here Shipley 1813 photoresist is used. The photoresist is left to harden on the film by subjecting it to a mild (100 C) heat for an hour. A shadow mask is then overlayed on the film and the film is exposed to UV light supplied by a Quintel mask aligner. Photoresist developer is then used to remove the exposed photoresist from the film. Next, the film is submerged in acid. HCl is diluted with distilled water to ~ 15 % in order to keep the rate of etching manageable. The etch is halted by transferring the film from the acid bath to a bath of distilled water. The films are then blown dry with a nitrogen gun. Complete etching of the film can be observed visually as STO is white and both PCCO and LCCO are black. Using a multimeter to measure two-wire resistance can verify full etching as both PCCO and LCCO have kilo-ohm resistances while STO is a good insulator with greater than megaohm resistance. Once the films are satisfactorily etched, the protective photoresist is removed by ultrasonicating the film in an acetone bath; acetone dissolves Shipley 1813 photoresist. This procedure typically produces good quality etches; however, care must be taken to ensure that no defects in the protective photoresist layer are present as this will translate into defects in

the patterning.

For delicate patterning jobs, where very fine features are required, ion milling offers the most defect-free method of patterning with the sharpest edges. The films are covered with the shadow mask and mounted inside of the ion mill, which is then pumped down to vacuum. A beam of argon atoms illuminates the sample with sufficently high energy to knock material off of the surface. Films are milled until all of the PCCO is removed and the ion mill is milling into the substrate itself. This procedure creates quite fine patterns; however, it is quite slow as the ion mill needs to pump down to vacuum.

After the films are patterned (by any method), they are visually checked under an optical microscope for defects in the patterning. Because the patterned films force current down a narrow channel, inhomogeneities in this bridge especially need to be avoided as this will negatively affect the quality of the measurement. If the patterning is satisfactory, wire leads are then contacted onto the films for transport measurements.

3.4 Electronic Transport Measurements Introduction

Electronic transport is an important tool in understanding material properties. In this thesis electronic transport measurements are primarily measurements of resistivity, the Hall effect, and magnetoresistance. The ability of materials to carry current under different conditions depends upon the underlying physics of the system. Resistivity, for example, is influenced by scattering from various sources like disorder or phonons. The number of charge carriers influences the Hall effect, and magnetic materials behave differently from non-magnetic ones in magnetoresistance. All transport measurements, how-

ever, require the understanding of a few basic experimental techniques discussed here.

3.5 Resistance Measurements

Transport measurements, ultimately, require contacts to be made to the films. For electronic transport, four-wire measurements are preferred. Four-wire measurements have an advantage over two-wire measurements due to the removal of contact resistance from the measurement. Four-wire resistance measurements consist of two current leads ($I+$ and $I-$) and two voltage leads ($V+$ and $V-$) electrically connected to the sample. A constant current is maintained between $I+$ and $I-$ and voltage is measured between $V+$ and $V-$. Contact resistance on the current leads can be neglected because the current source is tasked with outputting a constant current. Resistive contacts will require a larger voltage drop between current leads; this voltage is not the measurement voltage. Contact resistance on the voltage leads can be neglected due to their being at an equipotential and with no current flowing through them because of the high input impedance of the voltmeter. This picture does break down with sufficiently bad contacts, and neglects related potential issues like resistive heating due to contact resistance; however, for well-made contacts, four-wire electronic transport measurements measure sample resistance only and ignore contact resistance.

3.6 Measurement Geometry

Using a four-wire measurement scheme, a constant current is applied, the voltage is measured, and Ohm's Law, $V = IR$, is ultimately used to extract a resistance. Frequently,

however, resistivity is the more useful quantity, where $R = \frac{\rho}{t} \left(\frac{L}{w} \right)$ relates the two. The resistance, R, is an extrinsic property and depends upon the size and shape of the sample: the length, L; width, w; and thickness, t. Therefore, ρ, the resistivity, which does not depend upon sample geometry but is rather an intrinsic property of the material, is more useful. It is necessary to know the geometry of the sample, and it is frequently useful to modify the sample geometry for measurement convenience.

The simplest geometry is to put the contacts in a line on the sample with the current leads on the outside and the voltage leads on the inside (Figure 3.4). Here it is often useful for the contacts to extend the width of the sample in order to have the most uniform current flowing down the length of the sample. The relevant length for the measurement is the spacing between voltage contacts. This geometry is conceptually simple, but not preferred for films, as contacts are typically not fully uniform and substantial uncertainty in geometric factors can be present. Films can typically be easily patterned into more convenient shapes. Nevertheless, this is often a useful arrangement for samples, like crystals, that are difficult to pattern. When this method is used on crystals, the current contacts typically are made such that they completely cover the ends of the crystal in order to ensure uniform contact.

It is worth noting here another technique for measuring resistivity on unpatterned or irregular samples: the van der Pauw technique. It has been demonstrated that an *arbitrary* arrangement of four-wire contacts on the edges of a uniform, isotropic sample can be used to extract resistivity data, provided a series of steps are performed [60, 61]. The optimal configuration for van der Pauw measurements is for the leads to be at the corners of the film (Figure 3.5). A resistance is measured by running a current along one edge

45
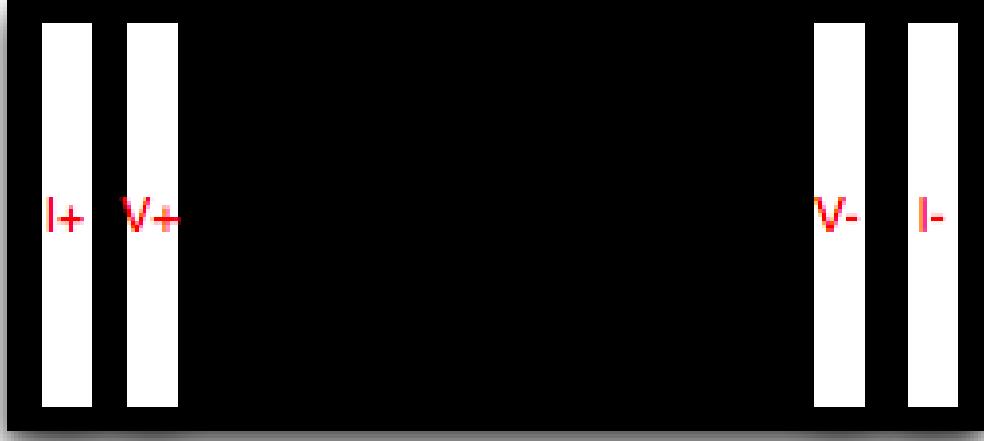
Figure 3.4: Simple four-wire resistance measurement.

and measuring the voltage drop along the other, for example, $R_{12,34} = \frac{V_{34}}{I_{12}}$. Resistance is also measured in the perpendicular direction ($R_{14,23}$). Re-naming the former $R_{vertical}$ and the latter $R_{horizontal}$, the sheet resistance, R_S, can be calculated by the van der Pauw formula:

$$e^{\frac{-\pi R_{vertical}}{R_S}} + e^{\frac{-\pi R_{horizontal}}{R_S}} = 1. \tag{3.1}$$

The sheet resistance is related to the resistivity by $\rho = \frac{R_S}{t}$, where t is the film thickness. For a uniform film, $R_{12,34} = R_{34,12}$ and, likewise, $R_{14,23} = R_{23,14}$. Likewise, reversing the polarity should also produce the same result, e.g. $R_{12,34} = R_{21,43}$. Averaging of various equivalent $R_{kl,nm}$ can produce more refined values of $R_{vertical}$ and $R_{horizontal}$. The van der Pauw formula has the disadvantage in that it typically can only be solved numerically; however, in the case of square films, a significant simplification exists. If

$R_{vertical} = R_{horizontal} = R$, then Equation 3.1 reduces to:

$$R_S = \frac{\pi R}{\ln 2}.$$

(3.2)

The film's resistivity, ρ, can then be easily calculated from there by dividing by the film's thickness. As most of our thin films are grown on 5 mm × 5 mm substrates, Equation 3.2 is a convenient simplification.

The van der Pauw method has the advantage of preserving most of the surface of the film for measurements that may require a large pristine surface area. Contacting a film for a van der Pauw resistivity measurement also often tends to be significantly faster than other methods, making this technique quite useful for rapid characterization of film quality and properties. The size of the contacts, however, can be an issue as the van der Pauw formula assumes that the contacts are on the edge of the film and large contacts can introduce error.

The best measurements are obtained from patterned films. Patterning is typically done in a Hall bar pattern that allows for both resistivity and Hall effect measurements (Figure 3.6). The current leads, at each end of the film, force the current to flow down the narrow bridge in the center. Voltage leads then sample the voltage at specific locations, depending upon the type of measurement.

Resistance measurements rely on Ohm's Law and have the voltage leads separated by a distance along the length of the bridge. This has the advantage of having the length and width fixed by patterning; the thickness of the thin film is already fixed. This geometry is also used for magnetoresistance measurements.
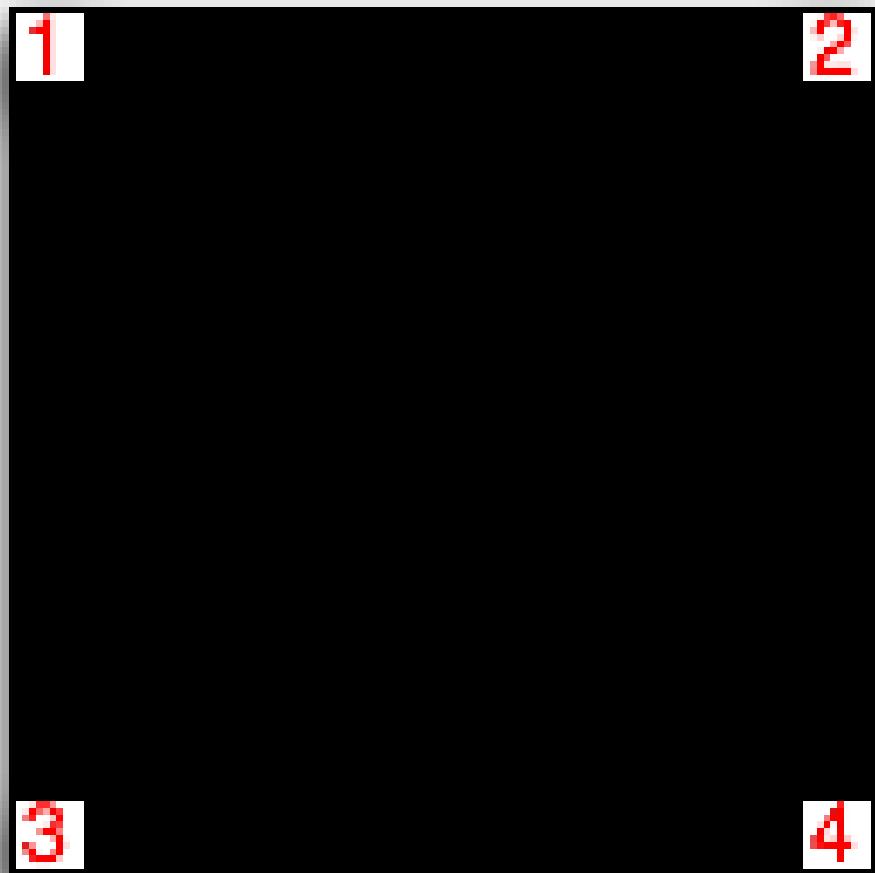
Figure 3.5: Film wired in the van der Pauw configuration (see text). Measuring V_{12} with applied current I_{34} and the equivalent vertical arrangement allows extraction of resistivity by Equation 3.2.
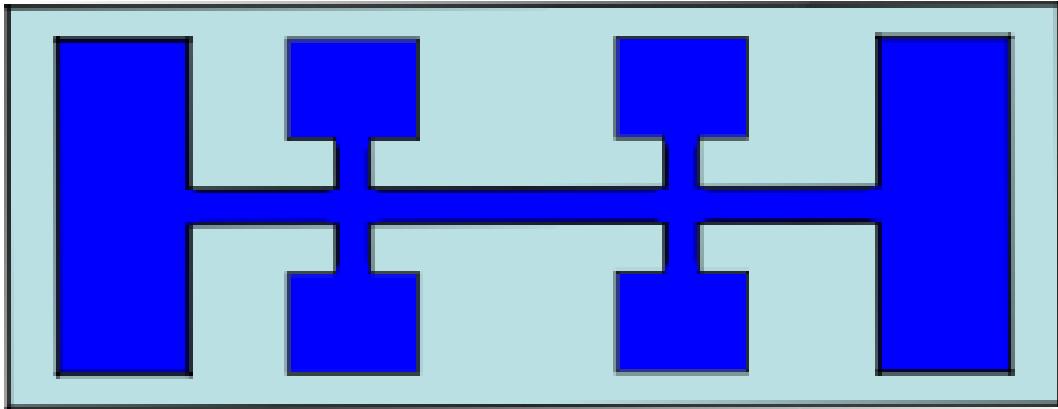
Figure 3.6: Film patterned as a Hall bar. The current leads on the ends maintain a constant current along the central bridge. Resistance measurements are performed using consecutive voltage leads on a single side of the bridge while Hall measurements are performed using voltage leads opposite each other across the bridge. For Hall effect, the magnetic field is applied into or out-of the page.

Magnetoresistance is the change in resistance in a magnetic field compared to the zero-field resistance. In a non-magnetic material the magnetoresistance should always be positive (the magnetoresistance is larger than the zero-field resistance). A very simple picture for why this happens is that in a magnetic field the Lorentz force causes charge carries to follow a curved path. This curved path is longer than the straight path. As long as the difference is larger than the mean free path of the charge carriers, there are more scattering events, hence more resistance. More detailed treatment of magnetoresistance can be found in Reference [4]. Much more complicated behaviors can occur in materials containing magnetic elements; in these situations, magnetoresistance can be either positive or negative.

To measure magnetoresistance, resistance is measured, but in a magnetic field. In anisotropic materials like the cuprates it is important to distinguish between in-plane and

out-of-plane magnetic fields. In particular, in PCCO and LCCO, it has been observed that there is an anisotropy in the in-plane magnetoresistance when the film is rotated such that the applied external magnetic field remains confined to the ab-plane. This is described further in Chapter 4.

Patterning of thin films is most useful for Hall effect measurements. The Hall effect is a transverse voltage that develops in response to current flowing through a magnetic field (Figure 3.7). A charge moving through a magnetic field feels a force perpendicular to its direction of motion, $\vec{F} = q\vec{v} \times \vec{B}$. This force separates negative and positive charges, creating a voltage perpendicular to current flow that can be measured by voltage leads positioned on opposite sides of the sample. As this voltage is quite small compared to the longitudinal voltage, patterning greatly helps Hall measurements by aligning the voltage leads to minimize longitudinal separation.
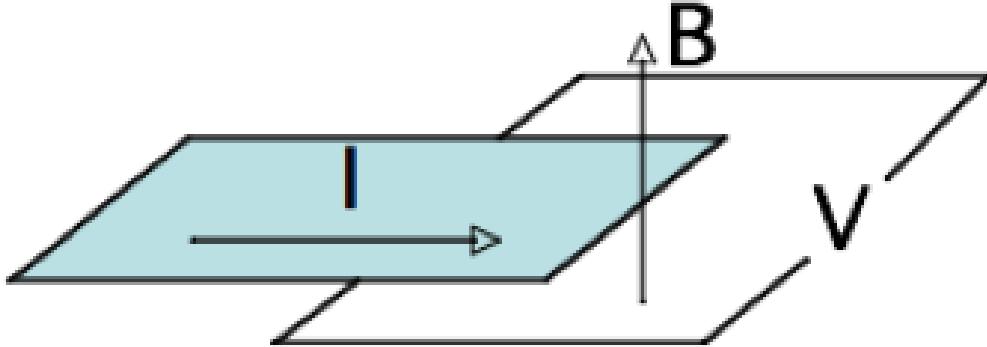
Figure 3.7: A magnetic field, B, applied perpendicular to current flow, I, causes a voltage, V, to appear perpendicular to both. The Hall resistance is this voltage divided by the applied current. If the voltage leads are not exactly aligned there will be an additional component due to magnetoresistance in the voltage signal.

Nevertheless, the raw Hall signal measured is typically a combination of Hall resistance, $R_{xy} = \frac{V_y}{I_x}$, and resistance, $R_{xx} = R\left(= \frac{V_x}{I_x}\right)$. In order to separate these two resistances, it is noted that the sign of R_{xy} depends upon the direction of the magnetic field, due to the $\vec{I} \times \vec{B}$ term. Therefore, by measuring the Hall effect twice, and reversing the magnetic field direction in between measurements, two resistivities can be obtained: $R^+ = R_{xx} + R_{xy}$ and $R^- = R_{xx} - R_{xy}$. From these, one sees that R_{xx} and R_{xy} can then be extracted by

$$\begin{pmatrix} R_{xx} \\ R_{xy} \end{pmatrix} = \frac{1}{2} \begin{pmatrix} 1 & 1 \\ 1 & -1 \end{pmatrix} \begin{pmatrix} R^+ \\ R^- \end{pmatrix}.$$

The average of the two measurements will cancel the Hall signal, $R_{xx} = \frac{R^+ + R^-}{2}$, and the Hall signal can similarly be extracted by $R_{xy} = \frac{R^+ - R^-}{2}$. The Hall coefficient, $R_H = \frac{E_y}{j_x B}$, then follows from R_{xy}. The Hall effect has the useful feature that $R_H = \frac{-1}{ne}$, i.e. its magnitude depends on the number of charge carries, n, and its sign depends upon the sign of the charge carriers, e. This allows, for example, measurement of the actual doping level in a sample. However, this interpretation of the Hall effect (a simple Drude model) is only valid for a one-band systems. If there are multiple charge carriers in the system the interpretation of Hall data is significantly more complicated.

3.7   Contacts

Transport measurements all rely upon making good contacts to the material. For $Pr_{2-x}Ce_xCuO_{4\pm\delta}$, contacts are typically made by soldering gold wires onto the films with an indium-based solder, either pure indium metal or an indium/silver alloy. "Normal" sol-

der, a lead/tin eutectic mix, is not preferred. $Pr_{2-x}Ce_xCuO_{4\pm\delta}$ films are damaged by the flux. The high temperatures needed to melt the lead/tin solder can thermally stress and, in some cases, crack the $SrTiO_3$ substrate if contacts must be remade frequently. Additionally, high temperatures can locally anneal $Pr_{2-x}Ce_xCuO_{4\pm\delta}$, changing the oxygen content and, therefore, transport properties. Indium's low melting point of 430 K (157 C, 314 F) combats this. Additionally, indium is able to wet glasses and ceramics, helping to make good electrical contact, and is quite ductile, making the contacts less likely to break. For patterned films, indium is soldered to the film to maximally cover the current or voltage pad; then the gold wire is soldered onto the indium. This creates a large contact with low contact resistance that is unlikely to heat the film. Larger contacts are also less delicate. When contacting unpatterned films, additional concerns regarding the size and shape of contacts must also be considered. Contacts are generally made by hand under an optical microscope. With practice, wires can be soldered to sub-millimeter-square contact areas by hand.

Occasionally, indium is not optimal for making contacts. In these cases, silver paint is often used. This conductive paint flows easily and can be applied with a paint brush or similar utensil. However, given the typical dimensions of samples, a wooden Q-tip, broken to create a long thin splinter, offers the best choice for fine control. Allowing the silver paint to dry slightly before application increases its viscosity and allows for more precise paint positioning. The silver paint contacts are then allowed to dry; gently heating the sample ($T \lesssim 100$ C) can hasten this process. Silver paint contacts have the disadvantage of being quite brittle; poor contacts can fail due to thermal stresses during measurement runs. However, silver paint can contact very delicate samples more gently

than indium. Silver paint contacts will also survive at high temperatures, for example, for transport measurements well above the melting temperature of solder. This specific application will be discussed in detail in Chapter 7 of this thesis in the context of high temperature resistivity measurements.

Chapter 4

Angular Magnetoresistance (AMR)

4.1 Introduction

The crystal structure of the cuprate superconductors consists of planes of copper and oxygen atoms sandwiching doping layers, usually consisting of rare earth elements. In the specific case of the 214 electron-doped cuprate superconductors, the unit cell is tetragonal and crystalizes in the T' structure. In this crystal structure, the copper atoms form square lattice planes that are staggered between layers. It has long been known that the cuprate superconductors have parent compounds with an antiferromagnetic (AFM) ground state that is suppressed with doping and that, in this state, the magnetic moments are on the copper atoms. The mechanism by which the magnetism is suppressed is not symmetric with doping: hole doped materials suppress magnetism by spin frustration, whereas electron doped materials suppress magnetism by spin dilution. One of the consequences of these differing mechanisms is an asymmetry in the phase diagram. Unlike in hole doped systems where the AFM state is rapidly suppressed well before superconductivity appears, electron doped cuprates exhibit a much more gradual suppression of AFM, leading to questions of competition and/or coexistence (either one being either macroscopic or microscopic) in under-doped superconducting samples. Evidence for magnetic ordering has come from neutron scattering (NS) and muon spin resonance (μSR) in crystals [44, 45, 47, 48, 49, 50].

Although neutron scattering techniques have been applied to magnetic thin films [63], in general, antiferromagnetism in the cuprates has not been measureable in thin films by these techniques. Spin-sensitive scattering measurements in the cuprates have used crystals. It has been assumed that the magnetic structure of electron doped cuprates like $Pr_{2-x}Ce_xCuO_{4\pm\delta}$, $Nd_{2-x}Ce_xCuO_{4\pm\delta}$, or $Sm_{2-x}Ce_xCuO_{4\pm\delta}$ is the same in both single crystal and thin film preparations.

Here, we used transport data to demonstrate detection of the antiferromagnetic phase in PCCO ($Pr_{2-x}Ce_xCuO_{4\pm\delta}$) thin films. These results compare well with what has been observed by NS and μSR in that system. In PCCO, we find that there is evidence for AFM order up to optimal doping. Its disappearance suggests a quantum phase transition inside of the superconducting dome. We subsequently used transport data to detect AFM in thin film preparations of T' LCCO ($La_{2-x}Ce_xCuO_{4\pm\delta}$), an electron doped cuprate superconductor that can only be prepared as a thin film.

The zero-field spin structure of the electron doped cuprates is noncollinear antiferromagnetism. The spins are aligned antiferromagnetically, alternating between the a and b crystallographic axes between adjacent CuO_2 layers (Figure 4.1). At sufficiently high magnetic fields applied in the plane there is a transition between the noncollinear AFM to a collinear spin-flop state. In this state, the antiferromagnetic structure in adjacent planes is no longer perpendicular; it has become parallel. In the zero field noncollinear AFM state, the spins prefer to align along the crystal axes, i.e. [100] and [010]. In the spin-flop state, the easy axes become the [110] directions and have a slightly lower magnetoresistance than when the spins are forced to lie along one of the [100] directions. This has been observed experimentally in $Pr_{2-z-x}La_zCe_xCuO_4$ (PLCCO) [35]. Antiferromagnetism can

be detected due to a slight angular dependence of magnetoresistance.

PLCCO, PCCO, and LCCO (in thin film form) are all the same T' crystal structure and it is expected that the magnetic structure is also the same. The T' phase of LCCO can only be stabilized as a thin film, which makes spin sensitive scattering experiments difficult. In PCCO, neutron scattering and μSR have been performed, yet there is some disagreement as to the phase diagram. An antiferromagnetic quantum phase transition (QPT) has been suggested for dopings from $x = .13$ [45] to $x = .16$ [64, 65]. These differing placements of the AFM QPT have correspondingly different interpretations as to whether AFM order coexists with superconductivity. Quantum critical points (QCP) in the cuprates at these dopings have been debated [66].

4.2   Experiment

In order to perform the angular magnetoresistance (AMR) measurement, it is necessary to have high quality thin films due to the small amplitude of the AMR oscillations. The thin films of $Pr_{2-x}Ce_xCuO_{4\pm\delta}$ and $La_{2-x}Ce_xCuO_{4\pm\delta}$ were grown on (100) oriented $SrTiO_3$ (STO) or $LaSrGaO_4$ (LSGO) substrates by pulsed laser deposition (PLD) using a LambdaPhysik KrF excimer laser with a 248 nm wavelength. The films were grown to a nominal thickness of 300 nm and were annealed in situ immediately after deposition by adjusting the substrate temperature and the chamber pressure to annealing conditions. Films were then characterized by x-ray diffraction, AC susceptibility, and resistivity prior to angular magnetoresistance measurements.

A large magnetic field placed in the ab-plane will force the copper magnetic mo-
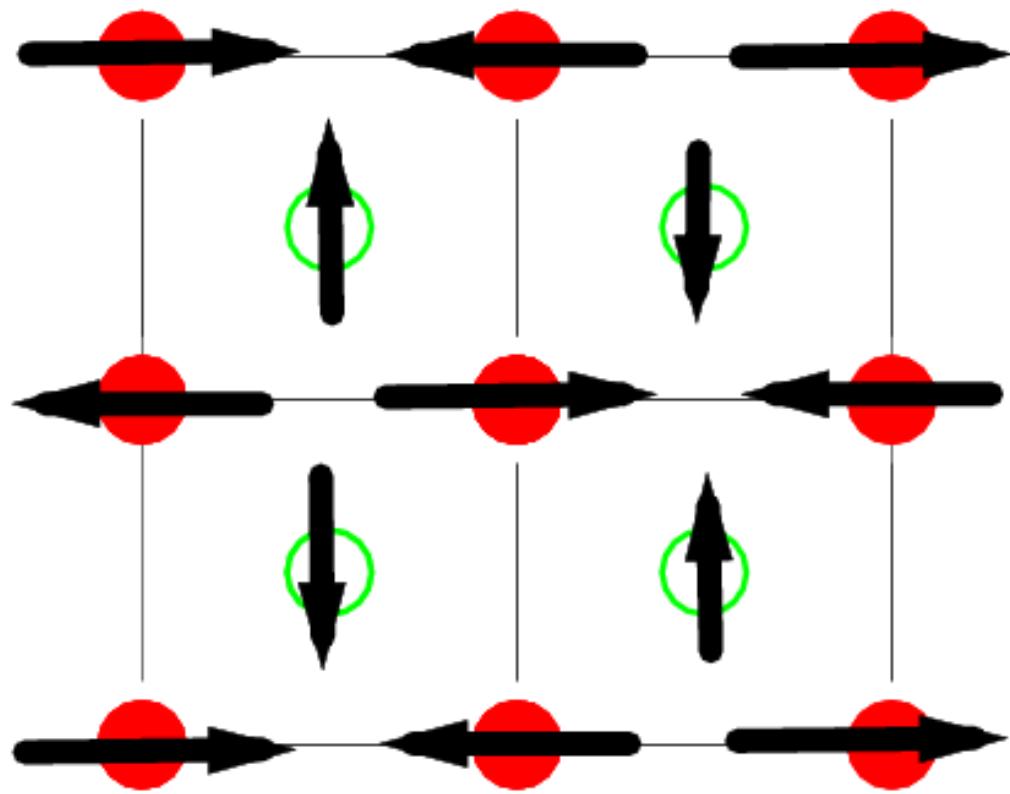
Figure 4.1: Zero field spin structure of $Pr_{2-x}Ce_xCuO_{4\pm\delta}$ as seen looking along the c-axis [36]. The solid and hollow balls are Cu atoms on adjacent CuO planes.

ments to switch to a collinear AFM state in the direction of the applied field. This was accomplished by mounting the films in a Quantum Design Physical Properties Measurement System (PPMS) capable of applying magnetic fields up to 14 T. The samples were mounted on a rotator stage that allowed $360°$ of rotation with the axis of rotation parallel with the c-axis of the crystal structure (Figure 4.2). As the magnetic field was rotated through the CuO_2 plane, the copper spins were alternately aligned along the easy and hard axes, [110] and [100] respectively.

The epitaxial nature of the pulsed laser deposition growth of both the films forces the crystallographic a- and b-axes to align with the substrate a- and b-axes. In the T' crystal structure, and in $SrTiO_3$, the a- and b-axes are the equivalent due to lattice symmetry. The films were patterned such that the current path was along the a-axis ($I \parallel$ [100]) unless stated otherwise. The films were mounted on the PPMS rotator stage such that the $\theta = 0°$ position is where $H \perp$ [100].

In PLCCO it has been observed experimentally that the magnetoresistance takes on measurably different values, depending upon whether the collinear AFM is aligned along the Cu-Cu direction, [110], or along the Cu-O-Cu direction, [100]. This difference can be seen at the largest applied fields in Figure 4.3, although the origin of the anisotropic scattering leading to these different values is not well understood. Rotation of the film through $360°$, at fixed applied magnetic field, causes the resistance to alternate between the high and low resistance directions. Due to the tetragonal symmetry of the crystal this should happen four times per $360°$ rotation.

These oscillations in magnetoresistance are due to an underlying magnetically ordered state and therefore their observation is an indication of the magnetic structure of
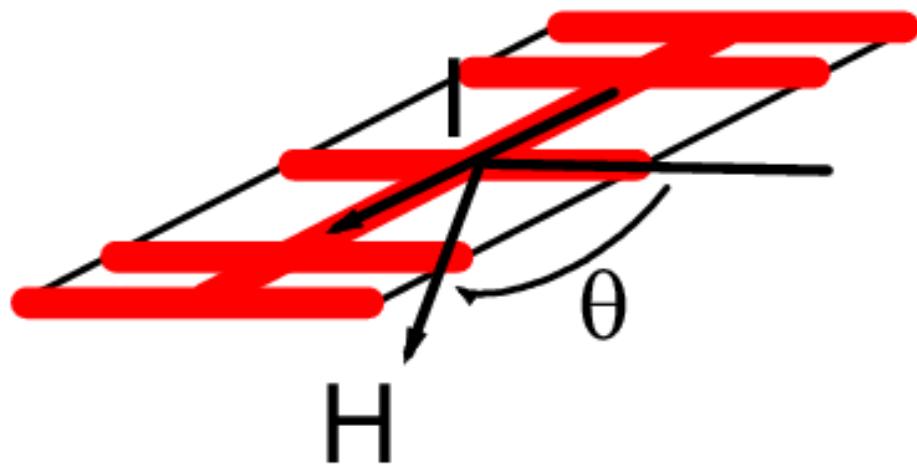
Figure 4.2: A patterned thin film rotated in an applied in-plane magnetic field [36]. The angle θ represents the angle between the field, H, and the current, I. The current direction is along the crystalline a-axis.
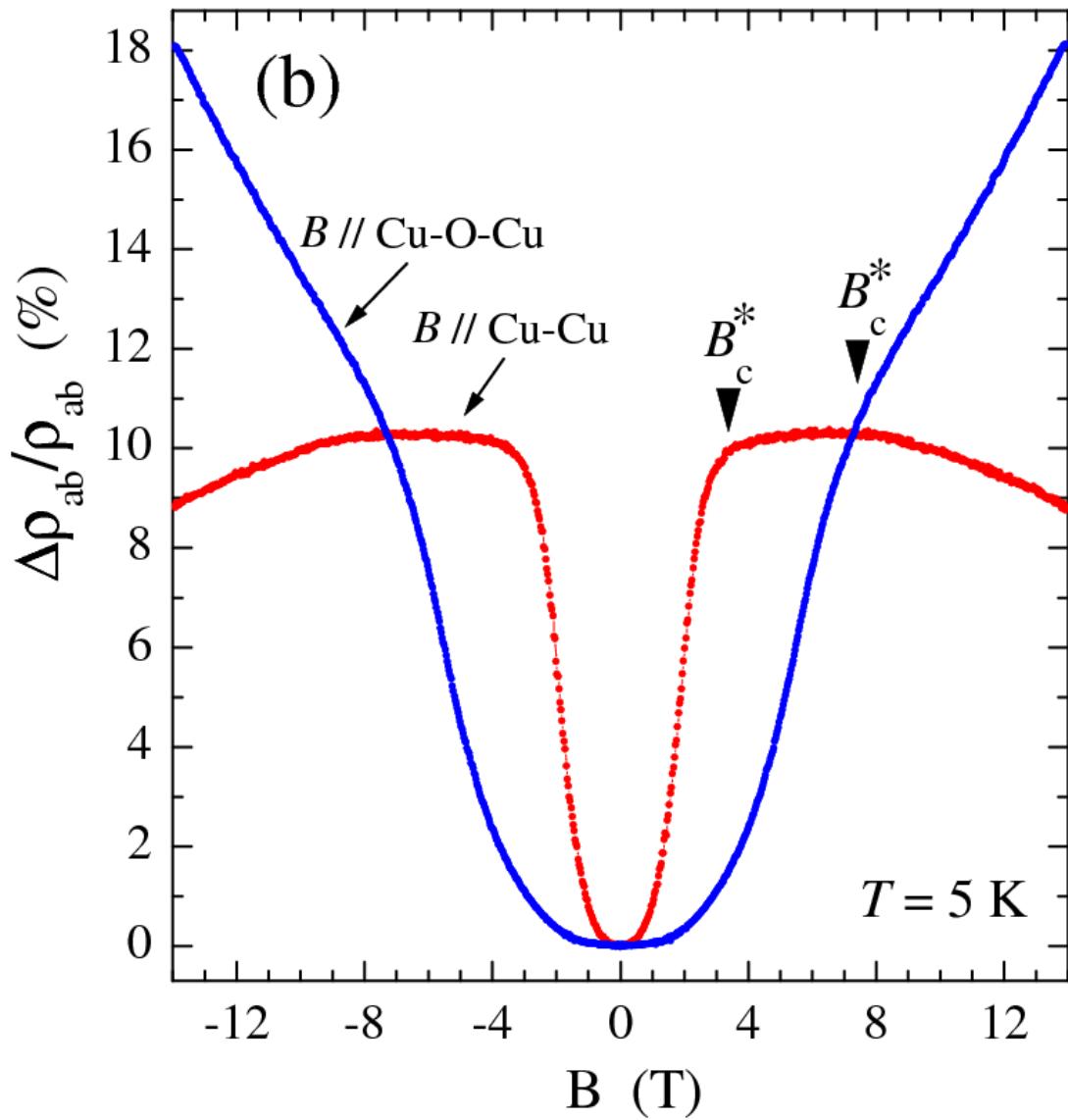
Figure 4.3: Magnetoresistance of $Pr_{2-z-x}La_zCe_xCuO_4$ along the [100] (B∥Cu-O-Cu) and along the [110] (B∥Cu-Cu) directions [35]. The transition to the collinear spin state in each direction is denoted by B_c^*.

the crystal lattice. The angular magnetoresistance oscillation's relationship to the crystal's magnetic structure is further strengthened by comparison to neutron scattering data. In $Pr_{2-z-x}La_zCe_xCuO_4$ (Figure 4.3), B_c^* is related to the end of the spin-flop transition as seen by neutron scattering. Neutrons have a magnetic moment and therefore are sensitive to the magnetic, as well as the structural, Brillouin zone.

These oscillations are generally quite small; typically the change in resistance is less than 1% of the average resistance value. The angular magnetoresistanceis measured as a change in magnetoresistance with angle, typically either $\delta\rho(\theta, H) = \frac{\rho(\theta,H)-\rho(\theta,H=0)}{\rho(\theta,H=0)}$, or this value normalized by setting the minimal $\delta\rho(\theta, H)$ to zero, e.g., $\delta\rho'(\theta, H) = \delta\rho(\theta, H) - \delta\rho(\theta_{R_{min}}, H)$ with $\theta_{R_{min}} = 180°$ normally. For this study, the most important feature of the angular magnetoresistance signal is the temperature where the amplitude of oscillations goes to zero; the numerical value of the angular magnetoresistance oscillation amplitude does not enter into the analysis.

4.3 $Pr_{2-x}Ce_xCuO_{4\pm\delta}$ Results

Thin films of under-doped $Pr_{2-x}Ce_xCuO_{4\pm\delta}$ show four-fold magnetoresistance modulation when a sufficiently high magnetic field is rotated in the ab-plane (Figure 4.4). The signal develops between 4 T and 8 T, indicating that the spin-flop transition in PCCO is in this field range and that above 8 T, the spins are in a collinear arrangement. At higher fields the signal is more pronounced.

The largest magnetic field that was accessible for these measurements was 14 T. Subsequent measurements were performed at that field in order to maximize signal am-
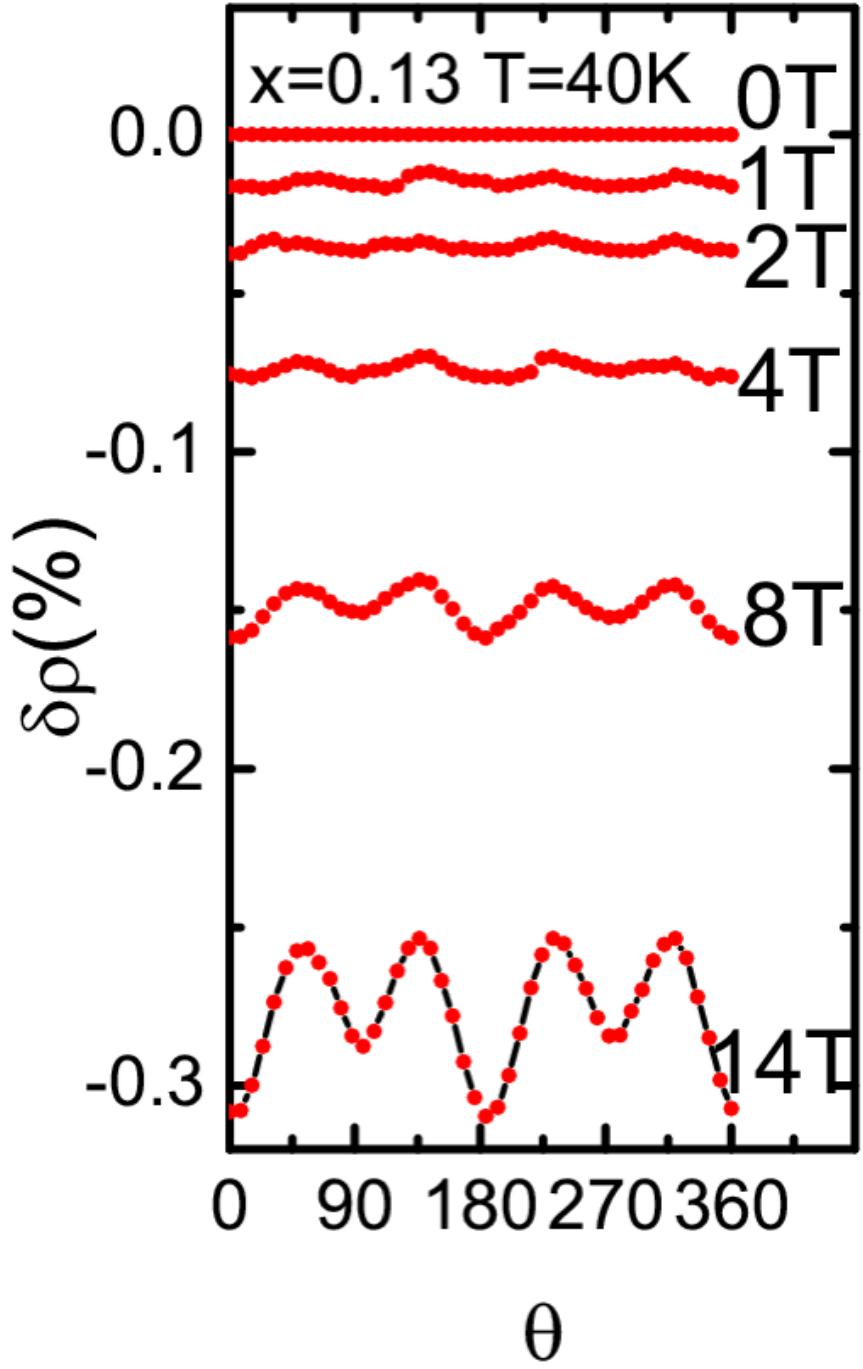
Figure 4.4: Magnetoresistance oscillations are seen in $Pr_{2-x}Ce_xCuO_{4\pm\delta}$ at sufficiently high magnetic fields [36]. Between 4 T and 8 T a four-fold oscillation develops, becoming more pronounced at 14 T. The amplitude of the angular magnetoresistance oscillations, $\delta\rho(\theta, H) = \frac{\rho(\theta,H)-\rho(\theta,H=0)}{\rho(\theta,H=0)}$, is related to the film's antiferromagnetism.

plitude. These measurements were performed on a range of dopings of PCCO.

On the overdoped side of the phase diagram, no angular magnetoresistance was observed. This is consistent with antiferromagnetism not being present at higher dopings. An AMR signal is seen at under- and optimal dopings (Figures 4.5, 4.6, 4.7, and 4.8). The underdoped side of the PCCO phase diagram has a signature of AFM and superconductivity at lower temperature.
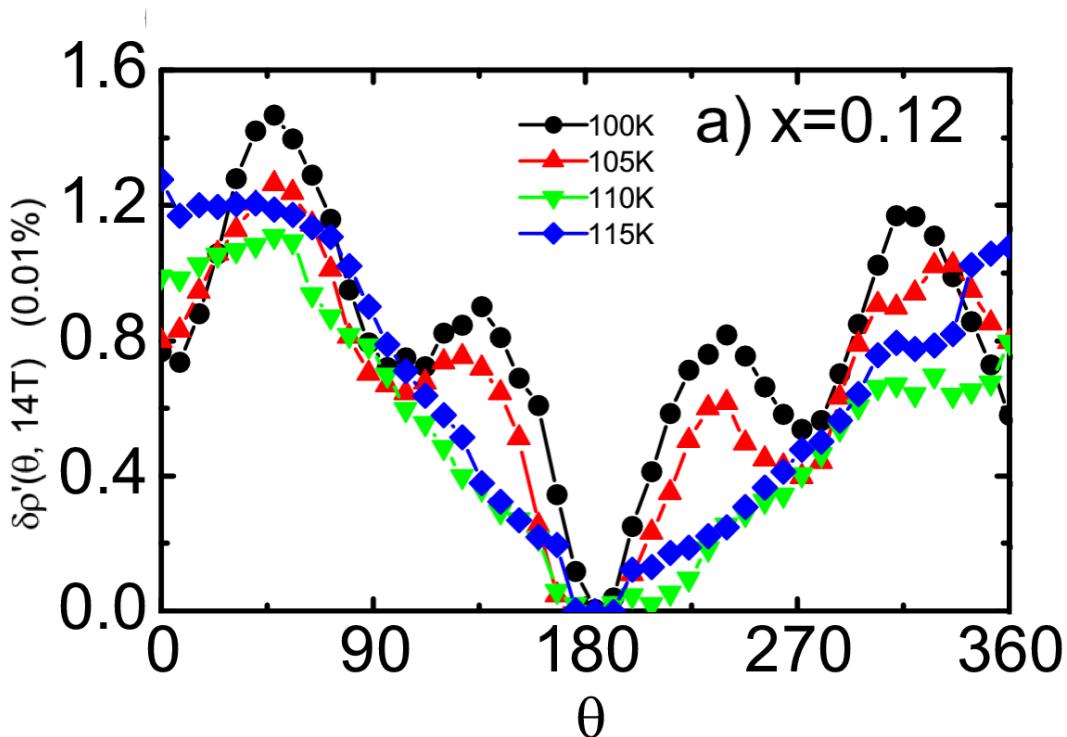
Figure 4.5: Magnetoresistance oscillations are seen in under-doped $Pr_{2-x}Ce_xCuO_{4\pm\delta}$ ($x = .12$) [36]. The Néel temperature, estimated from where the four-fold oscillations disappear, is between 105 K and 110 K.

It can be seen that the highest observed temperature for AMR oscillations decreases with increased doping (Figure 4.9). This trend holds across the underdoped side of the
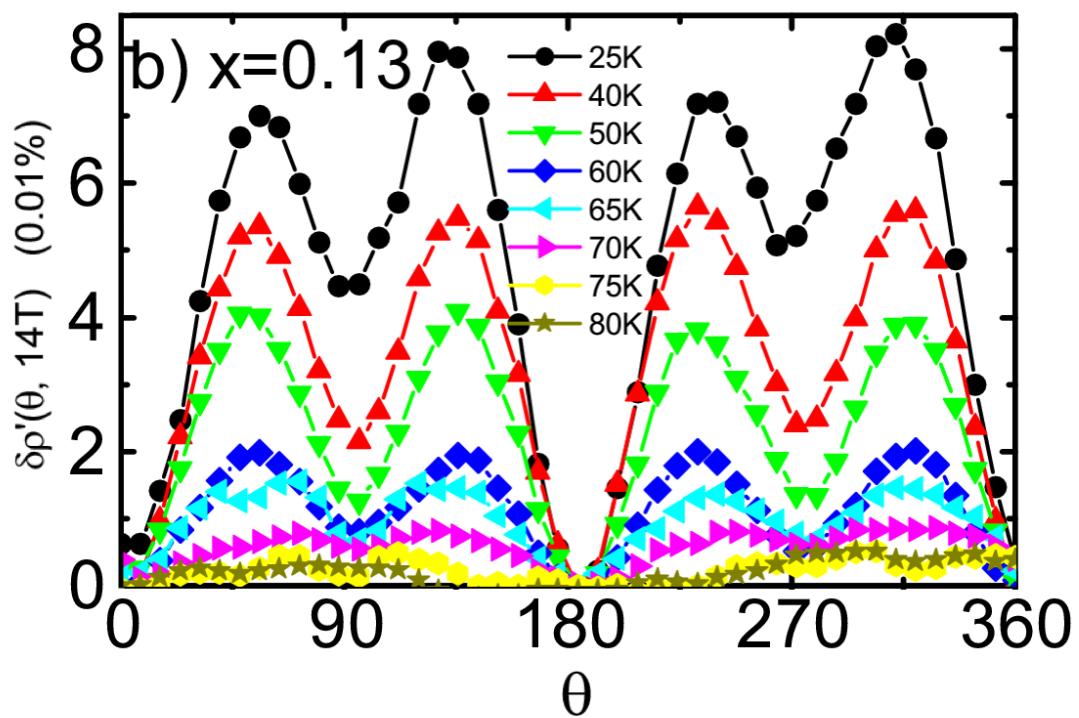
Figure 4.6: Magnetoresistance oscillations are seen in under-doped $Pr_{2-x}Ce_xCuO_{4\pm\delta}$ ($x = .13$) [36]. The Néel temperature is between 70 K and 75 K.
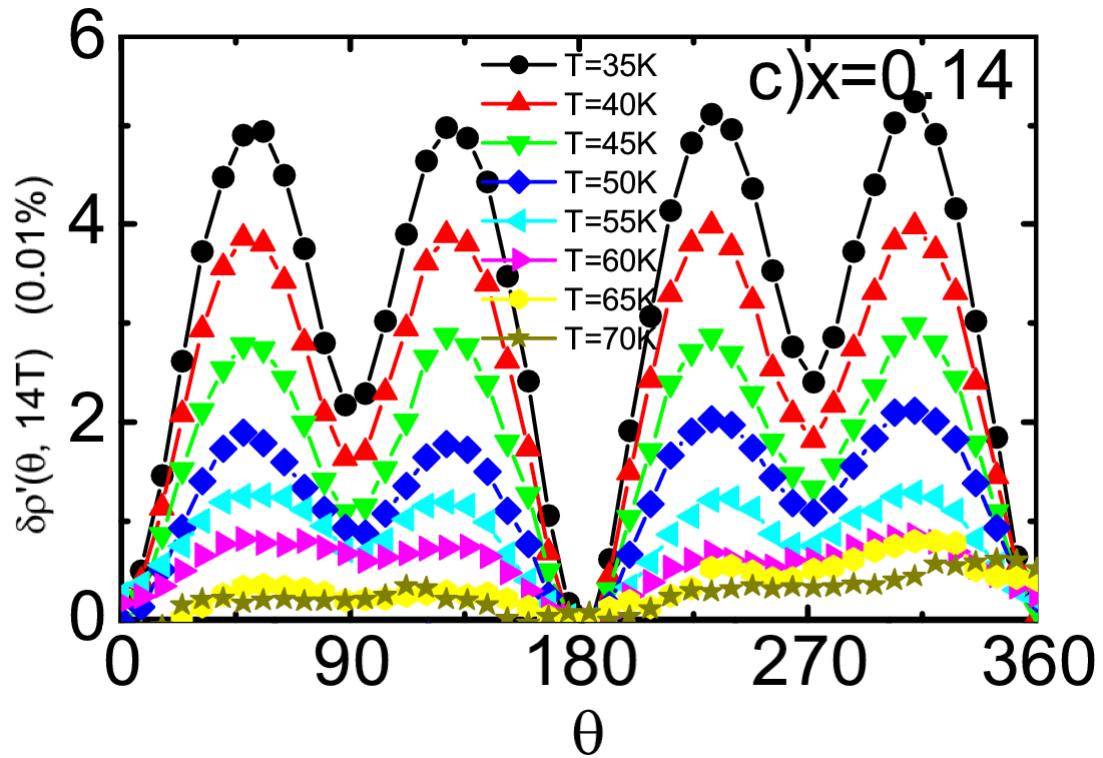
Figure 4.7: Magnetoresistance oscillations are seen in under-doped $Pr_{2-x}Ce_xCuO_{4\pm\delta}$ ($x = .14$) [36]. The Néel temperature is between 60 K and 65 K.
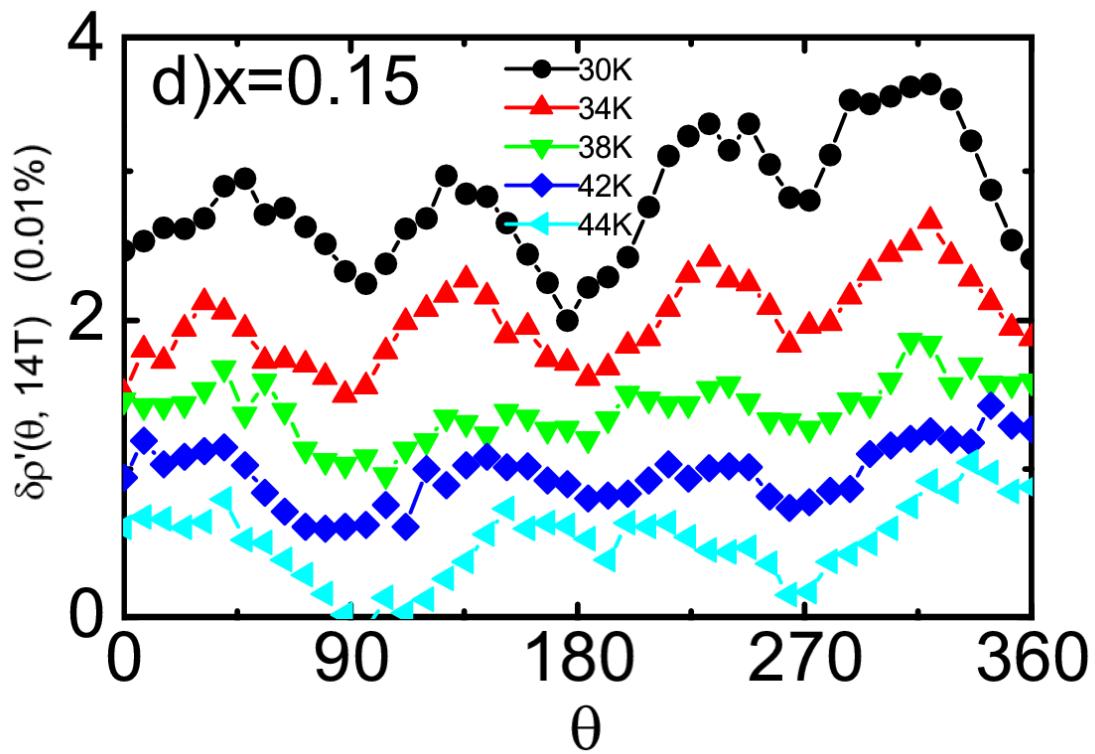
Figure 4.8: Magnetoresistance oscillations are seen in optimally doped $Pr_{2-x}Ce_xCuO_{4\pm\delta}$ ($x = .15$) [36]. The Néel temperature is between 34 K and 38 K.

phase diagram and indicates Néel temperature suppression with increased cerium doping. The AFM phase seems to disappear at around $x = .16$.
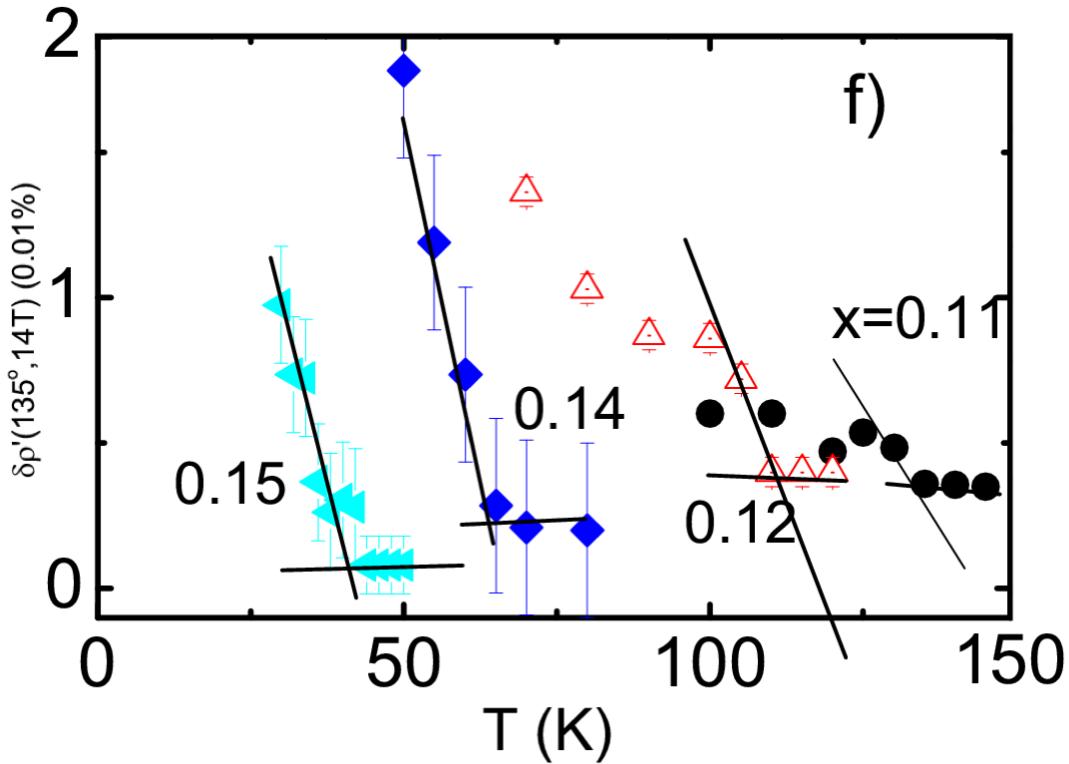
Figure 4.9: The amplitude of the magnetoresistance oscillations in $Pr_{2-x}Ce_xCuO_{4\pm\delta}$ decrease with temperature before disappearing completely [36]. The Néel temperature is the point at which the oscillations disappear. It decreases systematically with increasing cerium doping.

Although there is some disagreement between techniques like μSR and inelastic neutron scattering (INS) to determine the extent of the AFM phase in PCCO, our measurements indicate that AFM ordering is present up to $x = .15$ above T_c. AMR does not allow measurement of T_N in the superconducting state; however, the trend from lower dopings suggests that the AFM QPT is around $x = .16$ (Figure 4.10). Other studies have suggested a Quantum Critical Point (QCP) at around this doping [64, 65].
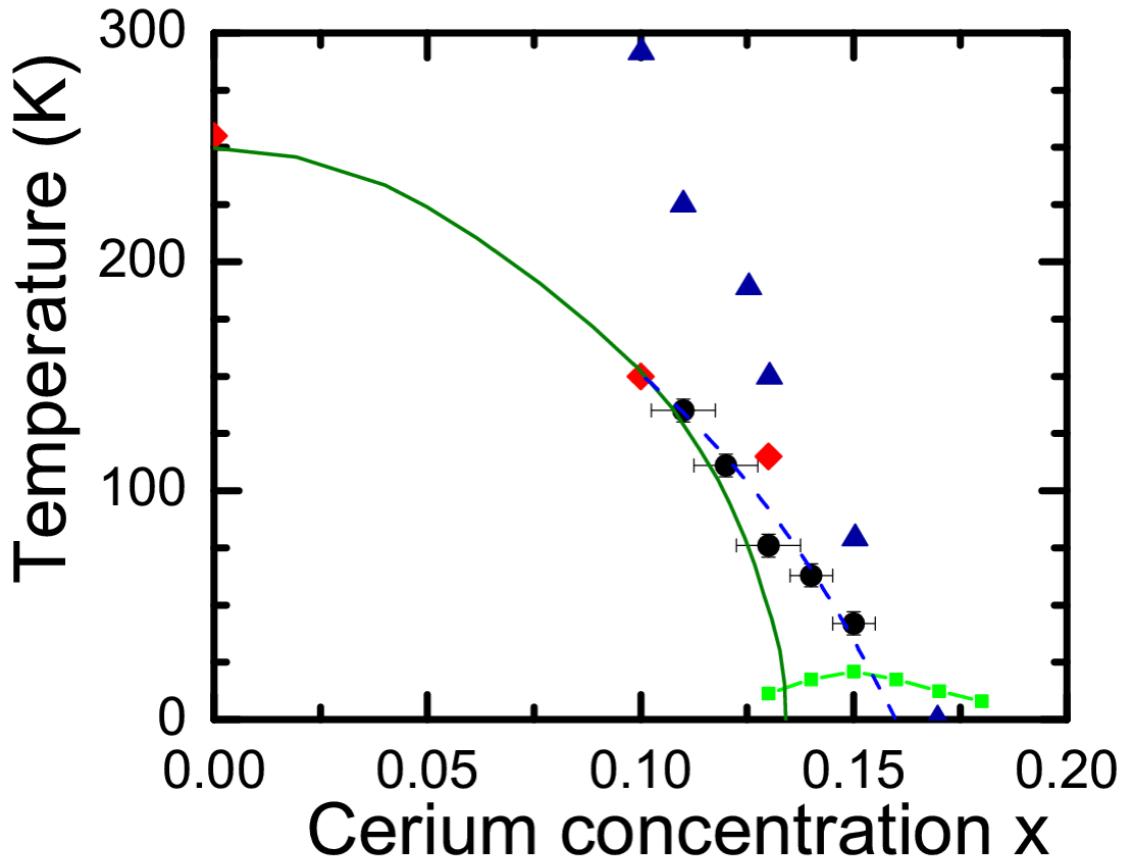
Figure 4.10: The Néel temperature as determined by angular magnetoresistance (circles) indicates a quantum phase transition at around $x = .16$ [36]. Diamonds and the solid line indicate T_N determined by μSR from [44] and by INS from [45] respectively. Triangles are optical determinations of a normal state gap from [67, 68], suggested to be the onset of 2D spin-wave fluctuations.

4.4 $Pr_{2-x}Ce_xCuO_{4\pm\delta}$ Discussion

AFM suppression at around $x = .16$ is suggestive of a quantum phase transition inside the superconducting dome. Transport studies [64, 65, 69], ARPES [43], and optical measurements [67, 68] on PCCO and NCCO have suggested a similar doping for an AFM QPT. This has been contradicted by INS on NCCO suggesting disappearance of antiferromagnetism at $x = .13$ and no coexistence of superconductivity and long range AFM [45]. It has also been contradicted by ARPES on SCCO suggesting short range AFM at $x = .14$ [46]. Neutron scattering and μSR have produced differing results [44, 45, 47, 48, 49, 50]. AFM extending to $x = .16$ indicates significant coexistence between antiferromagnetism and superconductivity.

The relationship between angular magnetoresistance and antiferromagnetism is largely empirical. It has been shown that in $Pr_{2-z-x}La_zCe_xCuO_4$, magnetoresistance anisotropy is related to the long range order antiferromagnetism seen by neutron scattering [35]. Likewise, in $Pr_{2-x}Ce_xCuO_{4\pm\delta}$ the angular magnetoresistance signal suggests a T_N that is consistent with some of the other measurements of T_N in that system. Antiferromagnetism due to possible magnetic impurities or magnetic impurity phases in the PCCO crystal lattice can be ruled out as a source of the angular magnetoresistance oscillations by considering oxygenated films. The addition of oxygen to optimally doped $x = .15$ films, for example, in as-grown or incompletely reduced films, shows that the AMR signal can be quite enhanced with oxygen addition (Figure 4.11) compared to optimally annealed films of the same doping (Figure 4.8). Oxygen can be reversibly added to or removed from $Pr_{2-x}Ce_xCuO_{4\pm\delta}$ films after initial growth and is not magnetic; oxygen-driven en-

hancement of the angular magnetoresistance signal is not due to magnetic disorder. Furthermore, neither oxygenation nor reduction introduces or removes impurity peaks in X-ray diffraction data, indicating little oxygen-induced change in impurity phases present in the film. Therefore, AMR dependence on oxygen suggests angular magnetoresistance oscillations are a feature of PCCO itself and not any impurity phase. Furthermore, insofar as oxygen can be treated as a dopant, the angular magnetoresistance signal depends on the number of charge carriers much more strongly than on disorder (see Chapter 5). AFM enhancement, with oxygenation, is consistent with the picture that AFM suppression, with cerium doping in the electron doped cuprates, is due to spin dilution [21]. The strong response to oxygen (Figure 4.11), which can easily be adjusted without damaging the crystal structure, suggests that the AMR signal is responding to AFM intrinsic to the PCCO crystal and its doping and not to any spurious phase.

Through the observation of angular magnetoresistance oscillations in $Pr_{2-x}Ce_xCuO_{4\pm\delta}$, we were able to show that transport measurements can be used to study antiferromagnetism in that system. The angular magnetoresistance oscillations in $Pr_{2-x}Ce_xCuO_{4\pm\delta}$ are observed to decrease with temperature and doping and are observed to disappear at the Néel temperature determined by spin-sensitive scattering experiments, as in PLCCO [35]. We observe that the Néel temperature found through AMR supports a phase diagram where antiferromagnetism extends up to $x = .15$ above T_c and suggests disappearance at $x \approx .16$ behind the superconducting dome (Figure 4.10). This work, therefore, supports the picture of Quantum Critical Point at around $x = .16$ [64, 65] and suggests that this QCP has an antiferromagnetic nature. Additionally, as these experiments are transport measurements and were performed on thin films, these conclusions further suggest that
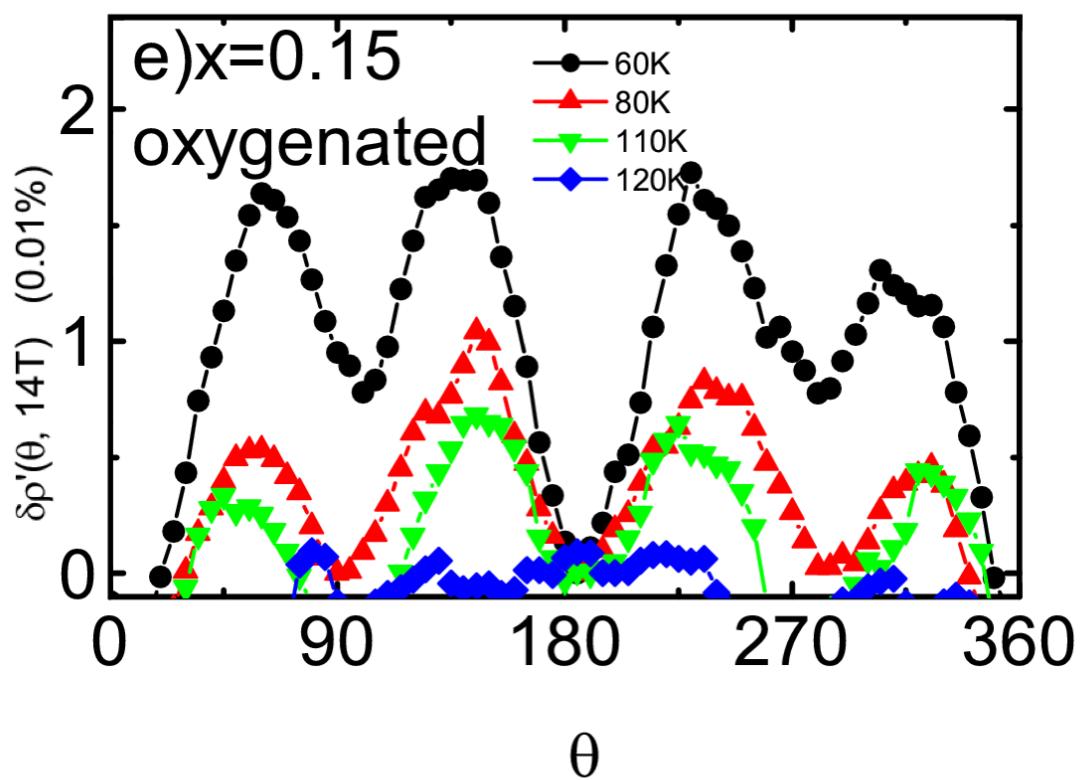
Figure 4.11: Angular magnetoresistance of an oxygenated $x = .15$ $Pr_{2-x}Ce_xCuO_{4\pm\delta}$ thin film [36]. Oscillations are observed to go to zero between 110 K and 120 K.

angular magnetoresistance is a useful technique for studying antiferromagnetism in systems that are not amenable to spin-sensitive scattering studies.

4.5 $La_{2-x}Ce_xCuO_{4\pm\delta}$ Results

A similar set of experiments was undertaken on $La_{2-x}Ce_xCuO_{4\pm\delta}$ (LCCO) thin films [70]. This electron-doped cuprate system cannot be grown as bulk crystals in the correct phase, preventing most measurements of magnetic structure. Thin films of LCCO can be grown in the T' phase for a range of cerium dopings. Here LCCO films were prepared with cerium dopings from $x = .06$ to $x = .15$. The $x = .06$ doping is the most lightly doped LCCO film that it is possible to synthesize; the parent compound does not form in the T' structure. In this system, optimal doping is around $x = .10$ or $x = .11$. The LCCO system is comparable to the PCCO system so antiferromagnetic ordering is expected to be present in the system.

Thin films of LCCO show two-fold angular magnetoresistance oscillations (Figure 4.12). This is in contrast to the four-fold oscillations seen in PCCO. However, like PCCO's four-fold oscillations, LCCO's two-fold oscillations decrease in amplitude with increasing temperature, eventually disappearing. The temperature at which these oscillations disappear decreases with cerium doping as well. This doping dependence suggests that angular magnetoresistance oscillations in $La_{2-x}Ce_xCuO_{4\pm\delta}$ follow the Néel temperature as in $Pr_{2-x}Ce_xCuO_{4\pm\delta}$. $La_{2-x}Ce_xCuO_{4\pm\delta}$ and $Pr_{2-x}Ce_xCuO_{4\pm\delta}$ are thought to be similar systems.

By comparing the amplitude of the angular magnetoresistance signal $90°$ apart,
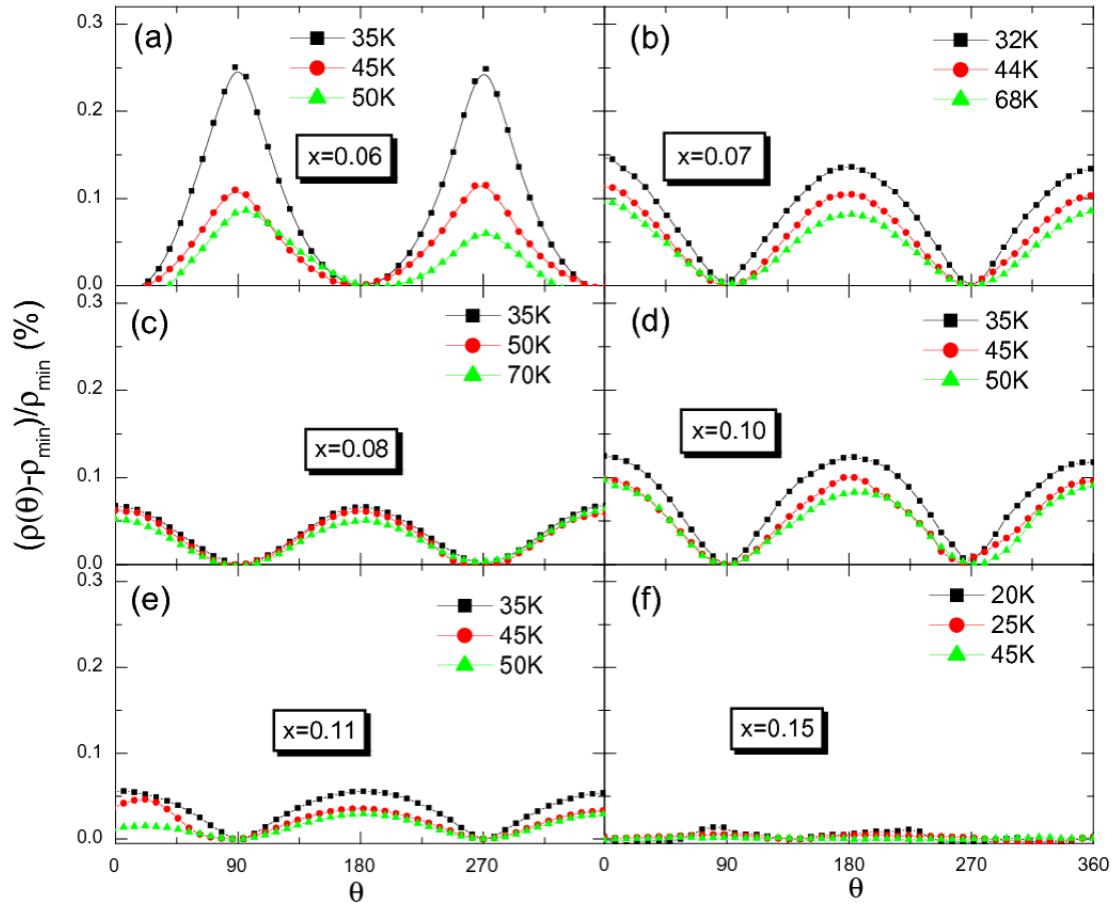
Figure 4.12: Angular magnetoresistance oscillations of a $La_{2-x}Ce_xCuO_{4\pm\delta}$ thin films with cerium dopings from $x = .06$ to $x = .15$ [70]. Measurements were taken at 14 T.

there is a clear difference in magnetoresistance in the two directions that both increases with increasing magnetic field (Figure 4.13a) and decreases with increasing temperature (Figure 4.13b). Except for having two-fold rather than four-fold symmetry, this is similar to the observed behavior of PCCO . The amplitude of the difference in magnetoresistance between the two directions decreases with increasing temperature, eventually reaching zero at a doping-dependent temperature (Figure 4.13c). This temperature at which the angular magnetoresistance oscillations reach zero, T_D, is found to trace a line similar to T_N in $Pr_{2-x}Ce_xCuO_{4\pm\delta}$ (Figure 4.13d).

One obvious difference between the angular magnetoresistance signal observed for $La_{2-x}Ce_xCuO_{4\pm\delta}$ and $Pr_{2-x}Ce_xCuO_{4\pm\delta}$ is the reduced symmetry of the $La_{2-x}Ce_xCuO_{4\pm\delta}$ oscillations. For $Pr_{2-x}Ce_xCuO_{4\pm\delta}$, the four-fold oscillations match the symmetry of the ab-plane of the crystal lattice; the spins that participate in the antiferromagnetism in the system are on the copper atoms. In $La_{2-x}Ce_xCuO_{4\pm\delta}$, however, it is less clear that assigning the two-fold oscillations in magnetoresistance to antiferromagnetism is correct, although two-fold oscillations have been assigned to spin density wave ordering in the barium 122 ferropnictide system [71, 72]. Furthermore, non-magnetic properties of $La_{2-x}Ce_xCuO_{4\pm\delta}$, like superconductivity or phase fluctuations measured by the Nernst effect [73, 74], do not have the same temperature and doping dependence as T_D. Recently, the parent compound, T'-$LaCuO_4$, has been synthesized in powder form and investigated by μSR, finding antiferromagnetism with a Néel temperature of 115 K [75]. The T_D found by angular magnetoresistance appears to extrapolate to near this value at zero doping (Figure 4.13d). It is likely, therefore, that the angular magnetoresistance signal found in $La_{2-x}Ce_xCuO_{4\pm\delta}$ is due to antiferromagnetism and its disappearance corresponds to
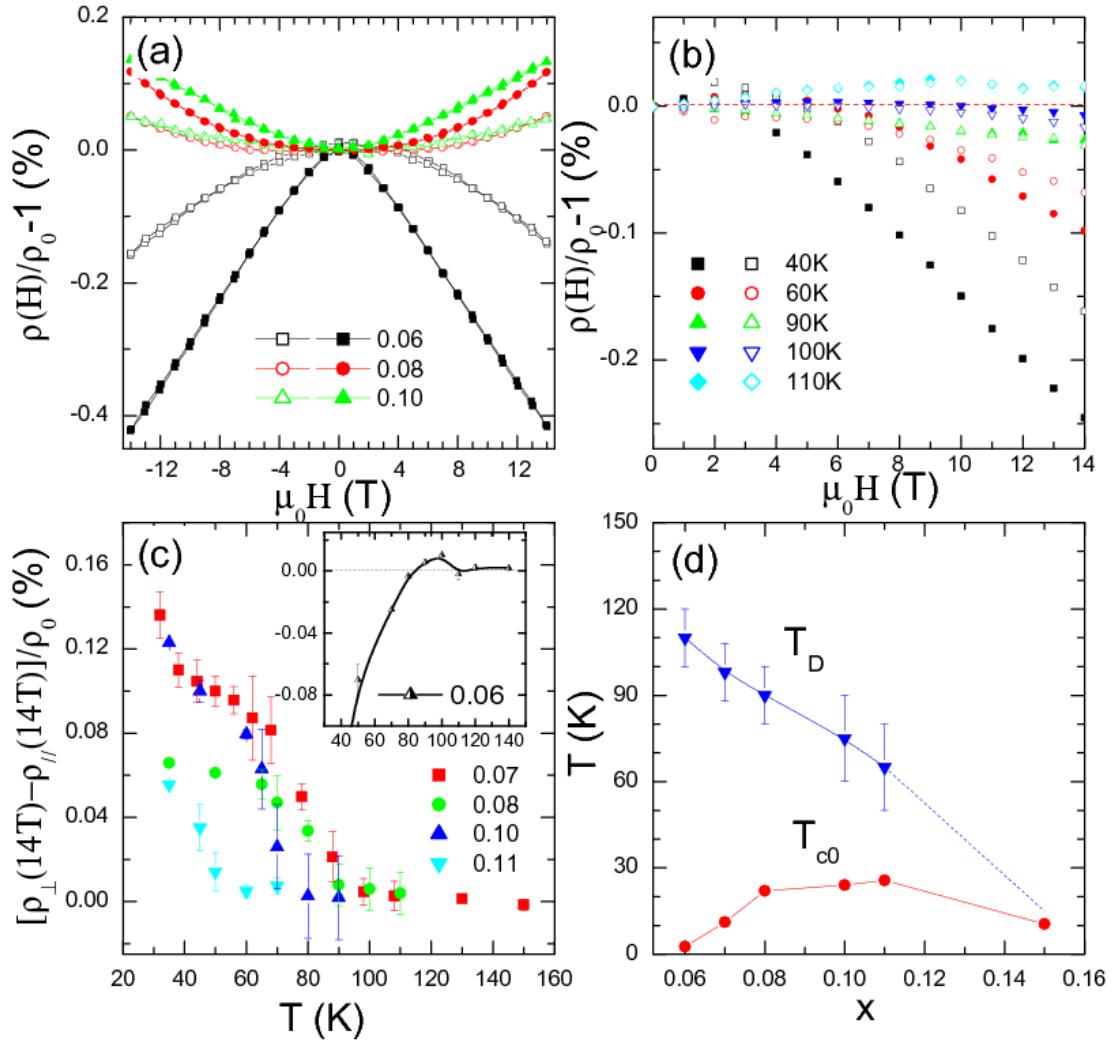
Figure 4.13: (a) Field dependence of magnetoresistance at 35 K for several dopings [70]. Open and closed symbols are taken with the magnetic field parallel and perpendicular to the direction of current respectively. (b) Field dependence of magnetoresistance for $x = .06$ at several temperatures. (c) The amplitude of the difference in magnetoresistance decreases with increasing temperature. The temperature at which this amplitude goes to zero is identified as T_D. (d) Phase diagram with $T_D(x)$ and $T_c(x)$.

the Néel temperature.

In $Pr_{2-z-x}La_zCe_xCuO_4$, anisotropic magnetoresistance was reported as related to the spins making a non-collinear to collinear transition in field [35]. This picture was used to understand the four-fold angular magnetoresistance oscillations that were observed in $Pr_{2-x}Ce_xCuO_{4\pm\delta}$. If $La_{2-x}Ce_xCuO_{4\pm\delta}$ does not have this transition, and the antiferromagnetism stays in the non-collinear state, this may result in a two-fold oscillation due to some unknown asymmetry between the (00ℓ) and $\left(00\frac{\ell}{2}\right)$ copper oxide planes. There is, however, currently no good explanation for the angular magnetoresistance signal in $La_{2-x}Ce_xCuO_{4\pm\delta}$ having two-fold, rather than four-fold, oscillations.

Two-fold oscillations are also seen in $Pr_{2-x}Ce_xCuO_{4\pm\delta}$. While there is a four-fold component to $Pr_{2-x}Ce_xCuO_{4\pm\delta}$ angular magnetoresistance, a two-fold signal can also be clearly seen (Figures 4.6, 4.7). This two-fold PCCO signal seems to be suppressed with temperature (and doping) in concert with the four-fold antiferromagnetism signal, suggesting that they are related phenomena. Additionally, the $La_{2-x}Ce_xCuO_{4\pm\delta}$ angular magnetoresistance oscillations further disappear at the same doping as $Pr_{2-x}Ce_xCuO_{4\pm\delta}$. This is suggestive of a common magnetic origin because antiferromagnetism in these systems is due to spin dilution. The antiferromagnetism would be expected to be suppressed with roughly the same number of charge carriers in either system.

Additionally, the angular magnetoresistance oscillations do seem to be a property of the material. $La_{2-x}Ce_xCuO_{4\pm\delta}$ films were patterned such that the bridge was both along the [100] and [110] directions and the in-plane angular magnetoresistance was measured. The observed magnetoresistance oscillations maintained the angular locations of their minima and maxima with respect to the underlying crystal structure and not the direction

of current flow (Figure 4.14). In each orientation, the angle, θ, was measured relative to the applied in-plane magnetic field such that $\theta = 0°$ occurred when the field was along the crystallographic b-axis ([010] $\parallel$ H). The film was patterned such that the current was oriented either along the a-axis ($I \parallel$ [100], $I \perp H$) at $\theta = 0°$ (Figure 4.14a) or such that the current was at $45°$ to this orientation ($I \parallel$ [110]) at $\theta = 0°$ (Figure 4.14b). In both cases, the resulting angular magnetoresistance oscillations (Figures 4.14c 4.14d) show matching features at the same orientations, i.e., minima occur at $H \parallel$ [100] and maxima occur at $H \parallel$ [010]. The features were not shifted $45°$ as the current bridge was. This excludes extrinsic effects due to the symmetry of the experimental setup and suggests that the observed angular magnetoresistance signal is connected to the crystal or magnetic structure of the material.

Material properties of T' $La_{2-x}Ce_xCuO_{4\pm\delta}$ are not as well explored as they are in $Pr_{2-x}Ce_xCuO_{4\pm\delta}$, due to lack of non-thin-film samples. Therefore, there can be speculation of structural distortions like in $La_{2-x}Sr_xCuO_{4\pm\delta}$ [76], magnetic stripe ordering like in $YBa_2Cu_3O_7$ [77], or disorder (like apical oxygen) in the films. However, if these effects were present, they would still be consistent with the picture that T_D is related to the magnetic structure of $La_{2-x}Ce_xCuO_{4\pm\delta}$. Even though it is not understood why the magnetic structure of $La_{2-x}Ce_xCuO_{4\pm\delta}$ produces two-fold angular magnetoresistance oscillations compared to the four-fold angular magnetoresistance oscillations seen in $Pr_{2-x}Ce_xCuO_{4\pm\delta}$, both angular magnetoresistance oscillations are likely tracking the same property: an antiferromagnetism ordering in the material.

The observation of angular magnetoresistance oscillations in $La_{2-x}Ce_xCuO_{4\pm\delta}$ are seen as similar to the angular magnetoresistance oscillations observed in $Pr_{2-x}Ce_xCuO_{4\pm\delta}$.
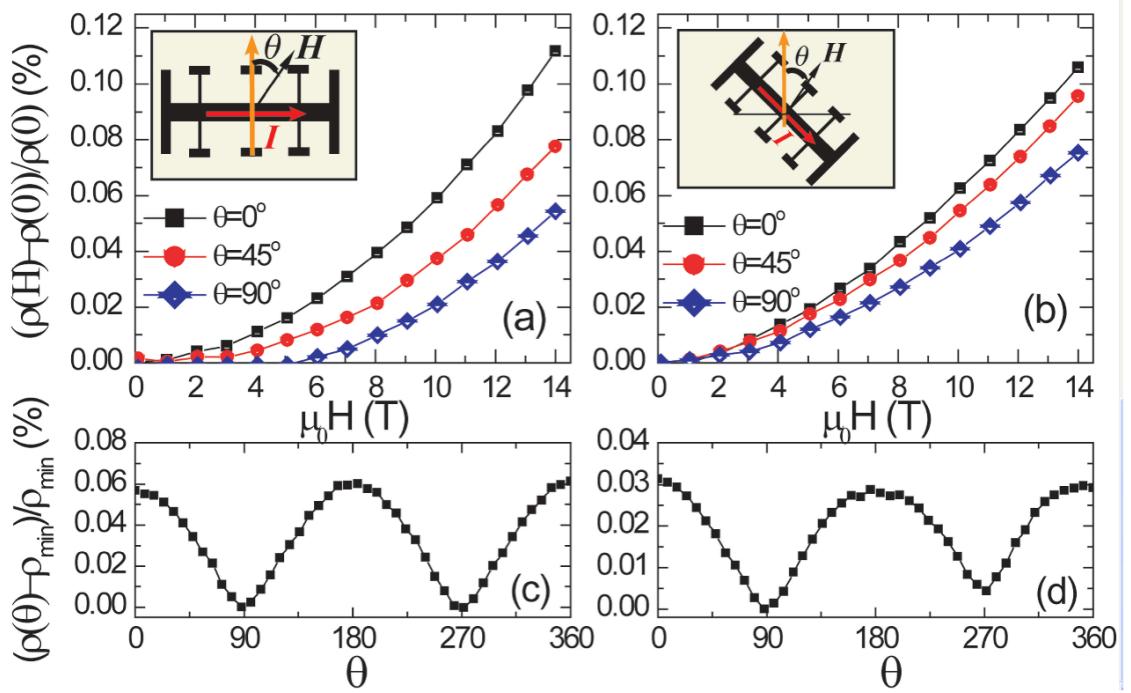
Figure 4.14: La$_{2-x}$Ce$_x$CuO$_{4\pm\delta}$ film patterned both with the current along the crystal axis (e.g., [100]) (a) and along the diagonal (e.g., [110]) (b) for a $x = .08$ film at 35 K [70]. An angular magnetoresistance signal is seen in both orientations (c,d) with the minima and maxima at the same angle θ in each case.

Compared to $Pr_{2-x}Ce_xCuO_{4\pm\delta}$, the angular magnetoresistance oscillations evolve similarly with doping and are fully suppressed at around $x = .15$. The disappearance of these oscillations appears to track the Néel temperature. The $La_{2-x}Ce_xCuO_{4\pm\delta}$ system cannot be explored by spin-sensitive scattering techniques. The oscillations are evidence for antiferromagnetism in $La_{2-x}Ce_xCuO_{4\pm\delta}$.

Chapter 5

Disorder and Oxygenation in $Pr_{2-x}Ce_xCuO_{4\pm\delta}$

5.1   Introduction

One of the outstanding issues in the electron-doped cuprates is the role that oxygenation plays in superconductivity and normal state properties. Oxygen addition can be considered both a doping and a disordering process. To disentangle these two effects, disorder can be introduced by irradiating the samples without altering doping. Transport studies were performed on optimal and under-doped $Pr_{2-x}Ce_xCuO_{4\pm\delta}$ films subject to proton irradiation and oxygenation. This separation of the disorder and doping effects also sheds light on oxygen reduction effects in electron-doped cuprates.

In the electron-doped cuprates, the as-grown material does not show superconductivity. It is necessary for PCCO to be annealed in an oxygen-depleted environment; the details of this reduction step (primarily temperature, oxygen partial pressure, and time) can greatly influence T_c. However, despite the necessity of low oxygen annealing, it is not established what effect this reduction has microscopically. Electron-doped cuprates have the T' crystal structure with CuO_2 planes sandwiched between layers of rare-earth atoms. Oxygen can exist at in-plane lattice sites (O(1)), out-of-plane lattice sites (O(2)), and, potentially, at apical sites (O(3)). It is not clear which oxygens are primarily reduced by annealing to enhance superconductivity. It is known, that in the parent compound, there is a significant change in the lattice parameters due to oxygen reduction, suggest-

ing significant removal of oxygen [26]. However, this change is not seen in the optimally doped material. In the cuprate superconductors, superconductivity is quite sensitive to the quality of the crystal structure, particularly the copper-oxide planes. For example, doping zinc on the copper sites suppresses superconductivity [78]. Oxygen in these materials is harder to control and although it is well known that an oxygen reduction step is necessary to maximize T_c, the origin of the removed oxygen is still unresolved.

The possibility of oxygen acting as a dopant can be understood via an ionic picture of $Pr_{2-x}Ce_xCuO_{4\pm\delta}$, although this picture is quite simplified. In the parent compound, Pr_2CuO_4, the praseodymium has a $3+$ valence, oxygen has a $2-$ valence, and charge balance forces copper to have a $2+$ valence: $Pr_2^{3+}Cu^{2+}O_4^{2-}$. Doping Ce^{4+} onto the Pr^{3+} sites adds electrons to the system. Due to Coulomb interactions, this doping is primarily accomplished on the copper sites [38]. While adding Ce^{4+} in place of Pr^{3+} adds electrons, adding O^{2-} at interstitial sites (0 valence) adds holes. Removing O^{2-}, therefore, can be thought of as adding electrons. If oxygen is acting as a dopant in $Pr_{2-x}Ce_xCuO_{4\pm\delta}$, it is doping the material in the opposite sense as cerium, i.e., adding oxygen acts like removing cerium and removing oxygen acts like adding cerium.

Our group has argued previously that apical oxygens are being removed and that oxygen primarily acts as a dopant in PCCO ($x = .17$) [27]. Recent work on $Pr_{2-x}Ce_xCuO_{4\pm\delta}$ and $Nd_{2-x}Ce_xCuO_{4\pm\delta}$ crystals report that the $4 \pm \delta$ in as-grown compounds is ≥ 4.0 and the excess oxygens are apical [79]. It has been reported that oxygen reduction does not change the charge doping significantly and oxygen primarily causes disorder in PCCO [80]. The parent compounds have also been made superconducting solely by oxygen reduction, which is suggestive of a doping effect, but it was reported as due to the effect of

81

perfecting the crystal structure [52].

The possibility of oxygen non-stoiciometry increasing disorder in $Pr_{2-x}Ce_xCuO_{4\pm\delta}$ has to take into consideration the effects of disorder on superconductivity. Magnetic disorder is detrimental to superconductivity; however, oxygen is non-magnetic. Non-magnetic disorder only weakly suppresses superconductivity in s-wave superconductors, superconductors where the superconducting order parameter is isotropic. The cuprates, however, are d-wave superconductors; their superconducting order parameter is not isotropic, but has nodes. In these d-wave superconductors, and more generally in nodal superconductors, non-magnetic disorder acts to strongly suppress superconductivity [81]. If oxygen disorders the $Pr_{2-x}Ce_xCuO_{4\pm\delta}$ crystal lattice, superconductivity ought to be quickly suppressed.

In order to achieve superconductivity in the electron-doped cuprates, a post-synthesis annealing step is required. The microscopic details of the annealing process, however, are debated. In the T' cuprates, like $Pr_{2-x}Ce_xCuO_{4\pm\delta}$, oxygen is initially incorporated into the crystal lattice in several locations: at in-plane, O(1), sites; at out-of-plane, O(2), sites; and at apical, O(3), sites. The apical oxygens are interstitial, lying directly above or below the copper atoms. Despite the O(3) site being interstitial, it is known to be populated at the several percent level in $Nd_{2-x}Ce_xCuO_{4\pm\delta}$ [24, 26]. Annealing in an oxygen-reducing environment is then necessary to induce superconductivity. The naïve answer, therefore, to the question of the role of annealing the electron-doped cuprates in a reducing environment is that annealing removes the apical oxygens. As these oxygens occupy non-regular lattice sites, this reduces the disorder in the crystal lattice. This view has been supported by neutron scattering [82] and transport [25, 27, 83] measurements. Competing models

for the role of annealing in the T' cuprates exist. It has been argued that annealing removes the O(1), rather than the O(3), oxygens. In this picture, the apical oxygens are mostly untouched by annealing as annealing removes oxygens from the CuO_2 planes, and in doing so, suppresses antiferromagnetism in the material [28, 29]. In this scenario, suppression of antiferromagnetism is what leads to superconductivity. It has also been proposed that annealing is primarily not about oxygen, but about copper. This argument suggests that copper vacancies are detrimental to superconductivity and that annealing allows the copper atoms to migrate and "heal" the CuO_2 planes [31]. This migration would come with the cost of generating intercalated copper-deficient $(RE,Ce)_2O_3$ phases, seen by scattering experiments [49], in the material. Copper excess growths of $Pr_{2-x}Ce_xCuO_{4\pm\delta}$ have been shown to lack this impurity phase [56]. The role played by the annealing step of electron-doped curates synthesis is quite varied among these three views; this is still an open question in the field.

Oxygenation in $Pr_{2-x}Ce_xCuO_{4\pm\delta}$ can have several effects. It could dope the system, disorder the system, or do both. Additionally, the related question of the role of annealing the T' cuprates to induce superconductivity has several proposed answers. The first scenario is that annealing removes apical oxygens from interstitial lattice sites, thereby reducing disorder and allowing superconductivity. The second scenario is that annealing removes in-plane oxygens from the CuO_2 planes, thereby suppressing antiferromagnetism and allowing superconductivity. The third scenario is that annealing allows migration of copper atoms, thereby healing defects in the CuO_2 planes and allowing superconductivity. In addition to understanding oxygen's role in either doping or disordering the $Pr_{2-x}Ce_xCuO_{4\pm\delta}$ system, understanding of the role of annealing in the electron-doped

cuprates might be gained by studying oxygenated members of this system.

In order to disentangle these two possible effects of oxygenation in $Pr_{2-x}Ce_xCuO_{4\pm\delta}$ and these three possible annealing scenarios, over-oxygenated $Pr_{2-x}Ce_xCuO_{4\pm\delta}$ was investigated. Here we expand upon the work done on $x = .17$ PCCO at lower dopings with the goal of better understanding the role of oxygen in the superconducting properties of the cuprates. Over-oxygenated films of both optimal doping ($x = .15$) and under-doped ($x = .12$) PCCO were prepared as was an optimal $x = .12$ film that was subsequently irradiated at a range of doses. In $x = .17$ it was established that oxygen doping opposes cerium doping but disorders the material sufficiently to not allow T_c enhancement [27]. On the underdoped side, extra oxygen would be expected to suppress T_c due to both doping and disorder. However, the underdoped side of the phase diagram does offer some advantages. It is known that at higher dopings the Hall effect changes sign at low temperatures, indicating two band transport [21]. Doping is therefore easier to understand on the single band underdoped side of the phase diagram. Also, PCCO has an antiferromagnetic (AFM) ground state that persists up to near optimal doping that can be observed in transport data [36]. This allows the use of the Néel temperature as an independent indicator of doping in the system. Finally, underdoped samples always have a low temperature resistivity upturn whose origins are not well understood; it has been proposed, however, that it is due to additional magnetic scattering due to strong correlations causing magnetic droplets to form around impurities [84]. Studying disorder at these dopings may offer some new insight into the PCCO system.

5.2 Experiment

Three series of PCCO thin films were studied: an irradiated series at $x = .12$ dop-
ing, an oxygenated series at $x = .12$ doping, and an oxygenated series at $x = .15$ doping
(Table 5.1). In all three series, the optimally grown member formed one endpoint, and
oxygen or irradiation was progressively added. In all cases T_c had been fully suppressed
prior to the maximal introduction of oxygen or disorder.

The thin films of $Pr_{2-x}Ce_xCuO_{4\pm\delta}$ were grown by pulsed laser deposition (PLD)
using a LambdaPhysik KrF excimer laser (248 nm wavelength) on (100) oriented $SrTiO_3$
substrates. The films were grown to a nominal thickness of 300 nm. Series of samples
were fabricated for irradiation and oxygenation measurements respectively. The former
was grown as a single under-doped film that was optimally grown and annealed. The
latter was grown as a series of films made under various oxygenation conditions.

Irradiated $x = .12$ films	Oxygenated $x = .12$ films	Oxygenated $x = .15$ films
0×10^{16}/cm^2 of 2 MeV H$^+$ 1.18×10^{16}/cm^2 of 2 MeV H$^+$ 2.32×10^{16}/cm^2 of 2 MeV H$^+$ 3.52×10^{16}/cm^2 of 2 MeV H$^+$ 4.72×10^{16}/cm^2 of 2 MeV H$^+$ 6.49×10^{16}/cm^2 of 2 MeV H$^+$	230 mTorr N$_2$O, optimal annealing 230 mTorr N$_2$O, no annealing 230 mTorr O$_2$, no annealing 400 mTorr O$_2$, no annealing 600 mTorr O$_2$, no annealing	230 mTorr N$_2$O, optimal annealing 230 mTorr N$_2$O, no annealing 230 mTorr O$_2$, no annealing 400 mTorr O$_2$, no annealing 600 mTorr O$_2$, no annealing

Table 5.1: $Pr_{2-x}Ce_xCuO_{4\pm\delta}$ film samples used for transport measurements.

For the irradiated film, an atmosphere of 230 mTorr N$_2$O was used during the de-
position process. The target consisted of a polycrystalline $Pr_{2-x}Ce_xCuO_{4\pm\delta}$ pellet with
a cerium doping of $x = .12$. The film was annealed in situ immediately after deposition
by lowering the substrate temperature and the chamber pressure to annealing conditions.

Deposition was performed at 800 C. Annealing was at 720 C in vacuum ($P < 10^{-4}$ Torr).
This produced a film with a superconducting transition temperature of 6.4 K. The film was
patterned such that it contained six consecutive regions prepared for Hall and resistivity
measurements (Figure 5.1). These regions were irradiated with protons with exposures
ranging from zero to $6.5 \times 10^{16}/\text{cm}^2$ spaced at roughly equal intervals (0, 1.18, 2.32,
3.52, 4.72, 6.49 $\times 10^{16}/\text{cm}^2$ of 2 MeV H$^+$). The regions were irradiated by B. Weaver at
the Naval Research Laboratory. In $\text{Pr}_{2-x}\text{Ce}_x\text{CuO}_{4\pm\delta}$, this type of radiation, 2 MeV H$^+$,
should primarily knock oxygen into interstitial sites from lattice sites, particularly from
copper-oxide plane lattice sites [85].
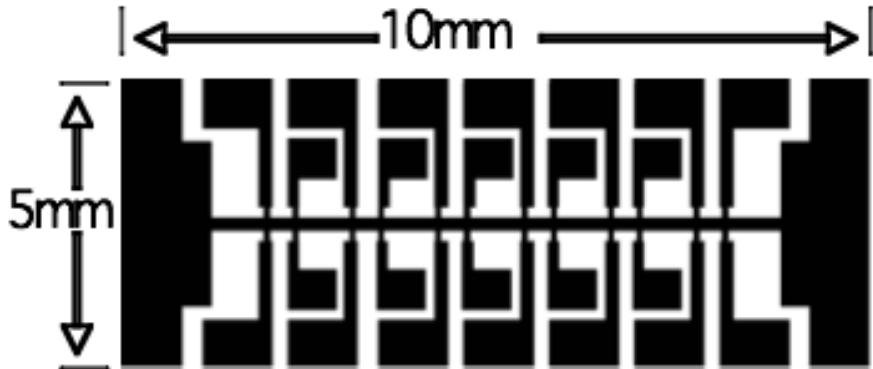
Figure 5.1: Patterned film for irradiation measurements (above) and oxygenation mea-
surements (below). A constant current is maintained in the central channel from current
leads attached at each end of the film. Voltage leads are periodically spaced along the
channel. The above film was irradiated in small patches such that consecutive voltage
leads could provide resistivity (or Hall) measurements corresponding to a single irra-
diation dose. Oxygenated films were patterned similarly (Figure 3.6), but had uniform
oxygen treatment across the entire film.

The oxygenated films were grown at two separate dopings (Table 5.1). A series of
films was grown with a $x = .12$ cerium concentration ceramic PCCO target and another

series was grown using an optimally doped PCCO target of Ce $= .15$. In each series the atmosphere and annealing times were varied to produce a range of oxygen concentrations in the final films. The least oxygenated films and the optimally grown films were annealed in situ following deposition using the above described conditions. Films grown to contain more oxygen were grown under higher partial pressures of oxygen and were not annealed. These conditions were 230 mTorr N_2O, no annealing; 230 mTorr O_2, no annealing; 400 mTorr O_2, no annealing; and 600 mTorr O_2, no annealing. In each case, the films were held at the annealing temperature following deposition but the atmosphere was not evacuated. After growth and any annealing, films were removed from the PLD chamber and exposed to air only after they had cooled to room temperature.

In order to prepare the films for measurement, the films were patterned for resistivity, Hall effect, and angular magnetoresistance (AMR) measurements. Oxygenated films were patterned either by ion milling or by acid etching. The irradiated film was ion-milled due to the need for smaller size features in that film.

All films were measured in a Quantum Design Physical Property Measurement System (PPMS) in fields up to 14 T. Measurements were performed using standard four-wire measurement techniques with contacts made by soldering $50 \, \mu$m gold wires to the film surface with an silver/indium alloy. The film quality was monitored by characterizing the films by both AC magnetic susceptibility measurements (where a T_c was present) and X-ray diffraction.

The PPMS rotation option was used for angular magnetoresistance measurements with the geometry such that the magnetic field was always in the ab-plane and the film was rotated about the c-axis. These measurements have been used previously to examine

the Néel temperature in PCCO [36]. All AMR measurements were performed at 14 T.

5.3   Results

Proton irradiation introduces disorder into the $Pr_{2-x}Ce_xCuO_{4\pm\delta}$ films. Therefore, measurements of irradiated films characterize the effects of disorder on PCCO. Resistivity was measured in the irradiated samples from 2 K to 300 K in zero field across the range of radiation exposures (Figure 5.2). At low temperatures the measurement was also performed in field, where necessary, to suppress T_c in order to access the normal state resistance. Increased irradiation increased the resistivity of the PCCO film and suppressed T_c as well as exaggerating the low temperature resistivity upturn seen in under-doped PCCO.

Hall effect data was also taken from 2 K to 300 K on the series of irradiated samples (Figure 5.3). These measurements were performed in a 14 T magnetic field applied along the c-axis of the PCCO films. The polarity of the magnetic field was applied both into and out of the plane of the film so that magnetoresistance effects could be removed from the Hall measurement by subtracting the data sets as described in Chapter 3. Irradiation produced a small suppressive change in the Hall resistivity, making it slightly less negative. This indicates that the charge carrier concentration remains largely unchanged due to disorder, and that disordering the film lessens conduction by introducing scattering defects.

Oxygenated films were also measured according to the same procedure (Figure 5.4). Both oxygen and irradiation increase the resistivity of the films, enhance the low temper-
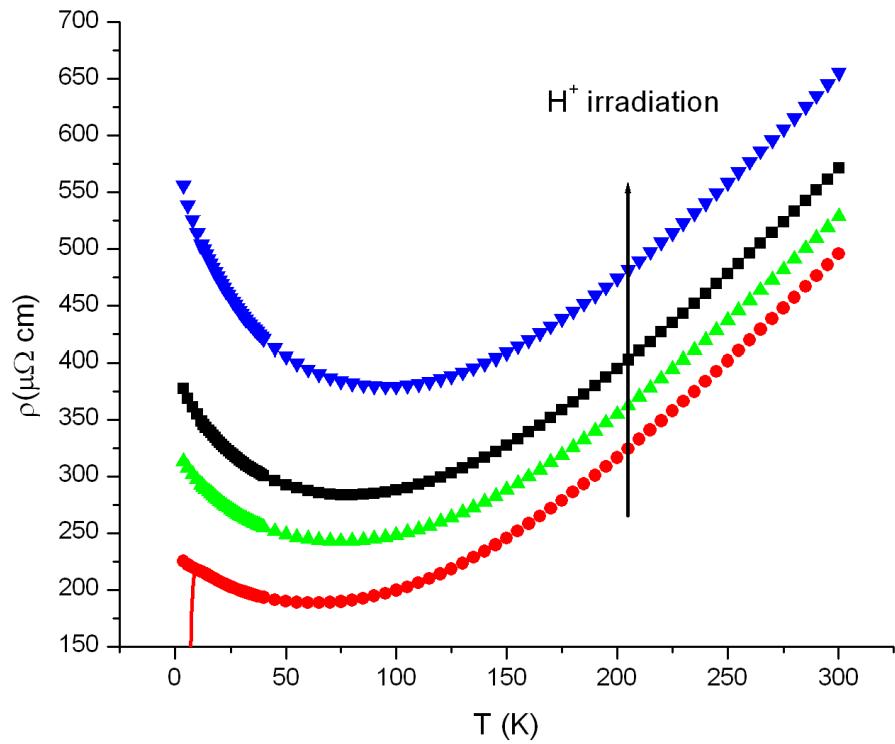
Figure 5.2: Resistivity of an optimally grown and annealed $x = .12$ under-doped $Pr_{2-x}Ce_xCuO_{4\pm\delta}$ film ($T_c = 6.4$ K) at different doses of irradiation. Irradiation levels range from 0 to 6.5×10^{16} cm^{-2} of 2 MeV H$^+$.
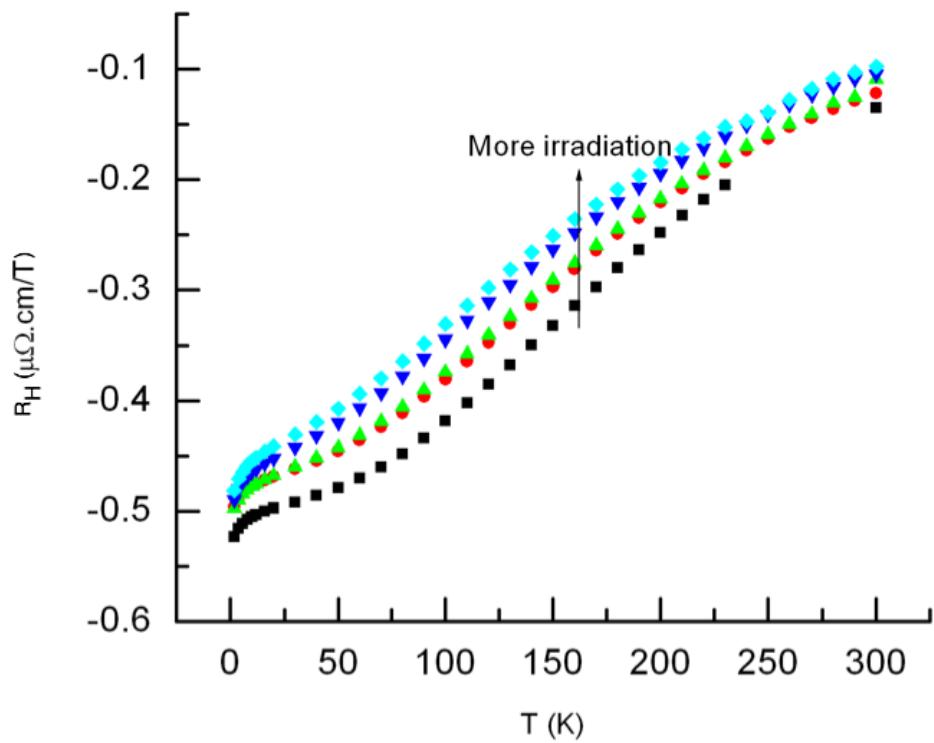
Figure 5.3: Hall effect of an optimally grown and annealed $x = .12$ under-doped $Pr_{2-x}Ce_xCuO_{4\pm\delta}$ film ($T_c = 6.4$ K) at different doses of irradiation. Irradiation levels range from 0 to 6.5×10^{16} cm^{-2} of 2 MeV H$^+$.

ature resistive upturn, and suppress superconductivity. However, the two treatments show clearly different behavior in Hall data (Figure 5.5). In a simple Drude model, the Hall effect, $R_H = \frac{E_y}{j_x B} = \frac{-1}{ne}$, depends only on the number of charge carriers; accordingly irradiation induced disorder does not have a significant effect on the charge carrier concentration in under-doped $Pr_{2-x}Ce_xCuO_{4\pm\delta}$, whereas oxygenation does have a significant effect on the charge carrier concentration. This indicates that oxygenation significantly dopes the film in addition to disordering it.
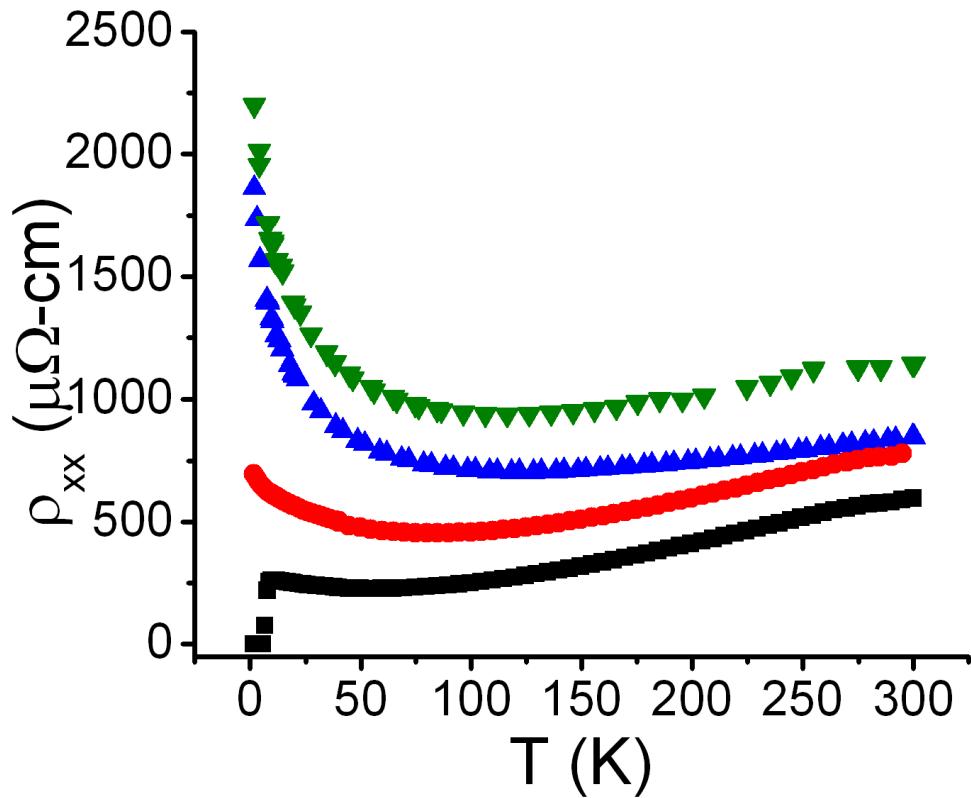
Figure 5.4: Added oxygen in $x = .12$ as-grown $Pr_{2-x}Ce_xCuO_{4\pm\delta}$ films (blue 230 mTorr O_2, green 600 mTorr O_2) produces more resistive films compared with optimally grown and annealed (black) and maximally irradiated (red) films.

Similar results were seen in optimally cerium doped films that were also produced
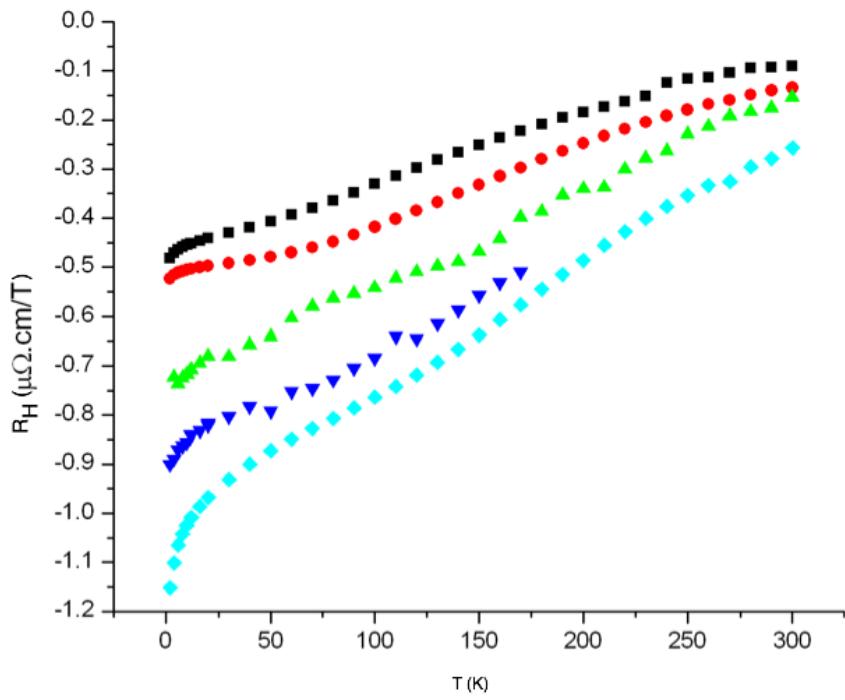
Figure 5.5: Added oxygen in $x = .12$ as-grown $Pr_{2-x}Ce_xCuO_{4\pm\delta}$ films (green 230 mTorr O_2, blue 400 mTorr O_2, cyan 600 mTorr O_2) strongly drives the Hall resistivity more negative compared to optimally grown and annealed films (red). This behavior differs both in magnitude and direction from irradiated films (black, maximally irradiated).

in a range of oxygen partial pressures (Figure 5.6) from optimal conditions, growth in

230 mTorr N_2O followed by vacuum annealing, to highly over-oxygenated films, growth

in 600 mTorr O_2 followed by no annealing. On all films, resistance measurements were

performed from 2 K to 300 K in zero field. Like the irradiated films, these over-oxygenated

films also show several behaviors that are indicative of increased disordering in the films'

crystal structure; a large increase in resistivity, a suppressed T_c, and an exaggerated low

temperature resistivity upturn are observed. The T_c is not yet fully suppressed in unan-

nealed samples (red curve, Figure 5.6), indicating that our growth conditions themselves

begin the annealing process since this is not observed in unannealed crystals.

Like for the $x = .12$ $Pr_{2-x}Ce_xCuO_{4\pm\delta}$ films, for optimally cerium doped ($x =$

.15) films, Hall measurements were performed from 2 K to 300 K in 14 T magnetic

fields (H∥c) on the range of film oxygenations grown (Figure 5.7). The Hall data show a

large increase in the magnitude of the Hall coefficient that is comparable to the shift seen

due to decreased cerium doping. Therefore, oxygenation is changing the charge carrier

concentration at a magnitude comparable to cerium doping. Doping is a significant effect

of oxygen concentration in $Pr_{2-x}Ce_xCuO_{4\pm\delta}$.

Oxygenation in $x = .15$ films is consistent with oxygenation in $x = .12$ films, and

both are consistent with $x = .17$ films [27]. Across the $Pr_{2-x}Ce_xCuO_{4\pm\delta}$ phase diagram,

oxygen addition acts to dope in the opposite direction to cerium addition. However, unlike

cerium doping, doping by oxygen is also introducing significant disorder in the process.

The picture of oxygen significantly doping $Pr_{2-x}Ce_xCuO_{4\pm\delta}$ can be strengthened

by observing a doping-dependent property unrelated to superconductivity: antiferromag-

netism (AFM). Angular magnetoresistence was measured on oxygenated and irradiated
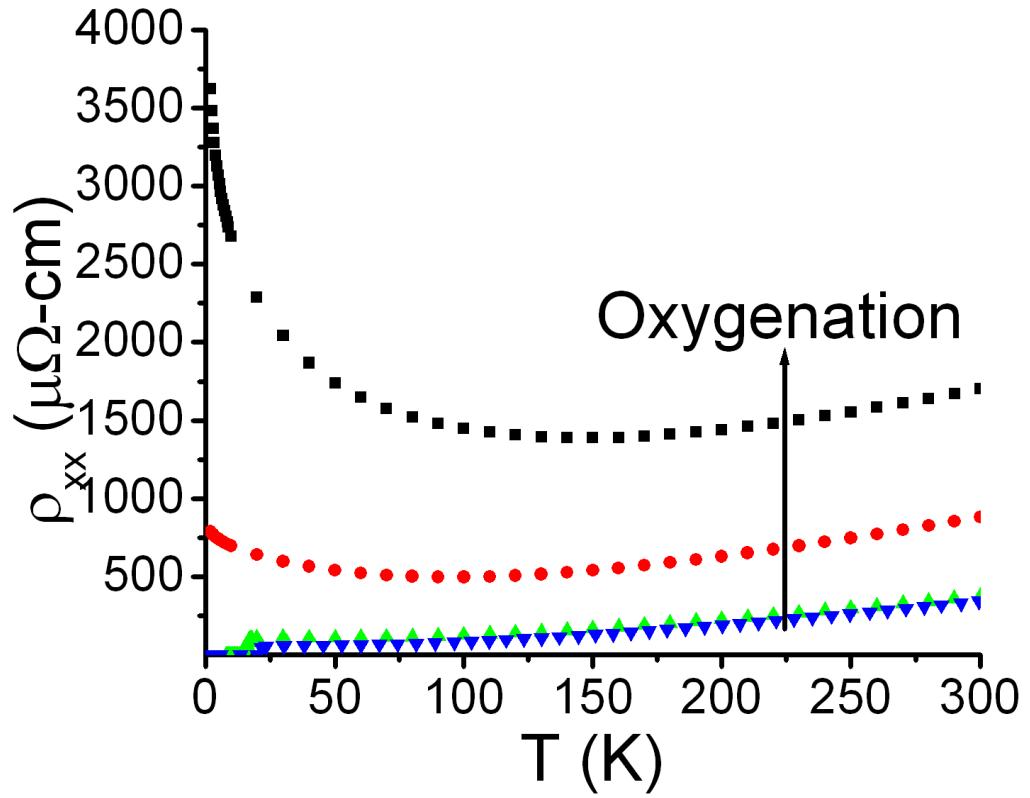
Figure 5.6: Resistivity of optimally doped ($x = .15$) $\mathrm{Pr}_{2-x}\mathrm{Ce}_x\mathrm{CuO}_{4\pm\delta}$ films. Optimal growth (230 mTorr $\mathrm{N}_2\mathrm{O}$, vacuum annealing) to high O_2 growth (600 mTorr O_2, no annealing).
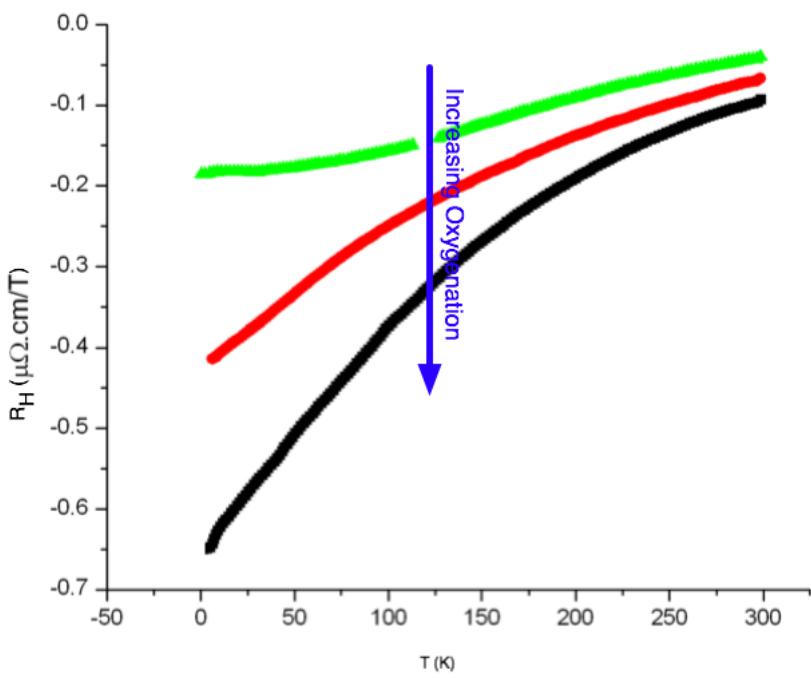
Figure 5.7: Hall effect of optimally doped ($x = .15$) $Pr_{2-x}Ce_xCuO_{4\pm\delta}$ films. Optimal growth (230 mTorr N_2O, vacuum annealing) to high O_2 growth (600 mTorr O_2, no annealing).

films according to the procedure given in Chapter 4. For this study, the irradiated films were all $x = .12$ films, while the oxygenated films were both $x = .12$ and $x = .15$ films. Films were rotated about the c-axis such that the magnetic field rotated through the ab-plane. Magnetoresistance was measured from $\theta = 0° - 360°$ and from $\theta = 360° - 0°$ at each temperature. The geometry of the experiment was constructed such that $\theta = 0°$ was when the magnetic field was parallel to the b-axis ($H \parallel [010]$) and perpendicular to the current, constrained to flow along the a-axis ($H \perp I$, $I \parallel [100]$). This rotation produces an oscillation in magnetoresistance that is related to the antiferromagnetism of the cuprates (Chapter 4). The amplitude of the resulting oscillations (Figure 5.8) decreases to zero at the Néel temperature (T_N).

In oxygenated samples, the AMR signal shows an enhancement of the Néel temperature with increased oxygenation in $x = .15$ films (Figure 5.9). This is compared to < 40 K for optimally grown and annealed $x = .15$ films (Figure 4.8). This is consistent with the Hall effect data that show oxygen doping the material in the opposite sense to cerium. The magnitude of the doping shift due to oxygen is similar between the two measurement techniques. As all of the over-oxygenated films were as-grown (un-annealed), changes in antiferromagnetism primarily involve adjustment of the oxygen concentration rather than that of any of the other chemical elements found in $Pr_{2-x}Ce_xCuO_{4\pm\delta}$.

Similar to optimally doped $Pr_{2-x}Ce_xCuO_{4\pm\delta}$, oxygen addition also enhances the Néel temperature in under-doped, $x = .12$, $Pr_{2-x}Ce_xCuO_{4\pm\delta}$ (Figure 5.10). The exact Néel temperature is difficult to determine due to both increased thermal noise over ~ 100 K and increased resistivity of heavily over-oxygenated films. However, weak AMR oscillations are observable at 140 K, above the 100 K Néel temperature of opti-
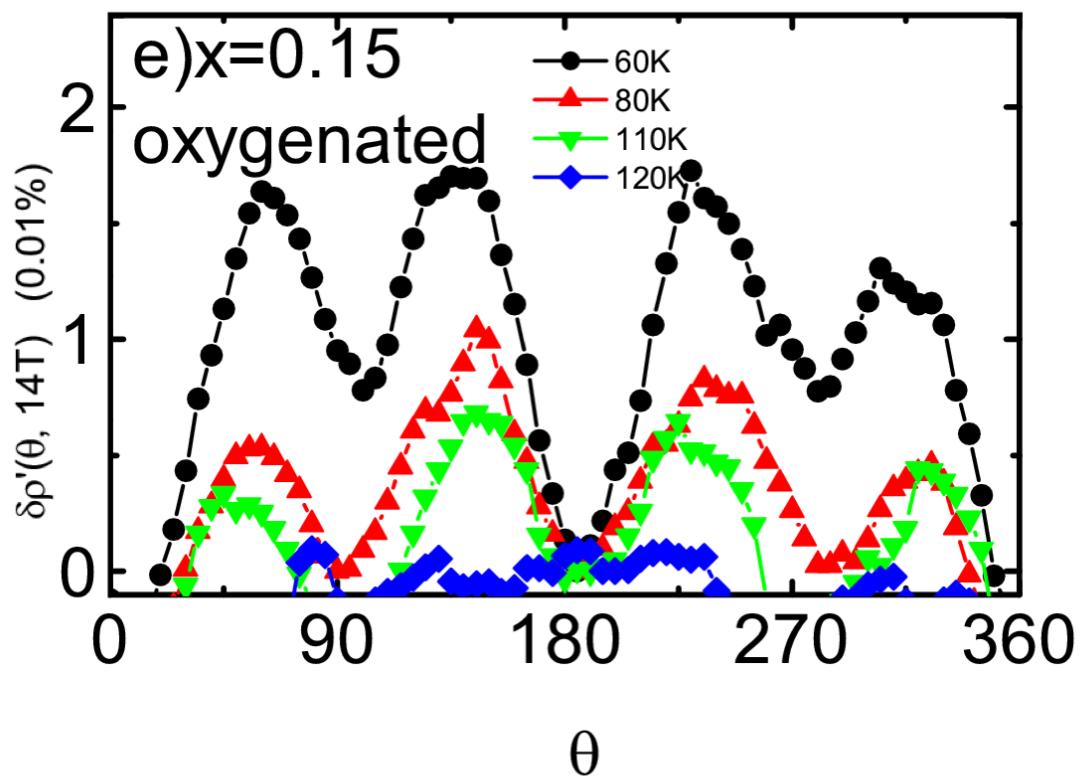
Figure 5.8: Angular magnetoresistance of an oxygenated $x = .15$ $Pr_{2-x}Ce_xCuO_{4\pm\delta}$ thin film [36]. Oscillations are observed to go to zero between 110 K and 120 K.
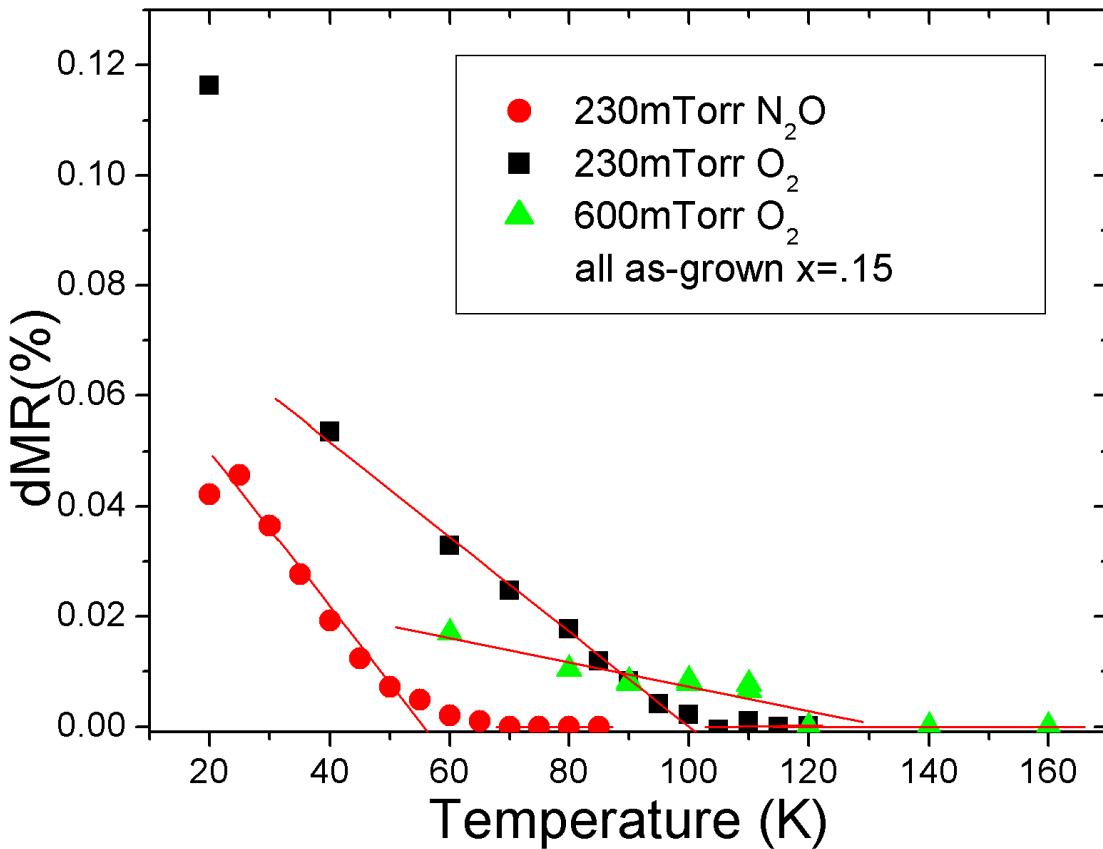
Figure 5.9: Amplitude of AMR oscillations as a percentage of magnetoresistance vs temperature for oxygenated $x = .15$ $Pr_{2-x}Ce_xCuO_{4\pm\delta}$ films. The temperature where the amplitude first goes to zero corresponds to the Néel temperature.

mal $x = .12$ films, suggesting consistent behavior between $x = .12$ and $x = .15$ over-oxygenated films.
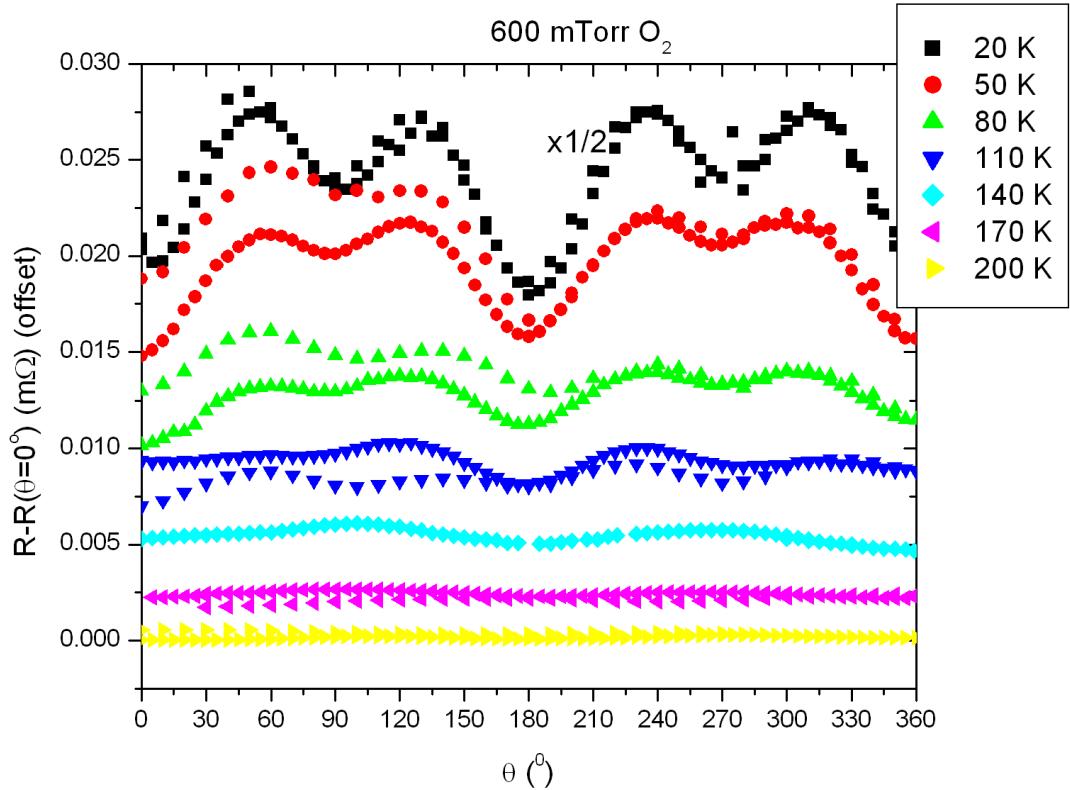
Figure 5.10: Angular magnetoresistance of an oxygenated $x = .12$ Pr$_{2-x}$Ce$_x$CuO$_{4\pm\delta}$ thin film grown in 600 mTorr O$_2$. Oscillations are observed to be present above 110 K. Optimally grown $x = .12$ has a Néel temperature between 105 K and 110 K [36].

The angular magnetoresistance oscillations for Pr$_{2-x}$Ce$_x$CuO$_{4\pm\delta}$ $x = .12$ films grown in 600 mTorr O$_2$ disappear between 140 K and 170 K (Figure 5.11). This is equivalent to a roughly .03 decrease in cerium doping, estimated from Figure 4.10. This is comparable to the doping change seen in optimally doped $x = .15$ Pr$_{2-x}$Ce$_x$CuO$_{4\pm\delta}$ films grown in 600 mTorr O$_2$ (Figure 5.9)

Oxygen enhancement of AFM could be counter-suggestive of oxygen as a disor-
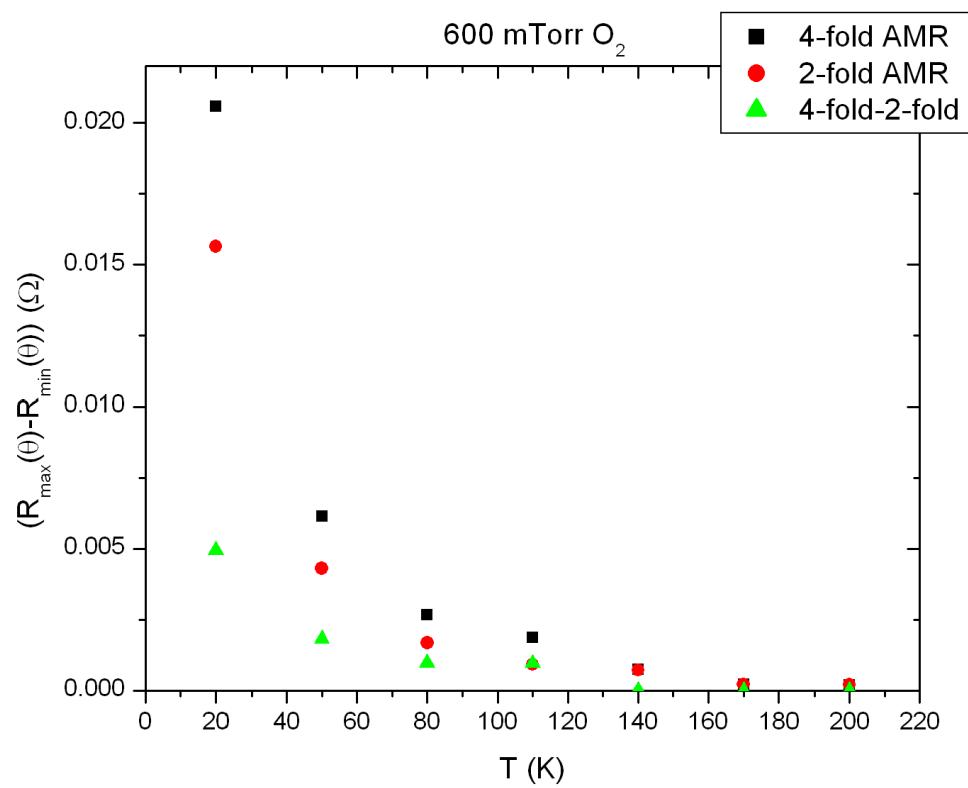
Figure 5.11: Amplitude of AMR oscillations as a percentage of magnetoresistance vs temperature for a oxygenated $x = .15$ $Pr_{2-x}Ce_xCuO_{4\pm\delta}$ film grown in 600 mTorr O_2. The temperature where the amplitude first goes to zero corresponds to the Néel temperature.

dering influence since AFM, being an ordered state, is not disrupted by oxygenation. However, irradiation does not significantly suppress the four-fold oscillations in AMR, indicating that the AFM state in PCCO is fairly robust against disorder. Four-fold oscillations are present in both highly irradiated $x = .12$ (Figure 5.12) and in the non-irradiated region of the same film (Figure 5.13). Irradiation induced disorder does not suppress antiferromagnetism. As 2 MeV H$^+$ irradiation primarily knocks oxygen out of in-plane sites into interstitial sites, removal of planer oxygens does not suppress antiferromagnetism.
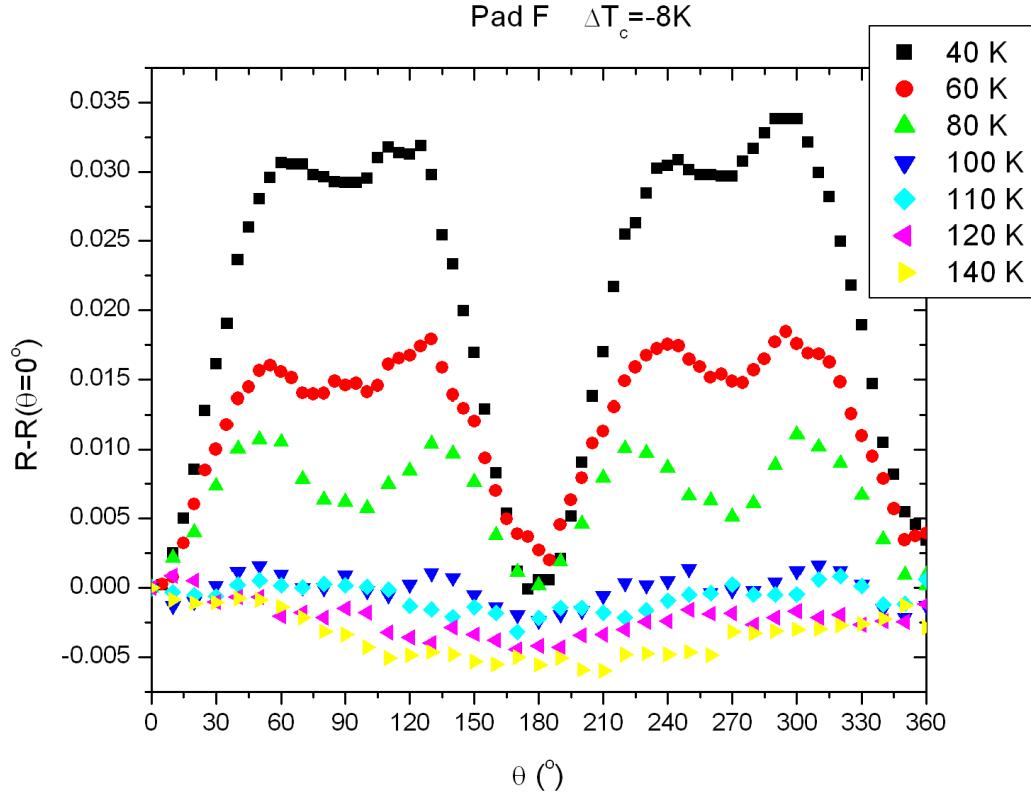
Figure 5.12: Angular magnetoresistance of an irradiated $x = .12$ Pr$_{2-x}$Ce$_x$CuO$_{4\pm\delta}$ thin film. The film received a dose of 4.72×10^{16} cm^{-2} of 2 MeV H$^+$ irradiation. This dose corresponds to a T_c suppression of -8 K (extrapolated).

In both the irradiated (Figure 5.14) and non-irradiated (Figure 5.15) regions of the
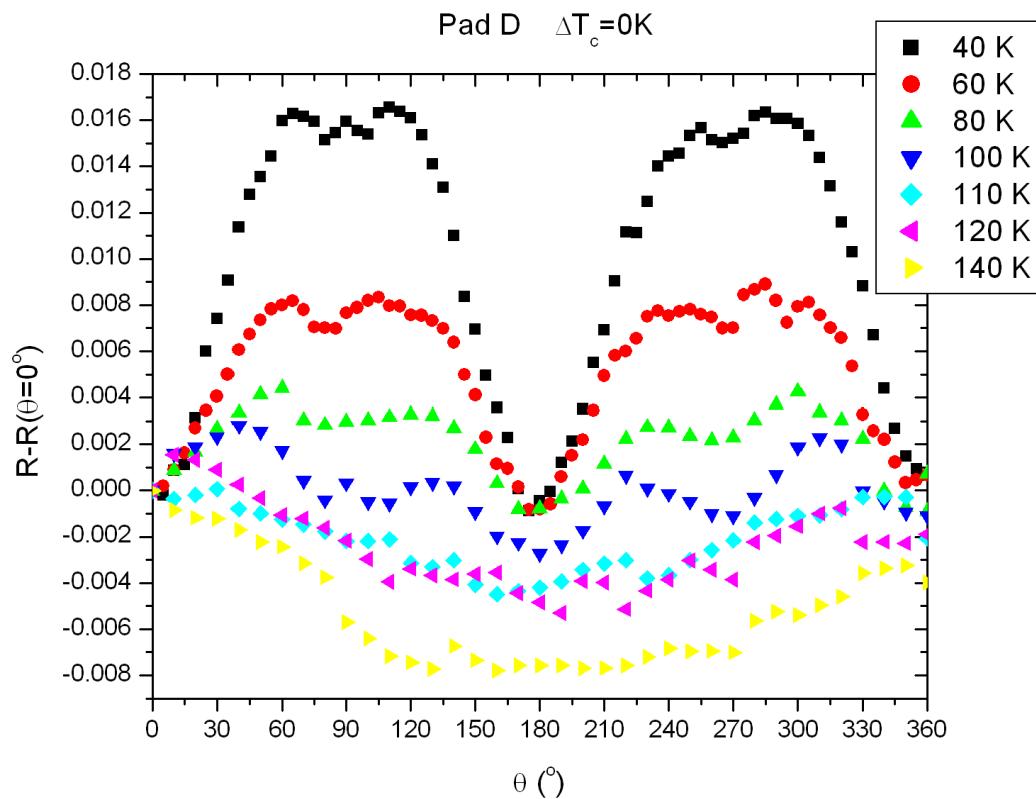
Figure 5.13: Angular magnetoresistance of an un-irradiated $x = .12$ $Pr_{2-x}Ce_xCuO_{4\pm\delta}$ thin film. This is the same film as Figure 5.12, but was not irradiated at this spot ($T_c = 6.5$ K).

$x = .12$ film, the amplitude of the angular dependence of the magnetoresistance decreases to zero between 100 K and 110 K, indicating a Néel temperature between these two temperatures. The Néel temperature seems to vary little with irradiation induced disorder, or with irradiation induced absence of in-plane oxygens caused by 2 MeV H^+ irradiation. The antiferromagnetism in $Pr_{2-x}Ce_xCuO_{4\pm\delta}$ is, however, sensitive to doping by cerium. Therefore, because the Néel temperature is largely insensitive to disorder, but sensitive to doping; oxygen enhancement of T_N is a doping effect.
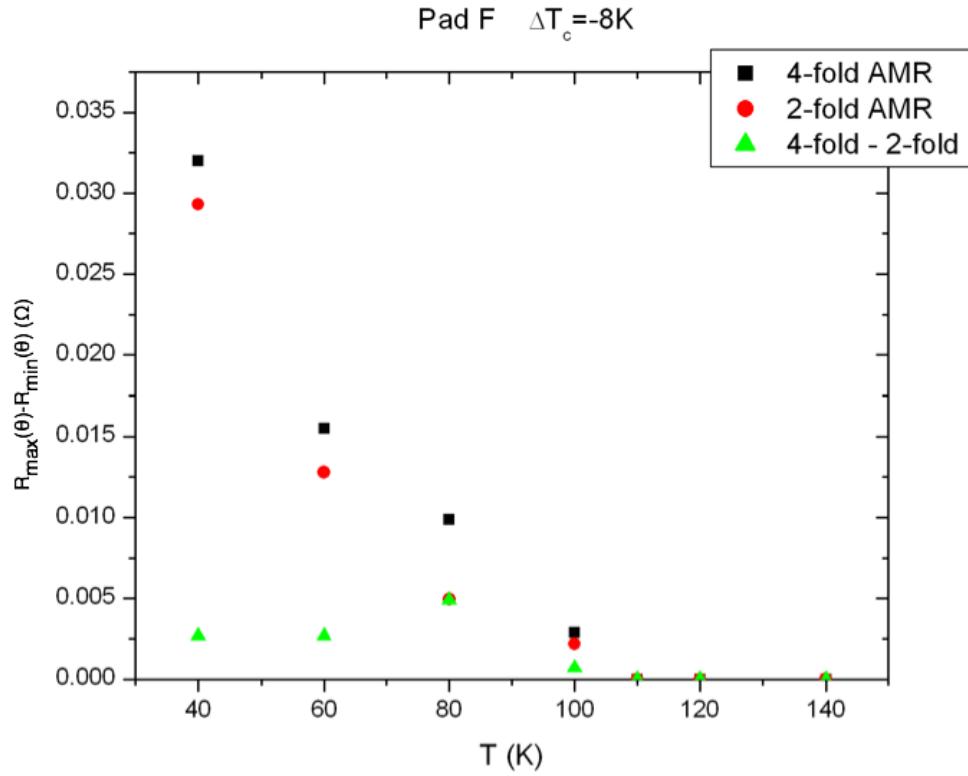
Figure 5.14: The amplitude of angular magnetoresistance oscillations (seen in Figure 5.12) of a heavily irradiated $x = .12$ $Pr_{2-x}Ce_xCuO_{4\pm\delta}$ thin film. Zero amplitude above 110 K shows a Néel temperature between 100 K and 110 K.
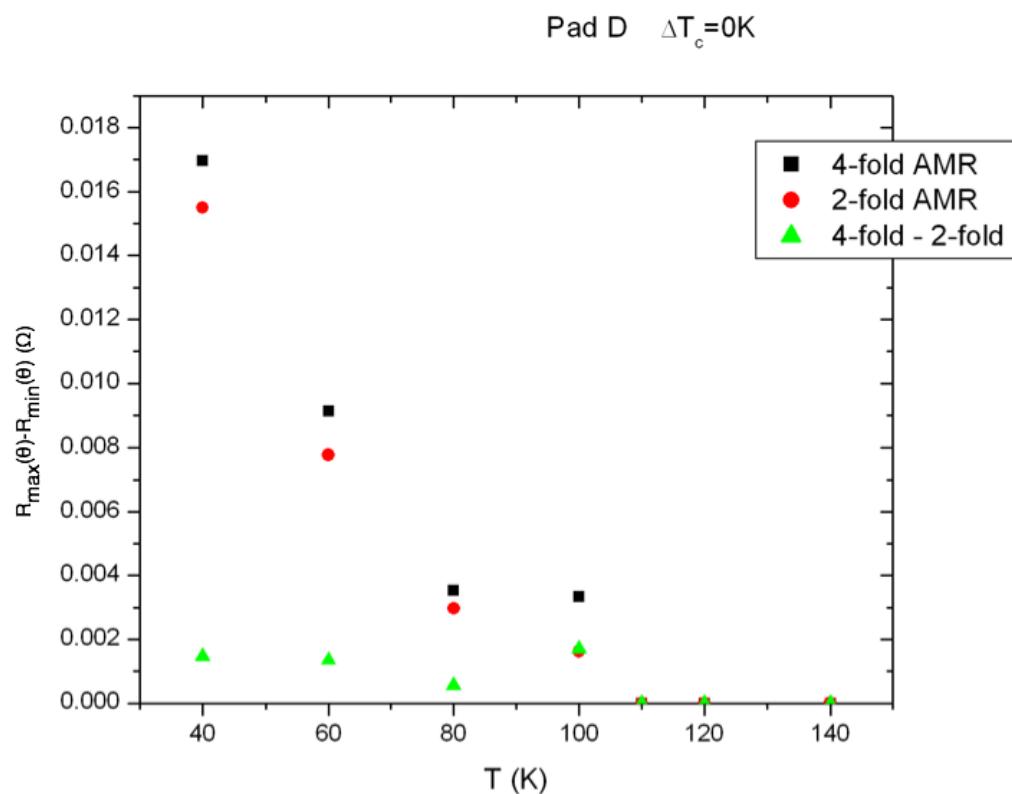
Figure 5.15: The amplitude of angular magnetoresistance oscillations (seen in Figure 5.13) of a un-irradiated $x = .12$ $Pr_{2-x}Ce_xCuO_{4\pm\delta}$ thin film. Zero amplitude above 110 K shows a Néel temperature between 100 K and 110 K.

5.4 Discussion

The Hall effect and angular magnetoresistance oscillations show oxygen to be a significant dopant in $Pr_{2-x}Ce_xCuO_{4\pm\delta}$. Resistivity data show significant disordering in the $Pr_{2-x}Ce_xCuO_{4\pm\delta}$ films as well. These positions are supported by comparison with intentionally-disordered irradiated films, which show significant disordering in resistivity and little change in Hall effect or angular magnetoresistance data. Annealing is also shown to be primarily about removing apical oxygen. Irradiation does not suppress antiferromagnetism, despite knocking oxygen out of the CuO_2 plane, and antiferromagnetism in as-grown oxygenated samples behaves consistently with annealed films, despite not undergoing an annealing step. These two conclusions are discussed below.

PCCO films become more resistive with increasing irradiation and develop a stronger low temperature upturn in resistivity. Both of these effects indicate that irradiation adds disorder to the system. Additionally, Hall effect measurements on irradiated films only show a small positive shift in the Hall effect, indicating that the total number and sign of charge carriers remain largely the same with irradiation. Charge carrier concentrations are not supposed to change in the irradiated films as the main effect of $2\,MeV\,H^+$ irradiation is to knock oxygen into interstitial sites from lattice sites, especially in the copper-oxide plane [85]. Little change due to irradiation is seen in angular magnetoresistance, suggesting nearly no suppression of antiferromagnetism due to disorder. The angular magnetoresistance results will be discussed at length below. Irradiating underdoped PCCO ($x = .12$) suppresses T_c at a rate of $\sim -2\,K$ per $1.2 \times 10^{16}\,2\,MeV\,H^+/cm^2$.

It is well known that $Pr_{2-x}Ce_xCuO_{4\pm\delta}$ must be annealed after initial growth in order

to achieve superconductivity and that this post-annealing step is oxygen-reducing. One effect of this annealing step ought to be reducing oxygen disorder in the films. Disorder due to off-stoichiometric oxygen concentration should be detrimental to superconductivity. Either adding additional oxygen or excessively removing oxygen would then have similar disordering effects. Explicitly over-annealing PCCO creates more resistive films with stronger low temperature upturns in resistivity. T_c is also suppressed in these films, further suggesting a disordering effect. This is consistant with previous work on the overdoped $Pr_{2-x}Ce_xCuO_{4\pm\delta}$ $x = .17$ system [27]. However, T_c suppression could be consistent with oxygen as a dopant as well, because, in a simple ionic picture, O^{2-} should hole dope while Ce^{4+} electron dopes. Oxygen doping should dope under-doped PCCO away from optimal doping. Measurements of the Hall effect on over-oxygenated films are not consistant with oxygen causing disorder like irradiation. Unlike irradiation, oxygen strongly changes the magnitude of the Hall effect both in magnitude and direction. Hall data suggest that oxygen dopes the material in the opposite direction of cerium doping.

Additional oxygen should dope $Pr_{2-x}Ce_xCuO_{4\pm\delta}$ independent of where it is incorporated into the crystal lattice. As-grown (and therefore over-oxygenated) crystals have excess oxygen initially and need to be reduced toward $4 + \delta = 4$ for superconductivity, rather than growing stoichiometrically and being reduced to $4 - \delta < 4$ [79]. Therefore, over-oxygenating the crystal should fully populate all of the oxygen lattice sites in the CuO_2 and PrO layers and start filling apical oxygen sites. In the $x = .17$ system it was proposed that this is the dominate source of oxygen-induced disorder [27]. Irradiation by 2 MeV protons knocks CuO_2 plane oxygens into apical sites [86] and produces disorder similar to oxygenation. This suggests that a major component of disorder in either

irradiated or oxygenated films is the presence of apical oxygens. Optimal annealing to achieve superconductivity, therefore, is likely removing apical oxygens in order to reduce the disorder they create.

Additionally, this doping effect due to oxygen seems to be a quite general effect. The magnetic properties of $Pr_{2-x}Ce_xCuO_{4\pm\delta}$ also respond to oxygen as a dopant with an enhanced Néel temperature seen in over-oxygenated samples. Oxygen does introduce some disorder and therefore might be expected to suppress T_N, due to AFM being an ordered state. The enhanced Néel temperatures seen in over-oxygenated samples suggest either that oxygen's disordering effect does little to frustrate antiferromagnetism, or that oxygen doping overpowers oxygen disorder in PCCO's magnetic structure. AMR measurements of irradiated films suggest the former. Spin dilution, the mechanism by which doping suppresses antiferromagnetism in the electron-doped cuprates, could be relatively insensitive to disorder. Doping in the electron-doped cuprates takes place in the Cu d-orbital, effectively changing $3d^9$ to $3d^{10}$, which is spinless[21]. In these materials, Ce doping on the Pr sites does not suppress antiferromagnetism by disorder, but by spin-dilution where fewer and fewer Cu atoms have a magnetic moment until long range antiferromagnetism cannot be maintained. Irradiation from 2 MeV protons cause little change in the total number of charge carriers in the system, as seen in the Hall effect data (Figure 5.3). The angular magnetoresistance data on irradiated $x = .12$ $Pr_{2-x}Ce_xCuO_{4\pm\delta}$ show that the Néel temperature also shows little sensitivity to disorder (Figures 5.14, 5.15). Despite AFM being an ordered state, its suppression via spin-dilution depends much more strongly on the number of charge carriers than on disordering of the crystal lattice.

AFM's robustness with respect to disorder could, however, be due to the dose of

irradiation since X-ray diffraction (XRD) was unable to distinguish between differently irradiated regions of PCCO. Radiation dose is difficult to translate into a density of point defects; however, the maximally oxygenated film is significantly more resistive than the maximally irradiated film (Figure 5.4). A $x = .15$ film grown in 600 mTorr O_2 looks similar to a $x = .11$ film in Hall and AMR data. Therefore, oxygen doping in this study covered a doping range equivalent to several percent cerium doping. Irradiation is unlikely to introduce a much larger concentration of defects than this level of additional oxygen as the increased scattering would be seen in resistivity data. On the other hand, several percent cerium doping has clearly measurable effects in the cuprates. For example, the doses of irradiation used in this study were large enough to have significant effect on T_c, indicating sufficient disorder to disrupt ordered states. Therefore, it is likely that AFM's insensitivity to irradiation in PCCO is due to crystal defects contributing little to spin-dilution.

Both Hall effect and angular magnetoresistance data suggest that oxygen has a significant doping effect. This conclusion seems to be at odds with ARPES data on as-grown and oxygen-reduced films which show no significant change in the electronic filling nor in the band structure parameters but does show significant reduction of long-range antiferromagnetic order [87]. In that study; however, the comparison was between as-grown and optimal films, which is a much smaller range of oxygen doping than investigated here. For example, the green and blue curves in Figure 5.6 are as-grown and optimal films respectively; this represents a much smaller range of oxygenation than between my optimal and maximally oxygenated films. The large change in antiferromagnetism seen by Richard et al. [87] can be understood due to their study's focus on optimally cerium

doped films. Near optimal doping, the Néel temperature changes rapidly with doping (Figure 4.10). When $\left|\frac{dT_N}{dx}\right|$ is large, small changes in doping will strongly affect antiferromagnetism; the Néel temperature is much more sensitive to doping near optimal doping. It is likely, therefore, that ARPES would show a significant change in the Fermi surface due to oxygenation if it were investigated over a larger range of oxygen.

In addition to the question of whether oxygen is primarily doping or disordering $Pr_{2-x}Ce_xCuO_{4\pm\delta}$, the related question of the role of annealing can be addressed by these measurements. The three scenarios presented were: first, annealing could remove apical oxygens from interstitial lattice sites, thereby reducing disorder and allowing superconductivity; second, annealing could remove in-plane oxygens from the CuO_2 planes, thereby suppressing antiferromagnetism and allowing superconductivity; and third, annealing could allow migration of copper atoms, thereby healing defects in the CuO_2 planes and allowing superconductivity. These three scenarios are discussed here.

The idea that annealing removes apical oxygens is supported by the over-oxygenated samples. Samples that are strongly oxygenated should have O(1) and O(2) sites fully populated and O(3) sites populated well above the 4% to 10% levels in annealed and as-grown crystals [24, 26]. Strongly over-oxygenating $Pr_{2-x}Ce_xCuO_{4\pm\delta}$ shows that transport properties, T_c and normal state resistivity, degrade in a consistent manner among annealed, as-grown, and over-oxygenated films. This indicates that annealing effects are clearly related to oxygenation effects. As apical sites are non-standard lattice sites, and, therefore, disorder, it is likely that the oxygen in question is apical. These measurements support the picture that has been proposed [25, 27, 82, 83] whereby annealing seems to allow superconductivity through a reduction in disorder caused by removing apical oxygens from

interstitial lattice sites.

The idea that annealing removes planer oxygens is contradicted by the irradiated samples. Samples that were irradiated by 2 MeV H^+ irradiation should have lattice oxygens knocked into interstitial sites; this irradiation especially targets lattice oxygens in the copper-oxide plane [85]. Oxygen, therefore, is removed from planer lattice sites by irradiation. Yet despite this, antiferromagnetism is not suppressed in irradiated films (Figure 5.15) compared to non-irradiated films (Figure 5.14). As the suppression of antiferromagnetism in the electron-doped cuprates is due to spin dilution and is most sensitive to doping level, no change in antiferromagnetism due to this type of oxygen movement would be expected in the absence of a special role played by in-plane oxygens. This indicates in-plane oxygens are not a major influence on antiferromagnetism, unlike as suggested in the picture [28, 29] where annealing allows superconductivity through the suppression of antiferromagnetism by removing O(1) oxygens from in-plane lattice sites.

One objection to this argument is that knocking in-plane oxygens into interstitial sites is, basically, a Frenkel defect. These defects do not change the net composition of the material, keeping the doping level the same. This might then suggest that there should be no change in antiferromagnetism because antiferromagnetism suppression by removal of in-plane oxygens is compensated by antiferromagnetism enhancement due to doping from the additional interstitial oxygen. This, however, would be a surprising coincidence if in-plane and out-of-plane oxygens play quite different roles in the antiferromagnetism in the material. If in-plane oxygens are more significant for antiferromagnetism than out-of-plane oxygens, the in-plane oxygen vacancies should not be compensated for by equal numbers of out-of-plane oxygens. Therefore, seems unlikely that the in-plane and out-

of-plane oxygens play significantly different roles with respect to antiferromagnetism in the crystal structure. AFM suppression due to in-plane oxygen vacancies and AFM enhancement due out-of-plane oxygen interstices are so well balanced that there is almost no change in antiferromagnetism between irradiated and non-irradiated films. Removal of apical oxygen suppresses T_N just as much as removal of in-plane oxygen does; however, apical oxygen removal removes disorder from the crystal lattice whereas in-plane oxygen removal adds disorder to the crystal lattice. The former would be more helpful to superconductivity than the latter; there seems to be no distinction for antiferromagnetism between O(1) and O(3) oxygens. Therefore, it is likely that annealing is not allowing superconductivity by suppressing antiferromagnetism by removing in-plane oxygens.

The idea that annealing fixes copper vacancies is contradicted by the oxygenated as-grown films. Samples that were never annealed, but were only deposited in different atmospheric pressures of oxygen show significantly different doping levels and Néel temperatures at different oxygen concentrations (Figures 5.5 and 5.9). This implies that annealing is not important for the number of charge carriers or antiferromagnetism because none of the oxygenated films are annealed and, therefore, that the effects of annealing on doping and antiferromagnetism are solely due to oxygen. Both in the $x = .12$ series and in the $x = .15$ series there is a continuous evolution of resistivity, Hall effect, and AMR from annealed to as-grown to over-oxygenated films, indicating that annealing effects are oxygen effects. This suggests that non-oxygen-related annealing effects are not a major influence in $Pr_{2-x}Ce_xCuO_{4\pm\delta}$, unlike as suggested in the picture [31] where annealing allows superconductivity through the healing of copper vacancies in the copper-oxide planes.

One complication to the argument is that as-grown films, in otherwise optimal conditions, do have a (low) T_c. This indicates that the deposition process itself is partially annealing the films as crystals do not behave in this way. However, both $x = .12$ and $x = .15$ films show the same trend in the oxygen series of films in resistivity, Hall effect, and angular magnetoresistance. The two cerium dopings studied, $x = .12$ and $x = .15$, anneal at different rates, as seen by the 20 to 25% difference in annealing times necessary to produce optimal films. If annealing during growth is significant, the two dopings should behave in noticeably different ways. In both systems, oxygenation from optimal to 600 mTorr O_2 growth results in a $.03$ reduction in effective cerium doping in both Hall effect (Figures 5.7 and 5.5) and angular magnetoresistance data (Figures 5.9 and 5.11 as compared to Figures 4.8 and 4.5 respectively). This indicates that oxygenation overwhelms any intrinsic annealing; otherwise, an $x = .12$ film should not be doped by oxygen the same as an $x = .15$ film, based upon different annealing rates. Therefore, intrinsic annealing can be neglected as not significant in the oxygenated films. The differences in properties in both of the oxygenated series are therefore due to oxygenation. The fact that annealed film behavior is consistent with the trend seen in un-annealed as-grown over-oxygenated films suggests that annealing is an oxygen effect. Therefore, it is likely that annealing is not allowing superconductivity by healing copper vacancies in the copper-oxide planes.

Several different scenarios for the role of annealing in leading to superconductivity in the electron-doped cuprates have been proposed: disorder reduction by removal of apical oxygens, antiferromagnetism suppression by removal of in-plane oxygens, and CuO_2 plane-healing migration of copper atoms. Scenario two is addressed by angular

112

magnetoresistance measurements on irradiated films. These suggest that removing oxygen from the CuO$_2$ plane does not suppress antiferromagnetism; therefore, this scenario is unlikely. Scenarios one and three are addressed by over-oxgenated films. These films are un-annealed and differ only in the growth atmosphere's oxygen concentration. Therefore, transport properties in these films evolve due to oxygen concentration. That these oxygenated and un-annealed films show a consistent trend with annealed films strongly suggests that annealing is an oxygen effect. With regards to scenario three, the fact that the over-oxgenated films are un-annealed, and behave consistently with annealed films, suggests that annealing is unlikely to have significant non-oxygen-related effects; therefore, scenario three is unlikely. Regarding scenario one, over-oxygenation should likely fully populate the oxygen lattice sites, O(1) and O(2), and add significant oxygen to the apical O(3) site. This suggests that the transport properties of over-oxgenated films evolve due to apical oxygen concentration. That these oxygenated films show a consistent trend with annealed films strongly suggests that annealing is not only an oxygen effect, but likely an apical oxygen effect; therefore, scenario one seems to be the best model to describe our data. In contrast to models predicting significant changes to the copper-oxide plane during the annealing process, our transport data suggest that removal of apical oxygen is the primary role of annealing and the reduction in crystal disorder do to this removal is then suggested as the main factor in the emergence of superconductivity in the electron-doped cuprate superconductors.

In conclusion, both disordering Pr$_{2-x}$Ce$_x$CuO$_{4\pm\delta}$ thin films as well as oxygenating them produce a disordering effect as seen by an increase in resistivity and suppression of T_c. However, oxygenation of PCCO significantly changes the Hall effect resistivity as

compared to irradiative disordering. Irradiation shows little change in the Hall resistivity, consistent with a pure disordering effect. Oxygen does not; it shifts the Hall effect significantly, indicating a change in the number of charge carriers. While oxygenation of PCCO does show a disordering effect, oxygen primarily acts as a dopant in PCCO.

Additionally, oxygenation of $Pr_{2-x}Ce_xCuO_{4\pm\delta}$ thin films supports the picture that the annealing step in electron-doped superconducting cuprate synthesis is primarily due to removing apical oxygen. A lack of irradiation-induced suppression of T_N and the consistent evolution of transport properties between annealed samples and a series of un-annealed as-grown over-oxygenated samples contradict other proposed models for annealing in the electron-doped cuprates.

Chapter 6

T_c Enhancement in Electron-Doped Cuprate Heterostructures

6.1 Introduction

Superconductivity in the cuprates is normally accomplished by doping into the CuO$_2$ plane. Counterintuitively, another method for inducing higher T_c superconductivity in the cuprates is to pair under- and over-doped cuprates. The close proximity of the different dopings contributes to an enhanced T_c. On the hole-doped side of the phase diagram, it has been shown that there can be an enhancement in T_c by pairing metallic and insulating cuprates [88, 89]. Similar behavior has been reported at the interface of different dopings of La$_{2-x}$Sr$_x$CuO$_{4\pm\delta}$ (LSCO) [90, 91]. It has been proposed that the T_c enhancement seen in these cases could arise from a combination of the under-doped side of the phase diagram providing a large pairing amplitude and the over-doped side of the phase diagram providing phase stiffness [92, 93].

This effect had not been seen on the electron-doped side of the cuprate phase diagram. The electron-doped cuprates are known to show a phase fluctuation Nernst signal above T_c on the under-doped side of the superconducting dome [74]. If the picture of a large under-doped pairing amplitude stabilized by over-doped phase stiffness is correct, the Nernst fluctuations suggest a T_c enhancement on the electron-doped side as well. However, this Nernst signal is weaker on the electron-doped side than it is on the hole-doped side and therefore the enhancement should be much smaller.

In order to investigate this effect, several heterostructures of the electron-doped cuprates, $Pr_{2-x}Ce_xCuO_{4\pm\delta}$ and $La_{2-x}Ce_xCuO_{4\pm\delta}$, were fabricated. This discussion will be restricted to heterostructures that take the form of superlattice thin films where multiple layers of under- and over-doped cuprates were stacked. Other heterostructures (e.g., bilayers) were not investigated in similar detail, but do seem to exhibit similar physics.

In both $Pr_{2-x}Ce_xCuO_{4\pm\delta}$ and $La_{2-x}Ce_xCuO_{4\pm\delta}$ superlattice thin films, an unexpected large enhancement in T_c was observed; although, the superlattice T_c was never higher than optimal single-doping T_c [94]. This effect was observed for multiple pairings of under-doped and over-doped layers. Our measurements indicate that the T_c enhancement is due to simple charge redistribution rather than any of the theoretical models mentioned above.

6.2   Superlattice Film Preparation

Superlattice films were produced as layers of under- and over-doped cuprates. These layers were layered along the c-axis of the crystal structure, i.e., the ab-planes of the under- and over-doped layers are coplaner (Figure 6.1). This stacking of the different film layers was achieved during the pulsed laser deposition (PLD) growth of the thin films. This required some modification of the pulsed laser deposition process described in Chapter 3.

For the $Pr_{2-x}Ce_xCuO_{4\pm\delta}$ superlattice films discussed here, the over-doped layer was always $x = .19$. Less over-doped $Pr_{2-x}Ce_xCuO_{4\pm\delta}$ over-doped layers do show some T_c enhancement, but were not systematically investigated. Less over-doped layers have
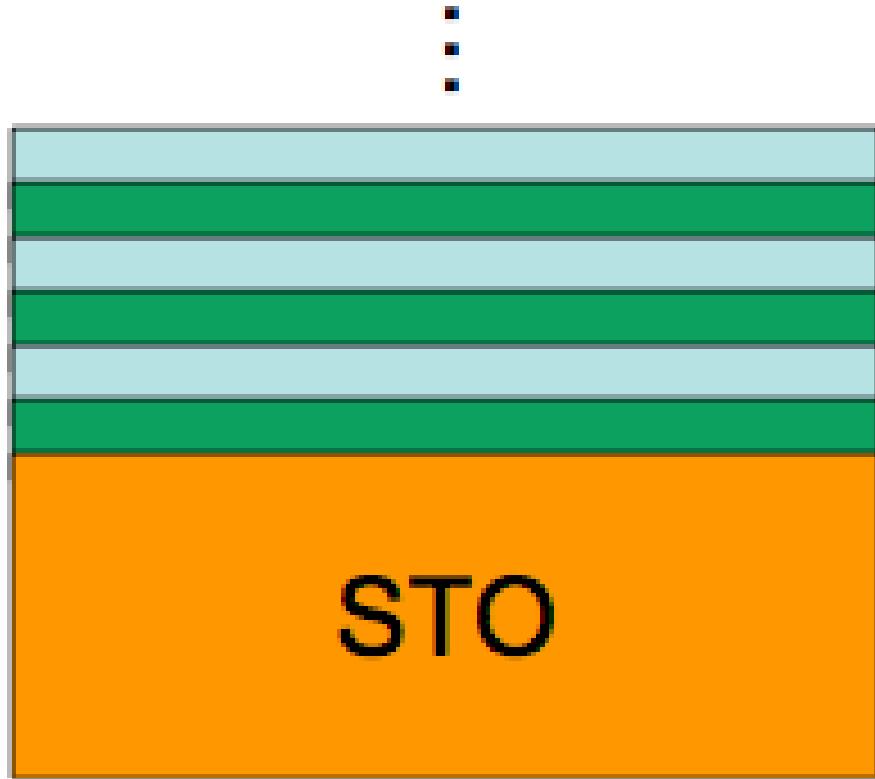
Figure 6.1: Schematic of the superlattice structure grown. Films were grown on SrTiO$_3$ (STO) substrates with alternating layers of under-doped and over-doped superconductors. The primary pairings grown and investigated were in the Pr$_{2-x}$Ce$_x$CuO$_{4\pm\delta}$ system $x = $ .19 paired with either $x = .00$, $x = .11$, or $x = .12$ and in the La$_{2-x}$Ce$_x$CuO$_{4\pm\delta}$ system $x = .06$ paired with either $x = .17$, $x = .19$, or $x = .21$.

higher T_cs themselves; .12/.17 superlattice films have T_cs that are only slightly higher than those of single-doping $x = .17$ films.

With the over-doped layer fixed at $x = .19$, the under-doped layer focused on was $x = .00$ and, to a lesser extent, $x = .11$ and $x = .12$. The highest T_c obtainable for single doping films is less than 10 K (0 K for $x = .00$, 0 K for $x = .11$, ~ 6 K for $x = .12$, and ~ 8 K for $x = .19$), while the .00/.19, .11/.19, and .12/.19 superlattice films have T_cs of at least 14 K.

6.2.1 Superlattice Film Growth

The pulsed laser deposition process grows epitaxial thin films with the concentration supplied by the target. In order to prepare the superlattice films, the PLD chamber was modified to allow two targets by replacing the original target holder with a carousel capable of holding up to six targets. Rotation of this carousel allowed any individual target to be rotated into or out of the path of the ablating laser. The films grow along the c-axis at a rate of an ångström per few laser pulses. The targets were alternated such that each target was (typically) ablated for one minute. At 10 pulses per second, the films grow roughly 20 Å in one minute.

One minute per target nominally produces superlattices with 20 Å layers, although the necessary time for a given thickness can be quite variable based upon the fluency of the laser. For example, many of the superlattice films were grown for longer times at a lower laser power prior to power-boosting laser maintenance. Superlattice films were grown with a range of layer thicknesses, for example 5 nm, 10 nm, or 20 nm layers,

and at a range of total thicknesses, with 20 total layers being the most typical. Generally, superlattice films were grown with equally thick layers of under- and over-doped material. The typical film also was terminated with the over-doped layer, regardless of whether the initial layer was under- or over-doped.

The top-most layer was over-doped due to the greater conduction in the over-doped compared to the under-doped layer, especially when the under-doped layers were un-doped Pr_2CuO_4 (PCO). The un-doped parent compound is quite insulating and, at low temperatures, exceeds the measurement range accessible by the Quantum Design Physical Properties Measurement System (PPMS). When attaching electrical leads to the films, films are top contacted; by having the top layer be over-doped, an insulating PCO cap layer could not prevent current from flowing.

Like other films grown by PLD, the oxygen content of the superlattice films was adjusted by a post-deposition annealing step. It was found that the annealing conditions appropriate for single-doping films were not optimal for superlattice films (Figure 6.2). The highest transition temperatures were achieved for anneals that were significantly longer than either individual layer's optimal annealing time. This is suggestive of oxygen behavior in the superlattice films differing from the single phase films.

Similar films were also prepared in the $La_{2-x}Ce_xCuO_{4\pm\delta}$ system. In $Pr_{2-x}Ce_xCuO_{4\pm\delta}$, the highest doping accessible is $x = .19$; the under-doped layer is more adjustable. In $La_{2-x}Ce_xCuO_{4\pm\delta}$, the lowest doping accessible is $x = .06$; the over-doped layer is more adjustable. A T_c enhancement was also found in this system for combinations of under-doped and over-doped films.
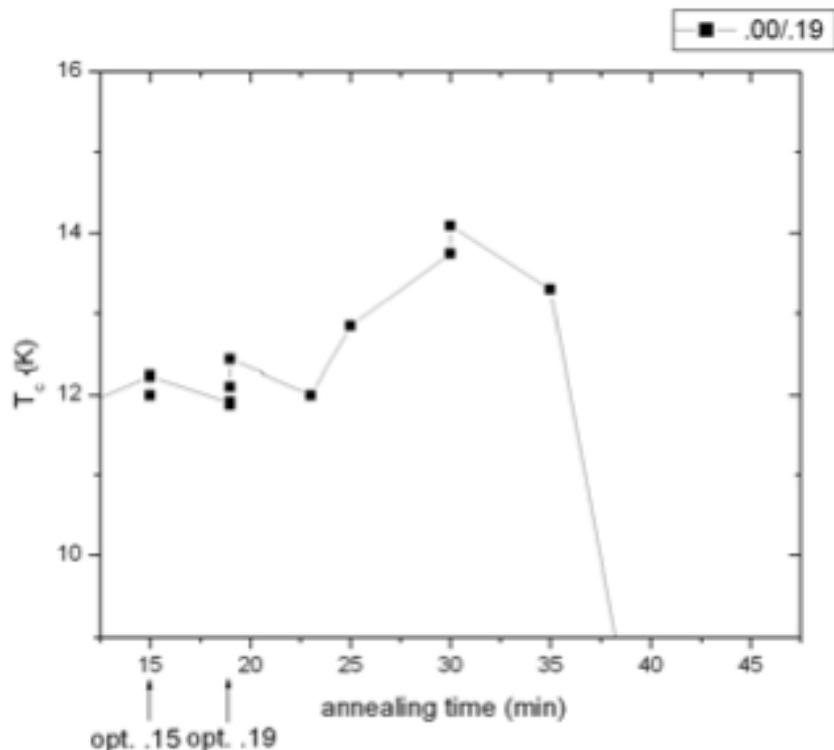
Figure 6.2: Superconducting transition temperature, T_c, compared to annealing time for a .00/.19 $\mathrm{Pr_{2-x}Ce_xCuO_{4\pm\delta}}$ superlattice thin film. The transition temperature is elevated compared to the T_cs of both constituent layers. T_c is relatively insensitive to annealing time and can be annealed for much longer than single layer films. The arrows indicate the optimal annealing times for single-doping $x = .15$ and $x = .19$ $\mathrm{Pr_{2-x}Ce_xCuO_{4\pm\delta}}$ thin films.

6.2.2   Superlattice Film Characterization

In order to investigate the T_c enhancement in the electron-doped cuprate superlattice films, it was necessary to verify that the films grown by pulsed laser deposition were, in fact, layered structures. It could have been that the cerium content could have redistributed and formed a uniform film of intermediate doping. If this were the case it would probably increase T_c due to the optimal single-doping film having a higher T_c than either superlattice component.

The superlattice films were characterized by X-ray diffraction after growth. These measurements were primarily $\theta - 2\theta$ scans on a Bruker D8 X-ray diffractometer. It was observed that, in addition to the expected $Pr_{2-x}Ce_xCuO_{4\pm\delta}$ X-ray diffraction peaks, there were additional satellite peaks around the main 00ℓ peaks. These were observed in both $Pr_{2-x}Ce_xCuO_{4\pm\delta}$ (Figure 6.3) and in $La_{2-x}Ce_xCuO_{4\pm\delta}$ (Figure 6.4). These satellite peaks are due to additional periodicity along the c-axis and correspond to the expected layer thicknesses of the superlattice films grown by pulsed laser deposition.

Satellite peaks arise due to the modulated structure in the superlattice and their presence is evidence for the formation of distinct superlattice layers. The periodicity of the superlattice, Λ, can be calculated by $\Lambda = \lambda/2(\sin\theta_i - \sin\theta_{i+1})$, where i indexes the satellite peaks [95, 96, 97, 98]. The periodicity is due to different c-axis lattice parameters in the under-doped and over-doped layers. X-rays fully penetrate these thin films; therefore, all planes are participating in constructive (or destructive) interference. If there are small changes in lattice spacings between layers, the interference peaks between one pair of crystal planes will be at a slightly different angle than those of another pair. Typically,

this causes a broadening of X-ray diffraction peaks as all of these slight angle differences are uncorrelated and cluster closely around the average value, producing a sharp peak with some non-zero full-width half-max value. In superlattice heterostructures, the slight differences in spacing between layers are not uncorrelated; the satellite peaks are evidence of regular deviations from the average c-axis lattice spacing.
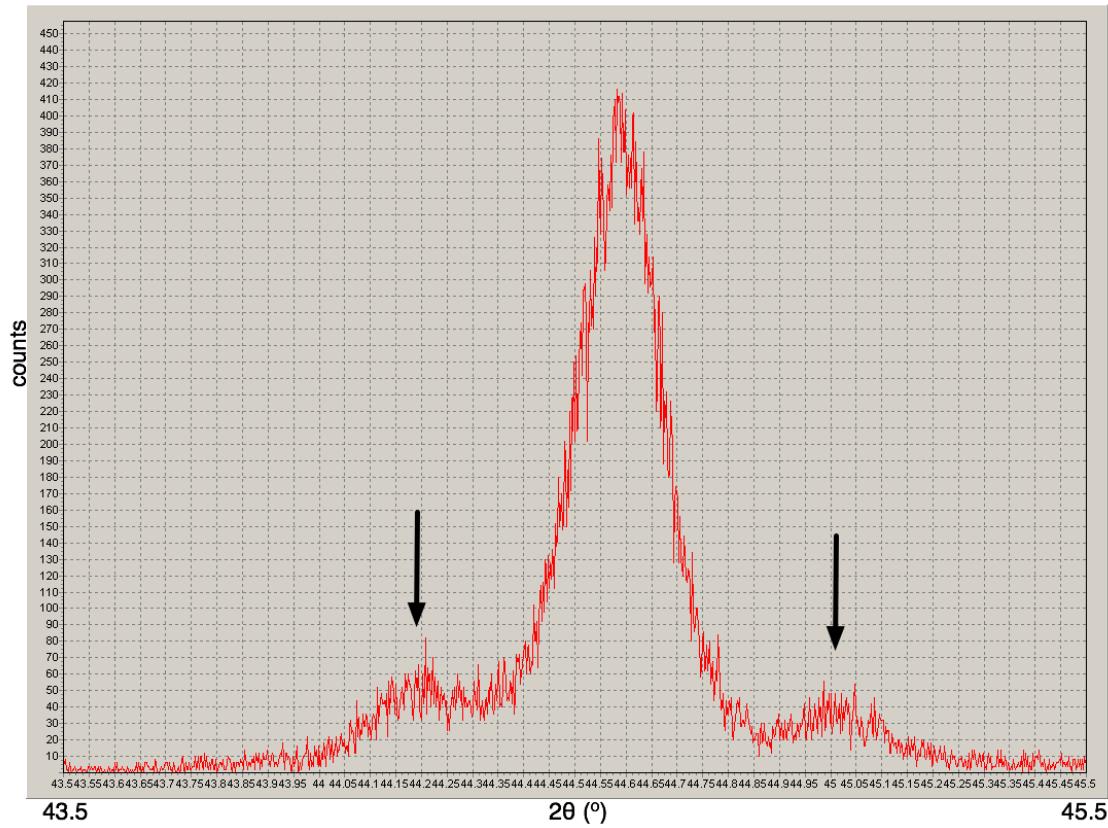
Figure 6.3: Satellite peaks in a .00/.19 $Pr_{2-x}Ce_xCuO_{4\pm\delta}$ superlattice thin film. The main peak is the 006 peak of $Pr_{2-x}Ce_xCuO_{4\pm\delta}$ and gives a c-axis lattice constant around 12.18 Å, suggesting a cerium content of $x = .08$ to $x = .10$. The superlattice film was grown with a nominal superlattice periodicity of 10 nm. The satellite peaks (labeled ↓) correspond to a 99.2 Å periodicity along the c-axis. This is showing evidence for superlattice formation.

The films were also characterized by AC susceptibility (ACχ). The superlattice films show magnetic screening comparable to the single layer films as seen in the real

122
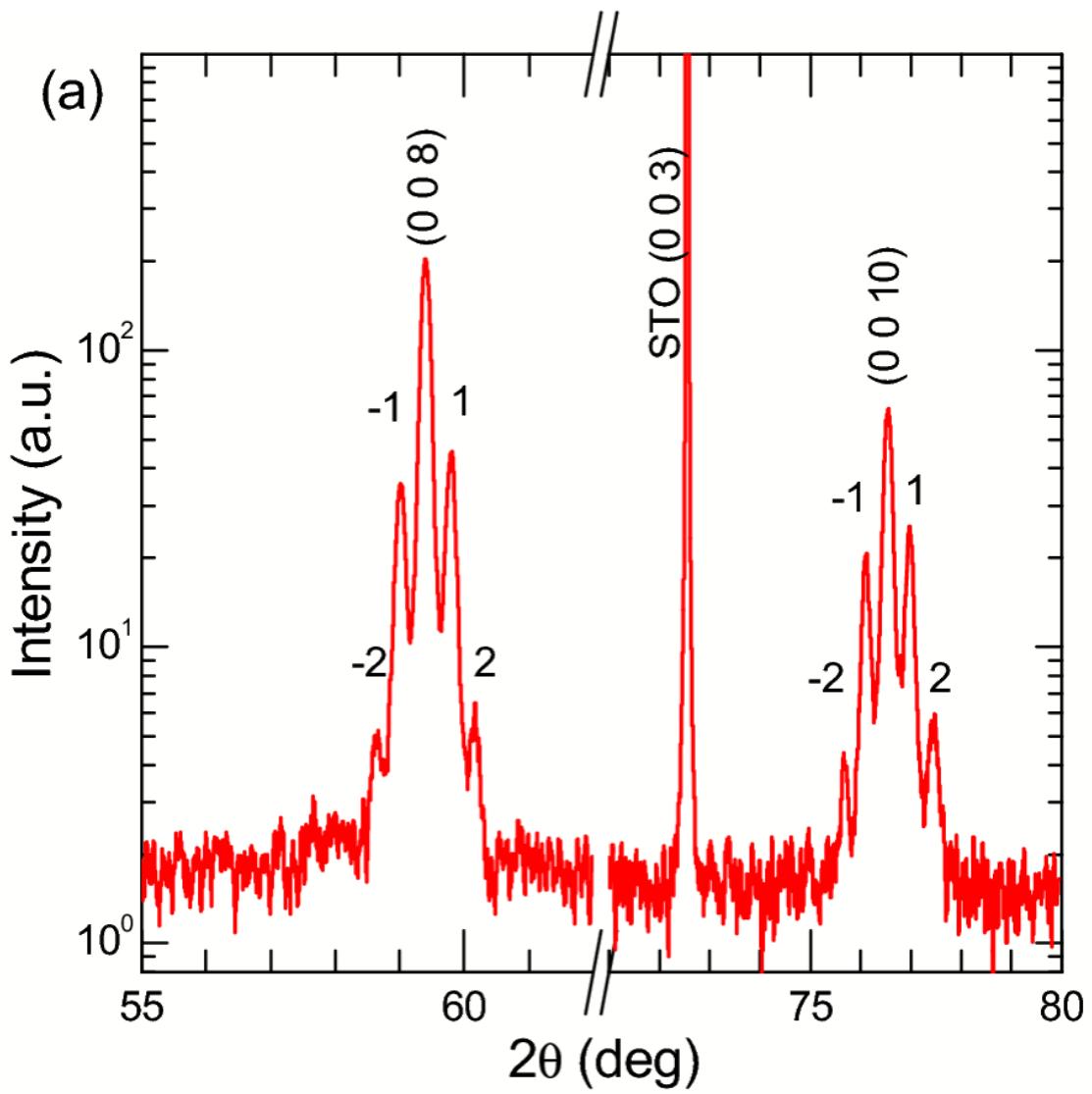
Figure 6.4: Satellite peaks in a .06/.19 $La_{2-x}Ce_xCuO_{4\pm\delta}$ superlattice thin film [94]. The 008 and 00 10 X-ray diffraction peaks show superlattice satellite peaks that are due to cerium modulation.

component of ACχ (Figure 6.5). These measurements were performed in a dip-probe in a liquid helium storage dewar.
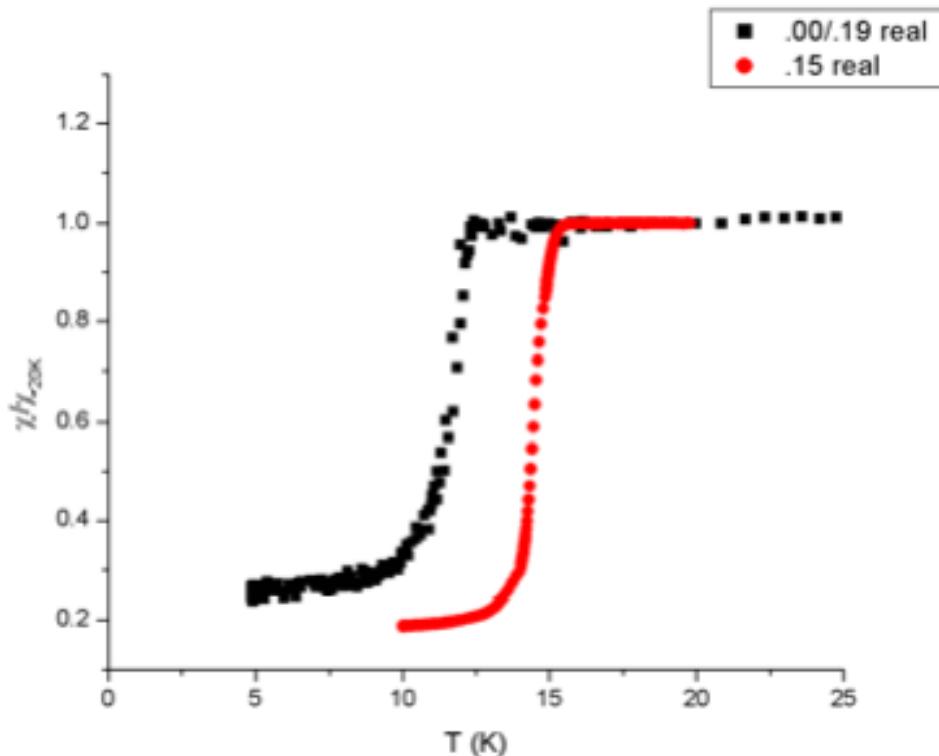
Figure 6.5: The real component of the AC susceptibility of a .00/.19 $Pr_{2-x}Ce_xCuO_{4\pm\delta}$ superlattice film compared to a .15 film. The superlattice film shows saturating behavior similar to the single layer film. This is indicative of a large volume fraction superconductivity and suggests that superconductivity is a bulk effect in the superlattice films.

Resistivity of the superlattice films was also measured (Figure 6.6). Even films with insulating $x = .00$ $Pr_{2-x}Ce_xCuO_{4\pm\delta}$ layers show metallic behavior and an elevated T_c. The normal state resistance indicates that either the over-doped layer is shorting out the more insulating under-doped layer or some charge redistribution has occurred and the superlattice is behaving like some intermediate doping. According to the X-ray diffraction

data (Figure 6.3), the most "average" doping is in the range $x = .08$ to $x = .10$. This is due to the X-rays diffracting off of all layers, so slight variations in the c-axis lattice parameter between layers get smeared out, and the main peak corresponds to the average c-axis lattice constant. Single phase films of these dopings however, are not supercon-ducting and have large low-temperature resistivity upturns. For .11/.19 and .12/.19 su-perlattice films, the "average" doping is closer to $x = .15$ or $x = .16$; however, .00/.19 does not behave substantially differently.
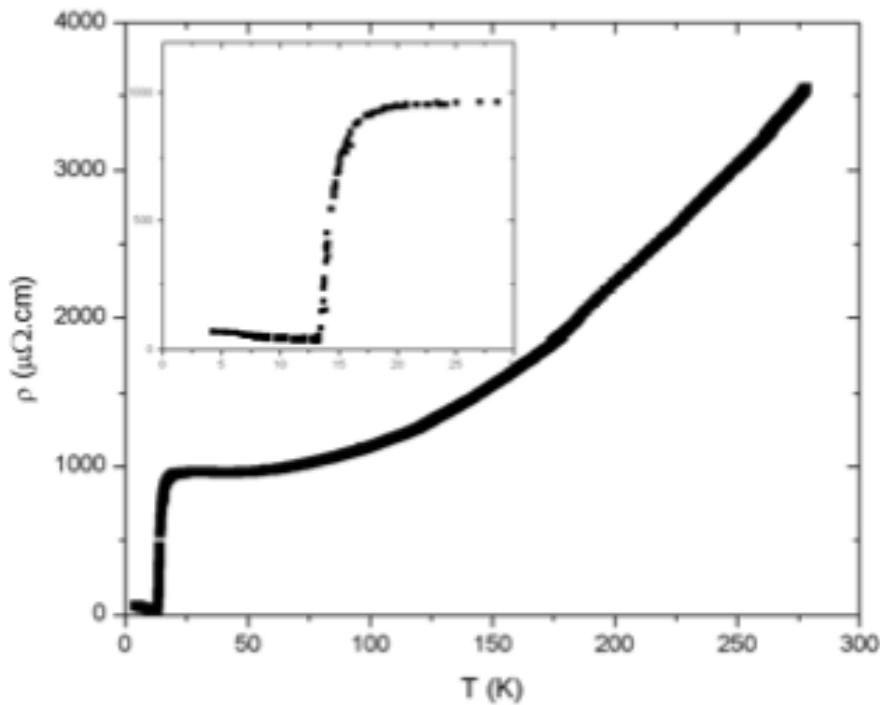
Figure 6.6: Typical resistance vs temperature curve for a .00/.19 $Pr_{2-x}Ce_xCuO_{4\pm\delta}$ super-lattice film. The T_c of $x = .19$ is ~ 8 K; $x = .00$ has no T_c.

6.3 Results

It was found that superlattice films do show an enhanced T_c, but this T_c-enhancement is probably due to charge redistribution rather than the interface effect of the various theoretical proposals. The superconducting transition temperatures in both $Pr_{2-x}Ce_xCuO_{4\pm\delta}$ and $La_{2-x}Ce_xCuO_{4\pm\delta}$ superlattices are enhanced relative to the T_cs of the constituent dopings. This was found in both $Pr_{2-x}Ce_xCuO_{4\pm\delta}$ (Figure 6.6) and in $La_{2-x}Ce_xCuO_{4\pm\delta}$ (Figure 6.7a). In neither system, however, did the superlattice T_c ever surpass the T_c of the single-doping optimally doped film. The possibility of using superlattices to surpass the optimal T_c of a material was reported in $La_{2-x}Sr_xCuO_{4\pm\delta}$ bi-layers [90]. More recently, however, that result was not reproduced, although a more modest T_c enhancement was seen [91].

In the PCCO and LCCO systems, different pairings of dopings were used. For LCCO, the under-doped layer was held constant at $x = .06$ and the over-doped layer was varied, $x = .17, .19, .21$ (Figure 6.7b). LCCO cannot be doped more lightly than $x = .06$ as contaminant T phase LCCO is preferred, but it can be doped beyond the superconducting dome. This system was, therefore, used to investigate the dependence on the over-doped layer for superlattice superconductivity. The choice of over-doped layer matters little for the superlattice T_c. For PCCO, the over-doped layer was held constant at $x = .19$ and the under-doped layer was varied, $x = .00, .11, .12$ (Figure 6.7c). PCCO cannot be doped more heavily than $x = .19$, but can be doped below the superconducting doping range. This system was, therefore, used to investigate the dependence on the under-doped layer for superlattice superconductivity. The choice of under-doped layer

matters little for the superlattice T_c.
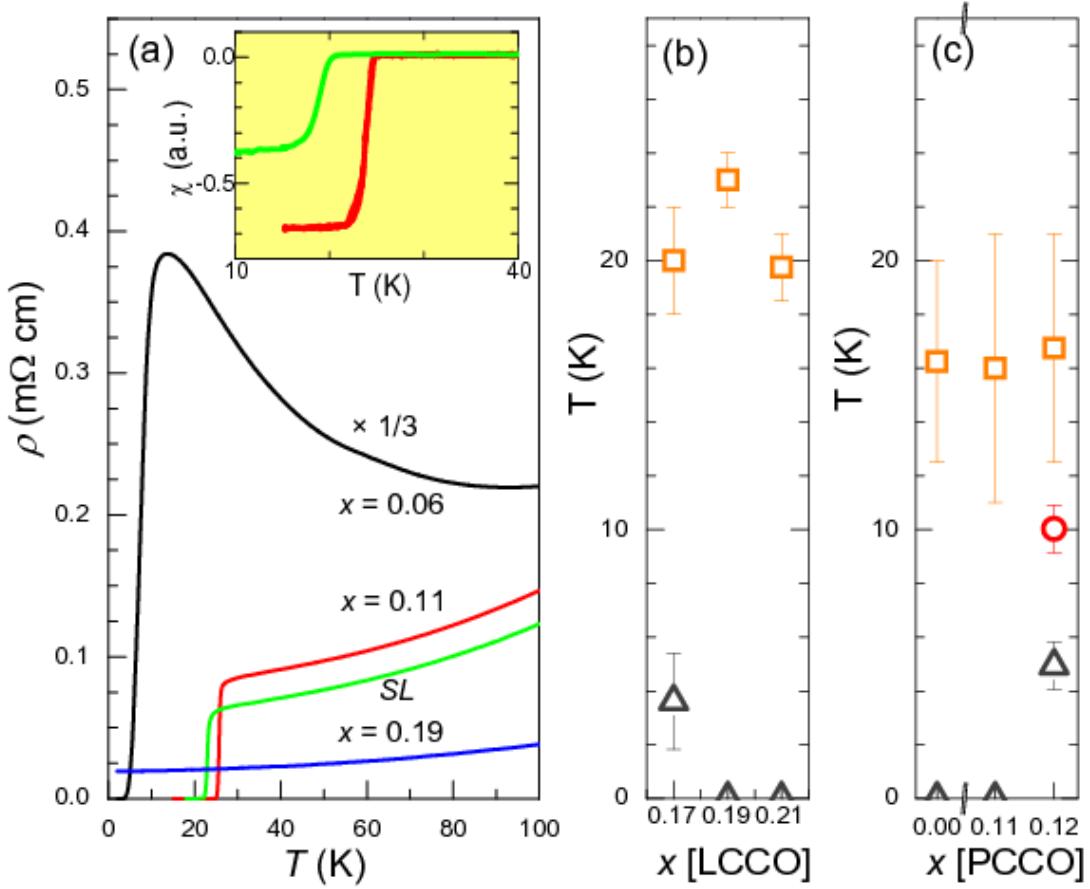
Figure 6.7: (a) Resistivity of a $.19/.06$ $La_{2-x}Ce_xCuO_{4\pm\delta}$ superlattice film compared with $x = .06$, $x = .11$ (optimal), and $x = .19$ LCCO superlattice films [94]. T_c is enhanced relative to constituent dopings. In LCCO this is observed for several $x/.06$ superlattices (b) and for PCCO this is observed for several $x/.19$ superlattices (c). The maximum T_c of each of these superlattice pairings ($\square$) is higher than that of the single-doping, x, films ($\triangle$). The $\bigcirc$ is a bi-layer film.

6.4   Discussion

In each system, the superlattice T_c was also found to be insensitive to the thickness of individual layers, from 5 nm to 20 nm. This observation suggests that possible

strain enhancement of T_c is unlikely. Thin films are strained relative to bulk crystals due to lattice mismatch with the substrate. (In the case of LCCO in particular, this substrate strain effect allows the superconducting T' phase to be stabilized.) Strain-induced superconductivity could be an explanation for superlattice superconductivity as there are more interfaces for potential lattice mismatches. However, this picture is unlikely due to the fact that layer thickness did not significantly alter superlattice T_c. Interface strain effects ought to decrease farther away from the interface, implying stronger effects for thinner layers than for thicker ones. This trend was not seen.

In each system, superlattice T_c was also found to be insensitive to the number of individual layers, from 6 to 40. This suggests that the T_c enhancement seen in the superlattice films may not be an interface effect between the two layers, but is rather caused by some long-range charge distribution. Our critical current measurements (discussed below) prove this is true. Varying the number of layers varies the number of interfaces. If the highest T_c were only found at the interfaces (or in a narrow region around the interfaces), the effective thickness of the superconducting regions of the films would be thinner. This would not affect the T_c seen by resistivity as *any* superconducting path between contact leads would short out non-superconducting regions; however, it would limit the total current that could pass through the film, reducing the critical current of the superlattice.

The critical current, I_c, was determined for $La_{2-x}Ce_xCuO_{4\pm\delta}$ superlattices of different layer thicknesses by measuring the current (I) - voltage (V) characteristics of the superlattice thin films (Figure 6.8a). In the superconducting state, current flow does not produce a voltage drop. This can be seen directly from Ohm's Law, $V = IR$, when

128

$R = 0 \; \Omega$ as in a superconductor. Too much current, however, will destroy superconductivity; the critical current is the current that completely suppresses superconductivity. The critical current can be thought of as a consequence of the upper critical field, H_{c2}. A current, I, will produce a tangential magnetic field $H = I/2\pi r$; if $H > H_{c2}$, the field produced by the current will suppress superconductivity.

The critical current density, $J_c = I_c/(w \times t)$, where w and t are respectively the width and thickness of the current bridge on the patterned films, was measured for several different numbers of layers, n (Figures 6.8b, 6.8c). J_c does not depend upon the number of layers in the superlattice; therefore, the superconductivity cannot be confined to the interface between over-doped and under-doped layers. If superlattice superconductivity were an interfacial effect, then it would be expected that $J_c = n \times J_c^{interface}$ because parallel conduction paths divide current.

The superlattice J_cs are, however, less than the single phase film with comparable $T_c, x = .11$ (Figure 6.8d). If charge is redistributed in some fashion similar to Figure 6.8e, some sub-region of the film is locally nearly optimally doped. This highest T_c region of the film then determines J_c and occupies some fraction of the total film thickness: $J_c = \frac{1}{m} \times J_c'(T_c^{max})$. J_c does depend moderately on the choice of over-doped layer (Figure 6.8d). This dependence on the over-doped layer doping suggests that the larger the doping range, the smaller the nearly optimally doped fraction of the film. This fraction, $1/m$, does not depend upon the number of layers because charge redistributes spatially over the entire layer. If the total thickness is constant, a $.21/.06$ superlattice film with any number of layers gives the same total thickness of both $x = .21$ and $x = .06$ regions as any other number of layers. The range of doping that charge has to redistribute over

matters more than the spatial range that charge has to redistribute over.

The spatial range of charge redistribution suggests that charge redistribution may not be uniform or that it may involve migration of dopants like oxygen. The Thomas-Fermi screening length in the cuprates is estimated to be 6 Å [89] to 10 Å [94]; our superlattice results suggest charge redistribution occurs over at least 20 nm. This anomalously long charge redistribution length is not well understood. Long charge redistribution lengths may suggest that superlattice films do not redistribute to a single doping, but rather continue to have some variable charge concentration with depth (Figure 6.8e). Long charge redistribution lengths could also suggest that there is some physical migration of dopant atoms in the superlattice films; this would likely suggest oxygen movement during annealing.

Because J_c does not depend upon the number of interfacial layers, the possibility of surface superconductivity at the interface is excluded. This suggests some manner of charge redistribution as the mechanism for superlattice superconductivity. Charge redistribution is unlikely to be due to cerium redistribution because the X-ray diffraction satellite peaks (Figures 6.3, 6.4) require a structural periodicity in the crystal lattice. This modulation is also seen more directly through electron energy-loss spectroscopy (EELS) (Figure 6.9). X-ray diffraction data also show that the c-axis lattice parameter for the superlattice films approaches that of the optimally doped single-doping films with increasing T_c (Figure 6.10). This suggests that charge redistribution occurs with some effect similar to cerium substitution in single-phase films.

Charge redistribution can also be investigated by Hall effect and angular magnetoresistance measurements. The Hall effect can give the number of charge carriers and is
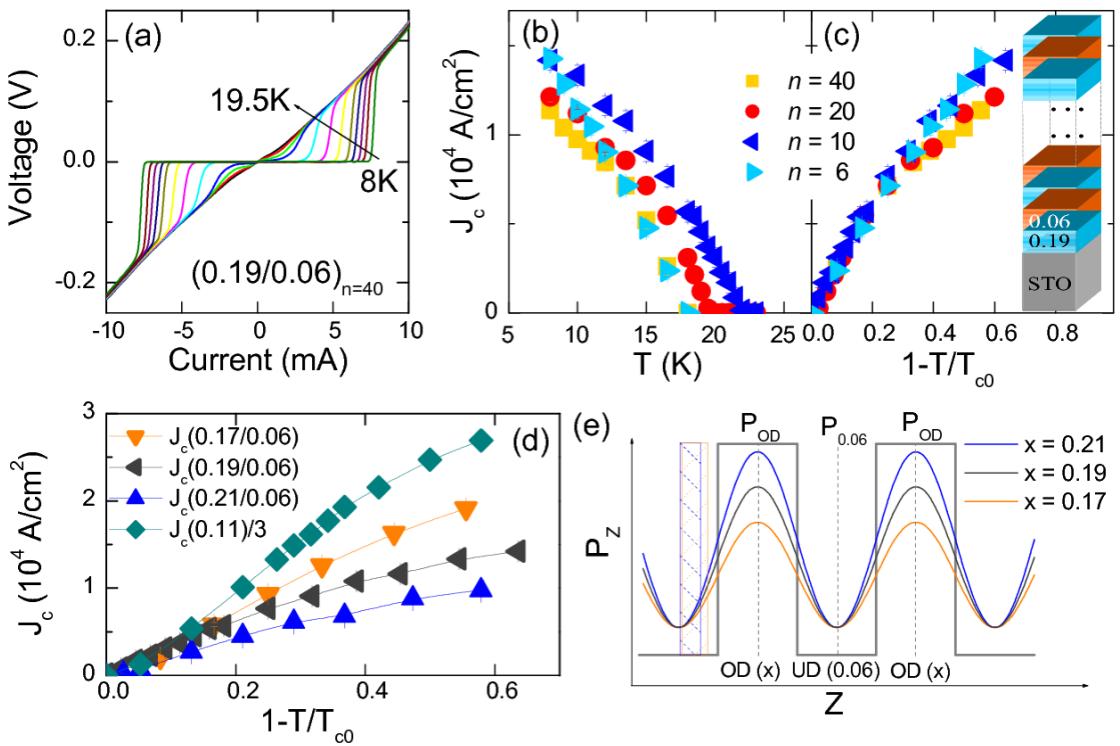
Figure 6.8: (a) I-V curves of a 40-layer $.19/.06$ $La_{2-x}Ce_xCuO_{4\pm\delta}$ superlattice [94]. The critical current densities for $x/.06$ for $x = .19$ different numbers of layers, n, ((b), (c)) and for $n = 10$ with different over-doped layers (d). Charge count (P_Z) varying along the c-axis (Z) is proposed in (e).
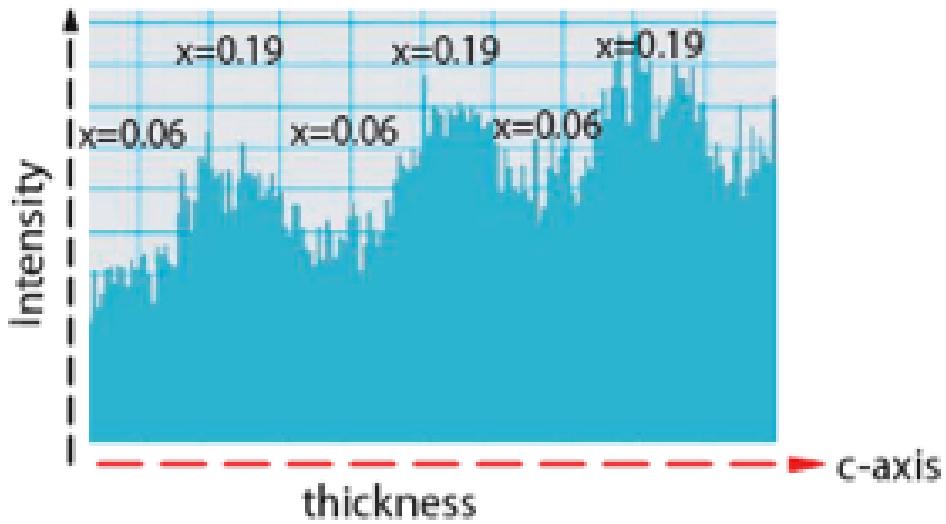
Figure 6.9: Electron energy-loss spectroscopy (EELS) of $0.19/0.06$ La$_{2-x}$Ce$_x$CuO$_{4\pm\delta}$ superlattice. The intensity is of Ce 3d3/2 which is a measure of cerium concentration.

thus sensitive to the overall doping of the material. Observation of angular magnetoresistance oscillations indicates magnetic ordering and, therefore under-doped regions due to an antiferromagnetic quantum phase transition in Pr$_{2-x}$Ce$_x$CuO$_{4\pm\delta}$ near optimal doping.

If there were strong charge redistribution, the films should behave electronically as though there is a single conduction channel of intermediate doping due to charge redistribution diluting the over-doped layer and fortifying the under-doped layer such than they have a single effective doping. Therefore, if the charges were fully redistributed between the layers, i.e., the $x = .00$ and $x = .19$ layers redistributed to form a single $x \approx .10$ layer, this would cause the film to behave as a single layer film of $x \approx .10$. A film with this "average" doping would be identifiable in both Hall effect and angular magnetoresistance data. The Hall effect would, therefore, see a $x \approx .10$ film in a single-band picture,
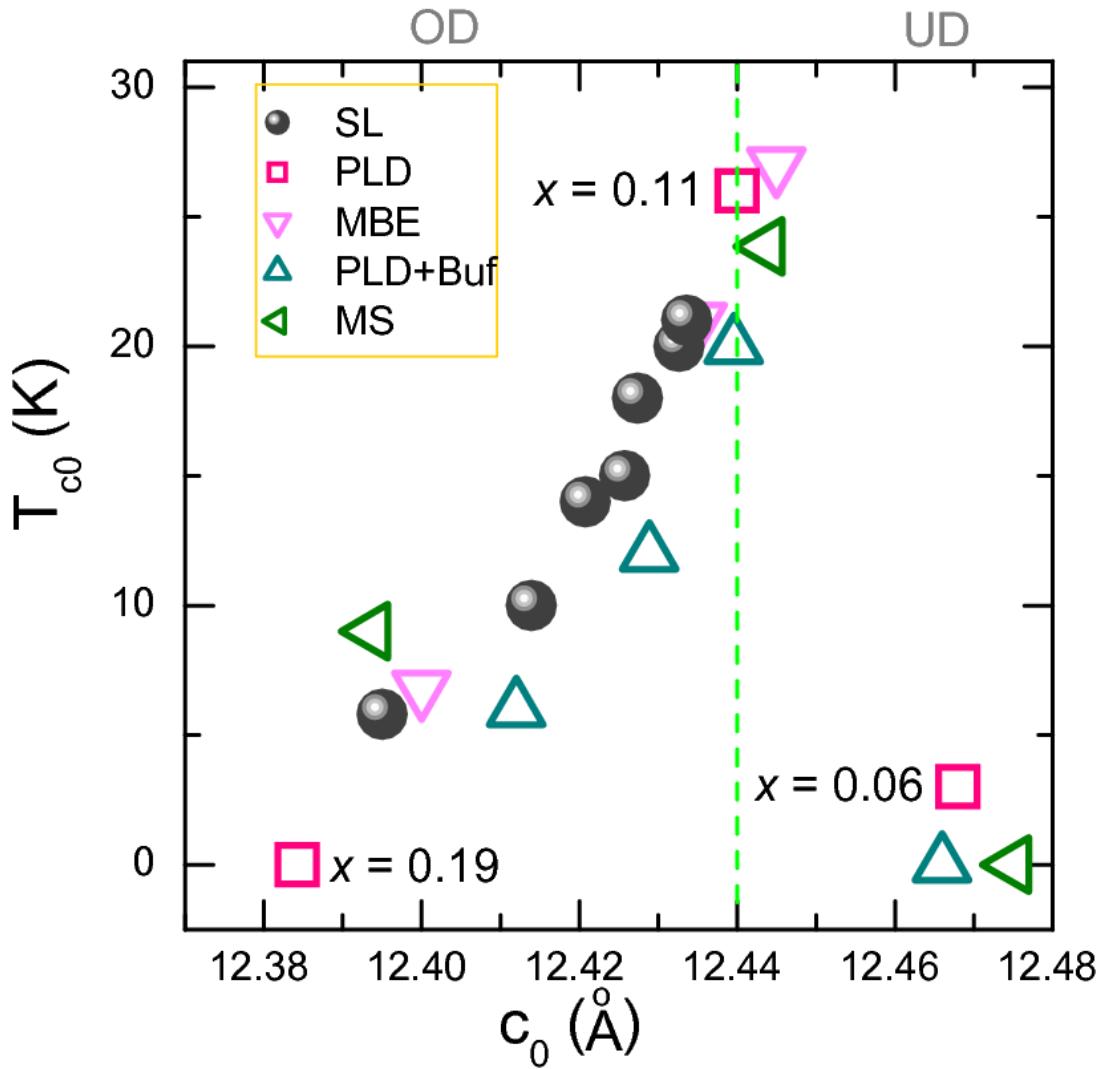
Figure 6.10: La$_{2-x}$Ce$_x$CuO$_{4\pm\delta}$ T_c as a function of the c-axis lattice parameter as measured by X-ray diffraction [94]. The superlattice films ($\bigcirc$) have T_cs that depend upon the c-axis lattice parameter in much the same way as single-doping films grown by various methods (open symbols). Optimally doped films have a c-axis lattice parameter of 12.44 Å.

i.e., $R_H = -\frac{1}{ne}$. Additionally, strong angular magnetoresistance oscillations would be expected with a Néel temperature of around 150 K (Figure 4.10). A single doping film of "average" doping, the expectation for strong charge redistribution, should be readily observable in Hall and angular magnetoresistance data.

If, however, the charges were well separated in the over- and under-doped layers, the film should behave as though there were two parallel conduction channels, one over-doped channel and one under-doped channel. This should also be observable in Hall effect and angular magnetoresistance data. A two-band Hall effect suggests what might be seen where the under- and over-doped layers provide independent conduction channels. For two-bands,

$$R_H = \frac{1}{\sigma_1 + \sigma_2} \left(\frac{\sigma_1 q_1 \tau_1}{m_1^*} + \frac{\sigma_2 q_2 \tau_2}{m_2^*} \right),$$

in the low-field limit [38]. In this model, R_H will be most strongly influenced by the more conductive channel, i.e., if $\sigma_1 \gg \sigma_2$ then $R_H(\sigma_1, \sigma_2) \approx R_H(\sigma_1)$. In the case of under-doped/over-doped cuprate superlattices, the over-doped layer is significantly more conductive than the under-doped layer. This suggests that the more conductive over-doped layers would tend to short out the less conductive under-doped layers and the Hall effect should be similar to the Hall effect of the over-doped layer. As angular magnetoresistance is a magnetoresistance measurement, $\frac{1}{R} = \frac{1}{R_1} + \frac{1}{R_2}$ suggests that with two parallel conduction channels in cuprate superlattices, angular magnetoresistance will, like the Hall effect, also behave similarly to the more conductive over-doped layer. As with the Hall effect the more conductive over-doped layer will tend to short out the under-doped layer. However, in these cuprate systems there are no angular magnetoresistance oscillations

to measure above $x \approx .15$, so the dominate over-doped layer will contribute no signal, and the angular magnetoresistance signal should show a Néel temperature comparable to the under-doped layer (≈ 250 K in Pr_2CuO_4). These behaviors in Hall effect and angular magnetoresistance data should be clearly distinguishable from the single conduction channel of the strong charge redistribution case.

Together, the Hall effect and angular magnetoresistance oscillations can provide a strong probe of charge redistribution in these under-doped/over-doped cuprate superlattices. A strongly charge redistributed sample will appear to have a doping level half way between the nominal under-doped and over-doped layer doping levels and will appear as such an "average" film in both Hall effect and angular magnetoresistance measurements. A superlattice without charge redistribution will appear, in contrast, to have conflicting doping levels reported by Hall effect and angular magnetoresistance measurements; the Hall effect will show a very over-doped film and the angular magnetoresistance oscillations will show a very under-doped film. By observing how well the doping levels recorded by these two measurements agree or disagree, the character of the charge redistribution can be investigated.

The Hall effect was measured on two $La_{2-x}Ce_xCuO_{4\pm\delta}$ superlattices (Figure 6.11). It was found that the Hall effect of these superlattice thin films is of a similar magnitude to that of the single-doping films (Figure 6.12). Naïvely, .17/.06 and .21/.06 superlattice films should either be like $x \approx .115$ and $x \approx .135$ films if charge is well distributed or like $x \approx .17$ and $x \approx .21$ films if charge is not well distributed. The superlattice films are reasonably similar to the optimally doped ($x = .11$) single-doping thin films. In $La_{2-x}Ce_xCuO_{4\pm\delta}$, the Hall effect is positive at high dopings like $x = .17$ or $x = .21$,

whereas the lower dopings are negative (Figure 6.13). The superlattice films are more like the "average" doping films, suggesting again, that there is significant charge redistribution in the superlattices.
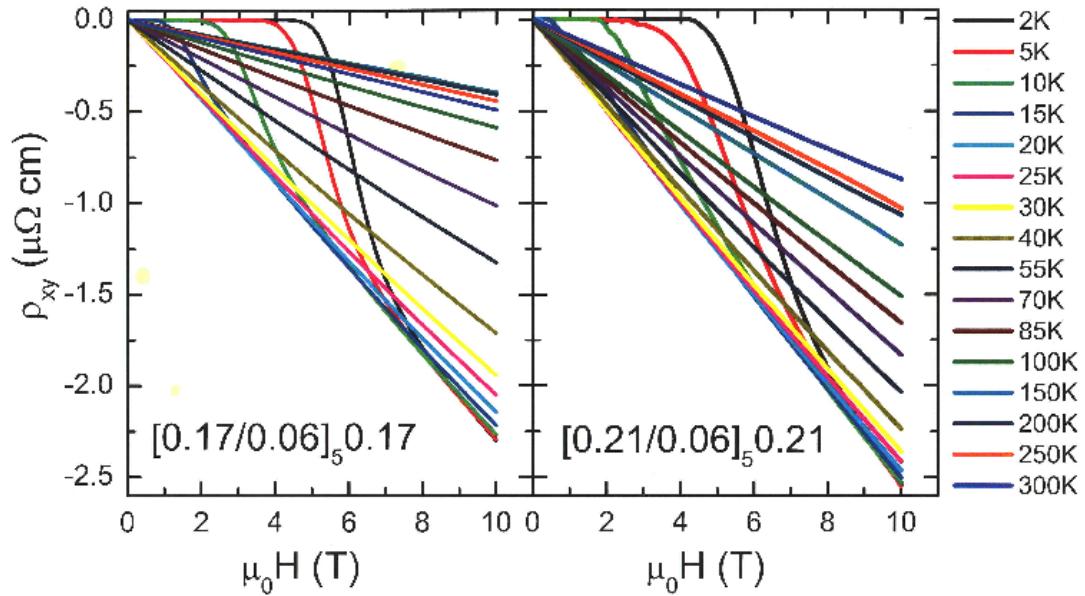
Figure 6.11: Hall effect versus field at various temperatures for $La_{2-x}Ce_xCuO_{4\pm\delta}$ super-lattices.

Superlattice structure could also be investigated via angular magnetoresistance measurements. These measurements, discussed in Chapter 4, probe the magnetic ordering of the thin film. The antiferromagnetism in both $Pr_{2-x}Ce_xCuO_{4\pm\delta}$ and $La_{2-x}Ce_xCuO_{4\pm\delta}$ is known to be an under-doped phenomenon, disappearing in over-doped films. The angular magnetoresistance of $Pr_{2-x}Ce_xCuO_{4\pm\delta}$ superlattice films does exhibit oscillations,
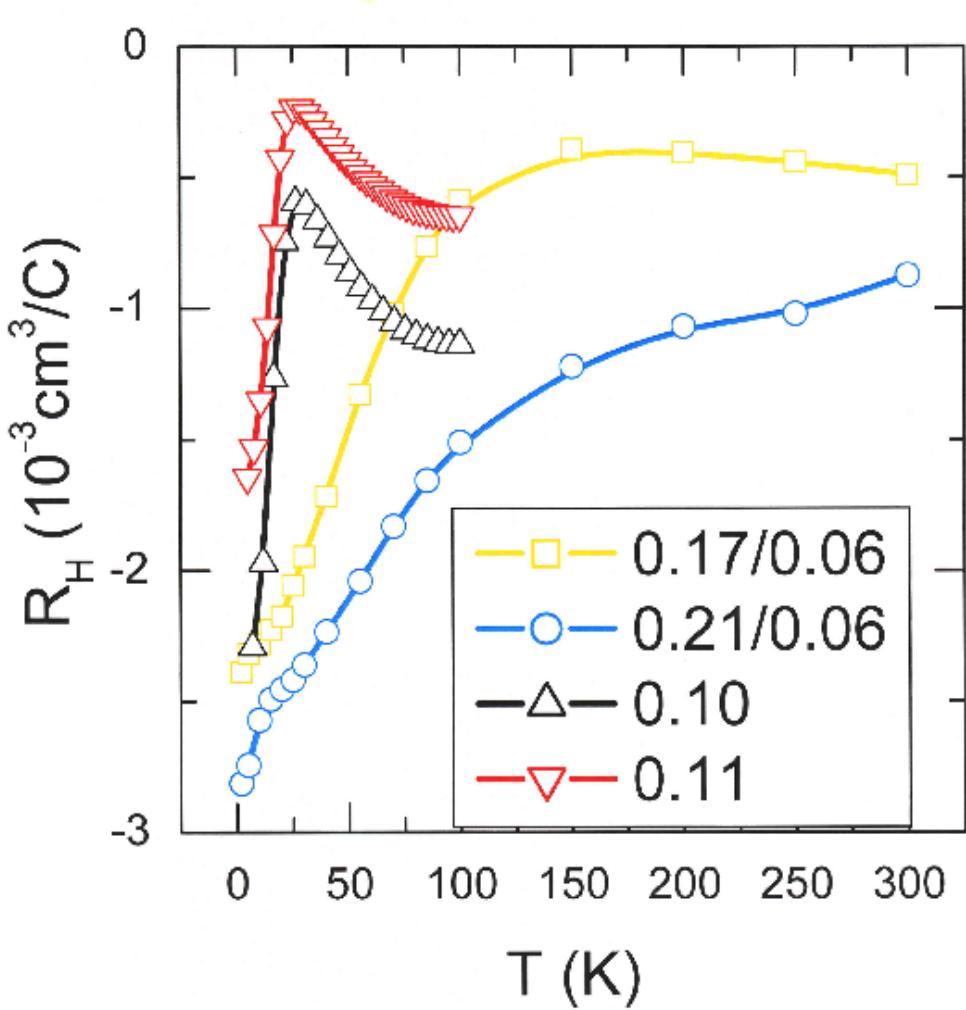
Figure 6.12: Hall effect versus temperature for $La_{2-x}Ce_xCuO_{4\pm\delta}$ superlattices compared to single-doping optimally doped LCCO films. The superlattices are similar in magnitude to the single-doping films.
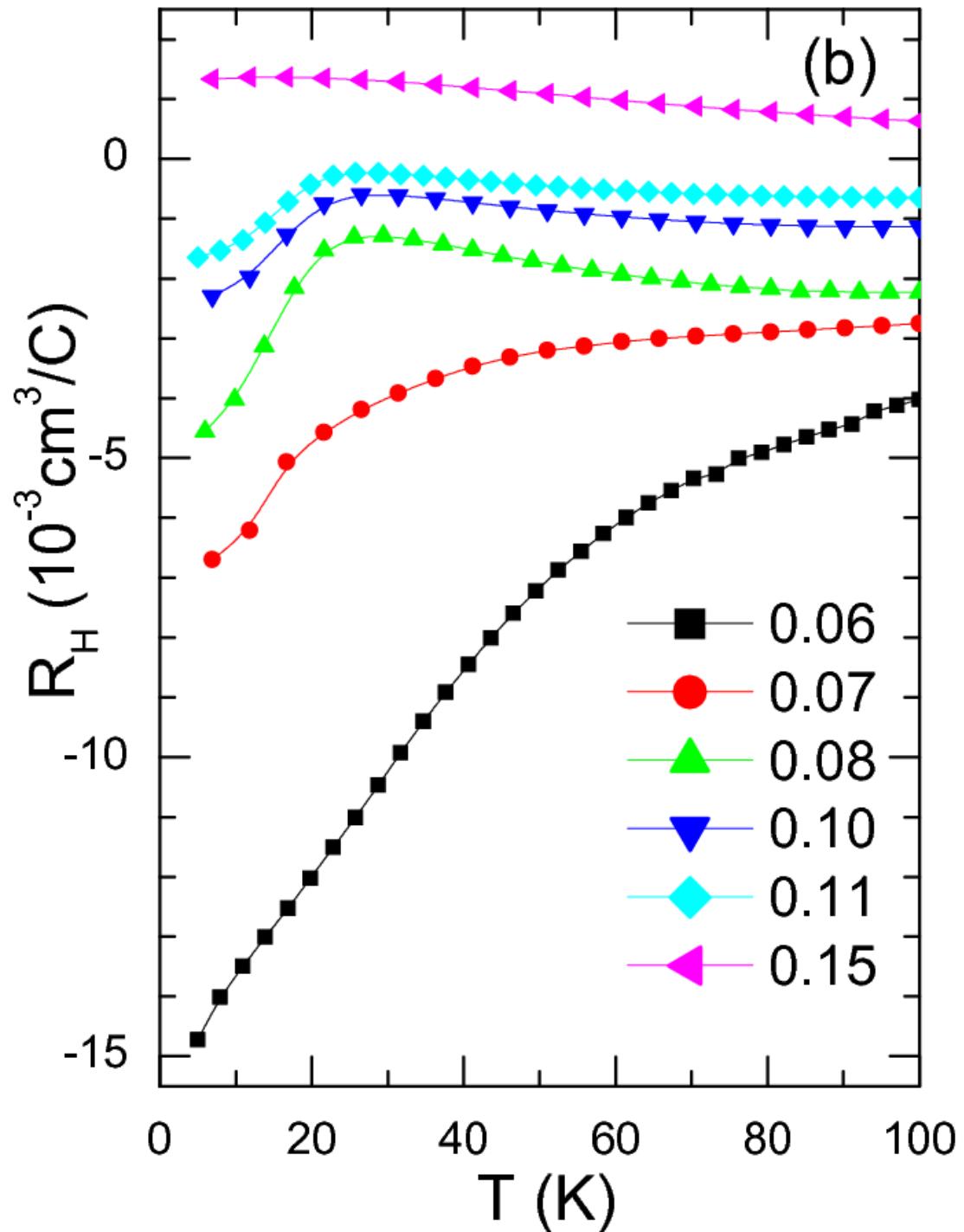
Figure 6.13: The Hall effect versus temperature for various $La_{2-x}Ce_xCuO_{4\pm\delta}$ dopings [70].

indicating that an under-doped region is present (Figure 6.14).

In the electron-doped cuprates, antiferromagnetism is suppressed by spin-dilution; the Néel temperature is sensitive to the doping level, rather than cerium concentration. This is seen, for example, in the antiferromagnetism enhancement due to oxygen doping discussed in Chapter 5. Therefore, oscillations seen in superlattice films suggest that the charge redistribution in the superlattice thin films may be incomplete or that charge redistributes to a slightly under-doped doping level.
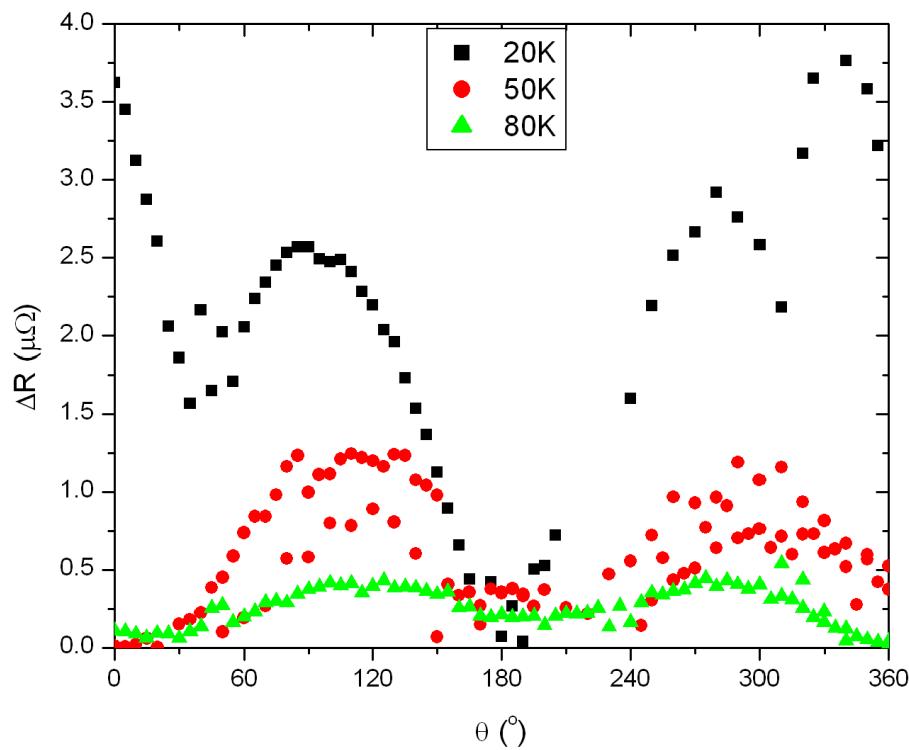
Figure 6.14: The angular magnetoresistance of a $Pr_{2-x}Ce_xCuO_{4\pm\delta}$ .11/.19 superlattice film. Oscillations are present, although they disappear at high temperatures. The angular magnetoresistance oscillations disappear at a temperature between the $x = .11$ and $x = .15$ Néel temperatures.

As angular magnetoresistance is a resistance measurement, the most conductive part of the film will tend to carry the bulk of the current. Therefore, if there is incomplete charge redistribution, the angular magnetoresistance measurement would preferentially sample the over-doped region. The observation of angular magnetoresistance oscillations, however, comes from under-doped regions as there is no angular magnetoresistance signal in $Pr_{2-x}Ce_xCuO_{4\pm\delta}$ above $x \approx .15$ (Chapter 4). Hall effect measurements on $La_{2-x}Ce_xCuO_{4\pm\delta}$ superlattices indicate significant charge redistribution to a doping level near the average of the under-doped and over-doped doping levels; however, the $Pr_{2-x}Ce_xCuO_{4\pm\delta}$ angular magnetoresistance data suggests that the most conductive, i.e., most highly doped, part of the superlattice film to show antiferromagnetism is, in fact, slightly under-doped. Based on angular magnetoresistance, the T_N of the .11/.19 super-lattice thin film is comparable to that of an $x = .13$ or $x = .14$ single-doping film. As angular magnetoresistance oscillations are observed in optimally doped $Pr_{2-x}Ce_xCuO_{4\pm\delta}$ (Figure 4.8), the T_N defined from the superlattice angular magnetoresistance signal indicates that a $x = .15$ region in the charge-redistributed film is not present and the superconductivity T_c is determined by slightly under-doped regions with effective doping levels around $x = .13$ or $x = .14$. The T_cs of these superlattice films are also comparable with single films at around this doping range. The Hall effect on $La_{2-x}Ce_xCuO_{4\pm\delta}$ superlattices is consistent with slightly under-doped superlattices (Figure 6.12).

The highest-T_c regions in the superlattice films are due to charge redistribution. If these regions are indeed slightly under-doped, this would provide a natural explanation for the superlattice T_c. Although it is not clear why charge redistribution creates slightly under-doped regions rather than optimally doped regions as its maximal-T_c regions, I

speculate here that it may be due to the doping effect of oxygen in the superlattice, based upon investigation of annealing superlattice films. Further experiments are needed to investigate the plausibility of this explanation.

It is known that superlattice films require different annealing procedures than single-doping films (Figure 6.2), suggesting that oxygen behaves differently in superlattice and single-doping films. As oxygen can function as a dopant in $Pr_{2-x}Ce_xCuO_{4\pm\delta}$ (Chapter 5), the superlattice is doped by the under-doped layers, the over-doped layers, and oxygen in both types of layers. Therefore, the "average" doping that might be expected from charge redistribution, e.g., $x \approx .15$ for a .11/.19 superlattice, could be modified by oxygen doping. However, naïvely adding oxygen doping to the model proposed for charge redistribution (Figure 6.8e) would suggest that the whole doping profile would shift, for example, rather than redistributing between $x = .11$ and $x = .19$, a .11/.19 superlattice may have charge redistribution between effective cerium dopings $x = .10$ and $x = .18$. If this is happening, however, there should still be some fraction of the superlattice at optimal doping as $x = .15$ still lies within the range covered by charge redistribution. The possibility that a slightly under-doped maximal T_c is due to oxygen doping shifting the whole doping region to below optimal doping, for example, a .11/.19 superlattice is oxygen doped to a .06/.14 superlattice, is unlikely due to the large amount of disorder that such aggressive oxygen doping would induce (Figure 6.15). If oxygen were doping the superlattice films that significantly, T_c would be suppressed and the superlattice films would be quite resistive. In order to have the highest-T_c region be non-optimally doped, the continuity of the doping in this model would seem to need to be broken by this oxygen doping.
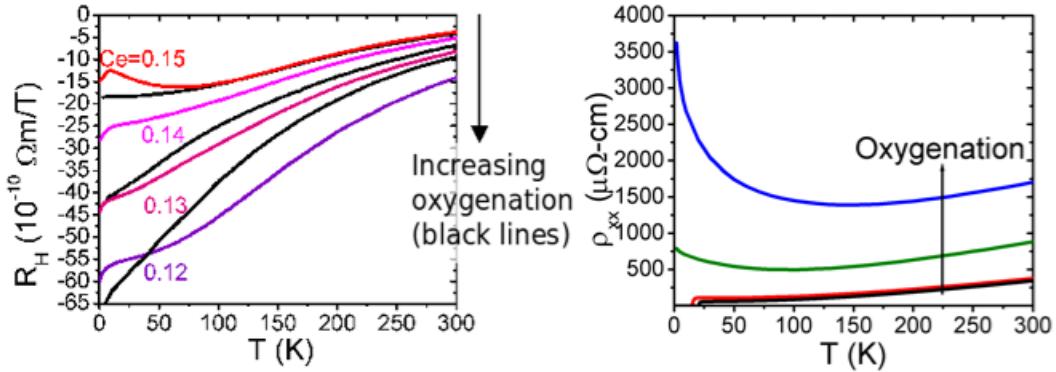
Figure 6.15: Hall effect and resistivity versus temperature of oxygenated optimally doped ($x = .15$) $Pr_{2-x}Ce_xCuO_{4\pm\delta}$ films. Left: Hall effect of oxygenated films (Figure 5.7) plotted against several optimally annealed cerium dopings [99]. Right: Resistivity of these oxygenated films (Figure 5.6) replotted here for comparison. Significant oxygen doping, equivalent to several .01 of cerium doping, suppresses T_c and notably increases the resistivity of the film.

Uniform oxygen behavior in the superlattice films would not disrupt the continuity of cerium doping suggested by (Figure 6.8e). However, oxygen concentration is not easily determined in $Pr_{2-x}Ce_xCuO_{4\pm\delta}$ thin films and there is no reason to believe that oxygen is behaving identically in the over-doped and under-doped layers. Therefore, let us speculate that there is some intrinsic oxygen diffusion from over-doped to under-doped layers in superlattice thin films. This oxygen movement would effectively over-anneal the over-doped layers and over-oxygenate the under-doped layers. If this happens in the superlattice films, it pulls both layers away from optimal doping as oxygen dopes in the opposite sense as cerium (Chapter 5). Oxygen depletion in the over-doped layers would add more electrons to the system, over-over-doping the over-doped layers, and oxygen concentration in the under-doped layers would remove electrons from the system, under-under-doping the under-doped layers. With this oxygen profile, the fact that superlattice anneal-

ing times are significantly longer than single-doping film annealing times (Figure 6.2) can be understood. The longer annealing times further over-anneal the over-doped layer, but they also over-anneal the over-oxygenated under-doped layer. The most over-doped regions would most likely be degraded and not participate significantly in transport. However, this longer annealing time would also over-anneal the over-oxygenated under-doped layers, thereby removing the excess oxygen and pulling the under-doped regions back to their Figure 6.8e behavior, even while the over-doped layers are over-annealed and are shifted to higher dopings. This picture would therefore have the region of highest T_c be slightly to the under-doped side of optimal doping.

This explanation is speculative and would require further experimental investigation. Oxygen concentration is quite difficult to determine in thin films of $Pr_{2-x}Ce_xCuO_{4\pm\delta}$, and even more difficult at the nanometer scale resolution probably needed to investigate its profile in these superlattices; however, this picture would also suggest a significant increase in disorder in the over-over-doped layers that might be detectable with careful X-ray diffraction investigation. Bi-layer films may provide an alternate method for investigating this possibility as ion milling could remove the top layer after film synthesis allowing film properties to be investigated on a more layer-by-layer basis.

Using ion milling or similar technique to slowly remove layers of bi-layer, or reduced layer superlattice, films may provide additional useful information on the nature of charge redistribution in the cuprate superlattices. If the charge redistribution is related to the film's structure, i.e., attached to the crystal lattice as synthesized and set by the details of that synthesis, ion milling to remove the top layer of a T_c-enhanced bi-layer film might preserve the elevated T_c. In such a study, comparing under-doped/over-doped

to over-doped/under-doped bi-layers might shed light on the most important regions of the superlattice films. At the very least, such a study should be able to determine whether charge redistribution is generally structural and static in nature, or more electronic and dynamic in nature.

6.5 Conclusion

Interface effects in heterostructures of electron-doped cuprate superconductors were proposed as a mechanism for enhancing T_c. This investigation of $\mathrm{Pr_{2-x}Ce_xCuO_{4\pm\delta}}$ and $\mathrm{La_{2-x}Ce_xCuO_{4\pm\delta}}$ superlattices found significant T_c enhancement by creating films of layered under-doped and over-doped cuprates. However, the enhancement of T_c in superlattices of $\mathrm{Pr_{2-x}Ce_xCuO_{4\pm\delta}}$ and $\mathrm{La_{2-x}Ce_xCuO_{4\pm\delta}}$ is not due to interface effects because critical current measurements reveal the superconductivity to be independent of the number of interfaces. The enhanced superconductivity appears to be a consequence of charge redistribution. The Hall effect and angular magnetoresistance measurements on superlattice films suggest that charge redistribution produces superlattice films with an effective doping that is somewhat less than optimal-doping. The T_c was enhanced in superlattice films relative to the constituent single-phase films; however, the possible interface effects, that initially motivated this study, seem unlikely to be present.

Chapter 7

High Temperature Resistivity Measurements

7.1 Introduction

The new iron-pnictide family of superconductors is often compared to the cuprate superconductors. Both families have similar phase diagrams with magnetic ordering in the parent compounds that is suppressed by doping; further doping yields a superconducting dome with quite high transition temperatures. However, the cuprate superconductors are doped Mott-Hubbard insulators with strong Coulomb interactions, whereas the pnictide parent compounds are metallic, suggesting that the pnictides might be more weakly correlated than the cuprates. Supporting this picture, resistivity saturation has been reported in PrFeAsO crystals as evidence for electron-phonon scattering [100]. However, magnetic susceptibility in $BaFe_{2-x}Co_xAs_2$ has been observed to show unusual linear temperature dependence up to 700 K (Figure 7.1), described as indicating strong magnetic fluctuations [71]. This susceptibility data suggest interesting physics above room temperature. Magnetic fluctuations have also been observed in neutron scattering [101, 102] and nuclear magnetic resonance (NMR) [103, 104] results.
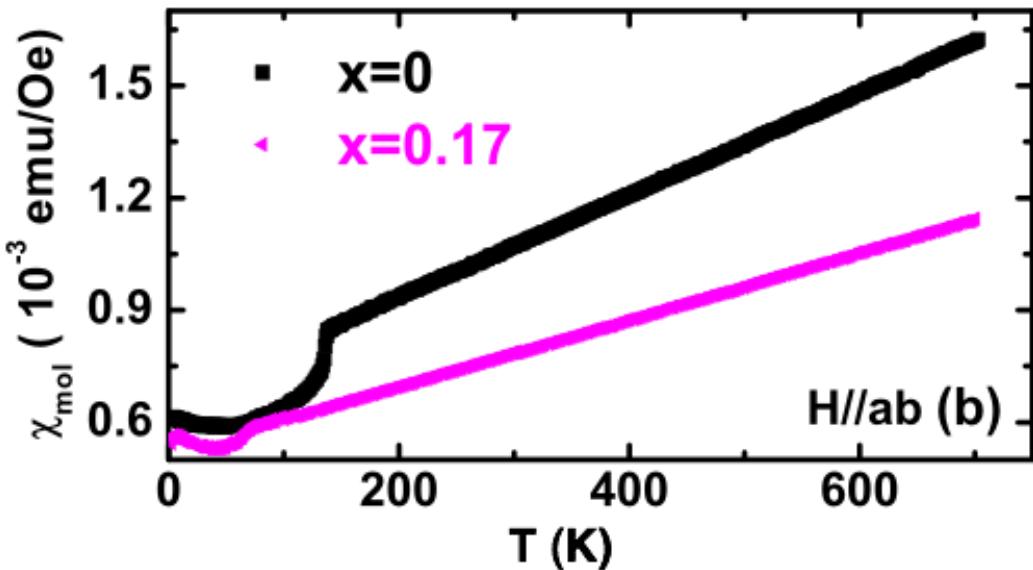
Figure 7.1: Susceptibility in $BaFe_{2-x}Co_xAs_2$ has been reported to exhibit unusual linear in T behavior up to 700 K [71].

7.2 Mott-Ioffe-Regel Limit

The Mott-Ioffe-Regel limit is a resistivity saturation at high temperatures. This saturation is due to the details of charge transport. In metals, where there are free conduction electrons, the electrons will move in response to an applied electric field. This movement, however, takes place in the context of a crystal lattice and is hindered by the electrons interacting with and being deflected by their local environment. At low temperatures this scattering can be accomplished by a number of things: crystal defects, other electrons, lattice vibrations. At high temperatures, however, the lattice vibrations dominate. These phonon modes are stronger at higher temperatures, causing much more frequent electron-phonon scattering.

For a wide range of temperatures, the resistivity of most metals is dominated by

phonons. In typical (weakly correlated) metals, high temperature resistivity depends on charge carriers scattering off of phonons. In these materials, $\rho(T)$ is described by the Bloch-Grüneisen theory:

$$\rho_{ph}(T) = A \left(\frac{T}{\Theta_D} \right)^5 \int_0^{\Theta_D/T} \frac{x^5 dx}{(e^x - 1)(1 - e^{-x})}.$$

This phonon-mediated resistivity is predicted to be linear above the Debye temperature, Θ_D, up to high temperatures [2].

This linear resistivity cannot continue indefinitely in real crystals as pointed out by Ioffe and Regel [105] and Mott [106] due to the finite size of the crystals' interatomic spacing. More electron-phonon scattering means more resistivity as the mean free path, ℓ, the distance between successive scattering events, decreases. Therefore, the resistivity increases with increasing temperature. However, phonons are lattice vibrations; they are displacements of atoms off of the lattice site. There is no phonon in the empty space between lattice sites, and, therefore, the mean free path cannot shrink to less than the interatomic spacing, a, in the crystal. This implies that there is a minimum mean free path in phonon-dominated metallic transport and, therefore, a maximum resistivity due to electron-phonon scattering. As electron-phonon scattering dominates the transport properties at high temperatures for normal metals, the resistivity as a whole will tend to saturate and no longer increase. The Mott-Ioffe-Regel limit occurs when this happens.

The Mott-Ioffe-Regel limit is due to electron-phonon coupling because phonons are the dominant scatterers at high temperature. Although several models have been proposed historically to explain why phonons lead to a restriction on $k_F \ell \sim 1$, phonons couple

to the hopping matrix elements that describe electron transport [107]. The phonons are atomic displacements to an otherwise periodic crystal lattice, and therefore effectively add to disorder in the system at high temperatures. Increased lattice vibrations in this model cause the electronic states to have less well defined wave vectors and the current depends less on individual states and more on the average [107]. Here, rather than the k_F being a good quantum number to describe the electronic states, the states mix together due to interactions with the phonons. The resistivity, then, is no longer described by the Bloch-Grüneisen theory mentioned above, but is more linear: $\rho \sim A\frac{d}{n}$ where d is the interatomic spacing and n is the orbital degeneracy [107]. This leads to an apparent mean free path of $\ell \sim cn^{1/3}d$. Scattering then tends to occur on this length scale and the apparent mean free path in this picture is then related to the nearest neighbor distance, $\ell \sim d$, the Ioffe-Regel condition.

The Mott-Ioffe-Regel limit (Figure 7.2) occurs in a wide variety of materials, indeed in the vast majority of metals. This is due to phonons being present in every solid material and their general dominance in high-temperature transport. For a 3D system with a spherical Fermi surface, the MIR limit is given [108] by $\rho = \frac{3\pi^2\hbar}{e^2k_F^2\ell}$. For a 2D system, which is more appropriate for the cuprates and pnictides, a cylindrical Fermi surface gives a MIR limit of $\rho = \frac{2\pi\hbar c}{e^2k_F\ell}$ where c is the inter-planar spacing [108]. Typically, metals have a MIR limit around $100 - 1000$ $\mu\Omega$·cm; this behavior has been observed in many ordinary metals [109].

It is worth noting that the Ioffe-Regel criterion, $\ell < a$, affects resistivity dominated by charge carriers scattering off of bosonic excitations. Generally this is electron-phonon scattering; however, bosonic magnetic scatterers, like electron-magnon scattering
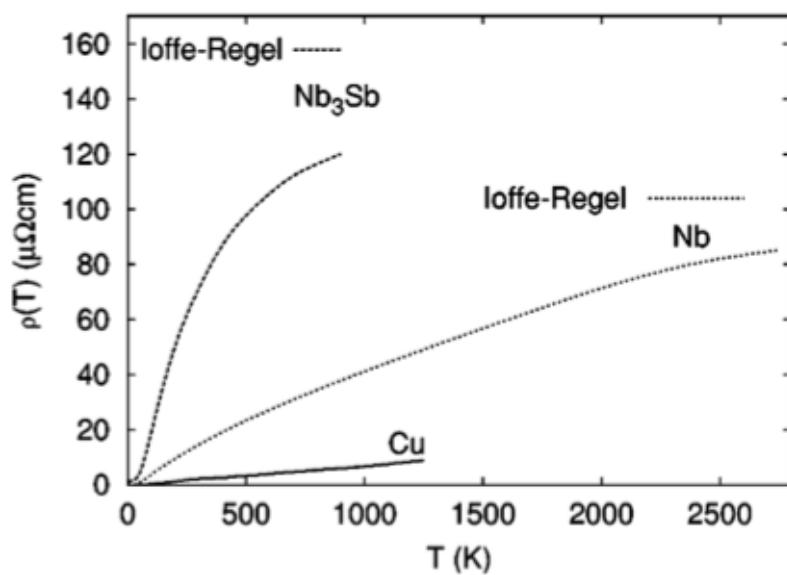
Figure 7.2: The Mott-Ioffe-Regel limit in several metals [108]. Most metals Mott-Ioffe-Regel limit and saturate by around a few hundred $\mu\Omega$·cm.

in $\gamma-\mathrm{Fe}_{80-x}\mathrm{Ni}_x\mathrm{Co}_{20}$, can also show Ioffe-Regel resistive saturation [110]. Any electron-boson scattering will produce a MIR saturation; however, scattering from other processes that do not depend on boson excitations will not MIR limit if the scatterers do not depend on the lattice spacing, such as electron-electron interactions in highly correlated systems [109].

These Mott-Ioffe-Regel limit violating materials are typically highly correlated systems as the electrons are scattering off of something that is stronger than electron-phonon interactions at high temperatures. The cuprate family of superconductors is a well known example of Mott-Ioffe-Regel limit violation. These materials are, indeed, highly correlated doped Mott insulators (Figure 7.3). The strong Coulomb interactions in $\mathrm{La}_{2-x}\mathrm{Sr}_x\mathrm{CuO}_4$ (LSCO) allow the t-J model to predict resistive saturation well above the MIR limit due to scattering caused by electronic interactions [108]. Experimentally, MIR limit violation is known to occur in the high-T_c cuprates like LSCO [111, 112] and $\mathrm{YBa}_2\mathrm{Cu}_3\mathrm{O}_7$ (YBCO) [113, 114].

The high-temperature ferropnictide superconductors are believed to be correlated systems, although more weakly correlated than in the cuprates. Because MIR limit violating behavior is typical in strongly correlated systems, high-temperature resistivity measurements are important for understanding the charge carrier dynamics in the ferropnictides.
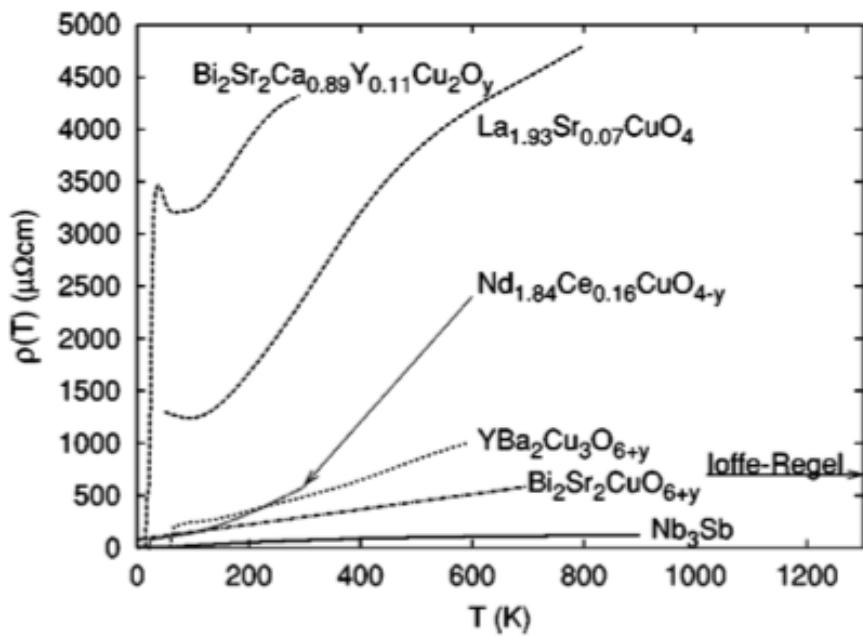
Figure 7.3: The Mott-Ioffe-Regel limit is violated in the cuprate superconductors [108]. The cuprates should have a Mott-Ioffe-Regel limit at around several hundred $\mu\Omega{\cdot}$cm, yet resistance increases well beyond that range.

7.3   SrFe$_2$As$_2$ Background

Pnictides are compounds that contain elements from the nitrogen column of the periodic table (and chalcogenides are compounds that contain elements from the oxygen column of the periodic table). Superconductivity in several iron based pnictide and chalcogenide compounds has been recently discovered (since 2008). Since then, superconducting transition temperatures in this family have reached up to 55 K. The common building block in this family is planes of iron and arsenic atoms (Figure 7.4), although significant modifications can be made to this basic form, for example by substituting arsenic for another pnictide or a chalcogenide. Between these planes there are (often) some other element or elements and the system can be doped by atomic substitution on most lattice sites.
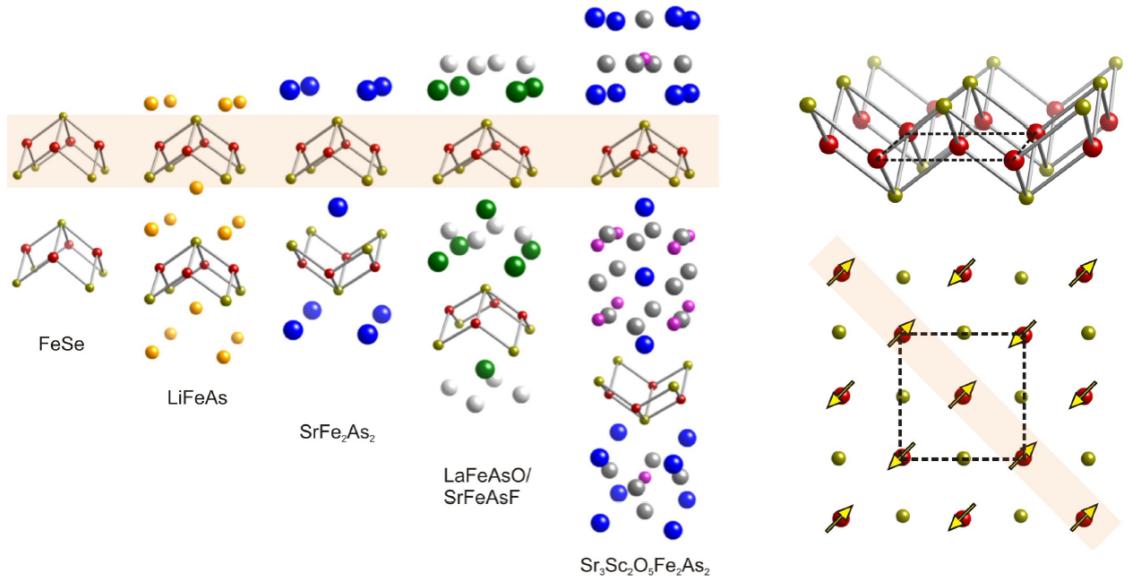
Figure 7.4: The crystal structures of the pnictide superconductors [115]. Iron-arsenide planes (and some modifications thereof) form the common element between the systems. Here we restrict our discussion to the SrFe$_2$As$_2$ system.

SrFe$_2$As$_2$ belongs to the 122 family of ferropnictide superconductors. It is metallic with a spin density wave ground state. Doping suppresses this antiferromagnetism and induces superconductivity. This doping can be accomplished by a wide range of elements on all lattice sites; here we focus on cobalt and nickel doping. Substitution of some fraction of iron for either element produces a superconductor.

The pnictide family of superconductors can be compared to the cuprate family. The phase diagrams for the pnictides (Figure 7.5) and the cuprates (Figure 7.6) seem to have quite similar structure. It is tempting, therefore, to suspect that the pnictides also possess other cuprate properties.
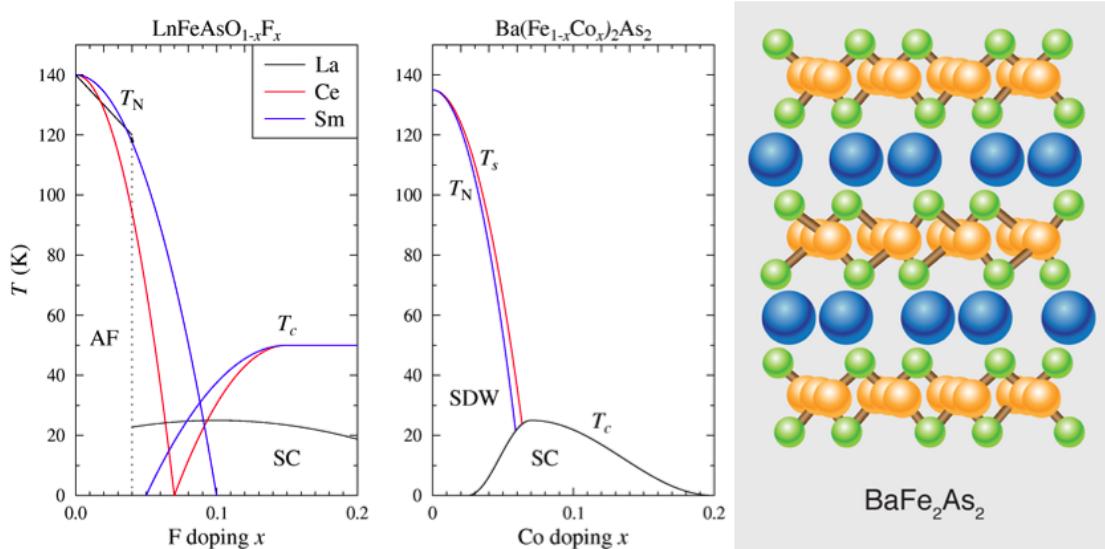
Figure 7.5: Pnictide phase diagram and unit cell [116, 117].

It is also useful to point out another way that the pnitides are similar to the cuprates: both are quasi-2D materials. The 2D nature of the cuprates can be seen not only in the crystal structure, but also in the Fermi surface (Figure 2.9). The pnictides are similar in
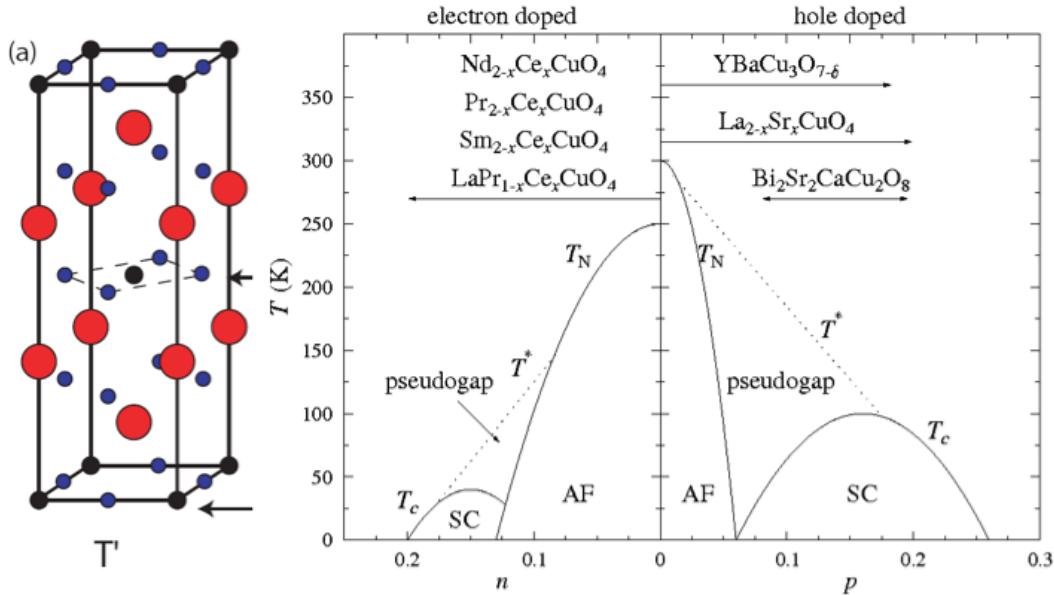
Figure 7.6: Cuprate unit cell and phase diagram [38, 116].

that they also have quasi-2D Fermi surfaces (Figure 7.7), although the pnictides are not as 2D as the cuprates. However, as the Mott-Ioffe-Regel limit depends upon the size and shape of the Fermi surface, the quasi-2D nature of the pnictide FS is interesting.

This comparison between high-T_c superconductor families is perhaps more sugges- tive that actual. In the cuprates, the strong Coulomb interactions that are present account for many of this family's unusual properties. The pnictides, unlike the cuprates, are not Mott insulators; they are metals. Therefore, it is not correct to assume that the pnictides and cuprates are analogues. In the many cuprates, strong Coulomb interactions can be seen in the fact that the cuprates violate the Mott-Ioffe-Regel limit. Here, the electron- doped cuprates $Nd_{2-x}Ce_xCuO_{4\pm\delta}$ and $Pr_{2-x}Ce_xCuO_{4\pm\delta}$ are observed to behave similarly. Saturating behavior is observed in the Sr-122 pnictides, suggesting much weaker elec- tronic correlations in that system than in the cuprates. This resistivity saturation around
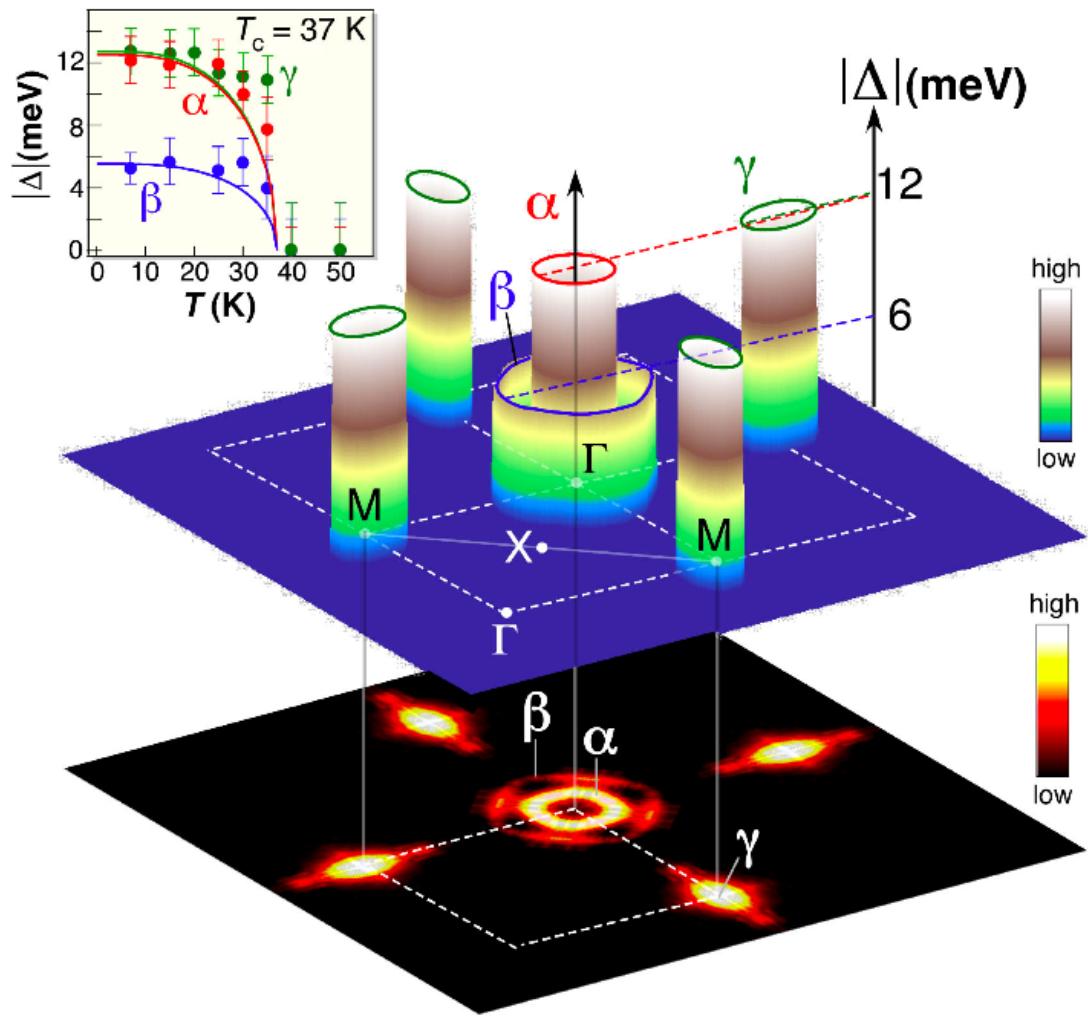
Figure 7.7: Pnictide Fermi surface [118]. The pnictides are quasi-2D materials with cylindrical Fermi surfaces.

the MIR limit in the $SrFe_2As_2$ (Sr-122) system contrasts with a MIR limit violation that is seen in the electron-doped cuprates. These results qualitatively support the picture of modest correlation strength in the ferropnictides. In addition, it is supportive of a recent prediction that pnictide transport can be explained in terms of magnetic interband coupling [119].

7.4 Experimental Detail

Resistivity was measured at elevated temperatures for cuprate and pnictide samples. The experimental methods used in this experiment required some work beyond the standard resistivity measurements of Chapter 3. Construction of a specialized experimental apparatus was necessary. Electrical continuity and signal noise reduction also needed to be addressed. These details of the experimental apparatus and contacts are briefly discussed prior to the experimental results.

7.4.1 Experimental Apparatus

In order to measure PCCO and Sr-122s at high temperatures it was necessary to design a system that could reach those temperatures without destroying the films and crystals. This required both a heater and the ability to control the atmosphere. Sr-122s will be oxidized at high temperatures and destroyed if oxygen is present. The cuprates will be annealed if the oxygen concentration is too high or too low.

A chamber used for pulsed laser deposition was modified for this purpose. The pulsed laser deposition process already requires high temperatures and a controlled at-

mosphere. By pumping the chamber down to vacuum and slowly leaking either argon or oxygen gas into the chamber, the films could be maintained in the necessary atmosphere. For the cuprates, the flow rate of oxygen had to be regulated in order to neither add nor remove oxygen from the crystal lattice. The pnictides only needed an inert atmosphere; a low pressure of flowing argon was used to exclude oxygen.

The temperature was controlled using the pulsed laser deposition heater and thermometer. These were controlled by a Neocera temperature controller. The heater is a resistive heater and the thermometer is a calibrated thermocouple. Additional wires were attached to the thermocouple so that the temperature could also be read by a GPIB-enabled voltmeter. This simplified computer logging of temperature data.

The resistance was measured as a standard four-wire measurement and was accomplished by modifying a low temperature dip-probe resistivity setup. Two major modifications were necessary to the system. First, the vacuum chamber required a feed-through for the wires. This was accomplished by modifying a spare heater flange and using the heater and thermometer feed-throughs to carry measurement wires across the vacuum chamber wall. Inside the pulsed laser deposition chamber, 50 μm diameter gold wires were soldered to the film or crystal and then mechanically secured to the chamber wall taking care to keep the wires away from the heater as much as possible to avoid melting insulation.

Second, the electronics needed to be modified in order to make good measurements. The high temperatures of the measurement produced a lot of thermal noise compared to low temperature ones and the feed-throughs required several wire-wire solder points that added to the resistance of the measurement leads. These were combated by switching

the measurement from DC to AC. The low temperature resistivity dip-probe uses a DC measurement setup: a current source produces a known, fixed current and a voltmeter measures it. With the high temperature setup, this produced excessively noisy data. High temperature measurements were performed with a Princeton Applied Research 5210 digital lock-in. The lock-in both produced the reference voltage and measured the signal voltage. The reference voltage was first passed through a large resistor (large compared to the sample resistance) in order to function as a current source.

Data were collected by a LabView VI written to sample the lock-in output and the voltmeter measurement of temperature. The state of the pulsed laser deposition chamber was controlled using techniques standard to pulsed laser deposition. For example, thermal control and ramping were provided by the Neocera temperature controller and gas flow was regulated by a needle valve between the argon or oxygen bottle and the pulsed laser deposition chamber.

7.4.2   Contacts

While contacts are always an important issue in transport measurements, at elevated temperatures, they become especially critical. This is due, primarily, to the failure of standard low temperature techniques and requires that extra care be taken in order to achieve the desired results. In both high and low temperature applications there are two types of contacts that must be considered. Electrically conducting contacts are used for the actual transport measurements and connect the sample to the wires used to probe the system. Thermally conducting contact also has to be made between the sample and the

heater or cold head in order to maintain good temperature control. This contact generally has to be electrically insulating in order to avoid shorting out the measurement through the temperature control setup. These two types of contacts must be made for either low or high temperature measurements.

While good thermal contact can be a significant experimental issue for low temperature measurements, in the PPMS, good thermal contact at low temperatures is often fairly straightforward. Samples are mounted on a PPMS puck with a dab of vacuum grease. The grease is electrically insulating and pressing the sample into the grease provides a good degree of thermal contact between the sample puck and the film or crystal to be measured. Above several hundred degrees centigrade, however, the grease does not survive. Charred vacuum grease is no longer sticky and allows the crystals or films to fall off of the heater.

In order to measure resistivity, wires must be connected to the sample. The most common technique is to solder gold wires to the film or crystal with indium solder. Indium solder is generally preferred over lead-tin eutectic solders due to its low melting temperature. Here, however, this feature is a liability. In order to measure resistivity up to 1100 K, the contacts cannot melt below this temperature. Therefore, neither indium nor lead-tin solder can be used in this application.

In the pulsed laser deposition process, silver paint is used to affix the substrate to the heater. Silver paint hardens at elevated temperatures and provides good thermal contact. This technique is appropriate for attaching films to the heater by silver painting the back of the substrate; the substrate itself is an insulator and isolates the film from the electrically conductive silver paint. Silver paint cannot, however, be used to thermally contact crystals to the heater as it will short out the crystal electrically.

Electrical contacts that will withstand elevated temperatures can, however, be created with silver paint. The silver paint must be allowed to dry well prior to measurements as it has but little mechanical strength and can easily be broken. It does, however, maintain itself at high temperatures and thus allows electrical contacts to be made that can survive up to 1100 K. Gold wires, typically used for low temperature measurement contact leads, were found to be adequate at high temperatures as well and were used to make leads to the samples.

The thermal contact between the crystals and the heater turned out to be best achieved by using GE varnish. At high temperatures the varnish hardens into a black resin that is difficult to remove. At lower temperatures GE varnish is frequently used to add insulation to bare wires that might accidentally touch. For small and/or delicate crystals, the crystal can be GE varnished to a bare film substrate that is subsequently affixed to the heater with silver paint. This can be more convenient as silver paint is easier to control than GE varnish and most of the more difficult sample mounting can then be done under microscope.

7.5   Experimental Details

High temperature resistivity measurements were performed on the electron-doped cuprates, $Nd_{2-x}Ce_xCuO_{4-\delta}$ (NCCO) and $Pr_{2-x}Ce_xCuO_{4-\delta}$ (PCCO), as well as on Ni and Co doped $SrFe_2As_2$. NCCO single crystals were prepared by self-flux with a typical size of 0.5 mm $\times$ 0.5 mm $\times$ 0.03 mm as described elsewhere [120]. Crystals were then reduced in a low oxygen anneal to achieve superconductivity. PCCO thin films were

grown by pulsed laser deposition (PLD) using a LambdaPhysik KrF excimer laser on 5 mm $\times$ 10 mm STO substrates as described in Chapter 3. The films were grown to a nominal thickness of 300 nm and were vacuum annealed to maximize superconductivity. Single crystals of $SrFe_{2-x}(Ni,Co)_xAs_2$ were prepared by self-flux, as described by Saha et al. [121], with a typical dimension of 2 mm $\times$ 0.5 mm $\times$ 0.1 mm.

Low temperature measurements were performed before and after the high temperature measurements to be certain that the crystals and films of both types of materials were not damaged by thermal cycling up to 800 K. Neither cuprates nor pnictides decompose at these high temperatures provided that they are maintained in an inert environment. When such damage did occur due to non-inert atmosphere contaminants, it would manifest itself in significant hysteresis between the up and down temperature sweeps. These incidents are obvious and also result in visual decomposition of the crystals, for example, color change. Any damage due to thermal cycling in properly maintained atmospheres was minimal and did not affect our measurements because the resistivity did not change when sweeping up and down in temperature.

For $Pr_{2-x}Ce_xCuO_{4\pm\delta}$ elevated temperatures suggest annealing, which changes the sample properties. At 500 C, these measurements are in the regime where PCCO is being annealed; however, this is the lower end of that range and annealing is consequently quite slow and a small amount of oxygen, roughly controlled, maintains the films. Sweeping down in temperature immediately after reaching the maximum temperature minimized the time spent at high temperatures and did not significantly over-anneal the PCCO films. Cuprate measurements, at higher temperatures, however, do require a controlled oxygen atmosphere to maintain proper oxygen stoichiometry.

The samples were contacted to gold wires by electrically conductive silver paint that maintained its bonding at high temperatures as described above and were heated by a Neocera substrate heater designed for pulsed laser deposition of films. The sample and heater were enclosed in a vacuum chamber and the atmosphere was maintained between 8 and 10 Torr of flowing argon to minimize the possibility of oxidation. The crystal geometry allowed a four-probe resistivity measurement; a 100 Hz, 1 mA current was applied and was measured by a Princeton Applied Research 5210 lock-in amplifier. Phase data were also collected on the high temperature measurements as a way to monitor the system. Jumps in phase signaled problems in the measurement like contacts breaking. For problem-free measurements, the phase was stable to less than a degree. Measurements below 300 K were performed in a Quantum Design PPMS.

The PPMS can measure up to 400 K. On some of the samples this was done to ensure good matching of data between the PPMS and the high temperature experimental setup. With the data sets overlapping across a 100 K temperature range, the two systems had to be well calibrated against each other.

7.6   Results

As shown in Figure 7.8, the ab-plane resistivity of optimally doped PCCO and NCCO violates the MIR limit with T^2 behavior up to 700 K and linear behavior at higher temperatures [122]. This trend is consistent with previous work on NCCO which showed resistivity increasing up to 600 K [67]. The MIR limit in these materials should be around 700 $\mu\Omega$·cm, similar to LSCO [108]. Optimally-doped NCCO can be fit reasonably well
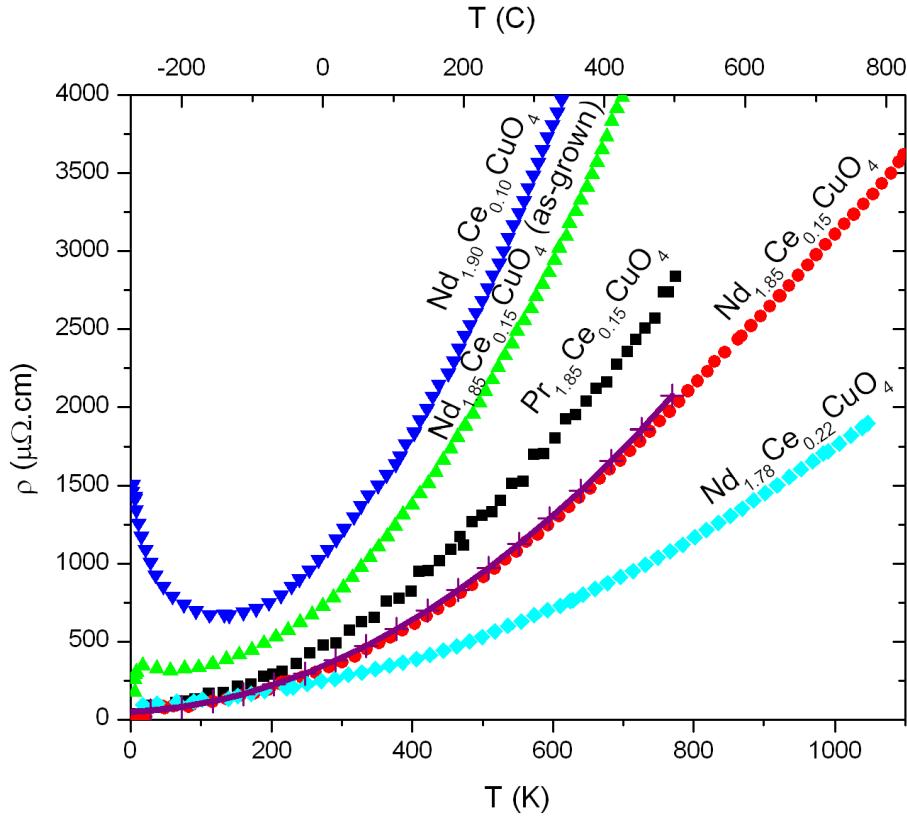
Figure 7.8: The ab-plane resistivity versus temperature of optimally doped ($x = .15$) and annealed $Pr_{2-x}Ce_xCuO_{4\pm\delta}$ films (■) and $Nd_{2-x}Ce_xCuO_{4\pm\delta}$ crystals [123]: optimally doped ($x = .15$) and annealed (●), optimally doped ($x = .15$) as-grown (unannealed) (▲), underdoped $x = .10$ (▼), and overdoped $x = .22$ (◆) [124]. Optimal crystals are fit to T^2 above T_c and below 700 K (+). The MIR limit in these materials is around 700 $\mu\Omega\cdot$cm.

to $\rho = \rho_0 + AT^2$ between T_c and 700 K; above 700 K resistivity is linear in T with a slope of ~ 5 $\mu\Omega\cdot$cm/K. The meaning of this T^2 behavior is not understood; at low temperatures T^2 dependence is often electron-electron scattering, but 700 K is much too hot to expect electron-electron scattering.

The ab-plane resistivity of some 122 Fe-pnictides up to 800 K is shown in Figure 7.9. The $SrFe_2As_2$ parent compound and x(Ni) = 0.14, x(Ni) = 0.18, and x(Co) =
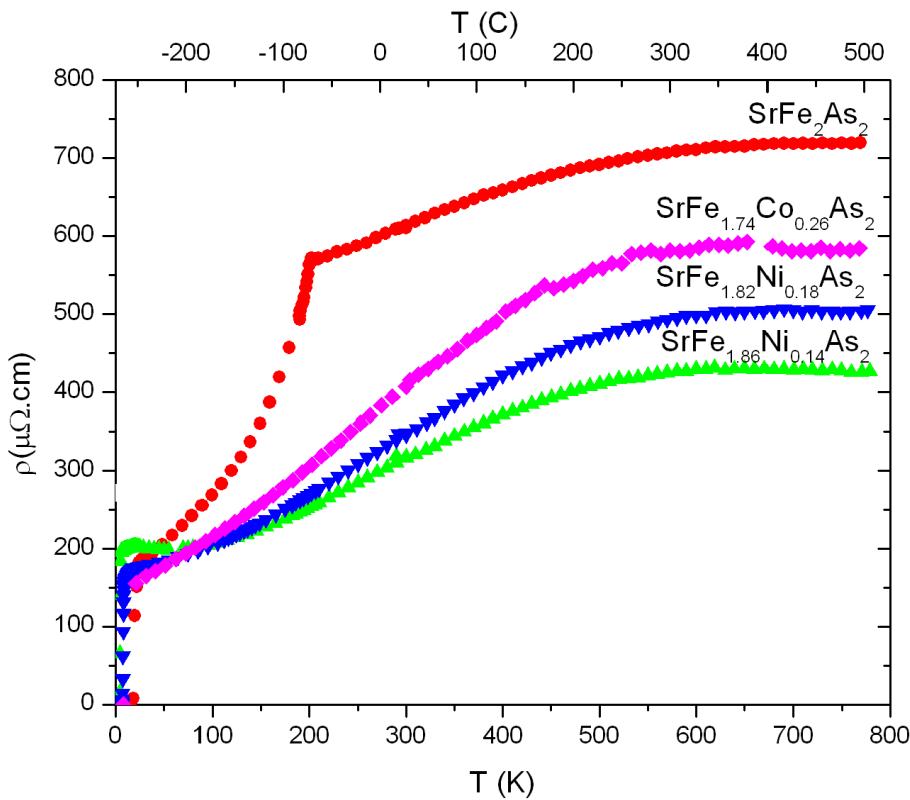
Figure 7.9: The ab-plane resistivity vs temperature, $\rho(T)$, up to 800 K for SrFe$_2$As$_2$ (●), SrFe$_{1.86}$Ni$_{0.14}$As$_2$ (▲), SrFe$_{1.82}$Ni$_{0.18}$As$_2$ (▼), and SrFe$_{1.74}$Co$_{0.26}$As$_2$ (◆) single crystals [124]. The resistivity saturates around $400 - 700$ $\mu\Omega$·cm; the MIR limit is around 600 $\mu\Omega$·cm.

0.26 dopings are shown. The two nickel dopings are under-doped and over-doped samples; the cobalt doping is near optimal. The resistivity increases smoothly above the SDW transition or T_c and saturates at high temperatures. Above 650 K the resistivity maintains a constant value of between 400 and 700 $\mu\Omega$·cm depending on doping.

7.7 Discussion

In the electron-doped cuprates, the MIR limit is strongly violated with $\rho \propto T^2$ up to 700 K as shown in Figure 7.8. A $\rho \propto T^2$ above T_c and up to ~ 250 K has been known for many years but its exact origin is not known [21]. For typical Fermi liquid metals, a resistivity proportional to T^2 usually comes from electron-electron scattering, but this is not expected to be observed above ~ 20 K. At higher temperatures electron-phonon scattering, or electron scattering off of other bosons, usually dominates the resistivity. At high temperatures ($T > \Theta_D$) T-linear behavior from electron-phonon scattering usually dominates. This picture, however, assumes a lack of strong correlations and would predict MIR limit saturation. The lack of resistivity saturation rules out dominant phonon scattering for the electron-doped cuprates.

In many strongly correlated metallic systems, the MIR limit has been shown to be violated, as in, $La_{1-x}Sr_xMnO_3$ [109, 112], Li_2VO_4 [109, 125], $Sr_{n+1}Ru_nO_{3n+1}$ [126], and the hole-doped cuprate high temperature superconductors (Figure 7.3). For example, neither $YBa_2Cu_3O_7$ nor $La_{2-x}Sr_xCuO_4$ show resistivity saturation up to 1100 K and LSCO still shows resistivity increasing linearly at those temperatures, well beyond the Ioffe-Regel resistivity [127]. Additionally, in many cuprates, the Ioffe-Regel criterion is violated below room temperature due to their high resistivity. The Ioffe-Regel condition assumes noninteracting electrons, so the electron-doped cuprates' lack of $\rho(T)$ saturation suggests strongly correlated behavior consistent with hole-doped high-T_c cuprates.

In the cuprates, the t-J model has been used to explain the normal state behavior in terms of strongly correlated electrons in doped antiferromagnets [128]. MIR limit

violation consistent with this picture has been reported in LSCO at similar temperatures [108]. Derived from the Hubbard model, the t-J model describes a system of strongly correlated electrons with antiferromagnetic interactions associated with a Mott-Hubbard insulator state at zero doping [128]. This model has been used to analyze LSCO where the MIR limit is violated but resistivity still saturates, although at a higher resistance, $\rho_{sat} \approx \frac{0.07c}{x(1-x)}$ mΩ·cm where c is the inter-CuO$_2$-plane spacing and x is the doping [108, 129]. Unfortunately, for PCCO and NCCO the saturation value in this model is around 3500 $\mu\Omega$·cm and 1100 K is not high enough to test this model. It would be instructive to look for saturating behavior up to 1300 K; however, it is doubtful that this could be done without complications due to oxygen loss and the crystal melting. In summary, strong correlations seem to dominate the PCCO and NCCO ab-plane charge transport because of the MIR limit violation.

In contrast to the cuprates, the Sr-122 pnictides do show resistivity saturation at high temperatures. This superficially resembles the picture expected for electron-phonon scattering in typical metals, which would suggest weak correlations in the ferropnictides. It has been suggested that the Fermi-liquid picture can explain the pnictide transport behavior [130]. However, there have been observations of non-Fermi-liquid [131] and quantum critical [132] behavior in the pnictides. Additionally, high temperature resistivity saturation has been proposed by Prelovšek and Sega as a signature of a two-band model with spin fluctuation coupling [119]. In this model, electron and hole bands are coupled by strong spin fluctuations that give rise to the transport properties.

A MIR limit often does suggest a typical band metal picture. If that picture holds, the electron-phonon coupling constant should be a meaningful quantity. The roughly

linear $\rho(T)$ from ~ 200 K to ~ 400 K has a slope of $0.5 - 0.9$ $\mu\Omega$·cm/K, about a tenth

that of NCCO, and suggests correspondingly weaker electron-phonon scattering. From

transport data, this value can be calculated [100] by $\lambda_{tr} = \frac{\hbar\omega_p^2}{8\pi^2 k_B}\frac{d\rho}{dT}$. For $SrFe_2As_2$, the

plasma frequency has been measured [133] to be $\omega_p = 1.4 \times 10^4$ cm^{-1}. This gives

a $\lambda_{tr} \sim 0.12$ for $SrFe_2As_2$. This is too small to reproduce the T_c of the 122s. This

mismatch between the electron-phonon coupling constant λ and the expected T_c is similar

to calculations done on several 1111 pnictides where $\lambda \sim 0.17 - 0.21$ predict a T_c of a

few Kelvin at most [134]. A $\lambda_{tr} \sim 0.12$ is also much smaller than the $\lambda_{tr} = 1.53$ reported

for PrFeAsO [100].

A stronger indication of charge carrier coupling to phonon excitations is the ob-

servation of a MIR limit. Depending upon the size, shape, and dimensionality of the

Fermi surface, the Mott-Ioffe-Regel limit can take on many different values. Quasi-two-

dimensional, the Fermi surface of the 122s is better approximated as a cylinder than as a

more 3D shape (Figure 7.7). With $k_F\ell \approx 1$, the MIR limit condition gives several hun-

dred $\mu\Omega$·cm as a reasonable estimate for the MIR limit in a quasi-2D system such as the

Sr-122s.

$SrFe_2As_2$ has a c-axis lattice parameter of 12.32 Å [121]. If it is assumed to be a

2D system, a cylindrical Fermi surface gives a MIR limit of $\rho = \frac{2\pi\hbar c}{e^2 k_F\ell}$ where c is the

inter-planar spacing [108]. Taking half the c-axis lattice parameter value as the inter-

planer spacing and $\ell \approx a$ gives a MIR limit of $\rho_{2D}^{MIR} = 634$ $\mu\Omega$.cm. If a spherical Fermi

surface is assumed instead, the MIR limit is given by $\rho = \frac{3\pi^2\hbar}{e^2 k_F^2\ell}$. With $k_F = \left(\frac{3\pi^2 N}{V}\right)^{1/3}$,

$\rho_{3D}^{MIR} = 2560$ $\mu\Omega$.cm. A spherical Fermi surface is clearly a poorer approximation than

cylindrical for the 122s but indicates that a cylindrical FS underestimates the MIR limit.

It should be noted that the value of the MIR limit can vary significantly depending upon MIR criteria used; $k_F \ell \sim 1$, $\ell \sim a$, and $k_F \ell \sim 2\pi$ are all used in the literature. Taking the 2D estimate as a lower bound on the Sr-122's MIR limit, saturation is expected by around 650 $\mu\Omega$·cm or so in order to not rule out electron-phonon coupling. The measured resistivity saturation is $400 - 700$ $\mu\Omega$·cm.

Although any calculation of the MIR limit is somewhat approximate, the Sr-122s saturate near the expected MIR limit for that system of ~ 650 $\mu\Omega$·cm. Electron-phonon scattering, therefore, could explain the value of the resistivity saturation in the 122s and would suggest that electron correlations do not play an important role in the scattering for transport.

Recently, however, a model has been proposed by Prelovšek and Sega where strong spin fluctuations couple the electron and hole bands in the system and produce a saturating $\rho(T)$ (Figure 7.10) [119]. In this model, the magnitude of the resistivity is primarily tuned by the spin-fermion coupling constant, g_0. A g_0 of order unity corresponds to ρ saturating at around $1000 - 1500$ $\mu\Omega$·cm; this compares to our measured value of $\approx 400 - 700$ $\mu\Omega$·cm. The measured resistivity saturation is a factor of $\approx 2 - 4$ less than predicted by the model; this implies a larger spin-fermion coupling, $g_0 \gg 1$, and the possible breakdown of the model [119]. This model, however, is only a two-band model where the 122 system is known to be more complicated; therefore, some discrepancy in magnitude cannot rule out relatively strong spin-fermion coupling in the 122s. As the pnictides are known to show spin fluctuations from neutron scattering [101, 102] and NMR [103, 104] results, coupling to spin fluctuations could produce MIR-like resistivity saturation in the pnictides.
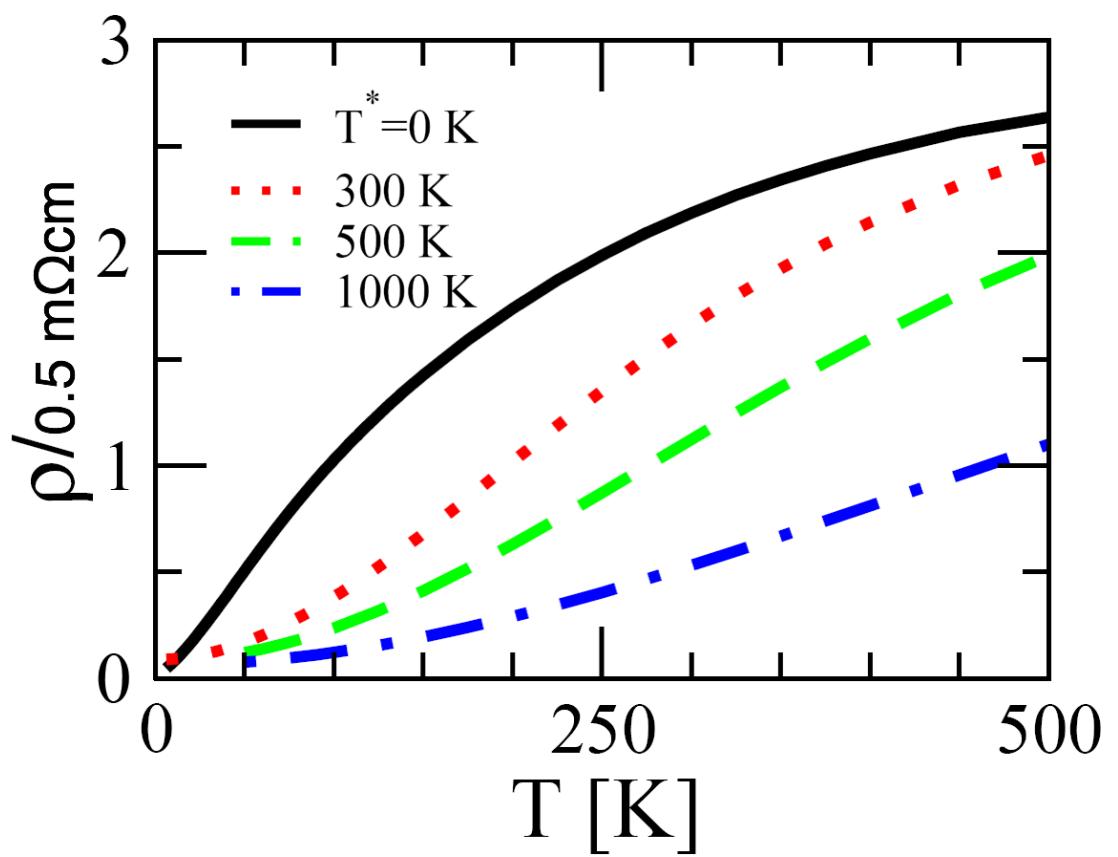
Figure 7.10: Predicted pnictide resistivity saturation due to spin fluctuations [119]. The T^*s are different Fermi liquid temperatures in the model.

Similar models predict $\rho(T)$ saturation due to two bands with unequal scattering [135]. The pnictides are known to be multi-band systems (Figure 7.7) and this may contribute significantly to their transport properties. If the two bands have different transport parameters, the more conductive band can "shunt" the less conductive band, saturating the high temperature resistance. The more conductive band, therefore, would begin to dominate transport properties and the material would appear less resistive. This is similar to the argument made in Chapter 6 to argue that cuprate superlattices have significant charge redistribution; there the more conductive layer was not observed to dominate transport, indicating a lack of distinct bands. In the case of the pnictides, Golubov et al. propose that the two bands of interest are a stronger interaction band consisting of a combination of the two electronic pockets and the inner hole pocket around the Γ-point and a weaker interaction band consisting of the remaining outer hole pocket [135]. If the first band is quite clean, with a low scattering rate, and the second band is quite dirty, with a high scattering rate, this could result in high temperature saturation of resistivity [135]. While there could still be a MIR limit in this model, it would not be the primary cause of resistivity saturation.

In similar systems to the 122s, much higher resistivity values have been reported in high temperature measurements on the 1111 oxypnictides. Large resistivities have been observed in the NdFeAsO [136] and LaFePO [137] systems and a resistivity saturation at $2500 - 3000$ $\mu\Omega$·cm has been reported in PrFeAsO crystals as evidence for a MIR limit [100]. This saturation is significantly higher than the $100 - 1000$ $\mu\Omega$·cm seen in most MIR limited materials. Low carrier concentrations can produce a large MIR limit [108] or a small spin-fermion coupling constant could produce a resistivity saturation at high

values [119].

An additional complication in interpreting the pnictide data is that resistivity saturation could also be due to the fact that the arsenides are semimetals. Semimetals can be thought of as indirect band gap semiconductors with a slightly negative band gap. As such a picture suggests, adding thermal energy, $k_B T$, to the system will activate more charge carriers at high temperatures. In the pnictides, the energy scale for this type of thermally activated behavior is $E_h = 300$ K, so semimetal behavior should describe transport above ~ 100 K [138].

The distinct behavior of semimetals is due to the fact that they have energy bands quite near the Fermi energy that can be thermally excited to participate in transport. Co- and Ni-doping may be expected to significantly influence this behavior by making the material more n-type and more metallic with respect to properties depending upon band structure. Hall effect measurements has argued that, with sufficient Co-doping, Ba-122 transport is dominated by a single charge carrier [139]. Having only a single dominate charge carrier would suppress much of the distinction between a semimetal and a metal, and might suggest differing behavior in the parent, and doped materials due to thermal excitation of charge carriers. Like the spin fluctuations model by Prelovšek and Sega that was discussed, the similarity in resistivity saturation between the undoped SrFe$_2$As$_2$ and the Co- and Ni-doped samples indicates a lack of doping dependence of the saturation mechanism, suggesting that either thermal activation of charge carriers near the Fermi energy does not change at high temperatures with doping, or that the resistivity saturation may be MIR-limited.

High temperature resistivity measurements ultimately cannot resolve this issue. For

metallic systems, MIR limited behavior is nearly universal with few exceptions. The temperature dependence of semimetals at high temperature does not have such clear expectations. The MIR limit criterion ($\ell \approx a$) would still be in effect in these systems; however, the expression of that limit may be obscured by large changes in the number of charge carriers. For example, elemental tungsten has a significant reduction in phonon frequencies at high temperatures that would substantially increase resistance in the absence of a MIR limit; the MIR limit makes this resistivity increase only moderate [108].

In semimetal systems that have been measured at high temperatures, resistivity exhibits diverse behaviors. At elevated temperatures (Figure 7.11), semimetal resistivity can, indeed, show saturation and even decrease as in the case of semimetal graphite [140] and graphene [141]. However, increase without limit is seen in semimetal CaB_6 [142]. Also, bismuth's resistivity increases with no saturation up to its melting point of 544 K [143]. Although pnictide semimetal behavior could describe the high temperature resistivity saturation seen, it is difficult to draw conclusions regarding semimetal behavior in the 122s from high temperature resistivity.

Thermal activation of charge carriers near the Fermi surface could influence the high temperature resistivity saturation in the Sr-122s. High temperature resistivity, however, is inconclusive on the ultimate mechanism for the observed saturation. The resistivity value of the saturation is suggestive of a MIR-limit; however, influences due to thermally activated behavior or spin-fluctuations cannot be ruled out with these measurements.

MIR limited behavior in a weakly coupled system, resistive saturation due to relatively strong spin-fermion coupling, or thermally activated charge carriers could explain

172
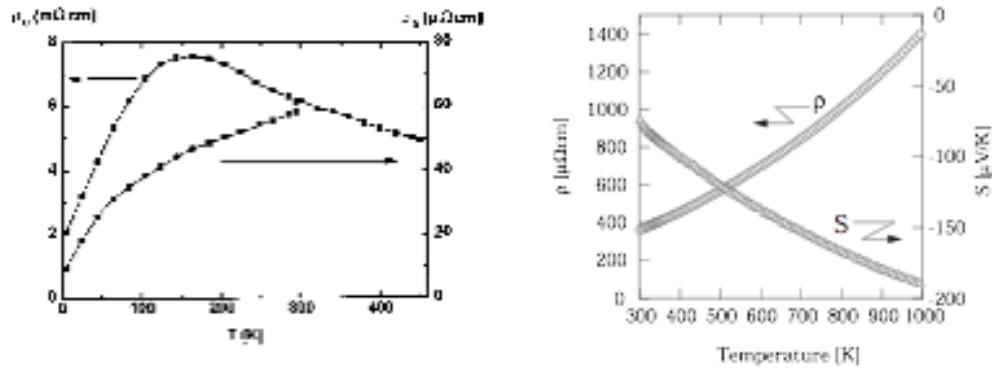
Figure 7.11: The resistance of semimetal graphite up to 450 K [140] (left) and of semimetal CaB_6 up to 1000 K [142] (right).

the high temperature resistive saturation in the Sr-122s. Saturating resistivity in the Sr-122s does rule out strong electronic correlation effects like those in the cuprates. In the Sr-122s, however, the resistivity saturation cannot by itself provide a conclusive picture of pnictide charge dynamics.

Finally, the similarity in resistivity saturation between undoped $SrFe_2As_2$ and Co- and Ni-doped samples reveals a lack of doping dependence of the saturation mechanism. If spin fluctuations are responsible, as in the model of Prelovšek and Sega or more generally as the bosonic scatterer, it may be expected that the suppression of AFM order with doping should result in a modification of this scattering and therefore a change in the resistivity saturation. Similarly, semimetal behavior is often quite sensitive to doping and may be expected to lessen with doping. However, the lack of change in the saturation temperature of $\rho(T)$ suggests that either the spin fluctuation spectrum or thermally activated behavior does not change at high temperatures with doping, or that phonon-scattering is indeed dominant at high-temperatures in the iron pnictides.

7.8   Conclusions

We measured the ab-plane resistivity of several Sr-122 superconductors and electron-doped cuprates. The electron-doped cuprates strongly violate the Mott-Ioffe-Regel limit while the 122s saturate at around $400 - 700$ $\mu\Omega{\cdot}$cm at high temperatures. Strong electronic correlations can explain the cuprate behavior; however, pnictide saturation can be explained either by electron-phonon scattering, by coupling between spin fluctuations and charge carriers, or by thermally activated charge carriers. The observed high temperature resistivity saturation in the Sr-122s supports both the picture of more weakly correlated physics in the ferropnictides than in the cuprates and recent predictions of magnetic interband coupling in the pnictides.

Chapter 8

Other Projects

8.1 Introduction

Significant time was spent on several film-growth projects that were ultimately less successful. Attempting to synthesize superconducting Pr_2CuO_4 by careful control of oxygen, the resistivity of Pr_2CuO_4 was decreased significantly and some metallic behavior ($d\rho/dT > 0$) was obtained. These results are promising, but incomplete. Additionally, attempts were made to synthesize thin film preparations of iron-based superconductors, with some preliminary success. Neither of these projects, however, were taken to completion due to competing demands of more quickly productive projects. The partial results obtained are here briefly discussed.

8.2 Superconductivity in Pr_2CuO_4?

The investigation into potentially oxygen doping Pr_2CuO_4 into a superconducting state extends the $Pr_{2-x}Ce_xCuO_{4\pm\delta}$ oxygen doping work performed in Chapter 5. As oxygen removal in $Pr_{2-x}Ce_xCuO_{4\pm\delta}$ has a similar doping effect to adding cerium, $Pr_2CuO_{4-\delta}$ might be made superconducting if introduction of disorder can be minimized during the oxygen reduction. Here, the experimental techniques attempted and some of the more promising results obtained are described in the hope that this project may be revived in

the future.

8.2.1   Introduction

The cuprate superconductors are doped Mott-like (charge-transfer) insulators (Chapter 2). This well-established picture has, however, recently been called into question, in particular, on the electron-doped side of the phase diagram. It has been proposed that, unlike the T-phase cuprates, the T'-phase cuprates are not Mott insulators. Rather, lacking apical oxygens, they are Slater insulators; their insulating behavior is due to their long range antiferromagnetism ordering [20, 144]. The apical oxygens in the T'-phase introduce significant disorder into the crystal structure; it has been proposed that they induce the copper magnetic moments which then act as Kondo (magnetic) scatterers [145]. Indeed, removing O(3) oxygens, the apical impurities, was reported to allow superconductivity to appear at lower dopings in $Pr_{2-x}Ce_xCuO_{4\pm\delta}$ [146]. If this is the case, removing apical oxygens fully would suppress antiferromagnetism, which, in turn, would allow superconductivity. This was reported to happen [52]. Increased oxygen concentration, presumably on the apical sites, does increase antiferromagnetism in $Pr_{2-x}Ce_xCuO_{4\pm\delta}$ (Chapter 5). The accepted electron-doped cuprate phase diagram has an antiferromagnetic parent compound that is then doped to induce superconductivity. It has been claimed, however, that Pr_2CuO_4 (PCO) is not a Mott insulator, but rather a 30 K superconductor [32, 52, 53, 54]. The Mott-like insulating state, therefore, is not intrinsic to the material, but is rather due to disorder.

In the T' cuprates, the charge-transfer gap is significantly smaller than in the T

phase cuprates and may even close [52]. As the main difference between the T and T' phases is the apical oxygen, O(3) oxygens (apical oxygen disorder in the T' phase) seem to increase the "Mott-like" nature of the T'-RE_2CuO_4 system. Apical oxygen can act as a scatterer, frustrating superconductivity and making a normal band metal insulating.

If oxygen plays such a sensitive role in determining the properties of the electron-doped cuprates, the amount and location of oxygen, especially O(3) oxygen, is quite important. However, oxygen content and location cannot be measured accurately in thin films and there could be impurity oxygen at the apical sites. If so, oxygen reduction might induce superconductivity by clearing apical oxygen.

Synthesis of these films was attempted at Maryland. Films were grown both by pulsed laser deposition (PLD) and metal organic deposition (MOD). However, the parameters necessary to obtain superconductivity were not found.

8.2.2 Film Growth

The reported superconducting thin films of PCO were grown either by MOD or by Molecular Beam Epitaxy (MBE). MBE is a technique for film growth similar to PLD, but with greater control over the layers of atoms being deposited. Here, films were grown by PLD, by MOD, and by PLD with PLD attempting to replicate the MBE or MOD growth.

8.2.2.1 Metal Organic Deposition

The process of growing thin films by metal organic deposition is quite different from pulsed laser deposition techniques. MOD deposition is a process in which the metallic

elements in the film are delivered in solution to the substrate. Rather than control the stoichiometry of metallic elements by PLD target synthesis, the metals are chemically bound to larger organic molecules. These organic molecules are then dissolved into a solvent in the proper ratios to maintain stoichiometry. The resulting solution is then spin-coated onto a clean substrate.

The spin-coated thin film is not, however, the correct material. The coated substrate must first be calcined by firing it at high temperatures. The heat of this step decomposes the organic molecules carrying the metallic elements, leaving an amorphous film of the constituent elements. This amorphous film is then baked at a high temperature to allow the film to crystalize in the proper structure.

To grow $Pr_{2-x}Ce_xCuO_{4\pm\delta}$ by metal organic deposition, praseodymium nitrate, cerium nitrate, and copper nitrate were used. These three compounds, $Pr(NO_3)_3 \cdot 6H_2O$, $Ce(NO_3)_3 \cdot 6H_2O$, and $Cu(NO_3)_3 \cdot 2\frac{1}{2}H_2O$, have atomic weights of 326.92 g/mol, 326.64 g/mol, and 232.59 g/mol respectively. The proper mixture was then determined by weighing, exactly as is done for oxides during pulsed laser deposition target synthesis (Chapter 3). All three nitrates are soluble in water. Sufficient water to fully dissolve the three nitrates was necessary; however, the solution will then be spin-coated onto substrates and this process is more easily done with thicker mixtures.

The spin-coating procedure is modified from the method for spin-coating photoresist onto thin films. A few drops of the MOD solution are pipetted onto a cleaned substrate which is then spun at 4000 rpm to produce a very thin film of the solution. It was found that modifying the basic solution recipe made this step easier. First, adding glycerol to the solution greatly increased its viscosity. This allowed the solution to spread out as a

thin film on the substrate by suppressing its tendency to be flung off. Second, a small amount of detergent was added to the solution. $SrTiO_3$ (STO), the substrate of choice for growing PCCO due to lattice matching, is hydrophobic. Adding detergent to the MOD solution allowed it to more easily wet STO. The addition of these extra organic molecules does not affect the final films produced as they will decompose along with the nitrates at high temperatures. However, one of the decomposition products of glycerol, acrolein, is toxic, so this step should be performed in a fume hood or properly vented pulsed laser deposition chamber under vacuum.

Once the solution is spin-coated onto the substrate it is then heated to remove the organics and to form the PCO film. A typical heating schedule (Figure 8.1) has three plateaus. The first plateau is to calcine the solution. This removes the organics and leaves only the PCO precursors. The second plateau synthesizes the compound. This temperature is determined from the PCO phase stability diagram. The third plateau is for annealing; this adjusts the oxygen content in the PCO film.
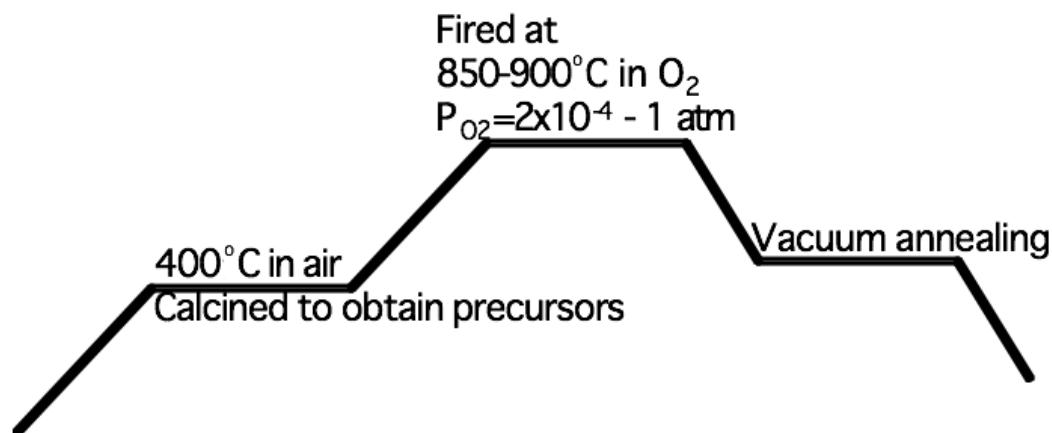
Figure 8.1: A typical heating schedule for metal organic deposition films.

The superconducting Pr_2CuO_4 films reported were calcined in air at 400 C. They were then heated to between 850 C and 900 C in an oxygen atmosphere between 2×10^{-4} atm and 1 atm (150 mTorr and 760 Torr). Annealing was the crucial step; varied time and temperature in vacuum ($P < 1 \times 10^{-7}$ atm $\approx 1 \times 10^{-4}$ Torr) produced a range of films shown in Figure 8.2.
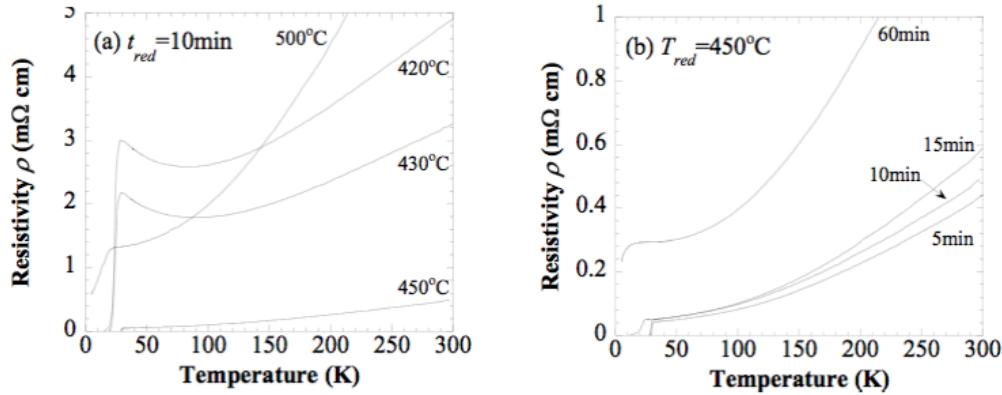
Figure 8.2: Optimization of PCO films by annealing temperature (left) and annealing time (right) [52].

A range of films were produced at Maryland (Table 8.1). All metal organic deposition films grown were highly resistive; the room temperature resistivity was a useful characterization to track progress. In general, crystalization at 850 C to 900 C was found to be too high; better results were obtained at 800 C or 750 C. Deposition in an oxygen atmosphere between 2×10^{-4} atm and 1 atm (150 mTorr and 760 Torr) was only explored in the 150 mTorr to 600 mTorr range due to chamber design limitations. The turbo pump speed is adjustable, the roughing pump is not. Therefore, to control the pressure well, pressure had to be low enough to not destroy the turbo pump. As lower pressure films seemed better, this limitation was not too severe.

180

Vacuum annealing was recommended (Figure 8.2) in the range 5 min to 60 min, with times less than 15 min preferred and in the temperature range 420 C to 500 C. For our films annealing temperatures significantly higher than this seemed to be better with 650 C seeming best. Annealing for 15 min was better than shorter anneals; longer annealing was not fully explored in favor of more promising methods.

Calcining	Crystalization	Annealing	Resistance at 300 K
10 min 400 C air	15 min 900 C in 150 mTorr O_2	5 min 450 C 3×10^{-6} Torr O_2	1 MΩ
10 min 400 C air	15 min 850 C in 150 mTorr O_2	5 min 450 C 1×10^{-5} Torr O_2	460 kΩ
10 min 400 C air	15 min 750 C in 150 mTorr O_2	5 min 450 C 9×10^{-7} Torr O_2	120 kΩ
10 min 400 C air	15 min 750 C in 600 mTorr O_2	5 min 450 C 4×10^{-6} Torr O_2	650 kΩ
10 min 400 C air	15 min 750 C in 150 mTorr O_2	15 min 450 C 6×10^{-6} Torr O_2	90 kΩ
10 min 400 C air	15 min 750 C in 150 mTorr O_2	15 min 720 C 8×10^{-7} Torr O_2	110 kΩ
10 min 400 C air	15 min 750 C in 150 mTorr O_2	15 min 650 C 8×10^{-7} Torr O_2	40 kΩ

Table 8.1: A sample of heating schedules used for Pr_2CuO_4 films grown by metal organic deposition. Room temperature resistance was used to characterize the Pr_2CuO_4 fims grown by metal organic deposition.

The most significant draw-back of the metal organic deposition procedure to pro-

duce thin films was a difficulty in forming single-phase epitaxial thin films. Like in pulsed laser deposition, epitaxy is supposed to be forced by the substrate (with good lattice matching between the film and substrate). In pulsed laser deposition, however, the film grows up off of the substrate. In metal organic deposition, all the material is present as the crystal is forming. This seems like it allows the substrate less influence over the crystallization. MOD films grown at Maryland did form in the correct phase as seen in X-ray diffraction (Figure 8.3). The resultant films were not, however, as high-quality as are grown by pulsed laser deposition. Further optimization of the MOD technique is necessary to obtain films comparable in quality to pulsed laser deposition.
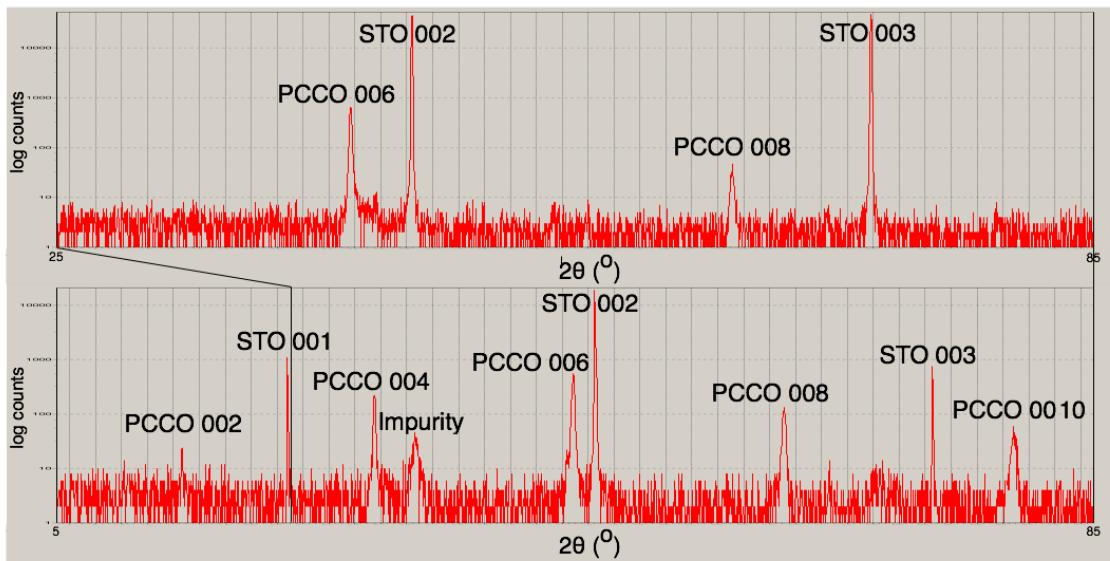
Figure 8.3: X-ray diffraction of an $x = .15$ $Pr_{2-x}Ce_xCuO_{4\pm\delta}$ thin film grown by metal organic deposition (above) and grown by normal pulsed laser deposition (below). Above: The 004 and 008 $Pr_{2-x}Ce_xCuO_{4\pm\delta}$ diffraction peaks are visible, indicating some epitaxy. 2θ is scanned from $25°$ to $85°$. Below: For high quality films grown by pulsed laser deposition, more X-ray diffraction peaks are seen. 2θ is scanned from $5°$ to $85°$.

8.2.2.2 Amorphous PLD

PLD was, however, adjusted to mirror the MOD technique. Films were grown by PLD at room temperature so that they would form an amorphous layer. After this step the films should be equivalent to MOD films after calcining and were subsequently processed like MOD films. Amorphous films had difficulty forming into the correct phase, however.

The same parameters for crystallization and annealing as used in metal organic deposition films were taken as a starting point for optimization. A range of films were produced at Maryland with this amorphous pulsed laser deposition technique (Table 8.2). While superconducting PCO films have been reported to produce a 30 K T_c when fully optimized, my films did not superconduct and were still resistive. These films were significantly improved over metal organic deposition films, however, and the most useful characterization used to track progress was the temperature at which the films became so resistive that the validity of the Quantum Design Physical Properties Measurement System resistivity measurement started to become questionable (~ 1 MΩ). A dip-probe resistivity measurement setup was available and was modified to allow reliable resistance measurements up to almost 10 MΩ; however, the additional information provided by measurement at higher resistances was rarely needed and only proved useful to distinguish PPMS measurement artifacts from actual data. The best parameters reported (Figure 8.2) were not directly transferable to our procedure here. This indicates that there are important uncontrolled parameters in the MOD growth process.

Films grown by amorphous pulsed laser deposition were significantly less resistive than metal organic deposition grown films. In addition, they tended to crystalize better.

Deposition	Crystalization	Annealing	$T(R > 1\,\mathrm{M}\Omega)$
20 min 100 C 230 mTorr N_2O	15 min 850 C in 230 mTorr N_2O	5 min 720 C 1×10^{-5} Torr	80 K
30 min 100 C 230 mTorr N_2O	15 min 733 C in 230 mTorr N_2O	5 min 720 C 3×10^{-5} Torr	40 K
30 min 100 C 230 mTorr N_2O	15 min 800 C in 230 mTorr N_2O	60 min 630 C 5×10^{-6} Torr	20 K
30 min 100 C 230 mTorr N_2O	15 min 800 C in 230 mTorr N_2O	45 min 720 C 9×10^{-6} Torr	30 K

Table 8.2: A sample of growth parameters for Pr_2CuO_4 films grown by amorphous pulsed laser deposition. For insulating films without a T_c^{onset}, the temperature where the resistivity surpassed 1 MΩ characterized films.

This suggests that calcining the metal organic deposition films may have left a residue that was harming growth; dirty substrates are known to produce poor-quality films in traditional pulsed laser deposition growths. Despite being more conductive than metal organic deposition films, in amorphous pulsed laser deposition films, one difficulty in optimizing PCO is still the large resistivity of the material. Resistivity is also a rather rough method of characterization; for an optimally doped $Pr_{2-x}Ce_xCuO_{4\pm\delta}$ film grown by normal pulsed laser deposition, films are optimized by maximizing T_c, which is a much more sensitive measure. Amorphous pulsed laser deposition films, however, show stronger X-ray diffraction peaks. It was reported that the c-axis lattice parameter can be used to optimize superconducting PCO films (Figure 8.4). A narrow window of lattice parameters around 12.19 Å gives superconductivity. Here, amorphous-PLD grown PCO films consistently have c-axis lattice parameters that are too small (Figure 8.5).
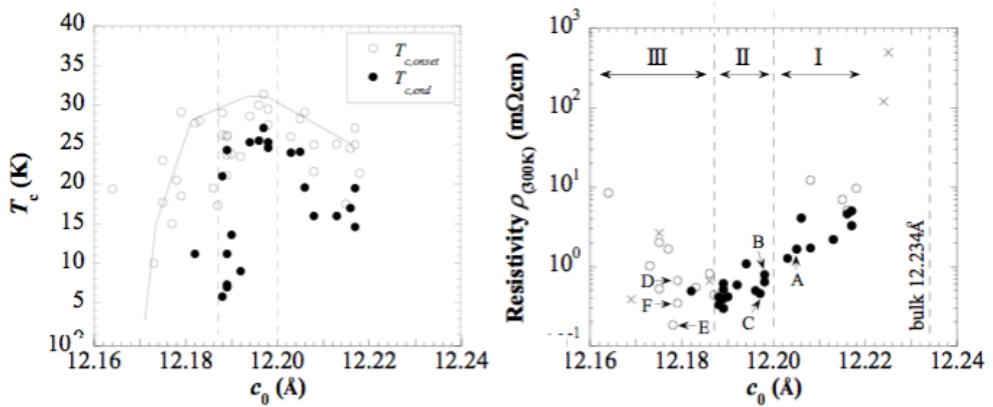
Figure 8.4: PCO film T_c and resistivity versus c-axis lattice constant [52, 147].

8.2.2.3 Pulsed Laser Deposition

Achieving superconductivity in Pr_2CuO_4 thin films should be a matter of controlling oxygen. Therefore, it should be possible to produce superconductivity in Pr_2CuO_4 via standard pulsed laser deposition processes. Films grown by the standard pulsed laser deposition procedure should have better crystallinity than metal organic deposition or amorphous-PLD films. However, as this procedure is a greater departure from that which was reported in References [32, 52, 53, 54], it's not clear that this is the best path to take.

Growing films by pulsed laser deposition should have only a few key parameters, deposition pressure, temperature, and time, and annealing pressure, temperature, and time. In order to make films that are less oxygenated, therefore, the films can either be grown in reduced oxygen or annealed more aggressively. As overly aggressive annealing can quickly degrade films, film growth in a less oxidizing atmosphere was attempted.

Focusing on deposition conditions, the extremal films are plotted in Figure 8.6. Decreasing the deposition pressure provoked a small decrease in resistivity; decreasing the
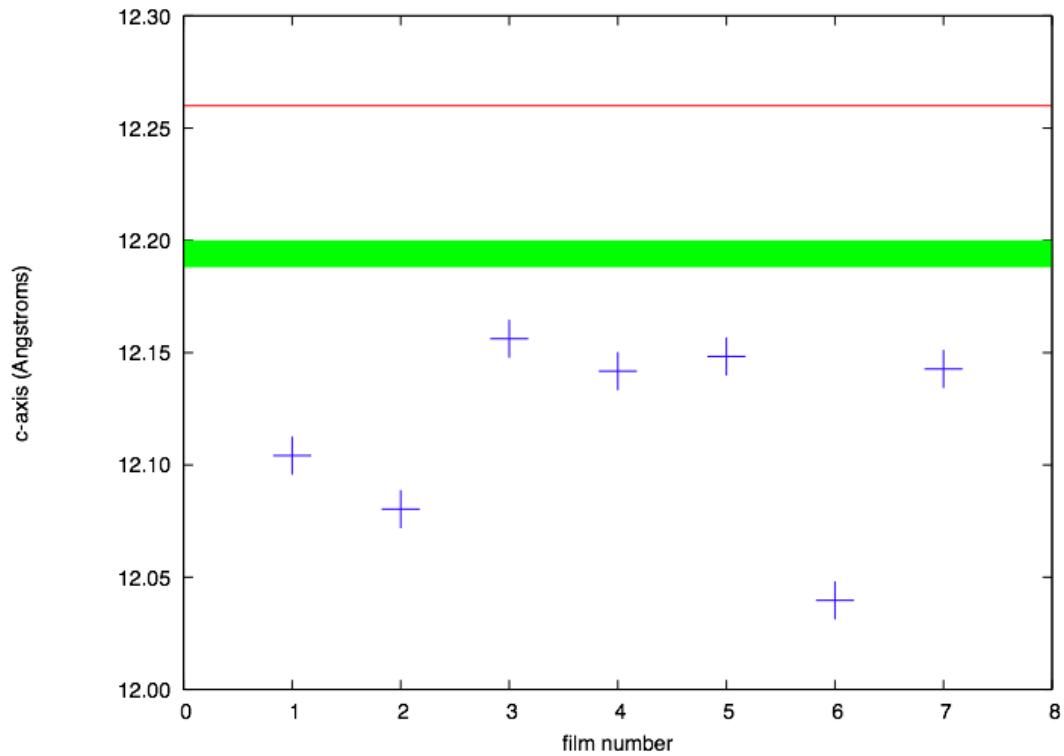
Figure 8.5: The c-axis lattice constant of several amorphous-PLD grown films. The red line represents the c-axis lattice parameter for un-annealed $x = .00$ films grown by normal PLD. The green area is the c-axis lattice parameter for maximal T_c superconducting Pr_2CuO_4 (Figure 8.4). The films (+) are ranked in order of increasing oxygen based upon the aggressiveness of the films' annealing schedules.

deposition temperature had a much larger effect. At lower deposition pressures, crystalline quality was noticeably degraded in X-ray diffraction. $Pr_{2-x}Ce_xCuO_{4\pm\delta}$ needs to be grown in some pressure oxygen. At lower deposition temperatures, the T' phase does not form. Further oxygen reduction must come from annealing.
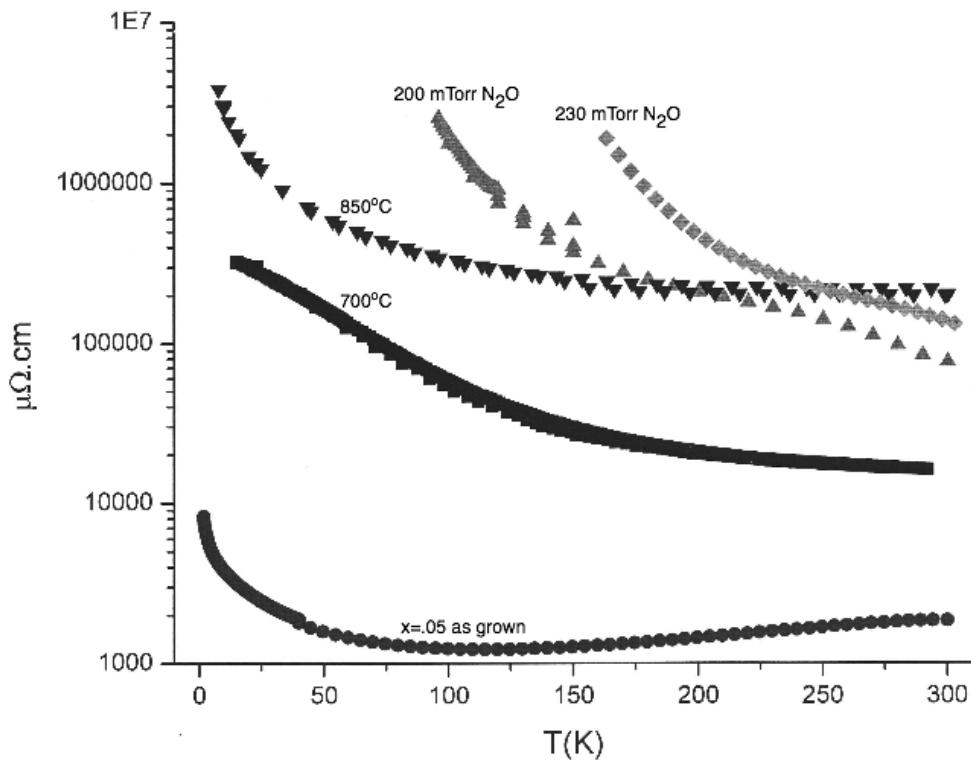
Figure 8.6: Pr_2CuO_4 thin films grown by pulsed laser deposition under various deposition conditions. Deposition temperatures were varied between 720 C (■) and 850 C (▼) with the pressure constant at 230 mTorr N_2O. Deposition pressures were varied between 200 mTorr N_2O (▲) and 230 mTorr N_2O (◆) with temperature constant at 800 C. A $x = .05$ $Pr_{2-x}Ce_xCuO_{4\pm\delta}$ film (●) is included for reference. All films were deposited for 30 min and were "as-grown" (not annealed).

With adjustment of the deposition parameters exhausted, the Pr_2CuO_4 films were then annealed under various conditions. Beginning with films deposited at 720 C, the

films were vacuum annealed at various temperatures for long times. By substantially lowering the annealing temperature from 720 C to 600 C, it was found that the films were more resistant to degradation. This allowed the films to be annealed for much longer times with a net result of greater annealing taking place. In this manner, the resistance of the Pr_2CuO_4 films was dramatically lowered by several orders of magnitude at low temperatures; resistivity measurements also suggested the beginnings of metallic behavior, $d\rho/dT > 0$ (Figure 8.7).
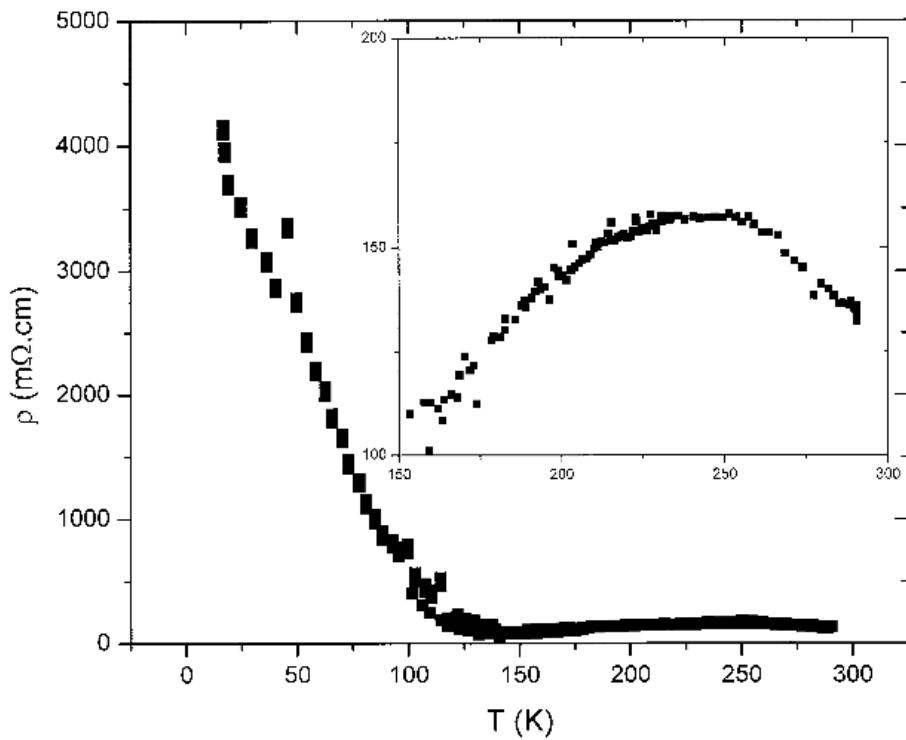
Figure 8.7: Pr_2CuO_4 vacuum annealed for 45 min. The annealed Pr_2CuO_4 film shows some metallic ($d\rho/dT > 0$) region (insert). The resistivity of the film is much less than the as-grown films (Figure 8.6).

In addition to becoming more metallic, some of the Pr_2CuO_4 films have shown

sharp low-temperature drops in resistivity consistent with partial superconductivity. However, these possible T_c^{onset} films have not been consistently reproducible and therefore are probably more indicative of uncontrolled parameters in the Pr_2CuO_4 growth/annealing process than they are indicators of anything else. The superconducting Pr_2CuO_4 films reported in the literature all had c-axis lattice parameters within a narrow range around of 12.194 Å, reduced from a bulk value of 12.234 Å [32, 52]. For my PLD-grown films, adjustment of deposition parameters and extension of annealing time did not seem to translate in any consistent ways to c-axis lattice parameters (Figure 8.8).
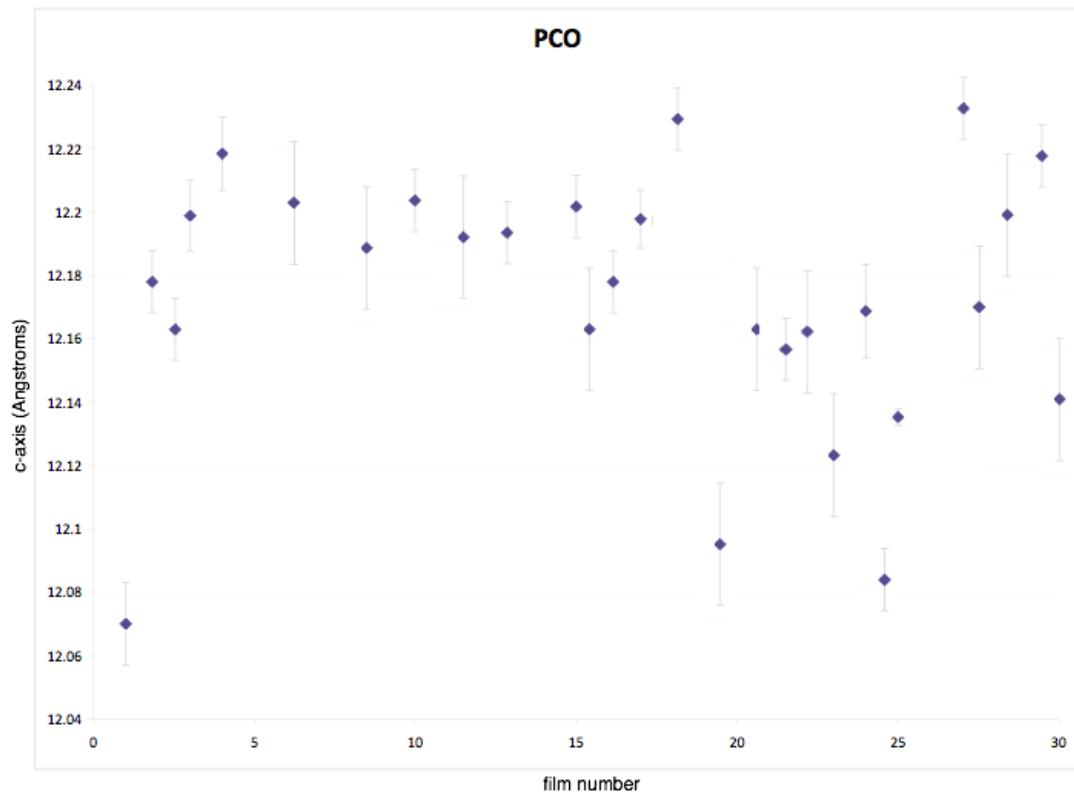
Figure 8.8: The c-axis lattice parameters of various Pr_2CuO_4 thin films grown by pulsed laser deposition. Adjustment of pulsed laser deposition parameters did not seem to consistently produce predictable c-axis lattice parameters.

8.2.3 Crystals

In addition to growing thin films of Pr_2CuO_4 for oxygen reduction, reducing parent-compound crystals was also attempted. Crystals of Pr_2CuO_4 (PCO), Nd_2CuO_4 (NCO), and Sm_2CuO_4 (SCO) were annealed. These crystals were available already synthesized. It was reported that in the parent compounds of $Pr_{2-x}Ce_xCuO_{4\pm\delta}$, $Nd_{2-x}Ce_xCuO_{4\pm\delta}$, $Sm_{2-x}Ce_xCuO_{4\pm\delta}$, $Eu_{2-x}Ce_xCuO_{4\pm\delta}$, and even $Gd_{2-x}Ce_xCuO_{4\pm\delta}$, there is superconductivity [53, 52]. It was hoped that reduction might be easier in crystals compared to films or in the NCO or SCO systems compared to PCO.

In order to anneal cuprate crystals powder and pellets of the same material and doping are required. The pellets are created identically to pulsed laser deposition targets (Chapter 3) with the exception of having a 1 cm diameter rather than a 1 inch diameter. The powder is created in this same process except it is not pressed into a pellet form but rather finely ball-milled as the final step. To anneal crystals, the crystal is sandwiched between two pellets of appropriate material and doping. This sandwich is then placed in a ceramic boat crucible and fully covered in powder. The anneal then takes place in a tube furnace under flowing argon, flowing at a rate of 1 bubble per second, for 3 days at 920 C. Additionally, a small amount of elemental titanium was placed in the furnace next to the Pr_2CuO_4, Nd_2CuO_4, or Sm_2CuO_4 to act as a getter to ensure a non-reactive atmosphere. The purpose of the pellets and powder is to slow the rate of oxygen diffusion from the crystals themselves and provide a more uniform environment.

The annealing of crystals proved to be more difficult to control than the annealing of films. One bubble per second of flowing argon does not allow the atmosphere to be as

accurately controlled as in the pulsed laser deposition chamber. Additionally, contaminate atmosphere is easily introduced into the tube furnace resulting in the crystals chemically reacting, as evidenced by color changes from black to red, green, and blue. The crystals of PCO, NCO, and SCO were, additionally, several years old. For most measurements, PCCO films do not significantly degrade over time; however, for delicate measurements, like tunneling, fresh films are preferred. Films appear to be the more optimal system for investigating superconducting Pr_2CuO_4.

8.3   Thin Films of Iron-Based Superconductors

Following the recent discovery of the ferropnictide superconductors and related superconducting compounds, attempts were made to synthesize thin films preparations of these materials. Thin films are easier than crystals for some measurements, like measuring the Nernst and Hall effects, and allow easier creation of devices. Here, the experimental techniques attempted and some of the more promising results obtained are described in the hope that this project may be revived in the future.

8.3.1   Introduction

Thin films are often more convenient than crystals for measurements. This is particularly true for measurements where geometry is important. The recently discovered pnictide and chalcogenide superconductors have mostly been investigated as crystals; only a few groups have successfully synthesized thin films of these iron-based superconductors. Here at Maryland, some effort was expended to synthesize these materials in thin

film form. Although this project is currently inactive, several modifications to the standard cuprate pulsed laser deposition process (Chapter 3) are significant and worth brief discussion.

8.3.2   SrFe$_{2-x}$Co$_x$As$_2$ Films

The 122 pnictides are not oxides. For cuprates, the pulsed laser deposition atmosphere is maintained at some partial pressure of oxygen. This provides the necessary oxygen for Pr$_{2-x}$Ce$_x$CuO$_{4\pm\delta}$ film growth (and the oxygen still has to be more finely adjusted via post-deposition annealing). Thin films of the pnictides, in contrast, have to be grown in vacuum. The requirements for this vacuum are fairly stringent. At $P = 10^{-8}$ Torr, the base pressure of a well-sealed pulsed laser deposition chamber must be reached. Chambers reserved for oxide use are generally not this well sealed and often have a base pressure one or two decades higher.

One of the consequences of growing films under these low pressures is that the plume of material from the laser-ablation of the target is not well columnated compared to cuprate plumes grown in higher pressure atmospheres. The plume of pnictide material, therefore, tends to spread out as it is ejected from the target and the deposition rate declines precipitously with increasing distance between the target and the substrate. In order to compensate for this tendency, the distance between the target mount and the substrate heater was decreased to < 1 inch and the optical path was modified in order to continue illuminating the target with laser energy. The laser power was also increased in order to boost the amount of material being deposited on the substrate.

Additionally, the arsenic content of $SrFe_{2-x}Co_xAs_2$ proved problematic. The toxicity of arsenic required that the chamber vacuum pumps be vented directly into the gas cabinet exhaust system. This system already vents the gas cabinets containing fluorine gas and prevents laboratory contamination. Arsenic also is fairly corrosive so the vacuum pumps have to be checked for degradation. Arsenic in the target itself and the resultant 122 thin films is chemically bound in the 122 crystal lattice; however, in the pulsed laser deposition process, the plume created by laser deposition is a plasma and will introduce elemental arsenic into the chamber atmosphere. This is especially likely due to arsenic's low vapor pressure.

The low vapor pressure of arsenic creates difficulties for film synthesis as well. Oxygen in $Pr_{2-x}Ce_xCuO_{4\pm\delta}$ is an extreme example of how the pulsed laser deposition process is affected by low vapor pressure: the oxygen in the target cannot be relied upon to travel with the rest of the elements in the plasma plume and deposit on the substrate. Thus, an oxygen atmosphere is required to maintain oxygen in the growing film. Arsenic is not nearly as bad as oxygen in this regard and an atmosphere of arsene gas is not necessary. Shrinking the distance between the target and the substrate, already useful to control for the thinner atmosphere, helps to prevent the arsenic from escaping from the films too much.

Films of $SrFe_{2-x}Co_xAs_2$ ($x \approx 0.25$) were grown. Superconductivity was seen in these films (Figure 8.9), however, with a lower onset temperature than has been reported elsewhere [148].
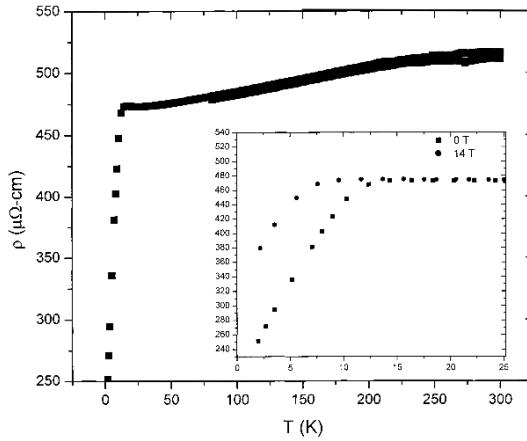
Figure 8.9: SrFe$_{2-x}$Co$_x$As$_2$ thin film with $T_c^{onset} = 10$ K. The resistivity drop is suppressed by several K in a magnetic field (insert) indicating that it is due to the onset of superconductivity.

8.3.3 FeSe$_{1-x}$Te$_x$ Films

Deposition of the 11 chalcogenides has many similarities to that of the 122 pnictides. The 11 chalcogenides are not oxides and must be grown in vacuum; although, $P = 10^{-6}$ Torr is sufficient. Selenium creates many of the same problems for pulsed laser deposition as arsenic. (Tellurium is similar to selenium in the problems that it creates.) Toxicity and low vapor pressure are dealt with similarly. The chamber pumps are vented into the gas cabinet exhaust system to address the former issue and the distance between the target and substrate is decreased to address the latter issue.

There is some question as to the "correct" stoichiometry of the FeSe system for superconductivity. Rather than having the iron and selenium in a 1:1 ratio, superconductivity is apparently favored in either slightly selenium-deficient ($\sim$1:0.88 [149, 150], $\sim$1:0.92 [151], $\sim$1:0.82 [152]) or iron-rich ($\sim$1.01:1 [153]) ratios. The difference between these two cases is a question of vacancies on the selenium sites or irons on interstitial sites.

194

Here, for the most part, FeSe in a 1:1 ratio was prepared. Selenium deficiency was partially investigated by growing combinatorial films.

The FeSe system can also be doped. Doping tellurium into the FeSe system can increase T_c [154, 155, 156, 157, 158, 159]. Sulphur can enhance superconductivity [160, 161], as can sodium and cobalt doping [162], although cobalt enhancing T_c is disputed [163]. Some investigation into the tellurium doped iron selenide system was investigated here by growing combinatorial films.

A commercial FeSe target was purchased and additional targets of FeSe, $FeSe_{0.6}$, and $FeSe_{0.5}Te_{0.5}$ were prepared. Unlike the target preparation of $Pr_{2-x}Ce_xCuO_{4\pm\delta}$ (Chapter 3), the targets were not synthesized as polycrystalline powders of the final material. Instead, elemental iron and selenium powders were mixed together and sintered. The laser should ablate the target into a plasma of its constituent elements, so this target-making procedure should not alter the resultant films. This, however, assumes that the elements are ablated at the same rate. With single-material targets this is less of an issue; but, the syntheses of the targets themselves are more difficult.

Thin films of FeSe were prepared at a variety of different substrate temperatures. For many different growth conditions, epitaxially oriented 11 films were growing on $SrTiO_3$ substrates. Epitaxy was monitored by observing film X-ray peaks in X-ray diffraction $\theta - 2\theta$ scans (Figure 8.10). A partial superconducting transition, with $T_c^{onset} = 12$ K, was seen for many different growth conditions (Figure 8.11). A T_c^0 was not, however, observed. Magnetic screening was not observed in AC susceptibility, although this is expected for partial superconductivity. However, the partial transition was suppressed by about 6 K in a 14 T magnetic field indicating that the 12 K drop in resistance is really due

to superconductivity.
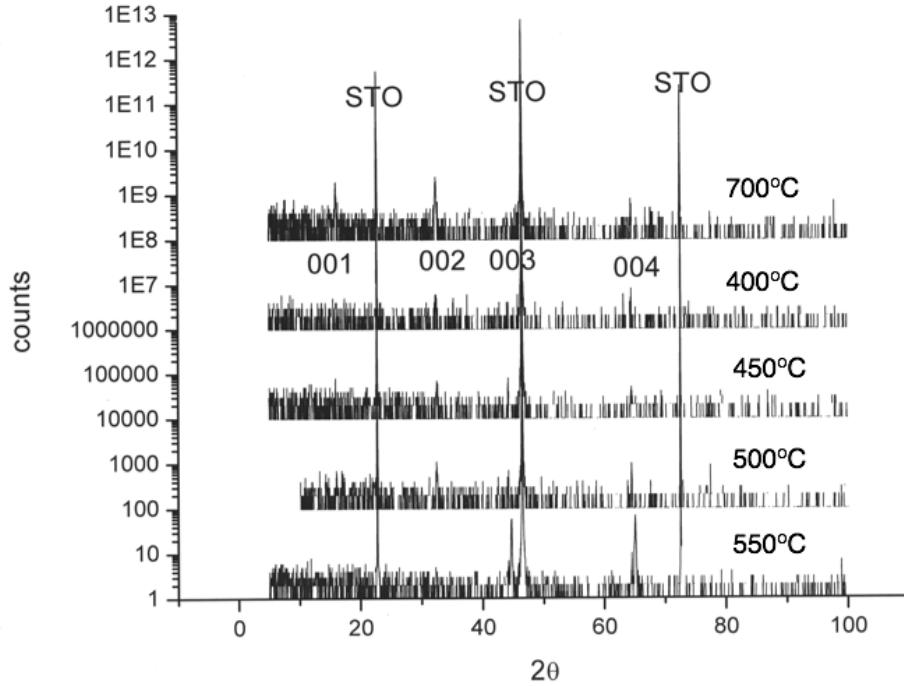
Figure 8.10: $\theta - 2\theta$ X-ray diffraction scans of several FeSe thin films (offset). Films were deposited at various substrate temperatures from 400 C to 700 C and show various amounts of epitaxy as indicated by the 00ℓ film peaks indexed.

The primary targets that were focused upon were FeSe; however, $FeSe_{0.6}$ and $FeSe_{0.5}Te_{0.5}$ targets were also synthesized for growth of combinatorial films. In this technique two targets are mounted on an adjustable carousel, like that which was used for growing superlattice films (Chapter 6). However, rather than simply alternating targets, a motorized mask is also made to move across the path of the ablated material. This creates a thickness gradient of the material being ablated. On the mask's return path, the other target is used. This creats a thickness gradient of that material as well, but in the opposite direction. The
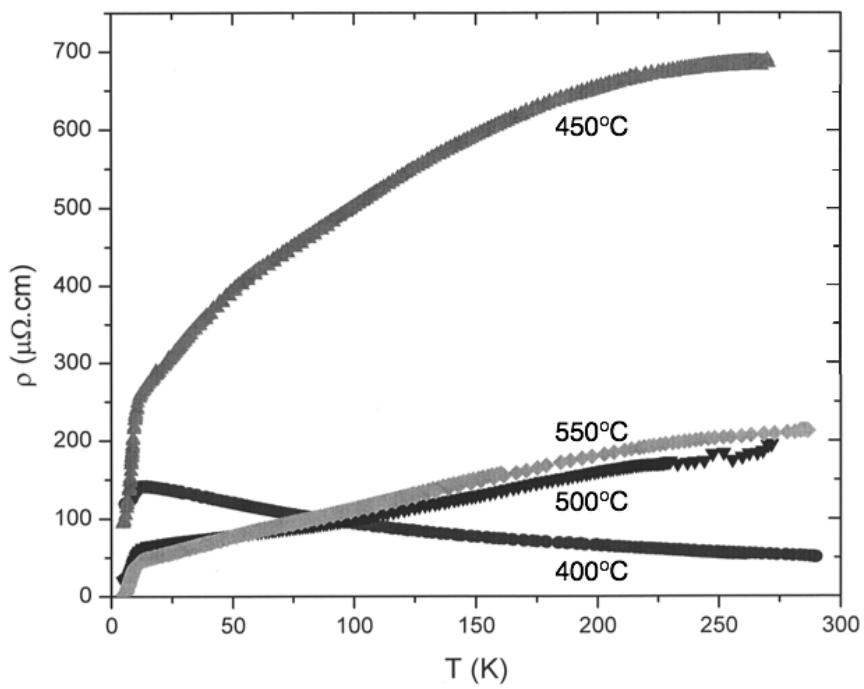
Figure 8.11: The temperature dependence of resistance for several FeSe thin films. Films were deposited at various substrate temperatures from 400 C to 550 C and all show $T_c^{onset} \approx 12$ K.

significant difference between these wedge-shaped layers of alternating material and uniform superlattice layers is the layer thickness. The superlattice layers were synthesized every ~ 5 to ~ 20 unit cells (5 to 20 nm for 12.2 Å unit cells). The combinatorial layers, however, are designed such that each is only a fraction of a unit cell thick. This is controlled by adjusting the shutter speed relative to the laser pulse rate and energy density. This adjustment must be performed individually for each target. Layers that are thinner than a unit cell will not produce a heterostructure, but, rather, will be uniformly incorporated into a single crystal lattice. Therefore, the net result will be a smooth gradient between the two end members along the length of the film.

This combinatorial technique was used to create gradients between FeSe and $FeSe_{0.6}$ to investigate the selenium deficiency needed for optimal superconductivity. It was also used to create gradients between FeSe and $FeSe_{0.5}Te_{0.5}$ for similar reasons. If this project is resumed, combinatorial growth techniques offer a method for rapidly characterizing doping phase diagrams of material systems.

Chapter 9

Summary and Future Directions

9.1 Angular Magnetoresistance

The magnetic structures of $Pr_{2-x}Ce_xCuO_{4\pm\delta}$ and $La_{2-x}Ce_xCuO_{4\pm\delta}$ were investigated by angular magnetoresistance measurements. Four-fold angular magnetoresistance oscillations were found in $Pr_{2-x}Ce_xCuO_{4\pm\delta}$ and two-fold angular magnetoresistance oscillations were found in $La_{2-x}Ce_xCuO_{4\pm\delta}$. The disappearance of angular magnetoresistance oscillations was found to track the Néel temperature in $Pr_{2-x}Ce_xCuO_{4\pm\delta}$ and suggested that magnetism in that system persisted up to $x = .15$. In $La_{2-x}Ce_xCuO_{4\pm\delta}$, angular magnetoresistance oscillations were also observed to evolve similarly with doping. The disappearance of these oscillations is also believed to track the Néel temperature and also occurs around $x = .15$. The oscillations are evidence for antiferromagnetism in this system.

In $Pr_{2-x}Ce_xCuO_{4\pm\delta}$, these angular magnetoresistance experiments support the idea of antiferromagnetism terminating at around $x \approx .16$, a proposed Quantum Critical Point. Quantum critical behavior in the cuprates has been long debated. In $La_{2-x}Ce_xCuO_{4\pm\delta}$, this work was the first to experimentally demonstrate the existence of antiferromagnetism in the $La_{2-x}Ce_xCuO_{4\pm\delta}$ system. While antiferromagnetism in $La_{2-x}Ce_xCuO_{4\pm\delta}$ had been assumed based on similar systems like $Pr_{2-x}Ce_xCuO_{4\pm\delta}$ or $Nd_{2-x}Ce_xCuO_{4\pm\delta}$, the lack of crystal samples of $La_{2-x}Ce_xCuO_{4\pm\delta}$ has frustrated spin-sensitive scattering experiments.

The angular magnetoresistance measurements avoided this difficulty.

In order to strengthen this conclusion, it would be useful to more carefully investigate the origins of the angular magnetoresistance signal. It is taken as an observation that the zeroing of the angular magnetoresistance amplitude coincides with suppression of antiferromagnetism. More careful understanding of the exact relationship between antiferromagnetism and angular magnetoresistance would be useful. This is especially true for the $La_{2-x}Ce_xCuO_{4\pm\delta}$ system where the angular magnetoresistance has only two-fold symmetry rather than the four-fold symmetry expected by the T' structure.

9.2 Oxygen and Disorder

Over-oxygenated and irradiated $Pr_{2-x}Ce_xCuO_{4\pm\delta}$ at $x = .12$ and $x = .15$ were investigated through resistivity, Hall effect, and angular magnetoresistance. Oxygen is found to act as both a source of doping and disorder in the system. The doping effect is found to be a significant effect of over-oxygenation. Under- and optimally-doped films are seen to behave similarly to over-doped films. Oxygen significantly changes the number of normal state charge carriers in the system. Additionally, oxygen is seen to have a strong doping effect in a separate probe of charge carrier concentration; Néel temperature suppression via spin-dilution can be controlled by oxygen doping and is largely insensitive to disorder. Also, annealing is indicated as an apical oxygen removal process and several other proposed annealing models are excluded.

The role of oxygen in $Pr_{2-x}Ce_xCuO_{4\pm\delta}$, and the influence of annealing on it, have long been an issue. By over-oxygenating $Pr_{2-x}Ce_xCuO_{4\pm\delta}$ films and observing the shift

of Hall effect and angular magnetoresistance oscillation data to effectively lower cerium dopings, oxygen is seen to act as a dopant, in contrast to models suggesting more complicated roles for oxygen in the electron-doped cuprates. This data support the simpler picture of O^{2-} hole-doping the system, even with the presence of additional disorder due to introducing excess oxygen. This data also addresses a long-standing uncertainty in the understanding of the electron-doped cuprates by supporting the picture that annealing is primarily about removing apical oxygen, while additionally rejecting several other proposals in the literature.

Oxygen studies in electron-doped cuprate thin films are always complicated, however, by a long-standing inability to accurately measure the oxygen concentration and position in the materials. Careful refinement of chemical analysis techniques as they relate to oxygen would, therefore, be of much use in understanding the behavior of complicated oxides like the cuprates. Successful work along these lines would greatly strengthen conclusions based upon oxygen studies. More careful correlation between oxygen levels due to oxygenation versus annealing procedures could strengthen this study's conclusions, as well as investigating several different annealing levels, annealing oxygenated films, and possibly irradiation of off-optimally grown films.

9.3 Superlattices

Enhancement of T_c in superlattices of $Pr_{2-x}Ce_xCuO_{4\pm\delta}$ and $La_{2-x}Ce_xCuO_{4\pm\delta}$ was investigated. These structures were pairings of under-doped and over-doped layers. T_c enhancement was found in these structures and was determined to not be an interface

effect by critical current measurements. The T_c enhancement was, instead, found to be due to charge redistribution. Hall effect and angular magnetoresistance measurements further clarify this position; charge redistribution appears to result in slightly net-under-doped films.

Interface effects between under-doped and over-doped cuprate superconductors were hoped to increase T_c. While this work demonstrates that T_c enhancement does occur in layered cuprate structures, it refutes proposed interface effects. We demonstrated that the interface between the layers is not critical for the observed T_c enhancement. These results discourage seeking enhanced T_cs in these materials via interfacial effects.

The critical current measurements suggesting charge redistribution are supported by Hall effect and angular magnetoresistance measurements. The two former data sets are not complete due to a blocked impedance in the PPMS at the time of this thesis writing. These measurements should be completed on a fuller set of doping pairs in both the $Pr_{2-x}Ce_xCuO_{4\pm\delta}$ and $La_{2-x}Ce_xCuO_{4\pm\delta}$ systems. Additionally, the observation of charge redistribution is speculated to be due to the role of oxygen in the superlattice films; this hypothesis should be investigated. Charge redistribution might also be able to be investigated more fully in bi-layer, or reduced layer superlattice, films by slowly removing layers via ion milling or similar technique and observing changes in transport properties.

9.4   High Temperature Resistance

The high temperature resistance of electron-doped cuprates and Sr-122 pnictides was measured. The electron-doped cuprates were shown to violate the Mott-Ioffe-Regel limit. This is consistent with the hole-doped cuprates and is evidence for strong correlations in these materials. The Sr-122s show a saturation at high temperatures at several hundred $\mu\Omega\cdot$cm. This saturation is consistent with Mott-Ioffe-Regel limited behavior in these materials or with coupling due to spin-fluctuations. While coupling due to spin-fluctuations cannot be ruled out, the likely Mott-Ioffe-Regel limit in the Sr-122s support the view that the new pnictide high-T_c superconductors are not strongly correlated systems, in contrast to the cuprate high-T_c superconductors. These measurements suggest that the pnictides are probably reasonably typical metals in terms of normal-state electron-phonon interactions.

These results are the first observation of possible Mott-Ioffe-Regel limited behavior in the 122s, a system where the strength of correlations is still under debate. Saturation at the Mott-Ioffe-Regel limit discourages exotic models for pnictide correlations. Ruling out strong, cuprate-like correlations in the 122s may additionally have implications for understanding superconducting properties, like the pairing mechanism, in the pnictides.

This work could easily be extended by the investigation of Mott-Ioffe-Regel limited behavior, an under-studied direction, in other related systems. The 11 and 1111 systems, for example, are not expected to have the same strength of electronic interactions as the 122s or as each other. The chalcogenides, in particular, have no high temperature resistivity data and may be the more correlated of the various iron-based high-temperature super-

conductor systems. Additionally, the Prelovšek and Sega model discussed also predicted specific behavior for thermopower and Hall effect at elevated temperatures. Modification of the experimental setup to allow these measurements is suggested as a useful continuing investigation.

9.5   Superconducting Pr_2CuO_4 and Pnictide/Chalcogenide Thin Films

Several additional film growth projects were attempted, synthesizing superconducting Pr_2CuO_4 by careful control of oxygen and growth of pnictide and chalcogenide thin films by pulsed laser deposition. These projects are still future work as-is, as these projects are left incomplete. For superconducting Pr_2CuO_4, the central issue is the ability to accurately and consistently control oxygen. The pulsed laser deposition chamber many not be able to provide the required accuracy in its current form. Modification of the chamber or replacement with other equipment for annealing may be productive directions. For the iron-based superconductor thin films, the growth parameters must be optimized, and Maryland's pulsed laser deposition chambers may need modification to allow tighter control of parameters. For the iron selenide system, combinatorial growth should be fully developed.

Bibliography

[1] H. Kamerlingh Onnes. The Superconductivity of Mercury. *Comm. Phys. Lab. Univ. Leiden*, Nos. 122 and 124, 1911.

[2] H. Ibach and H. Lüth. *Solid-State Physics*. Springer, Berlin, third edition, 2003.

[3] Charles Kittel. *Introduction to Solid State Physics*. John Wiley & Sons, Inc., seventh edition, 1996.

[4] Giuseppe Grosso and Giuseppe Pastori Parravicini. *Solid State Physics*. Academic Press, 2000.

[5] J. G. Bednorz and K. A. Müller. Possible high T_c superconductivity in the Ba-La-Cu-O system. *Zeitschrift für Physik B Condensed Matter*, 64:189–193, 1986.

[6] Yoichi Kamihara, Takumi Watanabe, Masahiro Hirano, and Hideo Hosono. Iron-Based Layered Superconductor $LaO_{1-x}F_xFeAs$ (x = 0.05-0.12) with Tc = 26 K. *Journal of the American Chemical Society*, 130 (11):3296–3297, 2008.

[7] Hiroki Takahashi, Kazumi Igawa, Kazunobu Arii, Yoichi Kamihara, Masahiro Hirano, and Hideo Hosono. Superconductivity at 43 K in an iron-based layered compound $LaO_{1-x}F_xFeAs$. *Nature*, 453 (7193):376–378, 2008.

[8] Yoichi Kamihara, Hidenori Hiramatsu, Masahiro Hirano, Ryuto Kawamura, Hiroshi Yanagi, Toshio Kamiya, and Hideo Hosono. Iron-Based Layered Superconductor: LaOFeP. *Journal of the American Chemical Society*, 128 (31):10012–10013, 2006.

[9] G. Wu, Y. L. Xie, H. Chen, M. Zhong, R. H. Liu, B. C. Shi, Q. J. Li, X. F. Wang, T. Wu, Y. J. Yan, J. J. Ying and X. H. Chen. Superconductivity at 56 K in Samarium-doped SrFeAsF. *Journal of Physics: Condensed Matter*, page 142203, 9 March 2008.

[10] W. Meissner and R. Ochsenfeld. Ein neuer Effekt bei Eintritt der Supraleitfähigkeit. *Naturwissenschaften*, 21:787–788, 1933.

[11] Neil W. Ashcroft and N. David Mermin. *Solid State Physics*. Thomson Learning, 1976.

[12] Michael Tinkhem. *Introduction to Superconductivity*. Dover Publications, Inc., second edition, 1996.

[13] F. London and H. London. *Proceedings of the Royal Society*, A149, 1935.

[14] F. London and H. London. *Physica*, 2, 1935.

[15] V. L. Ginzburg and L. D. Landau. *Zhurnal Eksperimentalnoi i Teoreticheskoi Fiziki (Journal of Experimental and Theoretical Physics)*, 20:1064, 1950.

[16] J. Bardeen, L. N. Cooper, and J. R. Schrieffer. Microscopic theory of superconductivity. *Physical Review*, 106(1):162–164, April 1957.

[17] J. Bardeen, L. N. Cooper, and J. R. Schrieffer. Theory of superconductivity. *Physical Review*, 108(5):1175–1204, December 1957.

[18] Michael P. Marder. *Condensed Matter Physics*. John Wiley & Sons, Inc., 2000.

[19] Feng Duan and Jin Goujun. *Introduction to Condensed Matter Physics*, volume 1. World Scientific, 2005.

[20] Cédric Weber, Kristjan Haule, and Gabriel Kotliar. Strength of correlations in electron- and hole-doped cuprates. *Nature Physics*, 6:574578, 2010.

[21] N. P. Armitage, P. Fournier, and R. L. Greene. Progress and perspectives on the electron-doped cuprates. *Review of Modern Physics*, 82(3):2421–2487, September 2010.

[22] L. Zhao, H. Wu, J. Miao, H. Yang, F. C. Zhang, X. G. Qiu and B. R. Zhao. Electron-doped superconducting $(La, Ce)_2CuO_4$ thin films grown by dc magnetron sputtering and their transport properties. *Superconductor Science and Technology*, 17, 2004.

[23] W. Jiang, J. L. Peng, Z. Y. Li, and R. L. Greene. Transport properties of $Nd_{1.85}Ce_{0.15}CuO_{4+\delta}$ crystals before and after reduction. *Physical Review B*, 47:8151–8155, 1993.

[24] P. G. Radaelli, J. D. Jorgensen, A. J. Schultz, J. L. Peng, and R. L. Greene. Evidence of apical oxygen in Nd_2CuO_y determined by single-crystal neutron diffraction. *Physical Review B*, 49:15322–15326, 1994.

[25] X. Q. Xu, S. N. Mao, W. Jiang, J. L. Peng, and R. L. Greene. Oxygen dependence of the transport properties of $Nd_{1.78}Ce_{0.22}CuO_{4\pm\delta}$. *Physical Review B*, 53:871–875, 1996.

[26] A. J. Schultz, J. D. Jorgensen, J. L. Peng, and R. L. Greene. Single-crystal neutron-diffraction structures of reduced and oxygenated $Nd_{2-x}Ce_xCuO_y$. *Physical Review B*, 53(9):5157–5159, March 1996.

[27] J. S. Higgins, Y. Dagan, M. C. Barr, B. D. Weaver, and R. L. Greene. Role of oxygen in the electron-doped superconducting cuprates. *Physical Review B*, 73:104510, 2006.

[28] P. Richard, G. Riou, I. Hetel, S. Jandl, M. Poirier, and P. Fournier. Role of oxygen nonstoichiometry and the reduction process on the local structure of $Nd_{2-x}Ce_xCuO_{4\pm\delta}$. *Physical Review B*, 70(6):064513, August 2004.

[29] G. Riou, P. Richard, S. Jandl, M. Poirier, P. Fournier, V. Nekvasil, S. N. Barilo, and L. A. Kurnevich. Pr^{3+} crystal-field excitation study of apical oxygen and reduction processes in $Pr_{2-x}Ce_xCuO_{4\pm\delta}$. *Physical Review B*, 69(2):024511, January 2004.

[30] P. Richard, M. Poirier, S. Jandl, and P. Fourier. Impact of the reduction process on the long-range antiferromagnetism in $Nd_{1.85}Ce_{0.15}CuO_4$. *Physical Review B* , 72:184514, 2005.

[31] Hye Jung Kang, Pengcheng Dai, Branton J. Campbell , Peter J. Chupas, Stephan Rosenkranz, Peter L. Lee, Qingzhen Huang, Shiliang Li, Seiki Komiya and Yoichi Ando. Microscopic annealing process and its impact on superconductivity in T'-structure electron-doped copper oxides. *Nature Materials*, February 2007.

[32] O. Matsumoto, A. Utsuki, A. Tsukada, H. Yamamoto, T. Manabe, and M. Naito. Reduction dependence of superconductivity in the end-member T' cuprates. *Physica C - Superconductivity and its Applications*, 469(15-20):940–943, August-October 2009.

[33] E. Maiser, P. Fournier, J.-L. Peng, F. M. Araujo-Moreira, T. Venkatesan, R. L. Greene, and G. Czjzek. Pulsed-laser deposition of $Pr_{2-x}Ce_xCuO_{4-y}$ thin films and the effect of high-temperature post-annealing. *Physica C*, 297:15–22, 1998.

[34] A. Tsukada, H. Yamamoto, and M. Naito. Doping of Ce in T-La_2CuO_4: Rigorous test for electron-hole symmetry for high-T_c superconductivity. *Physical Review B*, 74(17):174515, November 2006.

[35] A. N. Lavrov, H. J. Kang, Y. Kurita, T. Suzuki, Seiki Komiya, J. W. Lynn, S.-H. Lee, Pengcheng Dai, and Yoichi Ando. Spin-Flop Transition and the Anisotropic Magnetoresistance of $Pr_{1.3-x}La_{0.7}Ce_xCuO_4$: Unexpectedly Strong Spin-Charge Coupling in the Electron-Doped Cuprates. *Physical Review Letters*, 92(22):227003, June 2004.

[36] W. Yu, J. S. Higgins, P. Bach, and R. L. Greene. Transport evidence of a magnetic quantum phase transition in electron-doped high-temperature superconductors. *Phys. Rev. B*, 76(2):020503, July 2007.

[37] K. H. Bennemann and J. B. Ketterson. *Superconductivity*. Number 1. Springer, 2008.

[38] Joshua Higgins. *Disorder and Doping in the Oxygenated Electron-Doped Superconductor $Pr_{2-x}Ce_xCuO_{4\pm\delta}$*. PhD thesis, University of Maryland - College Park, 2006.

[39] Alexandre Zimmers. *Etude par Spectroscopie Infrarouge de l'Electrodynamique du Supraconducteur $Pr_{2-x}Ce_xCuO_4$ et de la Manganite $La_{2/3}Ca_{1/3}MnO_3$*. PhD thesis, ESPCI, 2004.

[40] N. F. Mott and R. Peierls. *Proceedings of the Physical Society of London*, 49:72, 1937.

[41] J. Hubbard. *Proceedings of the Physical Society of London*, Ser.A 281, 1964.

[42] Andrea Damascelli, Zahid Hussain, and Zhi-Xun Shen. Angle-resolved photoemission studies of the cuprate superconductors. *Reviews of Modern Physics*, 75, April 2003.

[43] N. P. Armitage, F. Ronning, D. H. Lu, C. Kim, A. Damascelli, K. M. Shen, D. L. Feng, H. Eisaki, Z.-X. Shen, P. K. Mang, N. Kaneko, M. Greven, Y. Onose, Y. Taguchi, and Y. Tokura. Doping dependence of an n-type cuprate superconductor investigated by angle-resolved photoemission spectroscopy. *Physical Review Letters*, 88(25):257001, June 2002.

[44] G. M. Luke, L. P. Le, B. J. Sternlieb, Y. J. Uemura, J. H. Brewer, R. Kadono, R. F. Kiefl, S. R. Kreitzman, T. M. Riseman, C. E. Stronach, M. R. Davis, S. Uchida, H. Takagi, Y. Tokura, Y. Hidaka, T. Murakami, J. Gopalakrishnan, A. W. Sleight, M. A. Subramanian, E. A. Early, J. T. Markert, M. B. Maple, and C. L. Seaman. Magnetic order and electronic phase diagrams of electron-doped copper oxide materials. *Physical Review B*, 42(13):7981–7988, November 1990.

[45] E. Motoyama, G. Yu, I. Vishik, O. Vajk, P. Mang, and M. Greven. Spin correlations in the electron-doped high-transition-temperature superconductor $Nd_{2-x}Ce_xCuO_{4\pm\delta}$. *Nature*, 445:186, 2007.

[46] S. R. Park, Y. S. Roh, Y. K. Yoon, C. S. Leem, J. H. Kim, B. J. Kim, H. Koh, H. Eisaki, N. P. Armitage, and C. Kim. Electronic structure of electron-doped order $Sm_{1.85}Ce_{0.15}CuO_4$: Strong pseudogap effects, nodeless gap, and signatures of short-range. *Physical Review B*, 75:060501R, 2007.

[47] T. Uefuji, K. Kurahashi, M. Fujita, M. Matsuda, and K. Yamada. Electron-doping effect on magnetic order and superconductivity in $Nd_{2-x}Ce_xCuO_4$ single crystals. *Physica C: Superconductivity*, 378-381:273–277, October 2002.

[48] H. J. Kang, Pengcheng Dai, J. W. Lynn, M. Matsuura, J. R. Thompson, Shou-Cheng Zhang, D. N. Argyriou, Y. Onose and Y. Tokura. Antiferromagnetic order as the competing ground state in electron-doped $Nd_{1.85}Ce_{0.15}CuO_4$. *Nature*, 423:522–525, 29 May 2003.

[49] P. K. Mang, S. Larochelle, A. Mehta, O. P. Vajk, A. S. Erickson, L. Lu, W. J. L. Buyers, A. F. Marshall, K. Prokes, and M. Greven. Phase decomposition and chemical inhomogeneity in $Nd_{2-x}Ce_xCuO_{4\pm\delta}$. *Physical Review B*, 70(9):094507, September 2004.

[50] H. J. Kang, Pengcheng Dai, H. A. Mook, D. N. Argyriou, V. Sikolenko, J. W. Lynn, Y. Kurita, Seiki Komiya, and Yoichi Ando. Electronically competing phases and their magnetic field dependence in electron-doped nonsuperconducting and superconducting $Pr_{0.88}LaCe_{0.12}CuO_{4\pm\delta}$. *Physical Review B*, 71(21):214512, June 2005.

[51] Y. Krockenberger, J. Kurian, A. Winkler, A. Tsukada, M. Naito, and L. Alff. Superconductivity phase diagrams for the electron-doped cuprates $R_{2-x}\mathrm{Ce}_x\mathrm{CuO}_4$ (R=La, Pr, Nd, Sm, and Eu). *Physical Review B*, 77:060505, 2008.

[52] Osamu Matsumoto, Aya Utsuki, Akio Tsukada, Hideki Yamamoto, Takaaki Manabe, and Michio Naito. Synthesis and properties of superconducting T'-$R_2\mathrm{CuO}_4$ (R =Pr, Nd, Sm, Eu, Gd). *Physical Review B*, 79(10), March 2009.

[53] O. Matsumoto, A. Utsuki, A. Tsukada, H. Yamamoto, T. Manabe, and M. Naito. Superconductivity in undoped T'-$RE_2\mathrm{CuO}_4$ with T_c over 30 K. *Physica C - Superconductivity and its Applications*, 468(15-20):1148–1151, September 15 2008.

[54] O. Matsumoto, A. Utsuki, A. Tsukada, H. Yamamoto, T. Manabe, and M. Naito. Generic phase diagram of "electron-doped" T' cuprates. *Physica C - Superconductivity and its Applications*, 469(15-20):924–927, August-October 2009.

[55] W. Yu, B. Liang, P. Li, S. Fujino, T. Murakami, I. Takeuchi, and R. L. Greene. Oxygen-doped Mott-Hubbard cuprate superconductor $\mathrm{La}_{1.85}\mathrm{Y}_{0.15}\mathrm{CuO}_{4-\delta}$ from transport measurements. *Physical Review B*, 75(2):020503, January 2007.

[56] G. Roberge, S. Charpentier, S. Godin-Proulx, P. Rauwel, K. D. Truong, and P. Fournier. Improving the growth of electron-doped $\mathrm{Pr}_{2-x}\mathrm{Ce}_x\mathrm{CuO}_{4+\delta}$ thin films made by pulsed-laser deposition using excess CuO. *Journal of Crystal Growth*, 311(5):1340 – 1345, 2009.

[57] Crystec GmbH. http://crystec.de/.

[58] G. S. Jenkins, D. C. Schmadel, P. L. Bach, R. L. Greene, X. Béchamp-Laganière, G. Roberge, P. Fournier, and H. D. Drew. Terahertz magnetotransport measurements in underdoped $\mathrm{Pr}_{2-x}\mathrm{Ce}_x\mathrm{CuO}_4$ and comparison with angle-resolved photoemission. *Physical Review B*, 79(22):224525, June 2009.

[59] G. S. Jenkins, D. C. Schmadel, P. L. Bach, R. L. Greene, X. Béchamp-Laganière, G. Roberge, P. Fournier, Hiroshi Kontani, and H. D. Drew. Origin of the anomalous Hall effect in the overdoped n-type superconductor $\mathrm{Pr}_{2-x}\mathrm{Ce}_x\mathrm{CuO}_4$: Current-vertex corrections due to antiferromagnetic fluctuations. *Physical Review B*, 81(2):024508, January 2010.

[60] L.J. van der Pauw. A method of measuring specific resistivity and hall effect of discs of arbitrary shape. *Philips Research Reports*, 13:1–9, 1958.

[61] L.J. van der Pauw. A method of measuring the resistivity and hall coefficient on lamellae of arbitrary shape. *Philips Technical Review*, 20:220–224, 1958.

[62] Bragg's law. http://en.wikipedia.org/wiki/Bragg%27s_law.

[63] A. Schreyer, T. Schmitte, R. Siebrecht, P. Bödeker, H. Zabel, S. H. Lee, R. W. Erwin, C. F. Majkrzak, J. Kwo, and M. Hong . Neutron scattering on magnetic thin films: Pushing the limits (invited). *Journal of Applied Physics*, 87:5443, 2000.

[64] Y. Dagan, M. M. Qazilbash, C. P. Hill, V. N. Kulkarni, and R. L. Greene, . Evidence for a Quantum Phase Transition in $Pr_{2-x}Ce_xCuO_{4-\delta}$ from Transport Measurements. *Physical Review Letters*, 92:167001, 2004.

[65] Pengcheng Li, K. Behnia, and R. L. Greene. Evidence for a quantum phase transition in electron-doped $Pr_{2-x}Ce_xCuO_{4-\delta}$ from thermopower measurements. *Physical Review B*, 75(2):020506, January 2007.

[66] Subir Sachdev. Where is the quantum critical point in the cuprate superconductors? *Physica Status Solidi B*, 247, No. 3,:537–543, 2010.

[67] Y. Onose, Y. Taguchi, K. Ishizaka, and Y. Tokura. Charge dynamics in under-doped $Nd_{2-x}Ce_xCuO_4$: Pseudogap and related phenomena. *Physical Review B*, 69(2):024504, January 2004.

[68] A. Zimmers, J. M. Tomczak, R. P. S. M. Lobo, N. Bontemps, C. P. Hill, M. C. Barr, Y. Dagan, R. L. Greene, A. J. Millis, and C. C. Homes. Infrared properties of electron-doped cuprates: Tracking normal-state gaps and quantum critical behavior in $Pr_{2-x}Ce_xCuO_4$. *Europhysics Letters*, 70, 2005.

[69] Y. Dagan, M. C. Barr, W. M. Fisher, R. Beck, T. Dhakal, A. Biswas, and R. L. Greene. Origin of the Anomalous Low Temperature Upturn in the Resistivity of the Electron-Doped Cuprate Superconductors. *Physical Review Letters*, 94:057005, 2005.

[70] K. Jin, X. H. Zhang, P. Bach, and R. L. Greene. Evidence for antiferromagnetic order in $La_{2-x}Ce_xCuO_4$ from angular magnetoresistance measurements. *Physical Review B*, 80(1):012501, July 2009.

[71] X. F. Wang, T. Wu, G. Wu, R. H. Liu, H. Chen, Y. L. Xie, and X. H. Chen. The peculiar physical properties and phase diagram of $BaFe_{2-x}Co_xAs_2$ single crystals. *New Journal of Physics*, 11(4):045003, 2009.

[72] X. F. Wang, T. Wu, G. Wu, H. Chen, Y. L. Xie, J. J. Ying, Y. J. Yan, R. H. Liu, and X. H. Chen. Anisotropy in the Electrical Resistivity and Susceptibility of Super-conducting $BaFe_2As_2$ Single Crystals. *Physical Review Letters*, 102(11):117005, March 2009.

[73] Yayu Wang, Lu Li, and N. P. Ong. Nernst effect in high-T_c superconductors. *Physical Review B*, 73(2):024510, January 2006.

[74] Pengcheng Li and R. L. Greene. Normal-state Nernst effect in electron-doped $Pr_{2-x}Ce_xCuO_{4-\delta}$: Superconducting fluctuations and two-band transport. *Physical Review B*, 76(17):174512, November 2007.

[75] R. Hord, H. Luetkens, G. Pascua, A. Buckow, K. Hofmann, Y. Krockenberger, J. Kurian, H. Maeter, H.-H. Klauss, V. Pomjakushin, A. Suter, B. Albert, and L. Alff. Enhanced two-dimensional behavior of metastable T'-La_2CuO_4 , the

parent compound of electron-doped cuprate superconductors. *Physical Review B*, 82(18):180508, November 2010.

[76] M. A. Kastner, R. J. Birgeneau, G. Shirane, and Y. Endoh. Magnetic, transport, and optical properties of monolayer copper oxides. *Review of Modern Physics*, 70(3):897–928, July 1998.

[77] Yoichi Ando, A. N. Lavrov, and Kouji Segawa. Magnetoresistance Anomalies in Antiferromagnetic $YBa_2Cu_3O_{6+x}$: Fingerprints of Charged Stripes. *Physical Review Letters*, 83(14):2813–2816, October 1999.

[78] H.-H. Klauss, W. Wagener, B. Büchner, M. Hücker, D. Mienert, W. Kopmann, M. Birke, H. Luetkens, D. Baabe and F. J. Litterst. Charge Carrier Dynamics in Zn-Doped Cuprates. *Hyperfine Interactions*, 133:203–206, 2001.

[79] Michael Lambacher, Toni Helm, Mark Kartsovnik, and Andreas Erb. Advances in single crystal growth and annealing treatment of electron-doped htsc. *The European Physical Journal - Special Topics*, 188:61–72, 2010.

[80] J. Gauthier, S. Gagné, J. Renaud, M.-È. Gosselin, P. Fournier, and P. Richard. Different roles of cerium substitution and oxygen reduction in transport in $Pr_{2-x}Ce_xCuO_4$ thin films. *Physical Review B*, 75(2):024424, January 2007.

[81] A. A. Nersesyan, A. M. Tsvelik, and F. Wenger. Disorder effects in two-dimensional d-wave superconductors. *Physical Review Letters*, 72(16):2628–2631, April 1994.

[82] P. K. Mang, O. P. Vajk, A. Arvanitaki, J. W. Lynn, and M. Greven. Spin Correlations and Magnetic Order in Nonsuperconducting $Nd_{2-x}Ce_xCuO_{4\pm\delta}$. *Physical Review Letters*, 93(2):027002, July 2004.

[83] Wu Jiang, S. N. Mao, X. X. Xi, Xiuguang Jiang, J. L. Peng, T. Venkatesan, C. J. Lobb, and R. L. Greene. Anomalous Transport Properties in Superconducting $Nd_{1.85}Ce_{0.15}CuO_{4\pm\delta}$. *Physical Review Letters*, 73(9):1291–1294, August 1994.

[84] W. Chen, Brian M. Andersen, and P. J. Hirschfeld. Theory of resistivity upturns in metallic cuprates. *Physical Review B*, 80(13):134518, October 2009.

[85] B. D. Weaver, G. P. Summers, R. L. Greene, E. M. Jackson, S. N. Mao, and W. Jiang. Radiation damage effects in $Nd_{2-x}Ce_xCuO_{4-y}$ thin films. *Physica C*, 261(3-4):229–236, May 1 1996.

[86] B. D. Weaver, E. M. Jackson, G. P. Summers, and E. A. Burke. Atomic disorder and the transition temperature of cuprate superconductors. *Physical Review B*, 46(2):1134–1137, July 1992.

[87] P. Richard, M. Neupane, Y.-M. Xu, P. Fournier, S. Li, Pengcheng Dai, Z. Wang, and H. Ding. Competition between Antiferromagnetism and Superconductivity in the Electron-Doped Cuprates Triggered by Oxygen Reduction. *Physical Review Letters*, 99(15):157002, October 2007.

[88] A. Gozar, G. Logvenov, L. F. Kourkoutis, A. T. Bollinger, L. A. Giannuzzi, D. A. Muller, and I. Bozovic. High-temperature interface superconductivity between metallic and insulating copper oxides. *Nature*, 455:782–785, 9 October (2008).

[89] S. Smadici, J. C. T. Lee, S. Wang, P. Abbamonte, G. Logvenov, A. Gozar, C. Deville Cavellin, and I. Bozovic. Superconducting Transition at 38 K in Insulating-Overdoped La_2CuO_4-$La_{1.64}Sr_{0.36}CuO_4$ Superlattices: Evidence for Interface Electronic Redistribution from Resonant Soft X-Ray Scattering. *Physical Review Letters*, 102(10):107004, March 2009.

[90] Ofer Yuli, Itay Asulin, Oded Millo, and Dror Orgad. Enhancement of the Superconducting Transition Temperature of $La_{2-x}Sr_xCuO_4$ Bilayers: Role of Pairing and Phase Stiffness . *Physical Review Letters*, 101:057005, 2008.

[91] G. Koren and O. Millo. Enhancement of the superconducting transition temperature of $La_{2-x}Sr_xCuO_4$ and $La_{1.875}Ba_{0.125}CuO_4$ bilayers: Bilayer and reference film prepared on the same wafer. *Physical Review B*, 81(13):134516, April 2010.

[92] Erez Berg, Dror Orgad, and Steven A. Kivelson. Route to high-temperature superconductivity in composite systems. *Physical Review B*, 78(9):094509, September 2008.

[93] S. Okamoto and T. A. Maier. Enhanced Superconductivity in Superlattices of High-T_c Cuprates. *Physical Review Letters*, 101:156401, 2008.

[94] K. Jin, P. Bach, X. H. Zhang, U. Grupel, E. Zohar, I. Diamant, Y. Dagan, S. Smadici, P. Abbamonte, and R. L. Greene. Anomalous Enhancement of the Superconducting Transition Temperature in Electron-Doped Cuprate Heterostructures. *submitted*.

[95] S. J. Zhu, J. Yuan, B. Y. Zhu, F. C. Zhang, B. Xu, L. X. Cao, X. G. Qiu, B. R. Zhao, and P. X. Zhang. Exchange bias effect and enhanced magnetoresistance in $La_{0.67}Sr_{0.33}MnO_3$/$SrTiO_3$ superlattices. *Applied Physics Letters*, 90:112502, 2007.

[96] K. E. Meyer, G. P. Felcher, S. K. Sinha, and Ivan K. Schuller. Models of diffraction from layered ultrathin coherent structures. *Journal of Applied Physics*, 52:6608, 1981.

[97] Ivan K. Schuller and Charles M. Falco. Layered ultrathin coherent structure. *AIP Conference Proceedings*, 58(1):197–202, 1980.

[98] Ivan K. Schuller. New class of layered materials. *Physical Review Letters*, 44(24):1597–1600, June 1980.

[99] Y. Dagan and R. L. Greene. Hole superconductivity in the electron-doped superconductor $Pr_{2-x}Ce_xCuO_4$. *Physical Review B*, 76(2):024506, July 2007.

[100] D. Bhoi, P. Mandal, and P. Choudhury. Resistivity saturation in $PrFeAsO_{1-x}F_y$ superconductor: evidence of strong electron-phonon coupling. *Superconductor Science and Technology*, 21(12):125021, 2008.

[101] Clarina de la Cruz, Q. Huang, J. W. Lynn, Jiying Li, W. Ratcliff II, J. L. Zarestky, H. A. Mook, G. F. Chen, J. L. Luo, N. L. Wang, and Pengcheng Dai. Magnetic order close to superconductivity in the iron-based layered $LaO_{1-x}F_xFeAs$ systems. *Nature*, 453:899, 2008.

[102] D. S. Inosov, J. T. Park, P. Bourges, D. L. Sun, Y. Sidis, A. Schneidewind, K. Hradil, D. Haug, C. T. Lin, B. Keimer, V. Hinkov. Normal-State Spin Dynamics and Temperature-Dependent Spin Resonance Energy in an Optimally Doped Iron Arsenide Superconductor. *Nature Physics*, 6:178–181, 2010.

[103] Hidekazu Mukuda, Nobuyuki Terasaki, Nobukatsu Tamura, Hiroaki Kinouchi, Mitsuharu Yashima, Yoshio Kitaoka, Kiichi Miyazawa, Parasharam M. Shirage, Shinnosuke Suzuki, Shigeki Miyasaka, Setsuko Tajima, Hijiri Kito, Hiroshi Eisaki, and Akira Iyo. Doping Dependence of Normal-State Properties in Iron-Based Oxypnictide Superconductor $LaFeAsO_{1-y}$ Probed by 57Fe-NMR and 75As-NMR/NQR. *Journal of the Physical Society of Japan*, 78:084717, 2009.

[104] F. L. Ning, K. Ahilan, T. Imai, A. S. Sefat, M. A. McGuire, B. C. Sales, D. Mandrus, P. Cheng, B. Shen, and H.-H. Wen. Contrasting Spin Dynamics Between Underdoped and Overdoped $Ba(Fe_{1-x}Co_x)_2As_2$. *Physical Review Letters*, 104:037001, 2010.

[105] A. F. Ioffe and A. P. Regel. *Prog. Semicond.*, 4:237, 1960.

[106] N. F. Mott. Conduction in non-crystalline systems IX. the minimum metallic conductivity. *Philosophical Magazine*, 1972.

[107] M. Calandra and O. Gunnarsson. Saturation of Electrical Resistivity in Metals at Large Temperatures. *Physical Review Letters*, 87(26):266601, December 2001.

[108] O. Gunnarsson, M. Calandra, and J. E. Han. Colloquium: Saturation of electrical resistivity. *Review of Modern Physics*, 75(4):1085 – 1099, October 2003.

[109] N. E. Hussey, K. Takenaka, and H. Takagi. Universality of the Mott-Ioffe-Regel limit in metals. *Philosophical Magazine*, 84(27):2847 – 2864, 2004.

[110] T. K. Nath and A. K. Majumdar. Resistivity saturation in substitutionally disordered γ-$Fe_{80-x}Ni_xCr_{20}$ ($14 \leq x \leq 30$) alloys. *Physical Review B*, 53(18):12148 – 12159, May 1996.

[111] H. Takagi, B. Batlogg, H. L. Kao, J. Kwo, R. J. Cava, J. J. Krajewski, and W. F. Peck. Systematic evolution of temperature-dependent resistivity in $La_{2-x}Sr_xCuO_4$. *Physical Review Letters*, 69(20):2975 – 2978, November 1992.

[112] K. Takenaka, J. Nohara, R. Shiozaki, and S. Sugai. Incoherent charge dynamics of $La_{2-x}Sr_xCuO_4$: Dynamical localization and resistivity saturation. *Physical Review B*, 68(13):134501, October 2003.

[113] B. Bucher, P. Steiner, J. Karpinski, E. Kaldis, and P. Wachter. Influence of the spin gap on the normal state transport in $YBa_2Cu_4O_8$. *Physical Review Letters*, 70(13):2012 – 2015, March 1993.

[114] N. E. Hussey, K. Nozawa, H. Takagi, S. Adachi, and K. Tanabe. Anisotropic resistivity of $YBa_2Cu_4O_8$: Incoherent-to-metallic crossover in the out-of-plane transport. *Physical Review B*, 56(18):R11423 – R11426, November 1997.

[115] Johnpierre Paglione and Richard L. Greene. High-temperature superconductivity in iron-based materials. *Nature Physics*, 6:645–658, 2010.

[116] High-temperature superconductivity. http://en.wikipedia.org/wiki/High-temperature_superconductivity.

[117] Michelle Johannes. The iron age of superconductivity. *Physics*, 1:28, October 2008.

[118] H. Ding, P. Richard, K. Nakayama, K. Sugawara, T. Arakane, Y. Sekiba, A. Takayama, S. Souma, T. Sato, T. Takahashi, Z. Wang, X. Dai, Z. Fang, G. F. Chen, J. L. Luo, and N. L. Wang. Observation of Fermi-surface-dependent nodeless superconducting gaps in $Ba_{0.6}K_{0.4}Fe_2As_2$. *EPL (Europhysics Letters)*, 83(4):47001, 2008.

[119] P. Prelovšek and I. Sega. Anomalous normal-state properties of iron pnictides: phenomenological theory. *Physical Review B*, 81:115121, 2010.

[120] J. L. Peng, Z. Y. Li, and R. L. Greene. Growth and characterization of high-quality single crystals of $R_{2-x}Ce_xCuO_{4-y}$ (R = Nd, Sm). *Physica C: Superconductivity*, 177(1 - 3):79 – 85, 1991.

[121] S. R. Saha, N. P. Butch, K. Kirshenbaum, and Johnpierre Paglione. Evolution of bulk superconductivity in $SrFe_2As_2$ with Ni substitution. *Physical Review B*, 79(22), June 2009.

[122] S. N. Mao. *Fabrication, characterization, and properties of $Nd_{2-x}Ce_xCuO_{4-y}$ superconducting thin films and heterostructures*. PhD thesis, University of Maryland - College Park, 1997.

[123] X. Q. Xu, S. N. Mao, Wu Jiang, J. L. Peng, and R. L. Greene. High Temperature resistivity of $Nd_{1.85}Ce_{0.15}CuO_4$ superconductors. *unpublished*.

[124] P. L. Bach, S. R. Saha, K. Kirshenbaum, J. Paglione, and R. L. Greene. High Temperature Resistivity in the Iron-Pnictides and the Electron-Doped Cuprates. *submitted*.

[125] C. Urano, M. Nohara, S. Kondo, F. Sakai, H. Takagi, T. Shiraki, and T. Okubo. LiV_2O_4 Spinel as a Heavy-Mass Fermi Liquid: Anomalous Transport and Role of Geometrical Frustration. *Physical Review Letters*, 85(5):1052 – 1055, July 2000.

[126] G. Cao, W. H. Song, Y. P. Sun, and X. N. Lin. Violation of the Mott-Ioffe-Regel limit: high-temperature resistivity of itinerant magnets $Sr_{n+1}Ru_nO_{3n+1}$ ($n = 2, 3, \infty$) and $CaRuO_3$. *Solid State Communications*, 131(5):331 – 336, 2004.

[127] M. Gurvitch and A. T. Fiory. Resistivity of $La_{1.825}Sr_{0.175}CuO_4$ and $YBa_2Cu_3O_7$ to 1100 K: Absence of saturation and its implications. *Physical Review Letters*, 59(12):1337 – 1340, September 1987.

[128] P. A. Lee, N. Nagaosa, and X.-G. Wen. Doping a Mott insulator: Physics of high-temperature superconductivity. *Review of Modern Physics*, 78(1):17–85, January 2006.

[129] M. Calandra and O. Gunnarsson. Violation of Ioffe-Regel condition but saturation of resistivity of the high-T_c cuprates. *EPL (Europhysics Letters)*, 61(1):88 – 94, 2003.

[130] F. Rullier-Albenque, D. Colson, A. Forget, and H. Alloul. Hall Effect and Resistivity Study of the Magnetic Transition, Carrier Content, and Fermi-Liquid Behavior in $Ba(Fe_{1-x}Co_x)_2As_2$. *Physical Review Letters*, 103(5):057001, July 2009.

[131] S. Kasahara, T. Shibauchi, K. Hashimoto, K. Ikada, S. Tonegawa, R. Okazaki, H. Ikeda, H. Takeya, K. Hirata, T. Terashima, and Y. Matsuda. Evolution from Non-Fermi to Fermi Liquid Transport Properties by Isovalent Doping in $BaFe_2(As_{1-x}P_x)_2$ Superconductors. *Physical Review B*, 81:184519, 2010.

[132] Melissa Gooch, Bing Lv, Bernd Lorenz, Arnold M. Guloy, and Ching-Wu Chu. Evidence of quantum criticality in the phase diagram of $K_xSr_{1-x}Fe_2As_2$ from measurements of transport and thermoelectricity. *Physical Review B*, 79(10):104504, March 2009.

[133] W. Z. Hu, J. Dong, G. Li, Z. Li, P. Zheng, G. F. Chen, J. L. Luo, and N. L. Wang . Origin of the Spin density wave instability in AFe_2As_2 (A=Ba, Sr) as revealed by optical spectroscopy. *Physical Review Letters*, 101:257005, 2008.

[134] L. Boeri, O. V. Dolgov, and A. A. Golubov. Electron-phonon properties of pnictide superconductors. *Physica C: Superconductivity*, 469(9-12):628 – 634, 2009.

[135] A. A. Golubov, O. V. Dolgov, A. V. Boris, A. Charnukha, D. L. Sun, C. T. Lin, A. F. Shevchun, A. V. Korobenko, M. R. Trunin, and V. N. Zverev. Normal state resistivity of $Ba_{1-x}K_xFe_2As_2$: evidence for multiband strong-coupling behavior. 8 November 2010.

[136] Ying Jia, Peng Cheng, Lei Fang, Huiqian Luo, Huan Yang, Cong Ren, Lei Shan, Changzhi Gu, and Hai-Hu Wen. Critical fields and anisotropy of $NdFeAsO_{0.82}F_{0.18}$ single crystals. *Applied Physics Letters*, 93(3):032503, 2008.

[137] J. J. Hamlin, R. E. Baumbach, D. A. Zocco, T. A. Sayles, and M. B. Maple. Superconductivity in single crystals of LaFePO. *Journal of Physics: Condensed Matter*, 20(36):365220, 2008.

[138] B. C. Sales, M. A. McGuire, A. S. Sefat, and D. Mandrus. A semimetal model of the normal state magnetic susceptibility and transport properties of $Ba(Fe_{1-x}Co_x)_2As_2$. *Physica C*, 470:304, 2010.

[139] Lei Fang, Huiqian Luo, Peng Cheng, Zhaosheng Wang, Ying Jia, Gang Mu, Bing Shen, I. I. Mazin, Lei Shan, Cong Ren, and Hai-Hu Wen. Roles of multiband effects and electron-hole asymmetry in the superconductivity and normal-state properties of $Ba(Fe_{1-x}Co_x)_2As_2$. *Physical Review B*, 80(14):140508, October 2009.

[140] L. Edman, B. Sundqvist, E. McRae, and E. Litvin-Staszewska. Electrical resistivity of single-crystal graphite under pressure: An anisotropic three-dimensional semimetal. *Physical Review B*, 57(11):6227–6230, March 1998.

[141] Q. Shao, G. Liu, D. Teweldebrhan, and A. A. Balandin. High-temperature quenching of electrical resistance in graphene interconnects. *Applied Physics Letters*, 92:202108, 2008.

[142] K. Yagasaki, S. Notsu, Y. Shimoji, T. Nakama, R. Kaji, T. Yokoo, J. Akimitsu, M. Hedo, and Y. Uwatoko. Resistivity and thermopower of CaB_6 single crystal. *Physica B: Physics of Condensed Matter*, 329:1259–1260, 2003.

[143] D. T. J. Hurle and S. Weintroub. The Electrical Resistivity of Monocrystalline and Liquid Bismuth. *Proceedings of the Physical Society*, 76:163, 1960.

[144] Cedric Weber, Kristjan Haule, and Gabriel Kotliar. Apical oxygens and correlation strength in electron and hole doped copper oxides. *Physical Review B*, 82:125107, 2010.

[145] Tsuyoshi Sekitani, Michio Naito, and Noboru Miura. Kondo effect in underdoped n-type superconductors. *Physical Review B*, 67(17):174503, May 2003.

[146] Matthias Brinkmann, Thomas Rex, Heinrich Bach, and Kurt Westerholt. Extended Superconducting Concentration Range Observed in $Pr_{2-x}Ce_xCuO_{4-\delta}$. *Physical Review Letters*, 74(24):4927–4930, June 1995.

[147] Osamu Matsumoto, Aya Utsuki, Akio Tsukada, Hideki Yamamoto, Takaaki Manabe, and Michio Naito. Erratum: Synthesis and properties of superconducting T'-R_2CuO_4 ($R =$Pr, Nd, Sm, Eu, Gd) (vol 79, 100508, 2009). *Physical Review B*, 81(9), March 1 2010.

[148] S. Lee, J. Jiang, Y. Zhang, C. W. Bark, J. D. Weiss, C. Tarantini, C. T. Nelson, H. W. Jang, C. M. Folkman, S. H. Baek, A. Polyanskii, D. Abraimov, A. Yamamoto, J. W. Park, X. Q. Pan, E. E. Hellstrom, D. C. Larbalestier, and C. B. Eom. Template engineering of Co-doped $BaFe_2As_2$ single-crystal thin films. *Nature Materials*, 9:397–402, 28 February 2010.

[149] Fong-Chi Hsu, Jiu-Yong Luo, Kuo-Wei Yeh, Ta-Kun Chen, Tzu-Wen Huang, Phillip M. Wu, Yong-Chi Lee, Yi-Lin Huang, Yan-Yi Chu, Der-Chung Yan, and Maw-Kuen Wu. Superconductivity in the PbO-type Structure α-FeSe. *Proceedings of the National Academy of Sciences*, 105(38):14262–4, September 23 2008.

[150] Y Han, W Y Li, L X Cao, S Zhang, B Xu and B R Zhao. Preparation and superconductivity of iron selenide thin films. *Journal of Physics: Condensed Matter*, 21:235702, 2009.

[151] Serena Margadonna, Yasuhiro Takabayashi, Martin T. McDonald, Karolina Kasperkiewicz, Yoshikazu Mizuguchi, Yoshihiko Takano, Andrew N. Fitch, Emmanuelle Suarde and Kosmas Prassides. Crystal structure of the new $FeSe_{1-x}$ superconductor. *Chem. Commun.*, pages 5607–5609, 2008.

[152] S. B. Zhang, Y. P. Sun, X. D. Zhu, X. B. Zhu, B. S. Wang, G. Li, H. C. Lei, X. Luo, Z. R. Yang, W. H. Song and J. M. Dai . Crystal growth and superconductivity of $FeSe_x$. *Superconductor Science and Technology*, 22:015020, 2009.

[153] T. M. McQueen, Q. Huang, V. Ksenofontov, C. Felser, Q. Xu, H. Zandbergen, Y. S. Hor, J. Allred, A. J. Williams, D. Qu, J. Checkelsky, N. P. Ong and R. J. Cava . Extreme Sensitivity of Superconductivity to Stoichiometry in $Fe_{1+\delta}Se$. *Physical Review B*, 79:014522, 2009.

[154] Kuo-Wei Yeh, Tzu-Wen Huang, Yi-Lin Huang, Ta-Kun Chen, Fong-Chi Hsu, Phillip M. Wu, Yong-Chi Lee, Yan-Yi Chu, Chi-Liang Chen, Jiu-Yong Luo, Der-Chung Yan and Maw-Kuen Wu . Tellurium substitution effect on superconductivity of the α-phase Iron Selenide. *Europhysics Letters*, 84:37002, 2008.

[155] G. F. Chen, Z. G. Chen, J. Dong, W. Z. Hu, G. Li, X. D. Zhang, P. Zheng, J. L. Luo, andN. L. Wang . Electronic properties of single-crystalline $Fe_{1.05}Te$ and $Fe_{1.03}Se_{0.30}Te_{0.70}$. *Physical Review B*, 79:140509(R), 2009.

[156] B. C. Sales, A. S. Sefat, M. A. McGuire, R. Y. Jin, Y. D. Mandrus, and Y. Mozharivskyj. Bulk Superconductivity at 14 K in Single Crystals of $Fe_{1+y}Te_xSe_{1-x}$. *Physical Review B*, 79:094521, 2009.

[157] E. Bellingeri, R. Buzio, A. Gerbi, D. Marrè, S. Congiu, M. R. Cimberle, M. Tropeano, A. S. Siri, A. Palenzona, and C. Ferdeghini. High quality epitaxial $FeSe_{0.5}Te_{0.5}$ thin films grown on $SrTiO_3$ substrates by pulsed laser deposition. *Superconductor Science and Technology*, 22(10):105007, 2009.

[158] Yoshinori Imai, Ryo Tanaka, Takanori Akiike, Masafumi Hanawa, Ichiro Tsukada, and Atsutaka Maeda. Superconductivity of $FeSe_{1-x}Te_x$ Thin Films Grown by Pulsed Laser Deposition. *arXiv:0908.1316v1, arXiv:0910.2301v1*, 2009.

[159] Y. Imaia, T. Akiikea, R. Tanakaa, H. Takahashia, M. Hanawab, I. Tsukadab, and A. Maeda. Growth of superconducting $FeSe_{0.5}Te_{0.5}$ thin films by pulsed-laser deposition. *Physica C: Superconductivity*, 470(20):1038–1041, 1 November 2010.

[160] M.H. Fang, B. Qian, H.M. Pham, J.H. Yang, T.J. Liu, E.K. Vehstedt, L. Spinu, and Z.Q. Mao. Superconductivity and antiferromagnetism in $Fe(Te_{1-x}S_x)_y$ system. *arXiv:0811.3021v2*.

[161] Yoshikazu Mizuguchi, Fumiaki Tomioka, Shunsuke Tsuda, Takahide Yamaguchi and Yoshihiko Takano. Superconductivity in S-substituted FeTe. *Applied Physics Letters*, 94:012503, 2009.

[162] Zhanqiang Liu, Aihua Fang, Fuqiang Huang, and Mianheng Jiang. Superconductivity in layered iron Selenide induced by cobalt- and sodium-doping. *arXiv:0808.1784v1*, 2008.

[163] Yoshikazu Mizuguchi, Fumiaki Tomioka, Shunsuke Tsuda, Takahide Yamaguchi and Yoshihiko Takano. Substitution Effects on FeSe Superconductor . *Journal of the Physical Society of Japan*, Vol. 78, No. 7:074712, July 2009.

[164] S. Finkelman, M. Sachs, G. Droulers, N. P. Butch, J. Paglione, P. Bach, R. L. Greene, and Y. Dagan. Resistivity at low temperatures in electron-doped cuprate superconductors. *Physical Review B*, 82(9):094508, September 2010.